UNIVERSITÀ DEGLI STUDI DI PADOVA

UNIVERSITA' DEGLI STUDI DI PADOVA

Dipartimento di Fisica e Astronomia "Galileo Galilei"

PhD school in Physics, XXXVII cycle

coordinator: Prof. G. Monaco

Final dissertation

Mixing between single-particle and intruder configurations towards the N=20 Island of Inversion

lifetime measurements in ^{37}S

Thesis written with the financial contribution of Istituto Nazionale di Fisica Nucleare, Laboratori Nazionali di Legnaro (INFN-LNL).

Supervisors:

Dott. José Javier Valiente Dobón,

Dott. Andrea Gottardo,

Dott. Franco Galtarossa

Candidate:

Luca Zago

#2039337

A.Y. 2023-2024

Luca Zago

Mixing between single-particle and intruder configurations towards the N=20 Island of Inversion: lifetime measurements in ^{37}S

Final dissertation of the PhD School in Physics, September 2024

Supervisors: Dr. José Javier Valiente Dobón, Dr. Andrea Gottardo and Dr. Franco Galtarossa

Referees: Prof. Simone Bottoni (Università degli Studi di Milano "La Statale") and Dr. François de Oliveira Santos (GANIL, CEA/DSM-CNRS/IN2P3, Caen, France)

University of Padova

Dipartimento di Fisica e Astronomia "G. Galilei"

PhD School in Physics

via F. Marzolo, 8

35121 Padova

Contents

List of Figures

List of Tables

Glossary

ADL	AGATA Data Library
AG	AGATA Alternative Generator
AGATA	Advanced GAmma Tracking Array
ATC	AGATA Triple Cluster
BU	Builder Unit
CAD	Computer Assisted Drawing
CoM (CM)	Center-of-Mass
DCM	Decay Curve Method
DCOD	Distributed Caen-Orsay DAQ
DDCM	Differential Decay Curve Method
DSAM	Doppler Shift Attenuation Method
DWBA	Distorted-Wave Born Approximation
EM	Electromagnetic
ESPE	Effective Single Particle Energy
FE	Fusion Evaporation
FWHM	Full Width Half Maximum
FWTM	Full Width Tenth Maximum
GANIL	Grand Accélérateur National d'Ions Lourds
GGP	Global Gigabit Processor
GRETA	Gamma-Ray Energy Tracking Array
HFB	Hartree-Fock-Bogoliubov
HPGe	Hyper-Purity Germanium
INFN	Istituto Nazionale di Fisica Nucleare
IoI	Island of Inversion
LF	Local Filter
LNL	Legnaro National Laboratories
MC	Monte-Carlo

MNT	Multi-nucleon Transfer
NARVAL	Nouvelle Acquisition temps-Réel Version 1.2 Avec Linux
OFT	Orsay Forward Tracking
OM	Optical Model
PCB	Printed Board Circuit
PSA	Pulse-Shape Analysis
RDDS	Recoil Distance Doppler Shift
RU	Read-out Unit
SM	Shell Model
SPIDER	Silicon PIe DEtectoR

Abstract

The disappearance of the N=20 shell closure in the so-called "island of inversion" around ^{32}Mg is one of the most striking examples of the strength of nucleon-nucleon correlations. In this region, the change in shell ordering leads to quadrupole-deformed intruder states (based on a multi-particle multi-hole configuration) competing in energy with the spherical ones, and yrast in the case of ^{32}Mg. Single-particle and intruder states can be mapped as function of Z in odd nuclei located one neutron away from shell closures. In the N=21 case, the available spectroscopic evidence points out the appearance of strong branching ratios among the single-particle and collective intruder configurations in ^{37}S, suggesting that they mix significantly, contrary to the notion of ^{37}S being well out the island of inversion. However, a precise quantification of this phenomenon in terms of transition strength is still lacking. The first excited state ($3/2^-$ state at 646 keV) is the only one with a measured lifetime, but no transition probability has been firmly determined for the intruder states, in particular those decaying to the *a priori* spherical single-particle states. A combined DSAM+RDDS measurement has been performed to measure such transition probabilities, in particular for the 2p-1h $3/2^+$ state at 1397 keV and the 3p-2h $7/2^-$ at 2023 keV, exploiting the performance of the AGATA spectrometer in terms of energy and angular resolutions. The ^{37}S nucleus has been produced via the ^{36}S(d,p) reaction in inverse kinematics, detecting the recoiling protons in the silicon array SPIDER to obtain an accurate reconstruction of the excitation energy of ^{37}S. The short lifetimes measured point to large M1 and/or E2 strengths connecting the intruder and spherical states. This would imply a significant mixing between the configurations, arising questions about the determination of the neutron $p_{3/2}$-$p_{1/2}$ single-particle strength distribution in ^{37}S.

Overview

Atomic nuclei can be described as an A-body quantum systems of strongly-interacting fermions, with A ranging from 1 to more than 200. As such, most nuclei are mesoscopic systems whose description poses a formidable physical problem. Therefore, Nuclear Physics has always been rooted in the fruitful conversation between the theoretical prediction and the experimental observation of phenomena to pin down the nature of the nuclear Hamiltonian.

A shell structure, similar to the one found in atomic orbitals, has been noticed quite early from the systematics of even-even nuclei. A shell structure has been proved to arise naturally from a system of A quasi-free fermions in a central potential, implying that the single-particle degrees of freedom rule the structure of the nuclear chart. On the other hand, low-energy excitations observed in mid-shell nuclei could be best described by models based on collective coordinates, as if nuclei were composed by a continuous fluid that undergoes quantum rotations and vibrations. As these two very different excitation modes coexist in the same energy range, they cannot be decoupled invoking the separation of scales argument. Therefore, the formalization of a single nuclear Hamiltonian that provides a unified description of all nuclear phenomena, applicable from hydrogen to the super-heavy elements, has proved elusive.

The non-perturbative nature of QCD in the low-energy regime makes the nuclear interaction in the nuclear medium already very difficult to solve. Therefore, nuclear theory has the task to derive an interaction that could be either effective or from first principles. After the interaction has been defined, the non-relativistic Schrödinger equation needs to be solved, and then observables can be computed. Different many-body methods can be

employed to perform these calculations. For example, nuclear potentials can be derived with chiral Effective Field Theory (χEFT) and Renormalization Group directly from QCD [1]. The ambition is then to calculate nuclear properties with the potential as only input. Many-body methods such as in-medium similarity renormalization group (IM-SRG) or Monte Carlo methods can be used to perform the calculations. This approach has been called *ab initio* method. Otherwise, a phenomenological interaction can be derived from the measured properties of nuclei in a region of the nuclear chart. This potential can then be used to derive the spectroscopic properties of nuclei by performing the exact diagonalization of the resulting nuclear Hamiltonian in a restricted space of configurations. This is the approach of Interacting Shell Model calculations [2]. An alternative approach to the one of the Shell Model is to derive the eigenstates of the hamiltonian with a variational approach, minimizing an energy density functional, such as the Skyrme or the Gogny, on a set of trial wavefunctions. The nuclear potential can then be either phenomenological or from χEFT. This is the so-called Energy Density Function (EDF) approach. Spectroscopic properties are then obtained with the use of many-body methods such as the Quasi-Random Phase Approximation (QRPA) or Projected Generator Coordinate Method (PGCM) [3, 4].

On the other hand, from the experimental side, the construction of high-intensity Radioactive Ion Beam (RIB) facilities has unlocked the possibility to reach previously unexplored regions of the nuclear landscape. The observation of exotic nuclei offers the opportunity to test the predictive power of the models far from the region in which they were benchmarked. Measurements and predictions in the extrema of the nuclear landscape are currently one of the most vivid conversations between models and experiments in Nuclear Physics.

While the unexplored regions of the nuclear landscape provide a fertile field for new discoveries, interest in the stability valley has not diminished. Indeed, while the spectroscopic information is abundant in these nuclei, new high-precision measurements are called to provide stringent experimental constraints on the predictions, highlighting successes and pointing towards deficiencies that might be amplified in the extrapolation towards the more exotic regions. Therefore, the stability valley still provides with ample opportunities for deepening our understanding of nuclear structure.

In this context, reduced transition probabilities are one of the most sensitive probes to small variations of the nuclear wavefunctions of excited states. This makes γ-ray spectroscopy an invaluable tool in the Nuclear Physics arsenal to understand the evolution of nuclear structure. As a consequence, precise nuclear lifetime measurements near the stability valley provide one of the most stringent benchmark tests of the theoretical predictions.

The subject of this thesis is the measurement of lifetime of excited intruder and single-particle states in the nucleus ^{37}S combining a direct transfer (d,p) reaction with the Recoil Differential Doppler Shift (RDDS) technique and Doppler Shift Attenuation Method (DSAM) in a single experiment. Located one neutron away from the stable ^{36}S, the low-lying excited spectrum of ^{37}S can be built not only by populating orbits above the N=20 shell gap, forming spherical single-particle states, but also populating "intruder" orbitals, i.e. orbitals which lie outside of the model space description of the *sd* shell nuclei.

The combination of two well-established methods for nuclear lifetime measurement, with a combined range spanning tens of femtoseconds to hundreds of picoseconds, with a highly selective reaction such as the (d,p) allows for a precise measurement in ^{37}S with a good control on the populations of both intruder and single-particle states. As lifetime measurements are biased by the presence of unknown or uncontrolled feeders, the high excitation energy resolution achievable with a (d,p) reaction allows to put stringent constraints on the population of excited states without severe loss of statistics that would decrease the statistical significance of the results.

Lifetimes obtained in this work are then compared to the predictions obtained with the *sdpf-u* and *sdpf-u-mix* interactions in the shell-model framework. The *sdpf-u* interaction was developed to perform calculations in the *sd* and *pf* shells. It was then modified to describe the driving force behind the appearance of the N=20 IoI, leading to the *sdpf-u-mix* interaction. Therefore, this latter interaction should accurately reproduce the mixing between single-particle and intruder states in a nucleus above the northern edge of the IoI, while the *sdpf-u* should instead only be able to reproduce the single-particle states, and not the intruder ones.

This thesis is organized as follows: **Chapter 1** introduces some nuclear physics concepts relevant to this work, with a short introduction on direct reactions, electromagnetic decays and some general frameworks for nuclear structure theoretical calculations, concluding with a focus on the role of ^{37}S in the nuclear structure evolution towards the so-called N=20 Island of Inversion; **Chapter 2** goes more into details into the technical aspects of the experiment subject of this work, focusing on the accelerator and the detection equipment; conversely, raw data processing is described in **Chapter 3**, along with the applied optimization procedures and the results of different simulation benchmarks; results of the analysis and their discussion is presented in **Chapter 4** and **Chapter 5**; these results are then compared to state-of-the-art shell-model calculations in **Chapter 6**. The thesis ends in **Chapter 7** with some concluding remarks and considerations for further development of the subject.

1 Introduction

In this Chapter only some basic concepts of nuclear physics theory will be covered, with a focus on the experimental observables that have been studied in this work. In Section 1.1 a basic portrait of the main concepts of the Nuclear Shell Model is given. This was the approach chosen to perform nuclear structure calculations for this work. As mentioned in the Overview, several other different models provide predictions in the *sdpf* shell, such as *mean-field* and *ab-initio* methods, with good accuracy. The shell-model approach is still however considered the golden standard in this region [5]. γ-ray decay in then illustrated in Section 1.2. In the same Section, two methods for the measurement of nuclear lifetimes are also described. In Section 1.3 the kinematics and the dynamics of the reaction used in this experiment, the direct one-neutron-adding reaction, will be given, along with some spectroscopic observables that will be discussed in the thesis. Finally, in Section 1.4, an overview of the physics case will be presented, along with some information present in literature.

1.1 The Shell Model

The Shell Model (SM) envisages the nucleus as an A-body quantum system of independent fermions immersed in a mean-field potential, to which a spin-orbit (SO) term is added. The single-particle energies are therefore the eigenvalues of this hamiltonian, and are grouped according to their oscillator quantum number n, forming *shells*. These shells are separated by a large energy gap

in correspondence to specific numbers of protons or neutrons, called *magic numbers*, which are traditionally 2, 8, 20, 50, 82, 126. Each magic number has an associated *shell gap*. The associated wavefunctions are denoted by three quantum numbers, n, l and j [6]. The standard ordering of the shell-model orbits can be found in Figure 1.

This hamiltonian however does not take into account the residual nucleon-nucleon interactions that cannot be reabsorbed in the central mean-field potential. The SM (or in this case, the Interacting Shell Model) substitutes the full hamiltonian $\mathcal{H}$ (containing all full self-energy and interaction terms) with an effective hamiltonian $\mathcal{H}_{\text{eff}}$ such that the eigenvalues (i.e. the energy) of this effective hamiltonian are the same of the original one. The effective eigenfunctions are then written in a base of Slater determinants of single-particle orbits [8].

The advantage of this approach is that while the Hilbert space of the real Hamiltonian is the full space of all single-particle orbits, the Hilbert space of the effective Hamiltonian is reduced to a valence space plus a inert core. The size of the valence space will determine the computational effort needed to perform the diagonalization of the secular problem. Since the number of needed Slater determinants increases factorially with the number of available valence orbits, the valence space needs to be truncated in order to keep under realistical computational conditions [9].

In general, any effective interaction can be split into a monopole ($\mathcal{H}_m$) and multipole ($\mathcal{H}_M$) terms [10, 11]. The monopole part is the m-state weighted average of the diagonal matrix elements of the interaction. It thus represents the properties of the original interaction that do not depend on the angular momentum orientation. It is therefore responsible of the evolution of the spherical single-particle field. The multipole part is the Hamiltonian component remaining after the subtraction of the monopole part. It contains terms depending on the angular momentum coupling and it responsible for correlations. Pairing and quadrupole interactions are its main components [12]. This latter part has been revealed to be universal and rather well understood. While the multipole part of effective interactions is quite reliably obtained from the Hamiltonian renormalization to the specific valence space, the monopole component is in general adjusted phenomenologically to reproduce the observed shell gaps. Even small variations in the centroids can produce large changes in the relative

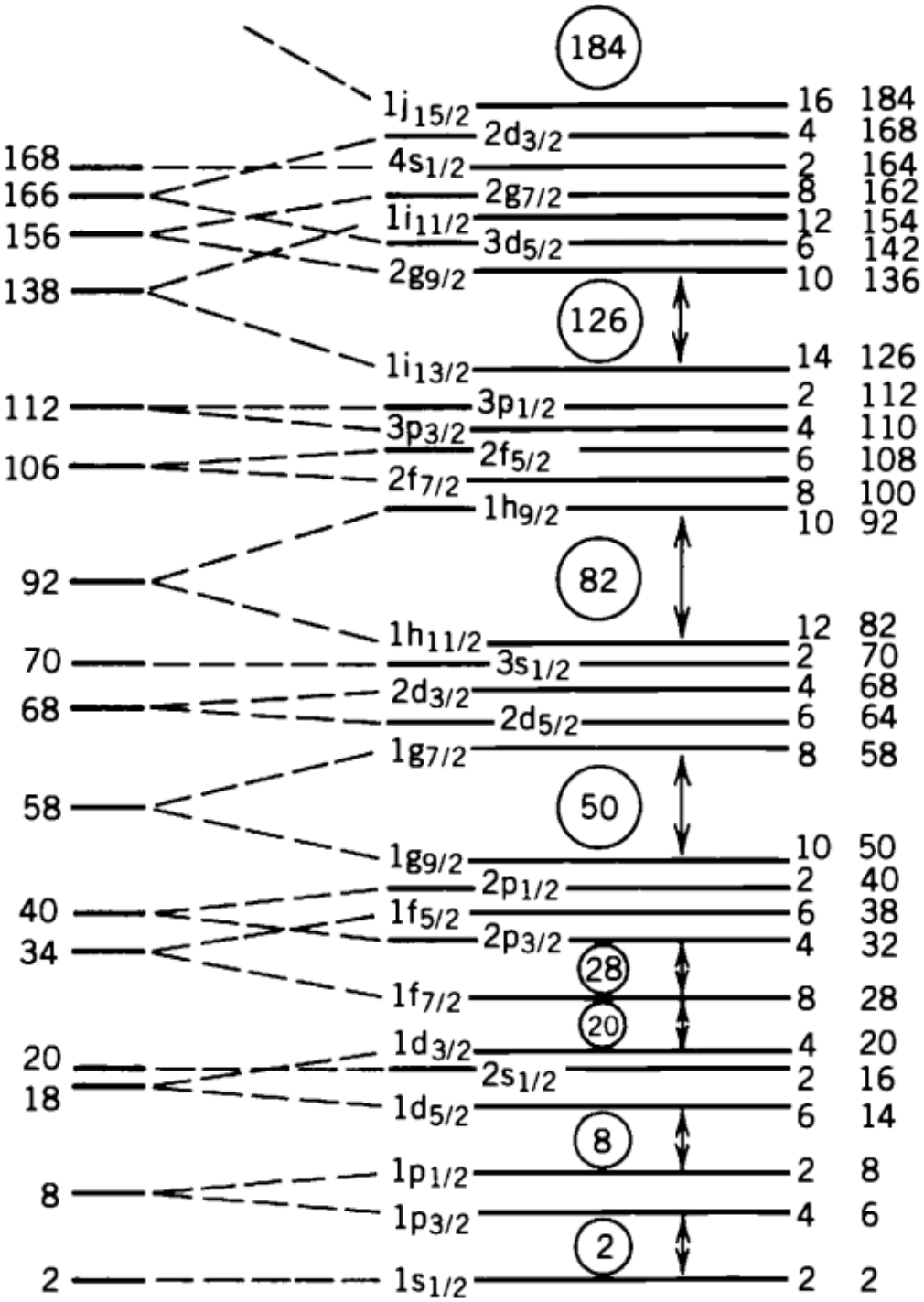

Figure 1: Shell-model single-particle orbits. Taken from [7].

position of the different configurations. Three-body contributions have been proven to provide an essential contribution to monopole Hamiltonian [13].

There are several well-known and used interactions publicly available, depending on the valence space chosen and the method used to derive them. They can be very roughly categorized in effective interactions, derived from G-matrix renormalization of the bare nucleon-nucleon interaction, or "fitted" interaction, where a large amount of experimental observables is used to derive the matrix elements of the interaction. An example of the first kind is the Kuo-Brown interaction [14], while for the second the USD [15], GXPF1 [16] or JUN45 [17]. Given the dependence of the interaction on the choice of valence space, all interactions cover different mass ranges of the nuclear chart. This work examines excitations in the pf shell, with possible core-breaking contributions from the sd shells. The tailored interaction for the region is the *sdpf-u-mix* proposed by F. Nowacki, A. Poves and E. Caurier [18], which is the interaction used by A. Poves to perform the calculations for this work. This interaction is an evolution of the previous *sdpf-u* interaction, itself based on the USD interaction, where the matrix elements were adjusted to reproduce the spectroscopy of the N=20 Island of Inversion (see §1.4).

Several suites are also available for carrying out the calculations, such as OXBASH [19], NUSHELL [20] and KSHELL [21]. The Strasbourg-Madrid codes (ANTOINE, NATHAN [22]) are capable of dealing with basis of 10^{10} Slater determinants, and are the ones used for the shell-model calculations performed for this thesis.

1.2 Electromagnetic transitions

A nucleus produced in an excited state will tend to reach the ground-state level by one or multiple subsequent decays. The decay that does not change the nature of a nucleus is the electromagnetic decay, or γ-ray decay, in which the nucleus produces a photon to de-excite from a higher excited state to a lower one.

It is convenient to describe the electromagnetic radiation produced by a nucleus in terms of a multipole expansion. Recalling Maxwell's classical theory

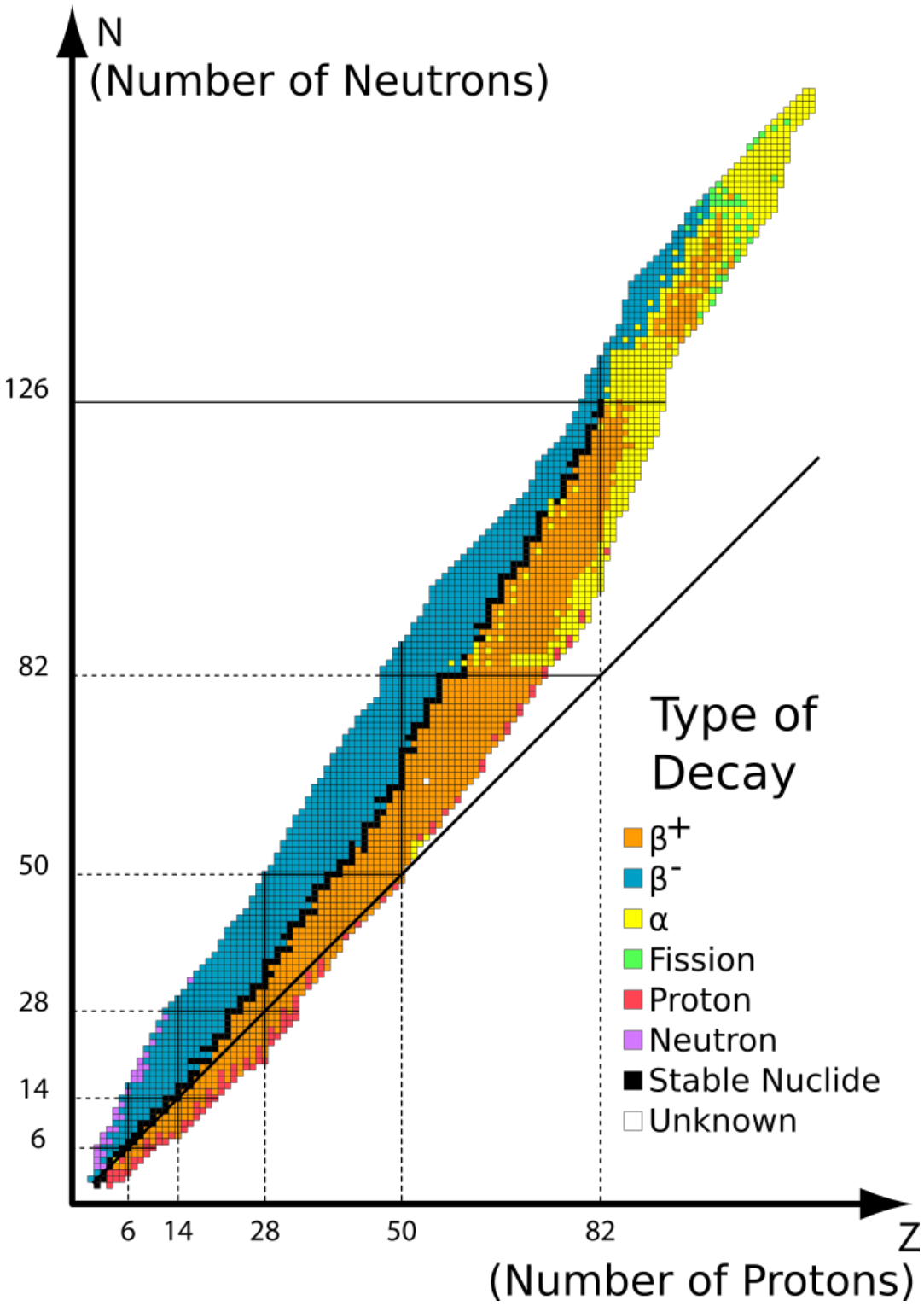

Figure 2: The Segré chart. Adapted from [23].

L	Electric (E)	Magnetic (M)
1	$1.590 \cdot 10^{15}$	$1.758 \cdot 10^{13}$
2	$1.225 \cdot 10^{9}$	$1.355 \cdot 10^{7}$
3	$5.705 \cdot 10^{2}$	$6.305 \cdot 10^{0}$
4	$1.696 \cdot 10^{-4}$	$1.875 \cdot 10^{-6}$

Table 1: Numerical coefficients for the calculation of the transition rates. Taken from [24].

of electromagnetism, applying canonical quantization and assuming the long-wavelength limit, it is possible to show that the transition rate Γ_{fi} of a γ decay connecting an initial state i to a final state f is connected to the wavefunctions of the two connected states via the following equation:

$$\Gamma_{fi} = \frac{8\pi}{\epsilon_0 \hbar} \frac{L+1}{L((2L+1)!!)^2} \left(\frac{E_\gamma}{\hbar c}\right)^{2L+1} B(\sigma L; J_i \rightarrow J_f), \tag{1}$$

where L, E_γ and σ are angular momentum, energy and multipolarity of the photon, J_i and J_f are the spin of the initial and final states, and $B(\sigma L; J_i \rightarrow J_f)$ is the so-called reduced transition probability, which is in turn connected to the wavefunctions of the initial and final states via the equation

$$B(\sigma L; J_i \rightarrow J_f) = \frac{1}{2J_i + 1} |\langle f||\hat{O}_{\sigma L}||i\rangle|^2, \tag{2}$$

where $\hat{O}_{\sigma L}$ is the electromagnetic operator of character σ (electric, E, or magnetic, M) and multipolarity L. For the lowest multipolarities, the numerical coefficients are given in Table 1. The lifetime of the decaying state is the reciprocal of the total width, i.e.

$$\sum_f \Gamma_{fi} = \frac{1}{\tau_i}, \tag{3}$$

thus the lifetime of the state is proportional to the reduced transition probability and thus to the overlap between the initial and final wavefunction through the electromagnetic decay operator.

In case of multiple γ-ray decays from the same state, then the total lifetime has to be multiplied by the corresponding *branching ratio* (BR) to get the partial

L	Electric (E)	Magnetic (M)
1	$1.0 \cdot 10^{14}\ A^{2/3}$	$5.6 \cdot 10^{13}\ A^{0}$
2	$7.3 \cdot 10^{7}\ A^{4/3}$	$3.5 \cdot 10^{7}\ A^{2/3}$
3	$3.4 \cdot 10^{1}\ A^{2}$	$1.6 \cdot 10^{1}\ A^{4/3}$
4	$1.1 \cdot 10^{-5}\ A^{8/3}$	$4.5 \cdot 10^{-6}\ A^{2}$

Table 2: Numerical coefficients for the calculation of the Weisskopf estimates. Taken from [24].

lifetime, and the corresponding reduced transition probability. If instead a single transition has different multipolarity components, then a *mixing coefficient* δ can be defined. In the example of a E2/M1 mixed transitions, the mixing coefficient is defined as

$$|\delta| = \left| \frac{\langle f \,||\, \hat{E2} \,||\, i \rangle}{\langle f \,||\, \hat{M1} \,||| \, i \rangle} \right| \propto \sqrt{\frac{B(E2; i \to j)}{B(M1; i \to j)}} \tag{4}$$

which translates in the measured lifetime as

$$\tau_{fi}(E2) = \frac{1}{1+\delta^2}\tau_{fi} \quad \tau_{fi}(M1) = \frac{\delta^2}{1+\delta^2}\tau_{fi}. \tag{5}$$

Transition rates are usually expressed in terms of Weisskopf (single-particle) units, W.u. [25]. One Weisskopf unit is the reduced transition probability value of a transitions in which a single nucleon from a pure spherical single-particle orbital decays to another one. Under these extreme single-particle assumptions, the transition amplitudes can be calculated analytically, and are often used as reference point when evaluating the hindrance or enhancement of a transition. The numerical coefficients for the Weisskopf estimates can be found in Table 2.

1.2.1 Nuclear lifetime measurements

Due to the huge range of nuclear lifetimes that are found in the Segré chart (from 10^{-15} to 10^{9} s), no single technique to measure lifetimes exists. Different techniques cover different ranges, e.g. see [24, 26, 27]. The techniques

employed for this work are the Recoil Distance Doppler Shift (RDDS) and the Doppler Shift Attenuation Method (DSAM). Both of them are methods based on the Doppler shift effect that cover the range $10 \div 100$ ps and $10 \div 1000$ fs, respectively.

When a γ ray is emitted by a moving nucleus, it is affected by Doppler shift, i.e. the measured energy in the laboratory E' is not the Center-of-Mass (CM) energy E of the transition, but

$$E' = \frac{E}{\gamma(1 - \beta \cos\theta)} \tag{6}$$

where β and γ are the Lorentz factors and θ is the relative angle between the direction of motion and of emission of the γ ray.

Recoil Distance Doppler Shift (RDDS) method

The RDDS technique exploits the fact that γ rays emitted in flight are affected by Doppler shift, while those emitted by a nucleus at rest are not. Therefore, after the production, the nucleus is slowed down in a different, high-Z material until completely at rest. In order to stop the produced nucleus, a sufficiently thick foil called *stopper* is placed immediately after the target at a known distance x. The distance must be chosen so that the travel time between target and stopper is comparable with the lifetime that is to be measured [28]. Control on the distance between the two foils is achieved through the use of a device called *plunger*, which will be described in detail in Chapter 2, thus the technique is also referred to as *plunger* technique.

In these conditions, the γ ray can be therefore emitted either while the nucleus is travelling between target and stopper or when the nucleus is at rest in the stopper. The total γ-ray spectrum therefore will show two components, a so-called *shifted* (S) component (affected by Doppler shift), and a *stopped* or *unshifted* (U) component, respectively. Since nuclear γ decay is a statistical process, the areas of the two components will be

$$S(x) = Ne^{-\frac{x}{\beta\gamma c\tau}} \quad U(x) = N(1 - e^{-\frac{x}{\beta\gamma c\tau}}) \tag{7}$$

where N is the total number of nuclei produced in the excited state of interest and β and γ the Lorentz factors. In the previous equation, direct population is assumed (i.e. no feeding transition from above). By calculating the ratio

$$R(x) = \frac{U(x)}{S(x) + U(x)} = e^{-\frac{x}{\beta\gamma c\tau}}, \tag{8}$$

the lifetime τ can be extracted by a fit of different datasets acquired for different values of the distance x. A pictorial representation of the RDDS technique can be found in Figure 1.3(a).

Doppler Shift Attenuation method (DSAM)

For short lifetimes, the RDDS technique becomes unfeasible, as the needed distances become sub-micrometric. For example, with a velocity of ∼0.1c, the lower lifetimes measurable are of the order of some picoseconds. The idea of the DSAM is therefore to set this distance to zero and immediately slow down the ion in a high-Z material by evaporating or gluing the target material on a suited backing. In this case, the observed γ ray will have energy equal to

$$E'(t) = \frac{E}{\gamma(t)(1 - \beta(t)\cos\theta)}, \tag{9}$$

where now β and γ are time dependent due to the slowing down of the ion from the production moment to the emission moment [27]. In the γ-ray spectrum, this will create a distribution which will not be anymore gaussian, but will be dependent on the lifetime, the response function and the angular coverage of the experimental setup. Such distribution is referred to as "lineshape". A pictorial representation of this technique can be found in Figure 1.3(b). The experimental spectrum can then be compared to a series of realistic Monte Carlo simulations, and the lifetime can be extracted by minimization of a statistical figure of merit, e.g. the chi-square χ^2 or the log-likelihood $-\log\mathcal{L}$.

1.3 Direct reactions

Direct reactions are fast, peripherical collisions with small energy and momentum transfer, and without the formation of an intermediate compound state.

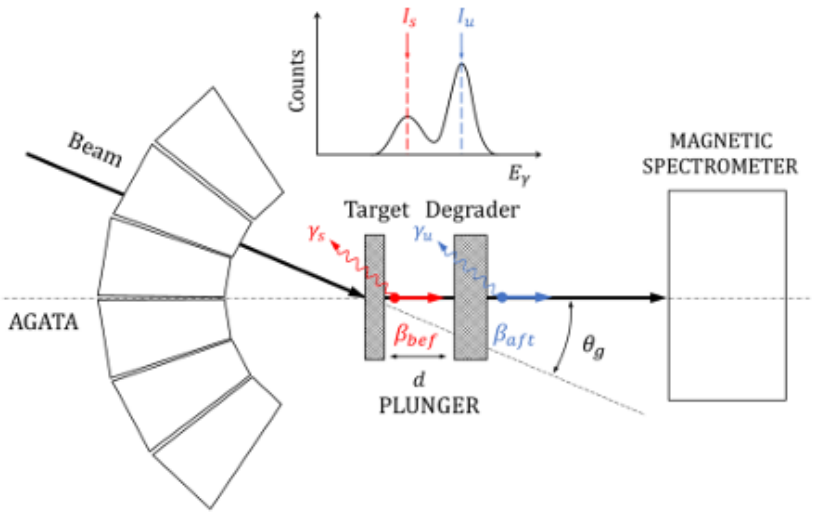

(a)

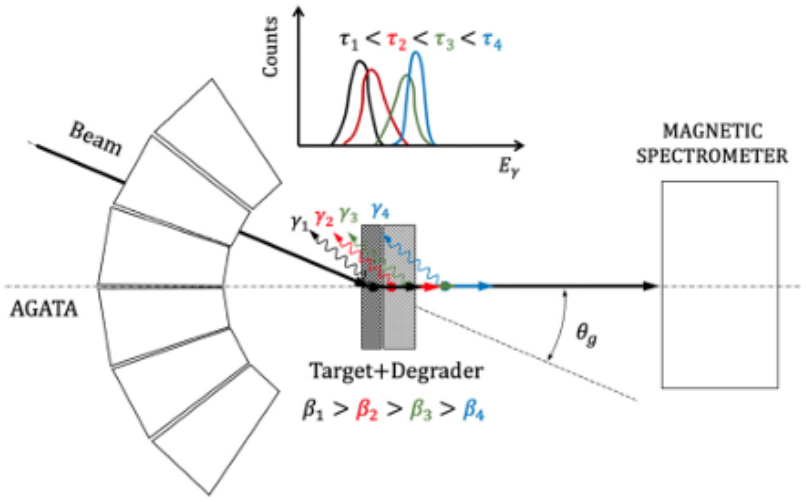

(b)

Figure 3: Pictorial representations of a) RDDS technique, b) DSAM technique. Taken from [29]. In their case, the authors were referring to the AGATA+PRISMA configuration, hence the "MAGNETIC SPECTROMETER" block on the right. In this case, a charged-particle detector at backwards angles has been used (see Chapter 2).

Only a few nucleons (in this case, only a neutron) are exchanged between the participants.

The typical setup for this kind of studies is an Enge-type spectrograph [30], where the reaction is performed in direct kinematics. They are still used in various laboratories, such as ANL, ANU, TUNL, FSU. The experimental method consists in curving with a magnetic field the emitted light particles at forward angles and measure at what distance they intersect a known axis. Since the particles are of identical species, the curvature is determined entirely by their momentum after the reaction. The resolution in excitation energy is therefore mostly determined by the granularity of the position detector. Furthermore, as these reactions involve light particles and in general thin targets, energy straggling is almost negligible. Such resolutions are hardly, if at all, attainable with other detection setups of light ions, and definitely not reachable in heavy-ion reactions. The limited acceptance and the necessity to physically rotate the array to scan the angular range however proved very cumbersome, requiring the use of fairly intense beams [31]. Compact segmented Si charged-particle detectors have become nowadays the standard setup in many laboratories. Covering portions of the solid angle, measurements at different polar angles can be done without the need to move the setup. On the other hand, the main drawback for these kind of detectors is their relatively low radiation hardness, which makes the detection of particles in very forward direction ($<$20 deg) very difficult. To compensate for the loss of angular coverage, inverse kinematics was instead used, as in this configuration the light ion is preferentially emitted at more backward angles in the laboratory frame. Furthermore, this is the only configuration possible with exotic ions such as the one produced in RIB facilities. In the last decades, direct transfer reactions are one of the flagship techniques of the ISOLDE-REX facility at CERN, ISAC at TRIUMF and LISE at GANIL. This kind of configuration is also the one used in the present experiment. The reason for this choice was not however due to the unfeasibility of a target, as ^{36}S is stable, but because the use of direct kinematics would have impeded lifetime measurements with the RDDS and DSAM methods, as the velocity of the outgoing ^{37}S ions (around 1% speed of light) would have been too low to appreciate variations in the Doppler shift.

The main advantage of compact charged-particle detectors is their relative small size and γ-ray transparency, which permits the coupling with a γ-ray spectrometer. Such configuration allows one to employ the good particle

resolution given by the transfer reaction to the superior γ-ray resolution of HPGe detectors. This setup is therefore the instrument of choice for precision experiments and at the forefront of nuclear structure research [32, 33].

Especially in the context of nuclear lifetime measurements, particle spectroscopy resolution is critical. In general, multiple excited states can γ decay to the same level. It has been known with the work of Bateman [34] that in case there is a presence of a feeder, the decay rate of the daughter species is a convolution between the decay rate of the daughter and the one of the parents. This is particularly critical in nuclear lifetime measurements, as the presence of (known or unknown) feeders can introduce a systematic deviation of the measured value with respect to the true one. This effect can be reduced or eliminated by imposing a condition on the Q value of the reaction, selecting only the direct population of the state of interest (as in Ref. [29]). This comes of course at the cost of statistics if excited states are not resolved. Particle energy resolution is therefore critical to reduce this cost to a minimum, and direct transfer reaction yield the best particle resolution available at LNL for low-energy experiments.

Given the importance that particle spectroscopy had in this experiment, a very short overview of the reaction kinematics and dynamics will be given in the following Sections. However, for the remainder of this discussion, the description of the theory of direct reactions will limit to the case of interest, the one-neutron-adding reaction d(^{36}S, p)^{37}S, also more simply (although incorrectly) denoted ^{36}S(d, p)^{37}S.

Reaction kinematics

Due to the absence of compound nucleus formation and the fact that the reaction is binary, the detection of the energy and direction of motion of one of the two partners of the outgoing channel is enough to completely determine the kinematics of the reaction.

Due to momentum conservation

$$\begin{gathered} p_d^\mu + p_{36}^\mu = p_p^\mu + p_{37}^\mu \\ p_d^\mu = (m_d, 0, 0, 0) \quad p_{36}^\mu = (m_{36} + E_{36}, 0, 0, \sqrt{E_{36}^2 + 2m_{36}E_{36}}) \\ p_p^\mu = (E_p + m_p, \vec{p}_p) \quad p_{37}^\mu = (E_{37}, \vec{p}_{37}) \end{gathered} \tag{10}$$

where E_{36} denotes the beam energy, E_{37} indicates the sum of kinetic energy, excitation energy and mass of the outgoing ^{37}S nucleus, while E_p only the kinetic contribution of the proton total energy. By measuring energy and position of the outgoing proton, p_p^μ is completely determined, and so is univocally p_{37}^μ. Denoting with θ and ϕ the spherical coordinates of the outgoing proton, and with $p_p = \sqrt{E_p^2 + 2m_pE_p}$ its momentum, the ^{37}S momentum explicitly results to be:

$$p_{37}^\mu = \begin{pmatrix} E_{36} + m_{36} + m_d - E_p - m_p \\ -p_p \sin\theta\cos\phi \\ -p_p \sin\theta\sin\phi \\ \sqrt{E_{36}^2 + 2m_{36}E_{36}} - p_p\cos\theta \end{pmatrix} \tag{11}$$

From the total energy of the ^{37}S, the excitation energy can then be extracted by subtracting the mass and the kinetic energy contributions.

Reaction dynamics

The probability of populating a state in ^{37}S, i.e. its cross-section, is determined by the dynamics of the reaction, which is briefly illustrated in this Section. The incoming channel, or *partition*, is composed of the beam and the target, while the outgoing partitions n, are composed of the beam-like and target-like partners in a particular excited state combination. Since the outgoing proton has no excited states, n indicates the excited state of ^{37}S, ordered by energy, that can be populated keeping momentum and energy conservation.

Both the incoming and the outgoing partitions have their own exact wavefunction Ψ, which is the eigenstate of total energy E of of the full Hamiltonian

$\mathcal{H}$. In general, this Hamiltonian will contain a kinetic part $\hat{T}$, both in and for the center of mass, and several potential terms which describe the internal structure of both projectile and target and their interaction. Out of all possible solutions of the problem, only the functions satisfying two conditions are chosen. The first one is that, asymptotically, the wavefunction, far upstream from the interaction point, reduces to a planar wave, i.e.

$$\Psi(\mathbf{K}, \mathbf{R}, \xi) \xrightarrow[R\to\infty]{} \phi(\xi) e^{i\mathbf{KR}} \tag{12}$$

where $\mathbf{K}$ is the momentum in the CM frame, $\mathbf{R}$ is the relative distance between target and projectile and ξ the set of internal variables that describe the structure of the projectile and target. The second one is that the wavefunction, far downstream the interaction point, has to be the sum of the incoming unscattered planar waves plus the scattered spherical waves produced by elastic, inelastic and transfer channel, modulated by a factor f called *scattering amplitude*:

$$\begin{aligned}\Psi_n(\mathbf{K}', \mathbf{R}', \xi') \xrightarrow[R'\to\infty]{} \phi(\xi) e^{i\mathbf{KR}} + \sum_n f_n(\theta, \phi)\phi(\xi') \frac{e^{i\mathbf{K'R'}}}{R'} \\ + \text{elastic} + \text{inelastic}.\end{aligned} \tag{13}$$

In the case of unpolarized beam and axial symmetry (as in this case), $f_n(\theta, \phi) = f_n(\theta)$. The scattering amplitude is also directly connected to the cross section of the reaction

$$\frac{d\sigma_n}{d\Omega} \sim |f_n(\theta)|^2 \sim |T_n(\theta)|^2, \tag{14}$$

where the transition matrix T has been introduced [35, 36].

Since the focus is on the neutron transfer channel, the incoming partition can be represented as the ensemble of a proton and a neutron, in the cluster deuteron, plus the ^{36}S nucleus, and the outgoing partition as the ensemble of a neutron and the ^{36}S, forming a cluster ^{37}S, plus a proton. The scattering problem can therefore be written in the two equal representations of the incoming partition, with its set of coordinates, or of the outgoing one. The two representations are called *prior* and *post*, respectively.

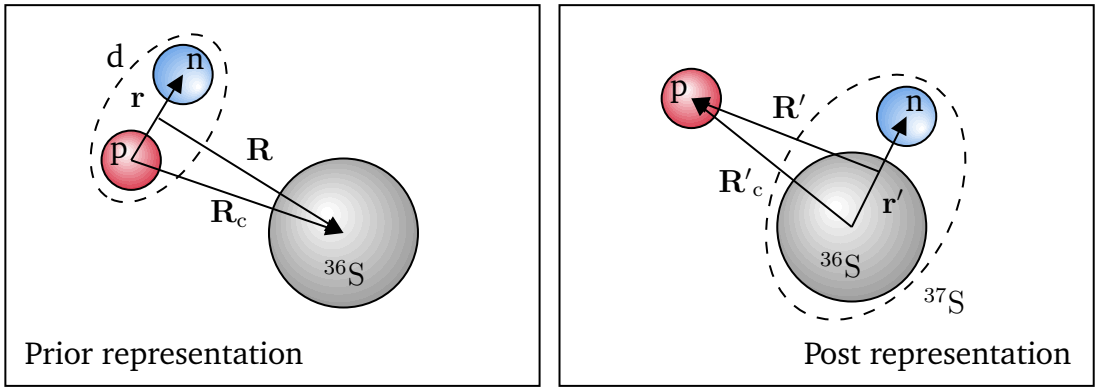

Figure 4: Prior (left) and post (right) representations.

The associated hamiltonians are:

$$\begin{aligned}\mathcal{H}_{\text{prior}} =& T_{\mathbf{R}} + U_{d-36}(\mathbf{R}) + \mathcal{H}_d(\mathbf{r}) + V_{\text{prior}}(\mathbf{r}, \mathbf{R}),\\ \mathcal{H}_{\text{post}} =& T_{\mathbf{R}'} + U_{p-37}(\mathbf{R}') + \mathcal{H}_{37}(\mathbf{r}') + V_{\text{post}}(\mathbf{r}', \mathbf{R}').\end{aligned} \tag{15}$$

where

$$\begin{aligned}V_{\text{prior}}(\mathbf{r}, \mathbf{R}) &= V_{n-36}(\mathbf{r}') + [U_{p-36}(\mathbf{R}_c) - U_d(\mathbf{R})]\\ V_{\text{post}}(\mathbf{r}', \mathbf{R}') &= V_{p-n}(\mathbf{r}) + [U_{p-36}(\mathbf{R}_c) - U_{p-37}(\mathbf{R}')]\end{aligned} \tag{16}$$

In these equations, $\mathbf{R}$ is the CM distance, while $\mathbf{r}$ is the distance between the two components of the cluster. $\mathbf{R_c}$ is then the vector connecting the proton to the ^{36}S nucleus. The prime is used to differentiate between prior and post representation coordinates. A graphical representation can be found in Figure 4. The first term is usually called *binding term*, while the term in bracket *remnants* [37]. The transition matrix in this case corresponds then to vector of matrix elements coupling the incoming wavefunction to the outgoing ones, either in the prior or post representation, through either the prior or post potentials.

The Distorted Wave Born approximation corresponds to swapping one of the exact wavefunctions with a distorted wave corresponding to a bound state created by an appropriate optical potential. In this way, the transition matrix can be calculated as

$$T_n(\theta) = \int \chi_n^{(-)*}(\mathbf{K_n}, \mathbf{R}) \Phi_n^*(\xi_n) V_{\text{post}}(\mathbf{r}', \mathbf{R}') \chi^{(+)}(\mathbf{K}, \mathbf{R}) \Phi(\xi) d\xi_n d\mathbf{R}' \tag{17}$$

where $\Phi_n^{(+)}(\xi_n)\chi_n$ is the outgoing distorted wave and $\chi(\xi)^{(-)}\Phi(\xi)$ the incoming wave. One also can assume that the interaction potential is independent of the internal degrees of freedom, so that the integral over the internal coordinates can be factorized in an overlap integral between the incoming and outgoing internal wavefunctions. Assuming that the outgoing internal wavefunction can be written as a single-particle bound state, then

$$\int \Phi_n^*(\xi_n) \Phi(\xi) d\xi_n = C^2 S \tag{18}$$

where the spectroscopic factor C^2S has been introduced. This factor makes sure that the base of the outgoing wavefunctions is properly normalized, but also estimates the overlap between the outgoing wavefunction and the initial wavefunction plus one neutron. Furthermore, since in general the potential is spherical, the transition matrix will consist of a combination of Legendre polynomials, scaled by spectroscopic factors. Since angular momentum conservation applies, only a selection of Legendre polynomials will contribute to the cross section of a particular state. The angular distribution of the cross section will therefore be peaked at different angles according to the transferred angular momentum l.

Equation 17 can be solved iteratively starting from a trial function to obtain the scattering matrix, and from that the differential cross-section. There are numerous codes that allow to perform such kind of calculations, such as DWUCK4 and DWUCK5 [38], PTOLEMY [39] and TWOFNR [40]. The calculations for this work were performed with the reaction code FRESCO [41] with the input file that can be found in Appendix A1. Several optical potentials for light particles exists in literature, drawn from various global fits of elastic scattering data. The ones used for these calculations are the ones of An and Cai for the deuteron potential [42], and the one of Koning and Delaroche for the proton optical potential [43].

1.4 ^{37}S and the N=20 Island of Inversion

It has been known for several decades now that the so-called "magic numbers" are not fixed reference point valid throughout the nuclear chart. Indeed, monopole terms of the nuclear interaction (e.g. tensor, p-n) may change the relative spacing between different shells, opening or closing gaps far from stability at different magic numbers than the ones close to the stability valley. In particular regions of the nuclear chart, furthermore, the strength of quadrupole correlations and pairing might equal the already weakened shell gap and subvert the expected standard ordering of shell-model configurations [44]. The first and most famous evidence of this comes from the systematics of the first excited 0^+ in even-even nuclei at N=20. The excitation energy of the deformed 0^+_2 state lowers with decreasing Z, until it becomes the ground-state in ^{32}Mg, while the spherical one becomes non yrast [45, 46]. ^{32}Mg has been considered therefore the center of the so-called N=20 "Island of Inversion" (IoI).

However, even at the boundaries of the IoI the expected ordering might be altered. Quadrupole correlations and pairing interaction still influence nuclear structure formation, and they lower the excitation energy of *intruder* configurations (configurations with particles in a higher HO shell), which then can mix with the regular ones. This mixing might provide further correlation energy and a a further decrease in excitation energy. The precise evolution of the mixing is however still not entirely understood and mapped all around the island, as spectroscopic studies become increasingly difficult with increasing exoticity due to the rapidly falling production cross sections.

The ideal playground for studies regarding the IoIs are clearly even-even nuclei along a neutron shell-closure. In the N=20 case, despite being fairly close to the stability line, nuclei near or in the island can only be reached with multi-nucleon transfer (MNT) or fragmentation reactions with stable nuclei such as ^{40}Ar, ^{36}S, ^{30}Si, ^{26}Mg, or with direct reactions/Coulomb excitation starting from radioactive ion beams.

In odd nuclei, the unpaired particle can populate directly an orbit above the Fermi level, forming a single-particle structure, or couple with npnh intruder configurations. As these npnh states lie low in excitation energy, in competition

with non-intruder configurations, the $(n+1)$pnh configurations in the odd nuclei coexist with the 1p ones.

The two most-studied nuclei of the N=21 chain below the Z=20 gap are ^{39}Ar and ^{37}S. For these two nuclei, extensive spectroscopic studies were performed in the past years, identifying a plethora of single-particle and intruder states. A comparison between the partial level schemes of these two nuclei can be found in Figure 5.

In the Figure, the first two $3/2^-$ and $7/2^-$ states of both ^{39}Ar (Z=18, N=21) and ^{37}S (Z=16, N=21) are depicted, along with the first $3/2^+$ state. In both nuclei, the lowest $3/2^-$ and $7/2^-$ are considered single-particle states with strong spectroscopic factor, while the higher lying ones are associated to intruder 3p2h configurations. They are depicted in black and blue color, respectively. From the comparison of the two level schemes, it can be noticed that the intruders configuration lower in energy with the removal of two protons, as correlations become stronger approaching the IoI. The greatest difference is in the decays of the $7/2^-$ states in the two isotones: while in ^{39}Ar it decays only to the $7/2^-$ ground state, in ^{37}S it decays to both the $7/2^-$ ground state and the $3/2^-$ first excited state. This latter pure E2 decay is not predicted by shell-model calculations with the *sdpf-u-mix* interaction [48]. However, the spin assignment of this state is uncertain, and its structure is still mostly unknown. As no lifetimes were ever measured in this nucleus (except for the first excited state), the same can be said for all excited states (single-particle and intruder alike) in this nucleus. The combination of particle spectroscopy and lifetime measurements can help pin down the structure of this nucleus, assess the accuracy of the shell-model predictions, and map shell evolution towards the IoI.

Moreover, odd nuclei allow for the study of another term of the nuclear interaction, which cannot be studied as precisely in even-even nuclei: the spin-orbit term.

Since the birth of the shell model, it was clear that a spin-orbit term was necessary to reproduce the observed shell structure. However, it appeared almost immediately that calculating the strength of this coupling to reproduce the experimental results was a much harder problem [49]. The characterization the spin-orbit monopole effect on effective single-particle energies has

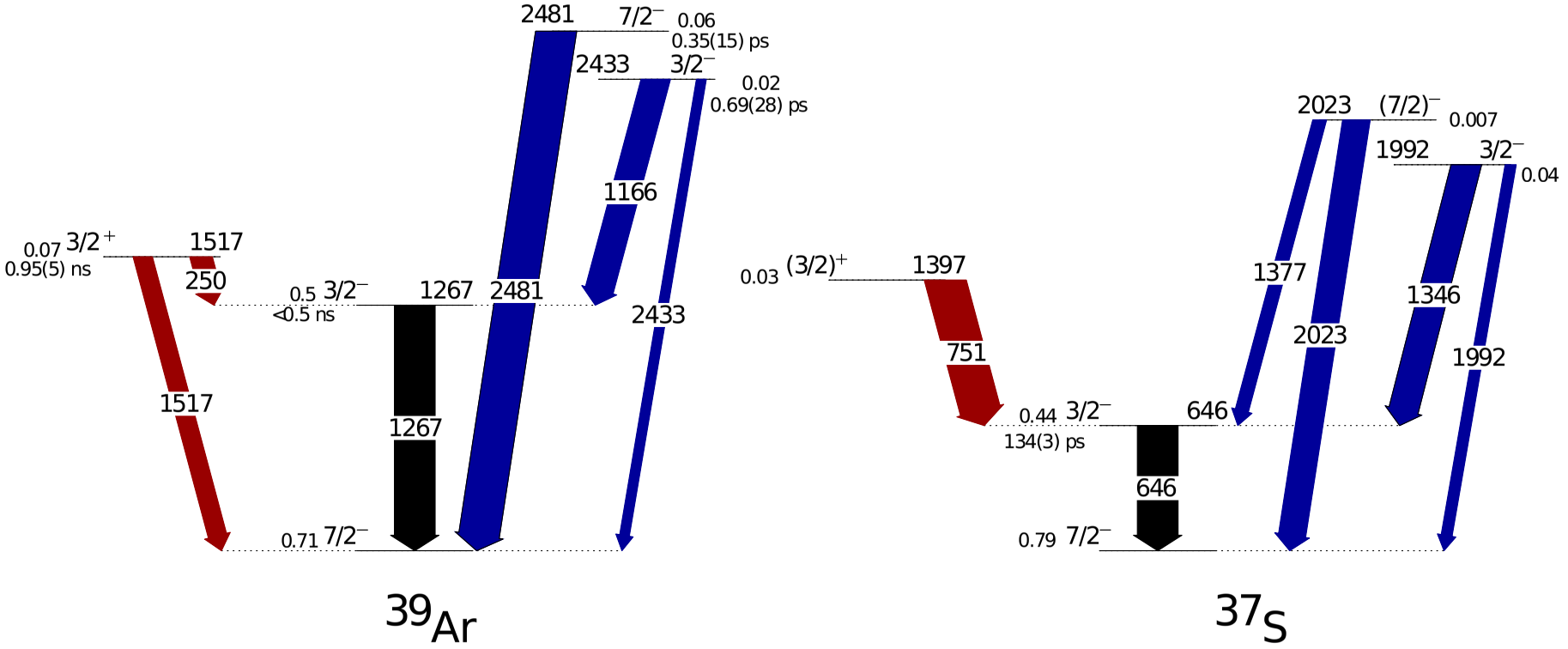

Figure 5: Comparison between the ^{39}Ar and ^{37}S low-energy partial level schemes. In both schemes, levels are organized in bands as follows: the central one for single-particle states, left band for the even parity intruders, right band for the odd parity intruders. In black, the decays coming from the single-particle states, in red and blue the ones from the even and odd parity intruder states. Arrow thickness is proportional to the branching ratio. Half-lives and spectroscopic factors (when known) are reported next to the spin values. All values are drawn from the Adopted values [47]. Y axis is not in scale.

been attempted by following the energy separation of spin-orbit partner shells along isotonic chains. This has been made possible by the the availability of radioactive beams since the years 2000s. At first such studies were carried out around N=28; however, the softness of these nuclei was not ideal for the deduction of quantities regarding this term [44]. The focus then moved to the region of the N=21 chain.

In the N=21, ^{39}Ar and ^{37}S can be populated with a direct reaction in stable beam facilities, while ^{35}Si and ^{33}Mg need radioactive ion beam facilities. Indeed, these two last nuclei have been mainly studied in facilities such as GANIL [50], RIKEN [51] and NSCL [52, 53]. From the spectroscopic evidence, the Effective Single Particle Energies (ESPE) can then be experimentally deduced, with the Baranger prescription [54]. However, there are several theoretical and experimental difficulties. From the experimental point of view, it is unclear how reliable the ESPE extraction is. Indeed, in the Baranger prescription, it is assumed to have complete spectroscopic knowledge at least up to the separation energy. This is hardly ever the case. Therefore, several criteria have been employed: for example, Kay *et al.* [55] suggest to use all the available states for the estimation of the ESPE, while Sorlin *et al.* [56] use only the strongest fragments of the single-particle strength. On the other hand, from the theoretical point of view, particular caution has been recently suggested when comparing the experimental estimates to shell-model calculations [57, 58].

In this region, the spin-partner shells are the $p_{1/2-3/2}$, the $d_{3/2-5/2}$ and the $f_{5/2-7/2}$ orbits. While no particular trend has been observed for the $f_{5/2-7/2}$ splitting, the $p_{1/2-3/2}$ splitting is known to decrease with decreasing Z - a unique feature in the Segré chart. More so, Sorlin *et al.* [56] argue that between ^{37}S and ^{35}Si the $p_{1/2-3/2}$ spin-orbit splitting drastically reduces. This has been explained with a sudden reduction of the spin-orbit coupling with decreasing Z, with contributions from correlations and the proximity to the continuum. Duguet *et al.* [59] concur with Sorlin *et al.* in arguing, with *ab-initio* calculations, that the existence of a drastic reduction of the spin-orbit coupling is a consequence of the existence of a so-called *bubble structure* in ^{34}Si. Most nuclei are characterized by an almost constant matter and charge density up to the nuclear radius. At the nuclear radius, the density rapidly falls to zero. This has been likened by Fermi to the behaviour of a drop of a classical liquid. A bubble nucleus, conversely, shows a density profile that reaches a

maximum at the nuclear radius and then depletes near the nuclear center. While this phenomenon was thought to exists in super-heavy nuclei, different calculations seem to agree in predicting the existence of a bubble structure in ^{34}Si, which then would be the lightest example of this phenomenon [60]. This prediction has not been experimentally verified by electron scattering experiments, but spectroscopic studies indeed have revealed that ^{34}Si has a proton $s_{1/2}$ shell completely depleted [61].

On the other hand, Kay *et al.* [55] argue that not only this splitting decrease is more modest as calculated by Sorlin *et al.*, but that the decrease can be fully explained by the proximity to the continuum, without invoking any weakening of the spin-orbit coupling. Low-l orbits react to the proximity to the continuum by becoming larger, hence gaining binding energy and lingering below the separation energy. They argue that this geometric effect would therefore account for the spin gap reduction when passing from S to Si.

The secondary objective of this thesis is to provide a complementary view on the issue. Experimentally, it is very difficult to discriminate between intruder states and weak fragments of single-particle strength on the basis of spectroscopic factors. On the other hand, intruder states should be characterized by very collective E2 transitions to other intruder states and suppressed E2 transitions to single-particle configurations, while single-particle states should decay to states of the same nature via E2 transitions of about 1 W.u.. Via lifetime measurements and a comparison with state-of-the-art shell model calculations, the results of this work can provide insight on the nature of the excited states in this nucleus. This perspective would be different and complementary with the one provided by particle spectroscopy. Furthermore, a re-measurement of the angular distributions and spectroscopic factors can be done, although the setup of the experiment was not optimized for this objective, as the main goal was to perform lifetime measurements.

This could only be made possible by the choice of a direct transfer reaction with respect to a MNT reaction. In general, exclusive cross section in MNT reactions are very difficult to calculate, while in direct transfer reactions the exclusive cross section is given by a DWBA calculation and the spectroscopic factor. Furthermore, MNT reactions preferentially populate medium-to-high spin and yrast states in these nuclei, while non-yrast levels are highly suppressed. A rather complete spectroscopy of the low-energy non-yrast states therefore

is highly hindered by the choice of a MNT reaction, while a direct transfer reaction allows one to have a high degree of control on the production cross sections.

This work builds of course on top of the abundant spectroscopic information that is already present in literature regarding excited states in ^{37}S.

Experimental studies on ^{37}S were performed as soon as enriched ^{36}S of Soviet origin became available at the end of the 60s, first in the United States, then in Europe. Before this landmark discovery, only (n,α) studies could be performed starting from ^{40}Ar, such as the one of Davis *et al.* [62] and Kardonsky *et al.* [63]. They both observe the ground state plus five excited states with an energy resolution of a few tens of keV.

Starting from 1978, a battery of (d,p) reactions from ^{36}S were performed to assess the excitation energy spectrum of this nucleus [64–66]. These studies show a single-particle structure dominated by the population of the $f_{7/2}$, $p_{3/2}$ and $p_{1/2}$ orbits, but also the presence of low-lying intruder states with small spectroscopic factors. They however frequently lacked γ-ray spectroscopy detectors, and only relied on particle spectroscopy to deduce structure information. In any case, the excellent proton energy resolution (a few keV) allowed for the disentanglement of most of the members of each multiplet of states. However, their spectra show high target contamination and high-statistics carbon build-up peaks that covered part of the excitation energy spectrum.

In 1985 and 1995 two (n, γ) studies were performed by Raman *et al.* [67, 68] and Beer *et al.* [69]. The first β-decay study reported is from Dufour *et al.* [70] in 1986, which produced ^{37}S nuclei by fragmentation of a ^{40}Ar primary beam in the then brand new LISE facility in GANIL. Several γ rays were observed but they were not placed in a level scheme, nor reported in the evaluations. These studies mark the cutoff point for the Adopted Levels. The evaluated and adopted level scheme can be found in Figure 6. With the advent of the large γ-ray spectrometers, ^{37}S was produced again in a CLARA-PRISMA experiment at LNL [71]. Their experimental reconstructed level scheme can be found in Figure 7. This is at the moment the most extensive γ-ray spectroscopic study performed so far in this nucleus. In Table 3, the Evaluated level energies plus the ones of Chapman *et al.* are reported.

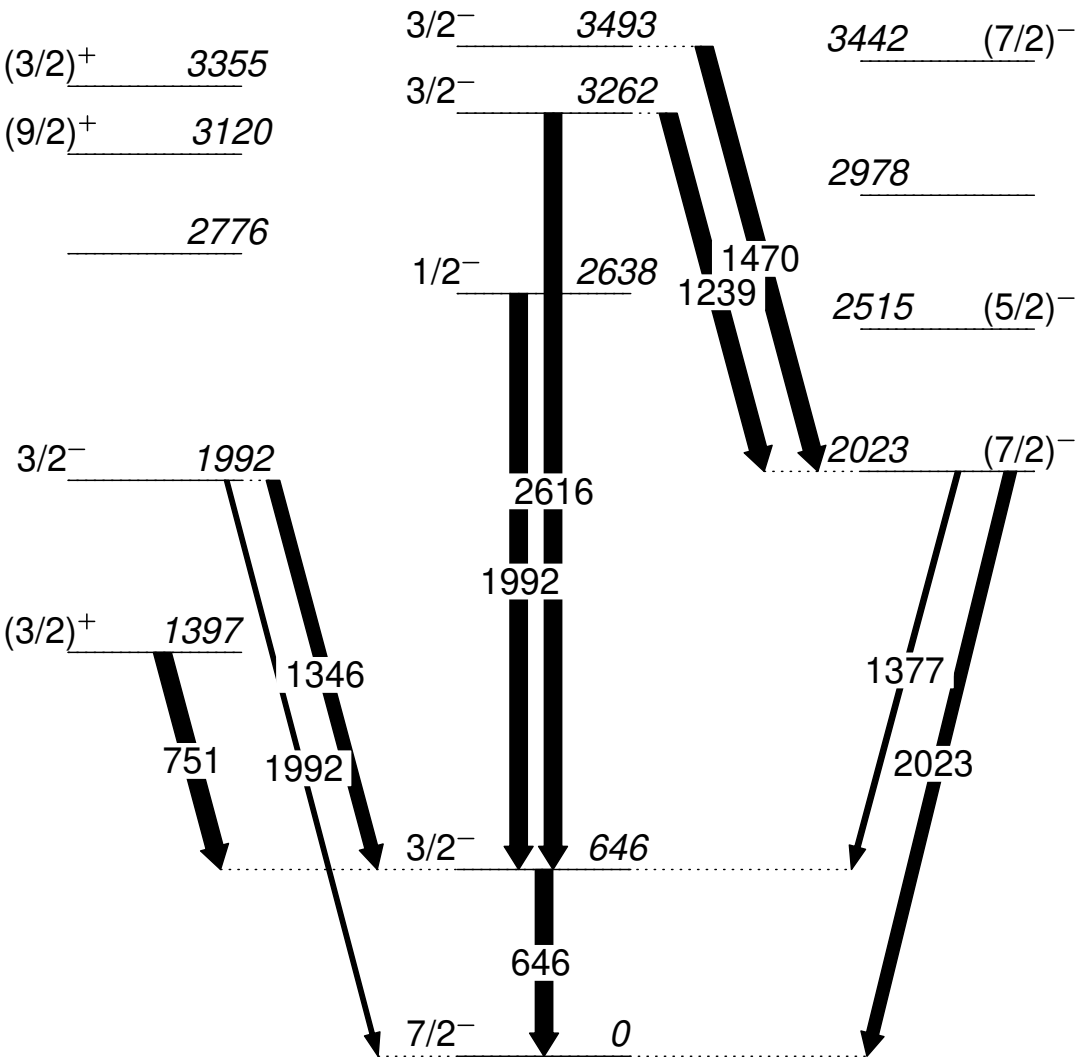

Figure 6: Partial adopted level scheme for ^{37}S. Only states below 3.5 MeV are represented. Arrow thickness is proportional to the γ decay branching ratio.

Subsequently, ^{37}S was studied again with the AGATAdemo+PRISMA setup [72] and more recently again in the AGATA+PRISMA campaign at LNL [73]. In these last two cases, the experiment was focused on lifetime measurements with the MNT reaction to probe the evolution of nuclear structure approaching the IoI, the former with the RDDS technique, the latter with the DSAM method. While the second is still under analysis, the former unfortunately did not have the sensitivity to measure any lifetimes in this nucleus. The first and only lifetime measurement in ^{37}S was performed by Wang *et al.* [74], who measured the half-life of the first excited state with fast-timing techniques and an array of fast scintillator detectors.

In conclusion, the goal of the experiment is to probe the microscopic nature of excited states in ^{37}S. Lifetime measurements can provide a complementary

E (MeV)	J^π	S	Also in
0	$7/2^-$	0.69	abcd
0.646	$3/2^-$	0.44	abcd
1.397	$(3/2)^+$	0.033	abcd
1.992	$3/2^-$	0.033	abd
2.023	$(7/2)^-$	0.0063	abd
2.515	$(5/2)^-$	0.023	bd
2.638	$1/2^-$	0.49	abd
2.776	$(11/2^-)$	–	bd
2.978	(1/2,3/2)	–	bd
3.120	$(9/2)^+$	0.012	d
3.262	$3/2^-$	0.085	abd
3.341	(7/2,9/2)	0.03	bd
3.442	$(7/2)^-$	0.02	bd
3.493	$3/2^-$	0.045	ab
3.555	(3/2)	(0.021)	b

Table 3: Literature ^{37}S states up to 3.5 MeV. Energies are reported as in the Adopted Levels [47], rounded to the keV digit. Spectroscopic factors (S) are drawn from Adopted levels as well, and rounded to the second digit. In the last column, it is also mentioned which kind of experiments observed the level: a neutron induced reactions ((d,p), (n,γ)) [64–69], b reactions involving protons ($(t$, ^{3}He), (n, $\alpha)$) [62, 63], c β and βn decay [70], d heavy-ion transfer reactions [71].

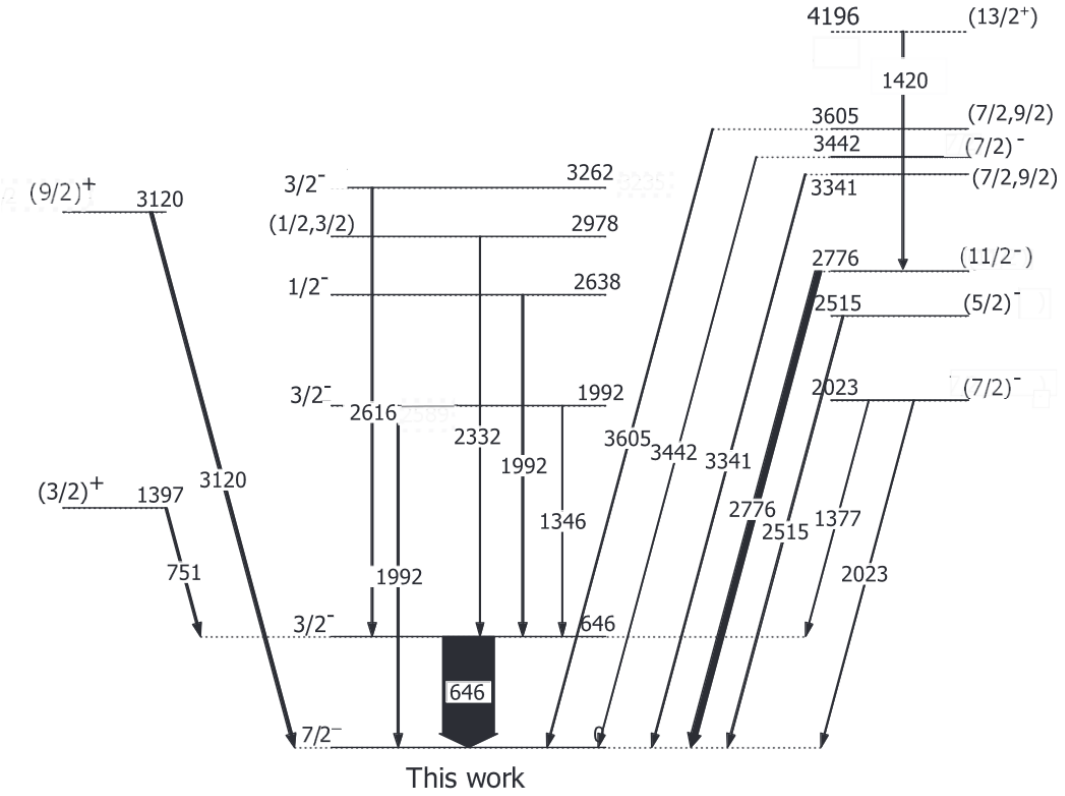

Figure 7: ^{37}S level scheme observed by Chapman *et al.*. Taken from [71].

point of view to the one offered by particle spectroscopy in discriminating between intruder and single-particle configurations, in the case of small-spectroscopic factor states. Indeed, E2 transitions between states with "normal" configurations should have strength of approximately 1 W.u., while transitions between normal and intruder configurations should be suppressed by an order of magnitude. Lifetime measurements can also provide insight on the mixing between single particle and intruder states in this nucleus, and whether this mixing increases from ^{39}Ar to ^{37}S due to the proximity with the IoI.

The precision measurement discussed in this thesis couples a direct reaction, that allows high degree of control in the population of excited states, with well established lifetime measurement techniques in γ spectroscopy. Along with highly-reliable methods, the superior efficiency and resolution of the AGATA γ-ray spectrometer has been employed. This spectrometer currently represents the state of the art in γ-ray germanium detectors for low-energy nuclear physics. A full description of the experimental apparatus will be given in the next Chapter.

Experimental setup

2

This Chapter describes the experimental setup used to measure lifetimes of excited states in ^{37}S. The experiment was performed at Legnaro National Laboratories between 27$^{\text{th}}$ May and 2$^{\text{nd}}$ June 2022. Section 2.1 illustrates the Tandem-XTU accelerator facility of Legnaro, used to produce and deliver the primary ^{36}S beam, while §2.2 and 2.3 focuses the detection apparatus, comprised of the γ-ray spectrometer AGATA and the charged-particle detector SPIDER. In Section 2.4 the signal handling, trigger and data flow from front-end electronics to disk storage is discussed. Section 2.5 describes the implementation of the RDDS technique during the experiment through the Plunger device. Immediately after, Section 2.6 describes the targets used during the experiment, which are of fundamental importance for the DSA method. Finally, Section 2.7 ties all previous sections together by illustrating the technical aspects of the experiment and the expected results.

2.1 The TANDEM accelerator

The 15 MV Tandem-XTU electrostatic accelerator is one of the five accelerator facilities of Legnaro National Laboratories. It is an electrostatic accelerator, capable of providing beams of stable isotopes (from ^{1}H to ^{238}U) with 1/300 MeV energy resolution up to 5-10 A MeV. A ^{137}Cs ion source acts as electron gun to negatively charge the beam ions, which are then injected in the beam tube. The high voltage terminal at the center of the tank provides the first acceleration stage to the beam ions. The terminal is charged via laddertron system, and due to the very high voltages needed, all the accelerator is encapsulated in a safety tank filled with SF_6 at 7 atm to prevent electrical discharges.

At the terminal, the negatively charged beam ions collide with one or two very thin ^{12}C sheet, called stripper foils. These foils increase the charge state of the beam ions from a -1 state to a positive state. The same terminal which attracted the ions in the first acceleration stage provides now the repulsive

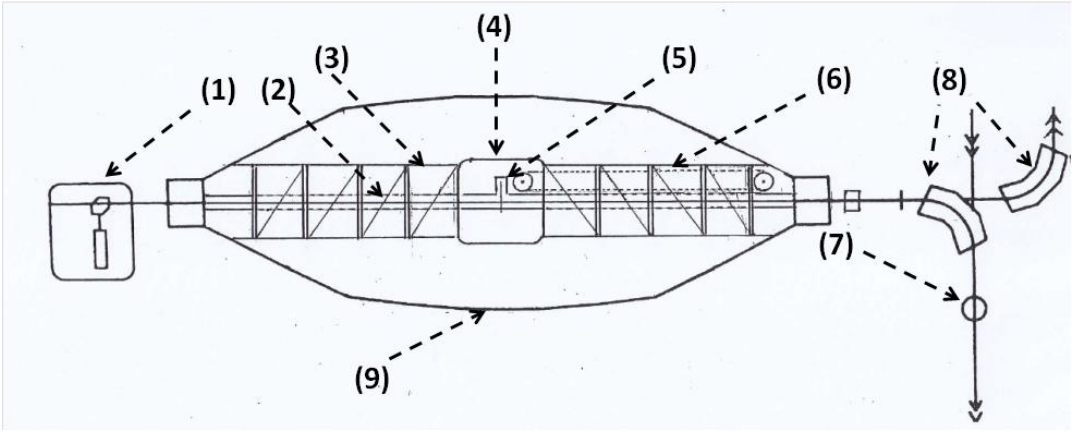

Figure 8: The Tandem-XTU accelerator at LNL (by F. Cervellera, from [75]): (1) the ion source platform, (2) the accelerating pipe, (3) the column, (4) the high voltage terminal, (5) the ion "stripping" station, (6) the "ladder tron" charging belt, (7) the diagnostic station, (8) the bending magnets, (9) the encapsulating tank filled in SF_6 at 7 atm pressure.

potential needed for the second accelerating stage. Downstream the tank, a switching magnet (not depicted in Figure 8) allows to deliver the beam to the experimental hall set-ups [75]. A schematical view of the Tandem accelerator can be found in Figure 8.

During the present experiment, the Tandem was put to a terminal voltage of 13.6 MV. This allowed to accelerate ^{36}S ions with charge state 12^+ to 168 MeV.

2.2 The AGATA spectrometer

The Advanced Gamma Tracking Array (AGATA) [76] is the state-of-the-art γ-ray detector based on the γ-ray tracking technique in electrically segmented hyper-pure germanium crystals.

Since the early nineties, the European and American experimental γ-ray spectroscopy communities coordinated efforts to build large scale high-resolution arrays, like the escape-suppressed EUROBALL and GAMMASPHERE spectrometers. The Compton-suppression technique provided excellent peak-to-total (P/T) ratio, at cost of a high decrease in efficiency due to a large part of the solid angle being covered by the anti-Compton shields.

The latest generation γ-ray arrays, AGATA and GRETA/GRETINA [77], address this limitation by dropping the anti-Compton shields and employing the γ-ray tracking concept, which consists in reconstructing the full 3D track of every γ-ray seen by the array based on the interactions points inside the array. Tracking algorithms require position resolutions which are not achievable with the previous generation arrays, and could only be addressed via electrical segmentation of the Germanium crystals and digital electronics [78].

Both arrays are conceived as itinerary spectrometers to maximize the possible scientific output [79]. In the case of AGATA, after a first demostrator phase in LNL [80], and a first physical campaign again at LNL [81], it moved to GSI Helmholtzzentrum für Schwerionenforschung (Darmstadt, Germany) [82, 83] and subsequently to GANIL laboratories (Caen, France) [84, 85], after which again in LNL [86], where it is foreseen to stay until at least the end of 2026. The superior resolving power of the array allowed it to be elected as one of the cardinal points of the Nuclear Structure program of Italian Physics MidTerm Plan 2022-2027 [87].

The AGATA campaign of LNL has been divided into two phases according to the configuration chosen for the spectrometer: the AGATA-PRISMA configuration and the *zero-degree* configuration. In the AGATA-PRISMA configuration (the one of the present experiment), AGATA is coupled to the large-acceptance heavy-ion spectrometer PRISMA [88]. Alternatively, an array of charged-particle detectors such as SPIDER [89], EUCLIDES [90], DANTE [91, 92], TRACE [93, 94] and OSCAR [95], can be mounted inside the chamber. A photo of the experimental hall with AGATA in the AGATA-PRISMA configuration can be found in Figure 9.

In the zero-degree configuration, AGATA will be decoupled from PRISMA and coupled instead to other ancillary devices such as NEDA [96], PARIS [97] and GRIT [98, 99], cryogenic targets such as CTADIR [100] and CHyMENE [101], or gas-jet targets such as SUGAR [102]. During its stay in LNL, AGATA is foreseen to employ the stable-beam facility of LNL (Tandem-Alpi-Piave complex).

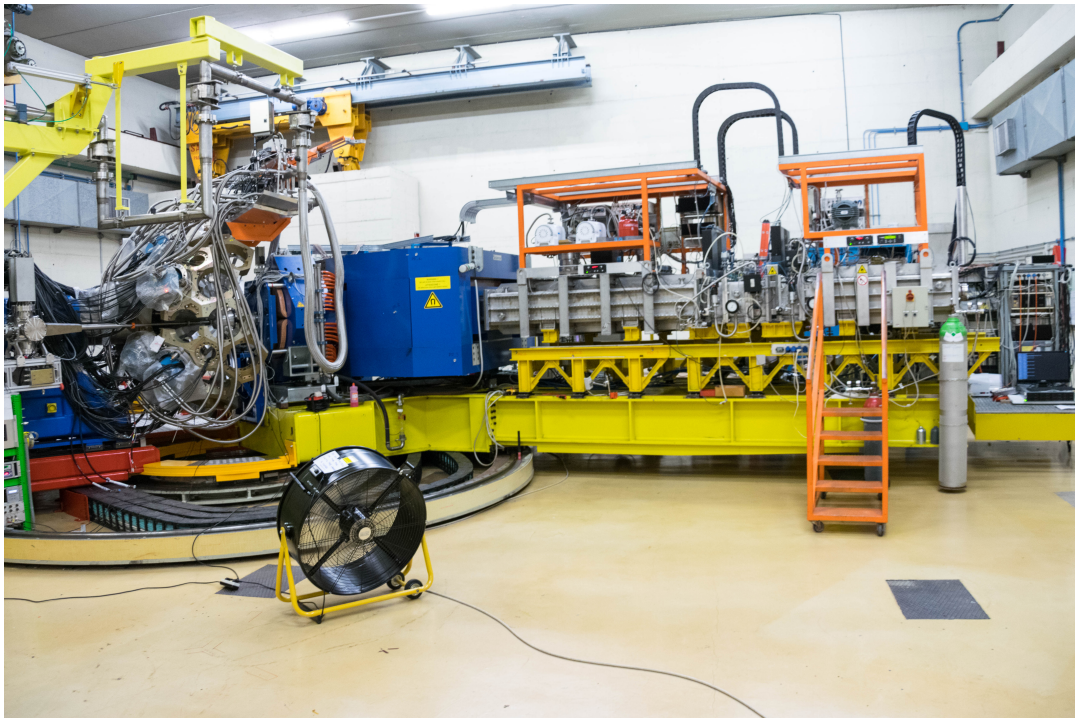

Figure 9: Photo of the experimental hall, taken 20 December 2022. The AGATA spectrometer is visible on the left side of the picture, the dipole of PRISMA is in bright blue, followed by the focal plane detectors of the PRISMA spectrometer, on the right side. Courtesy of M. Balogh.

The array

AGATA detectors are 36-fold segmented, encapsulated coaxial n-type hyper-pure Germanium crystals. The detectors have tapered hexagonal geometry with three different asymmetric shapes (called type *A*, *B*, and *C*) to optimize 4π coverage with 180 units. These 180 crystals are arranged in 60 clusters of three detectors each in the same cryostat (*AGATA Triple Cluster*, ATC) [81].

The holding structure, the so-called *honeycomb*, was installed at LNL with the first ground-break on 10 March 2021 and the installation of the final aluminium flange on 26 November 2021. A total of 30 flanges were installed on the central shaft, with a total capacity of 30 ATCs (2π configuration). The hexagonal flange holding the Triple Clusters are labelled with a progressive number from 0 to 29. The numbering progresses in three concentrical circles, starting from the innermost one, as in Figure 10. Due to the choice of coupling AGATA with PRISMA, the beamline does not pass through the shaft of AGATA, but through one of the lateral flanges. In this configuration, ATC positions 3, 12, and 26 are unavailable to host a triple cluster due to mechanical clashes

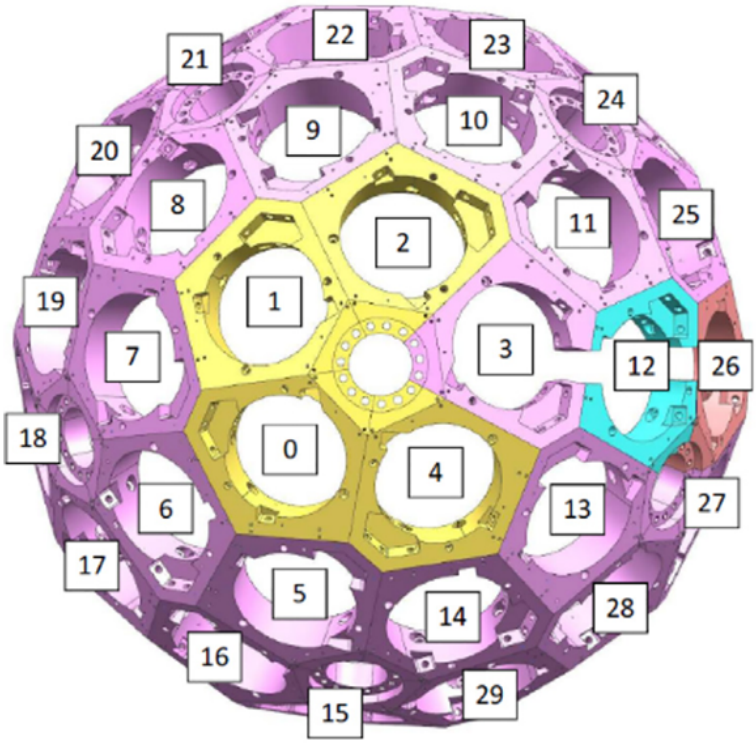

Figure 10: The ATC numbering system, from a backward view. Taken from [86].

with the beamline. The central shaft holding the honeycomb is able to rotate and translate around the center of the scattering chamber [103]. In this way, the distance between the reaction point and the front face of the detectors can vary continuously between the so-called *nominal* position, 23.5 cm, and *close-up* position, 18 cm, depending on the physics case [104].

Triple clusters have been assembled, pumped, cooled and characterized at LNL before being mounted on the frame [105]. During mounting, a laser tracker is used to ensure proper alignment on the honeycomb. The maximum difference accepted from the nominal position of each ATC is of 0.2 mm [106], while the difference between the nominal position of each crystal in a cluster is 0.4 mm [105].

During the present experiment, 11 ATCs were installed in the honeycomb, in positions 0, 1, 2, 4, 5, 6, 7, 8, 9, 10, 11, for a total coverage of about 0.7π srad. A picture of the AGATA γ-ray spectrometer at the time of the experiment can be found in Figure 11.

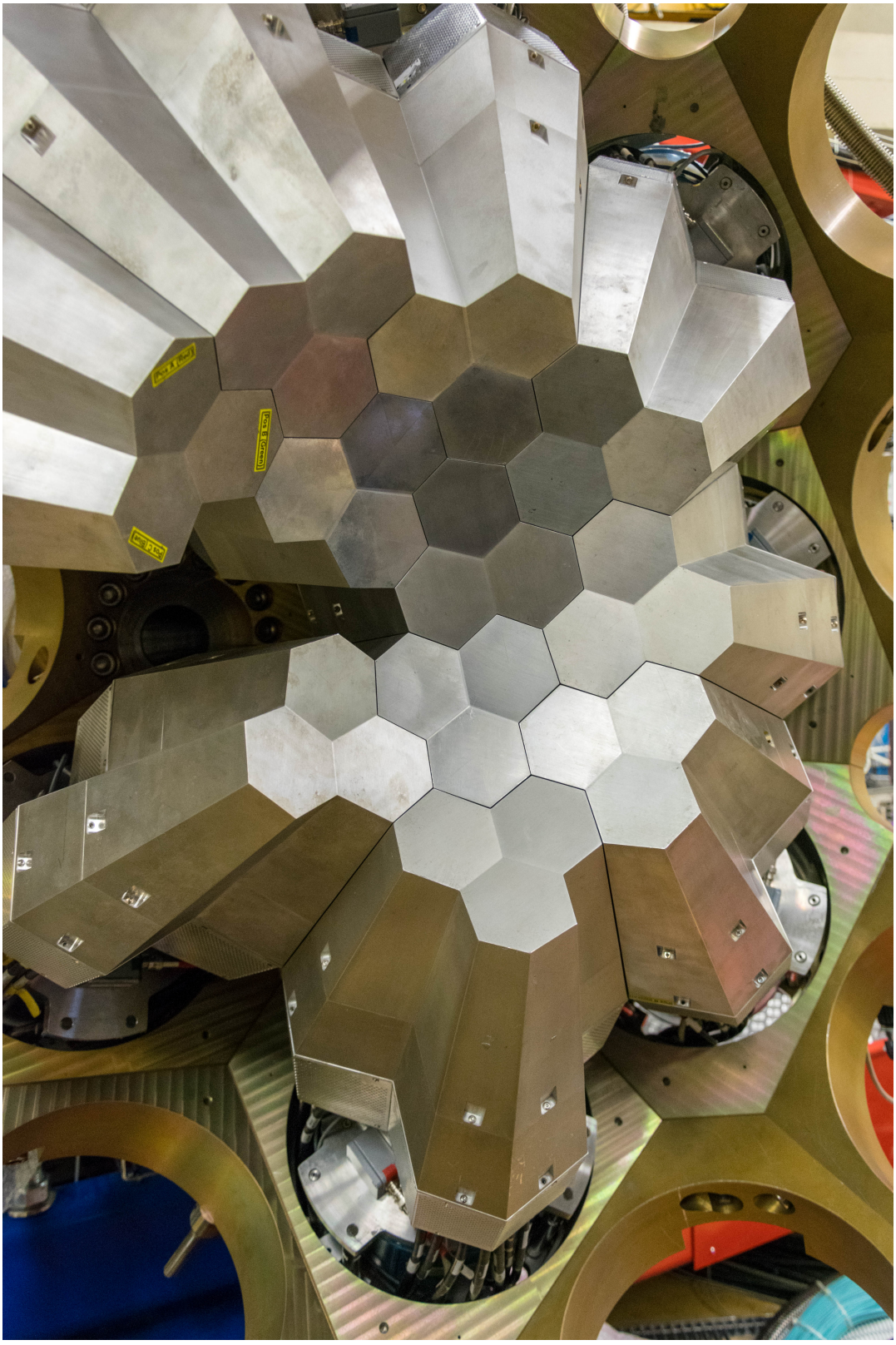

Figure 11: Photo of AGATA taken on 27 May 2022, as seen from the target. Courtesy of M. Balogh.

Position	Capsule		
0	A006	B005	C001
1	A011	B006	C012
2	A016	B017	C013
4	A004	B004	C010
5	A001	B001	C004
6	A008	B009	C002
7	A014	B010	C016
8	A002	B007	C007
9	A017	B018	C018
10	A013	B015	C011
11	A010	B011	C009

Table 4: AGATA look-up table for the present experiment.

The crystals

As anticipated in the previous section, AGATA crystals are encapsulated coaxial n-type HPGe crystals. The crystals have tapered hexagonal geometry with three different asymmetric shapes. The crystals dimensions are 90 mm length and 80 mm diameter before shaping [107]. All crystals are produced by Mirion Technologies, Inc.. Each crystal is electrically segmented in 6 azimuthal and 6 longitudinal channels, providing 36 independent outputs. These segments are labelled A through E for the azimuthal segmentation and 1 through 6 for the longitudinal one (see Fig. 12), with 1 being the front face and 6 the rear end of the detector (close to the dewar). Two other signals are collected from the central contact (core signals), differently amplified: one corresponds to a 5 MeV (so-called *high gain*) and the other to 30 MeV (so-called *low gain*) full range.

Each capsule has a single identification number and associated perfomance table and PSA basis (see Chapter 3, §3.1.2) . The lookup table used for the present experiment can be found in Table 4.

Front-end electronics

When an interaction deposits energy inside the crystal lattice, it creates electron-hole pairs inside the crystal. Being positively polarized on the central contact, the negative charges (electrons) are collected in the central contact,

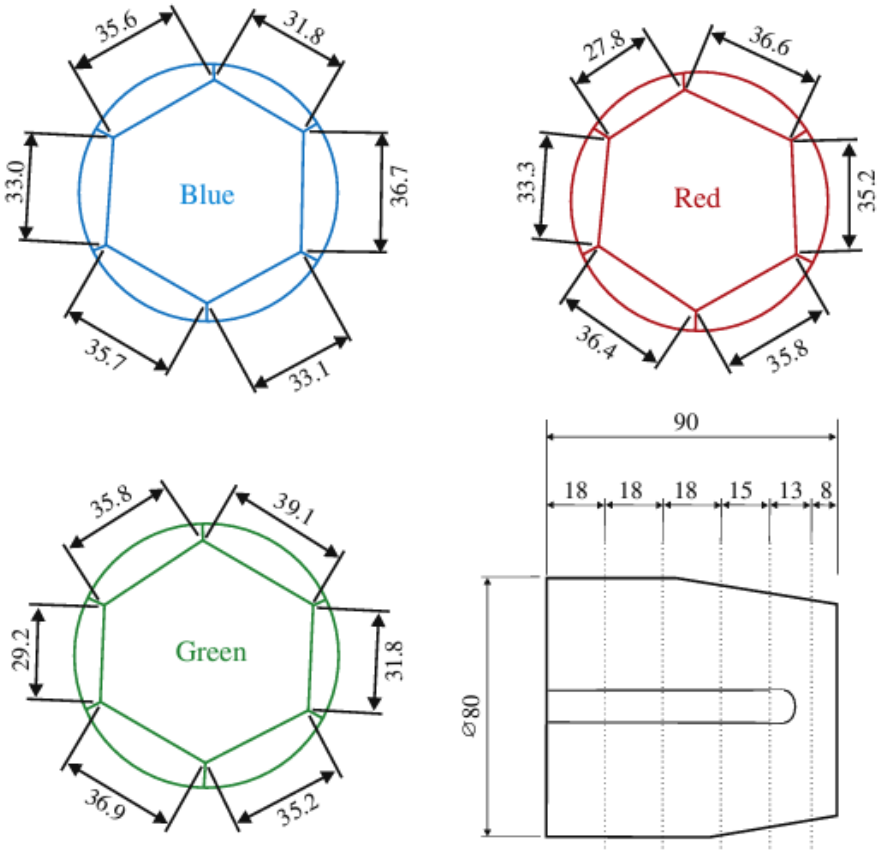

(a)

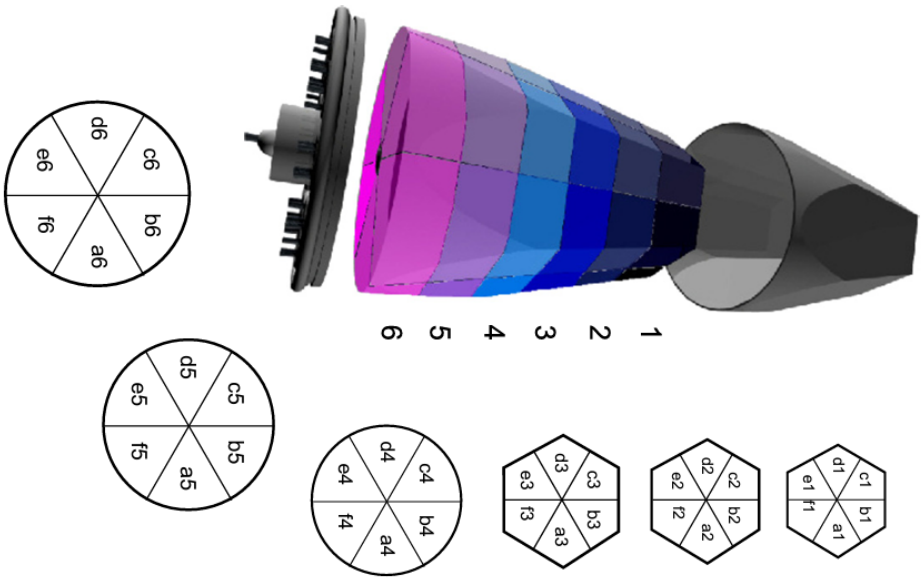

(b)

Figure 12: The AGATA crystals, taken from [76]. In (a), the dimensions in mm of the three crystals types (denoted blue, red and green according to historical notation, now type A, B and C), and the longitudinal segmentation. In (b), the segment labeling convention.

while the positive charges (holes) are collected in the segments. Each channel is equipped with cold (80 K) and hot circuit that have been custom designed to ensure optimal perfomances and minimal noise.

The preamplifiers have three-stage structure, consisting of a charge-sensing loop, a passive pole-zero stage and a differential output buffer, with an additional de-saturation circuit for prompt discharge of the preamplifier in case of high-energy or pile-up events. This de-saturation circuit allows to keep good energy resolutions up to rates of about 50 kHz. Such design yielded 1.99 keV FWHM at ^{60}Co energies in the first coupling with an AGATA detector [108].

The output of the respective preamplifiers is then digitized by means of a 100-MHz 14-bit Fast Analog-to-Digital Converter (FADC). The sampled data are then sent to the pre-processing electronic boards. The energy is obtained by applying a digital trapezoidal filter or Moving Window Deconvolution (MWD) technique [109–111] that takes into account the response function of the preamplifier. The shaping time has been adjusted at ^{60}Co energy to maximize resolution. The time information instead, mainly for triggering purposes, is determined with leading-edge algorithm on the high-gain core signal.

The scattering chamber

The new custom chamber has been developed taking into account several mechanical requirements: i) the study of quasi-elastic and deep inelastic reactions implies that the spectrometers (AGATA and PRISMA) have to rotate solidarily with each other, ii) the scattering chamber should be sufficiently transparent to γ rays so that AGATA efficiency is not compromised, iii) the scattering chamber should be able to accomodate all ancillary devices present in LNL, iv) the beam dump should be located as far as possible from the target position and be well shielded to minimize spectrum contamination and parasitic counting rate.

The AGATA scattering chamber comprises of a fixed body and a set of three movable shells that allow the coverage of angles from 7° to 88°. These movable shells are anticorodal Aluminium 6082 alloy hemispheres with a radius of 170 mm and a thickness of 2 mm.

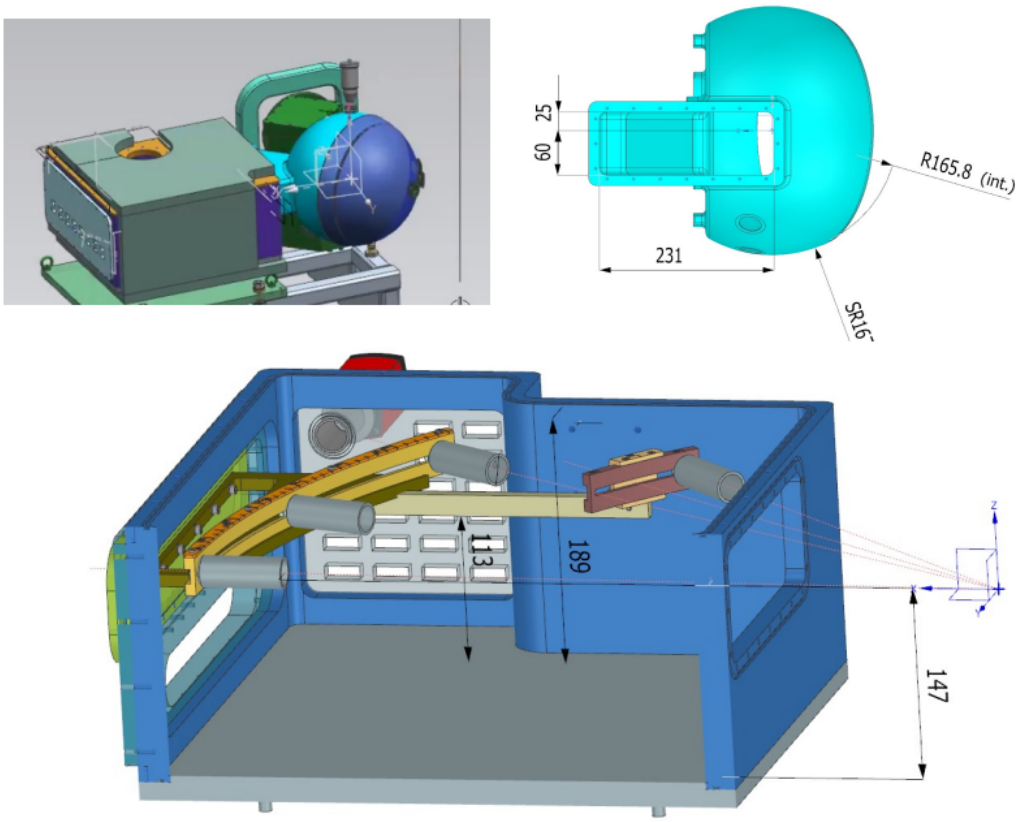

Figure 13: CAD drawing of the AGATA scattering chamber. Top left: view of the ensemble of the scattering chamber, expansion chamber and movable shell; top right: dimensions of the scattering plus expansion chambers; bottom: view of the expansion chamber and the beam dump available positions. Taken from [112].

The body of the scattering chamber is composed of two elements, the reaction chamber and a service chamber called “expansion chamber" designed to host beamdumps, cables and ancillary front-end electronics, as well as feed-through connectors and two viewports for beam centering purposes [112]. The CAD representation of the project can be found in Figure 13.

In the configuration chosen for the experiment, the PRISMA angle was set to 50°, and AGATA was put into the close-up position. In this configuration, the beamdump was located in the expansion chamber in the forward position [113].

2.3 The SPIDER silicon array

The SPIDER array consists of independent, trapezoidal-shaped, silicon detectors. A picture and the schematic drawing of two of these detectors can be found in Figure 14 and 15. In the original project, it was foreseen to be used in conjunction with a modern γ-ray spectrometer, such as GALILEO [114] and AGATA, to provide the experimental set-up of choice for Coulomb excitation measurements at LNL. Each detector of SPIDER is segmented into eight annular strips in the front surface (junction side), with strips labelled starting from the bottom to the top from 0 to 7 (see Fig. 15). Each strip is 300 μm thick, with dead layer of 50 nm on the junction side and 350 nm on the ohmic side [89]. During the 2019 GALILEO Phase II campaign [115], and for this experiment, the array was repurposed for direct reaction measurements.

The array can be arranged in different configurations depending on the number of sectors of choice: for the AGATA campaign, a cone-shaped configuration with 7 detectors at backwards angle was chosen as the standard one [116]. An aluminium frame was produced to hold the detectors in place in the scattering chamber (see Fig. 16).

The nominal distance between the vertex of the cone and the target position is equal to 8 cm; in this configuration the total solid angle subtended by the entire array is equal to 0.692π. Each detector covers 37.4° in the polar angle, and $2\pi/7 = 51.4°$ in the azimuthal coordinate. The strip per strip nominal angular coverage is show in Table 5. Biasing of the detector can be performed

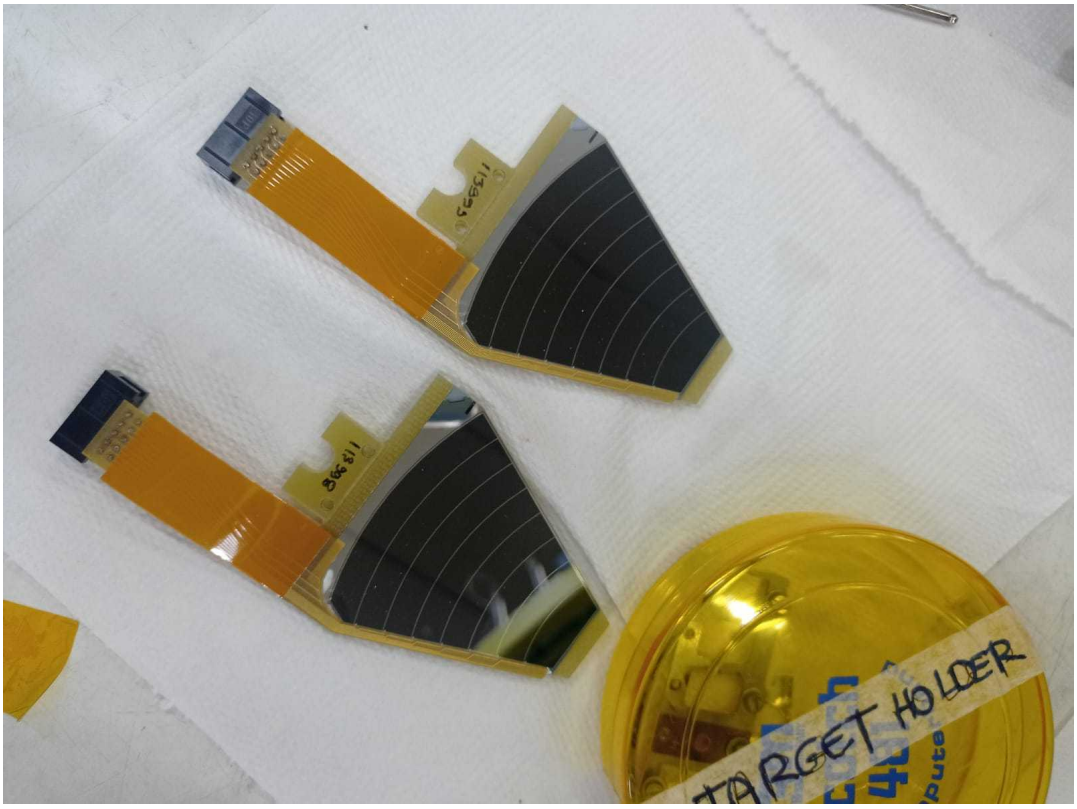

Figure 14: Photo of two bare SPIDER sectors, taken 20 May 2022. Courtesy of M. Balogh.

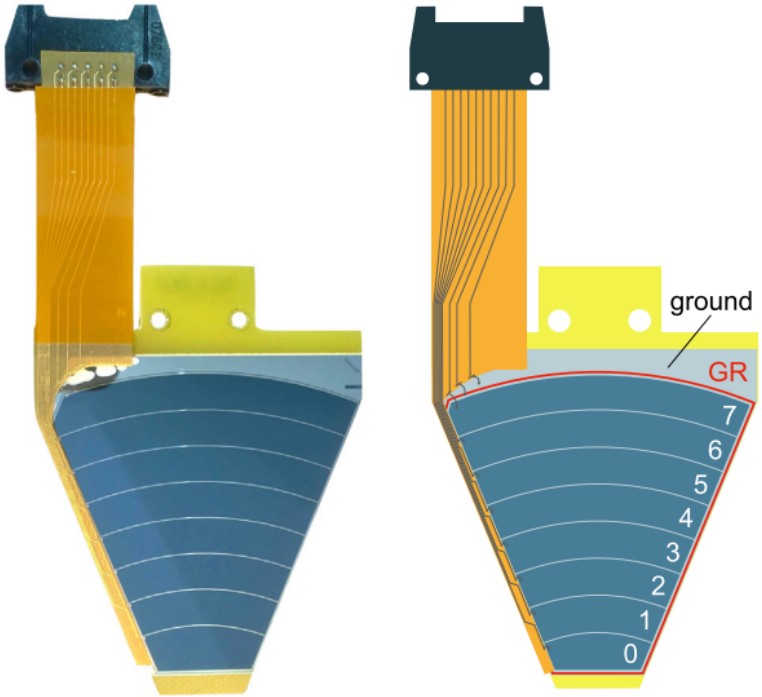

Figure 15: Schematic drawing of a SPIDER sector, showing its numbering convention. Taken from [89].

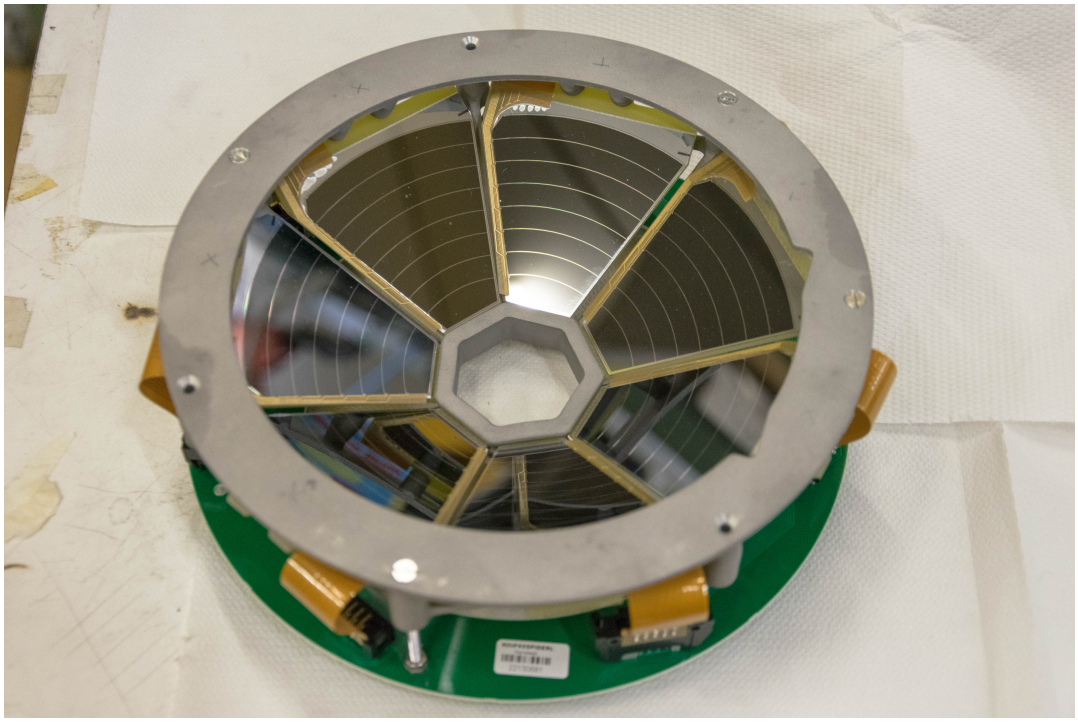

Figure 16: Photo of SPIDER array mounted on its aluminium frame. On the top, the segmentation of the sectors is visible; on the bottom, the electrical PCB that allows for the read-out of the detector is visible in green. Taken on 21 May 2022. Courtesy of M. Balogh.

either from the back, or strip-by-strip. Signals are collected via a Printed Circuit Board (PCB) that is visible in Figure 17.

2.4 Data Acquisition and Trigger System

The Data Acquisition System (DAQ) is in charge of processing the signals provided by the front-end electronics of the detectors up to their storage on disk. In the present experiment, the data flow followed two main streams, parallel to each other - one for the 30 AGATA crystals and one for the SPIDER silicon detectors.

AGATA data flow

In AGATA DAQ, all crystals are treated as independent entities: the 36 segments and the two signals coming from the central core are continuously sampled by digitizer cards at 10 ns intervals. This data flow is then sent to a custom PCI

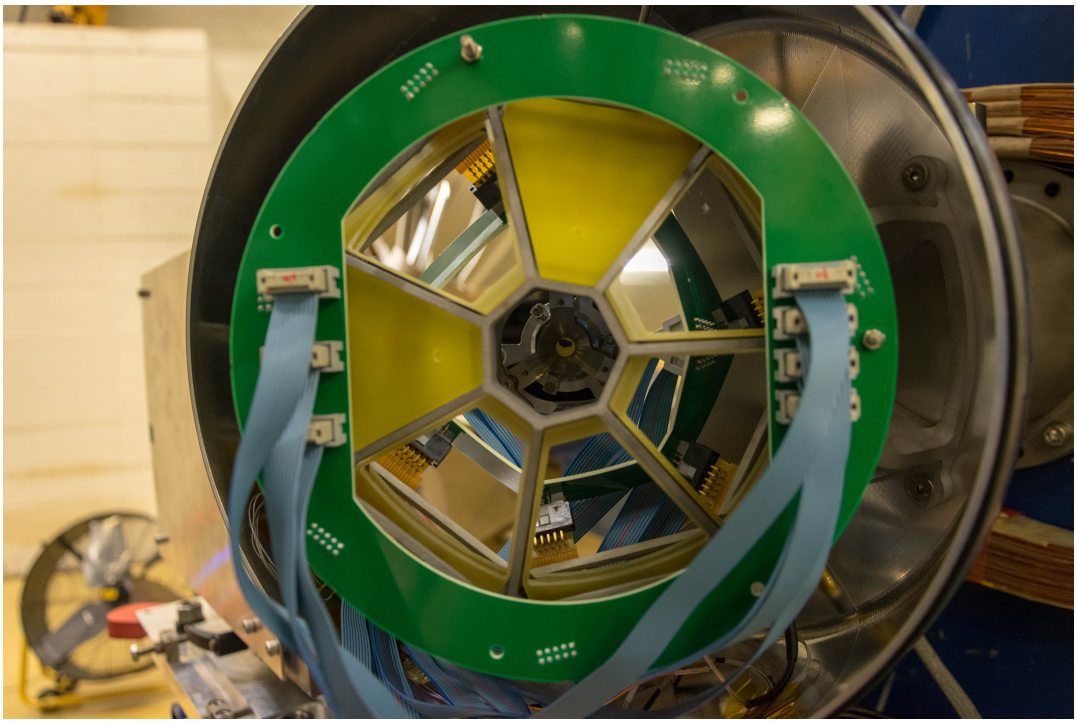

Figure 17: Photo of SPIDER installed in the scattering chamber, as seen from the beamline. Taken 21 May 2022. Courtesy of M. Balogh.

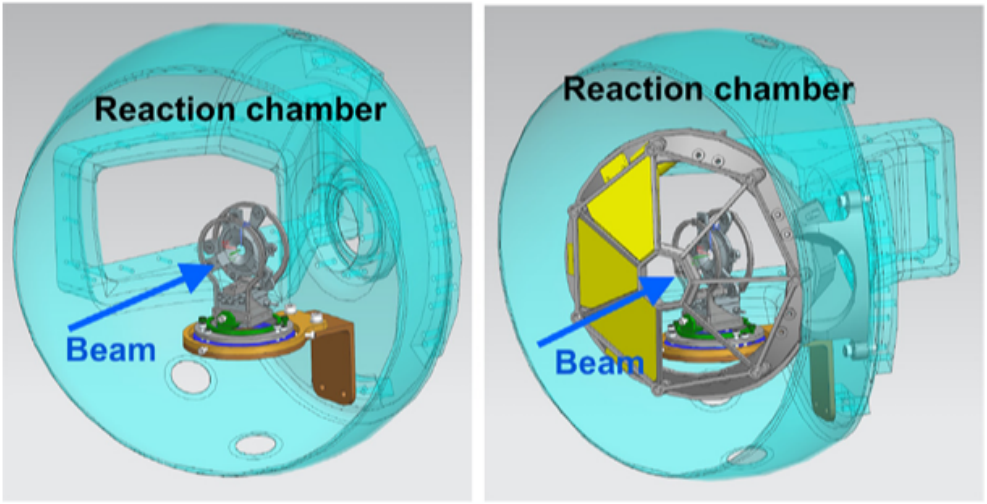

Figure 18: CAD drawing of the scattering chamber, SPIDER and the Plunger device. Taken from [86].

Strip	θ_{min} [deg]	θ_{mean} [deg]	θ_{max} [deg]	$\Delta\theta$ [deg]	Ω [srad]
7	123.5	125.4	127.5	4.0	0.046
6	127.5	129.6	131.8	4.3	0.046
5	131.8	134.0	136.4	4.6	0.045
4	136.4	138.7	141.2	4.8	0.043
3	141.2	143.6	146.1	5.0	0.040
2	146.1	148.6	151.2	5.1	0.035
1	151.2	153.7	156.3	5.1	0.030
0	156.3	158.8	161.3	5.1	0.028

Table 5: SPIDER nominal angular coverage.

express board, called the Global Gigabit Processor (GGP). Once the high-gain core signal overcomes a settable threshold, an event is generated, consisting in 100 samples distributed around the trigger and the energy of each individual channel [117]. Each event is timestamped and stored in the GGP buffer until its validation or rejection by the trigger system. In case of validation, the event is transmitted forward in the data stream through PCI link. The DAQ server performs the sorting process which produces the final PSA files starting from the samples (more details will be given in Chapter 3). All GGPs are time-aligned via the GTS system, which will be illustrated in the next paragraph. During this experiment, thanks to the low acquisition rate, all traces were directly written to disk for offline reprocessing.

SPIDER data flow

In SPIDER, the output of the differential to single ended modules are fed to four CAEN V1725 digitizers, programmed with moving window deconvolution firmware (DPP-PHA). The digitizers were programmed to lock their internal 250 MHz clock signal on a 100 MHz external one, provided by the GTS system (see next paragraph). The energy of the incoming signal is extracted using a settable trapezoidal filted, while the timing information is given by a digital CFD algorithm. The data stream is handled by a custom acquisition system based on XDAQ framework [118]. Three main XDAQ applications were developed for the ancillaries DAQ in LNL: the Read-out Unit (RU), the Local Filter Unit (LF) and the Builder Unit (BU). All three applications are written in C++ language [86, 119].

While the RU is only in charge of taking data coming from the digitizer and both writing them to disk and forwarding them to the data stream, the LF is in charge of applying the first level of processing of the data, as well as translating them from CAEN format [120] into Agata Data Format (ADF). At RU level, the events are coded in frames consisting of a five 32-bit word header, followed by all information coming from the detector (ID, measurement, timestamp, pile-up rejection flag, saturation flag, fault flag, etc.). At LF level, they are reduced to blocks of six 32-bit words and converted to ADF. Finally the BU is in charge of filtering flagged data, time-ordering them, and creating a complete event within a configurable coincidence window (set to 500 ns).

Synchronization and Trigger

Synchronization between all units is kept via the Global Trigger and Synchronization System (GTS) [121]. All internal clock signals are phase-locked on a single one coming from a master unit (the so-called *root* node). To ensure proper communication, the whole system is organized in a strongly hierarchical tree-like structure (the *GTS tree*), with the root node at the upmost level and the GGPs at the lowest one. The GGPs send trigger requests up the tree towards the root, which then is the only one with direct communication with the Trigger Processor Unit (TP). The TP receives from the root a list of timestamps and ID and rules if the events are valid based on a user-configurable trigger condition. In case of a positive answer, the root unit is responsible to broadcast the list of validated timestamps down the tree, triggering the GGP to dump the data to disk and transmit them to the DAQ servers. In case the event does not satisfy the trigger condition, no list is propagated, and after a configurable time-out period, the GGPs delete the event from their buffers.

During the present experiment, due to the low trigger rate ($\sim$800 Hz/crystal), all events were validated.

2.5 The Plunger device

Plunger devices, developed in the 50s, have nowadays become one of the standard tools for in-beam γ-ray spectroscopy. The device should be as compact and transparent as possible to γ rays, but it should be stable and reliable

in reaching micrometric distances in a reproducible fashion. The GALILEO Plunger device [122] was devised to address all these requirements and provide a reliable tool for the measurement of excited nuclear levels. The device was developed as collaboration between LNL and IKP Cologne [123]. While initially designed for optimal compatibility with the GALILEO γ-ray spectrometer [114] of LNL, it has been adapted to work also in the first phase of the AGATA+PRISMA campaign in LNL, before the final development of the custom AGATA Plunger [124].

In the GALILEO plunger (see Fig. 19), the target and stripper foils are mounted on stretcher cones, held on the respective supports. The stretcher cones are used to ensure not only positioning and alignment of the two foils, but also that the foils are regular and wrinkle-free. Stretching is done manually during the mounting of the device using a set of three screws. The parallelism is achieved step by step by bringing the foils to electrical contact and adjusting the parallelism screws.

Target and stopper holders are interchangeable depending on the physics case. In the present experiment, the target holder was lying directly on the aluminium frame, while the stopper holder was mounted on a sliding rail on top of the motor. In this way, the target remained fixed at the center of the scattering chamber, while the stopper was movable. This choice was designed to prevent perturbation on the measured angular distributions by the choice of distance. A picture of the Plunger inside the scattering chamber can be found in Figure 20. The motor slides the target with sub-micrometric precision ($\sim$ 40 nm) with respect to the stopper. The position is set by a piezoelectric linear drive LPS-24 from Physik Instrumente, controlled via a custom LabVIEW software developed by the IKP staff.

During the present experiment, due to the rather long lifetimes that were to be measured with the Plunger, a set of “long" distances has been chosen: the set of distances with the relative amount of measuring time can be found in Table 6. Additionally, 7h 40’ were spent on the reference self-supporting CD_2 target, plus another 3h on the so-called DSAM target (1 mg/cm^2 CD_2 plus 30 mg/cm^2 ^{197}Au).

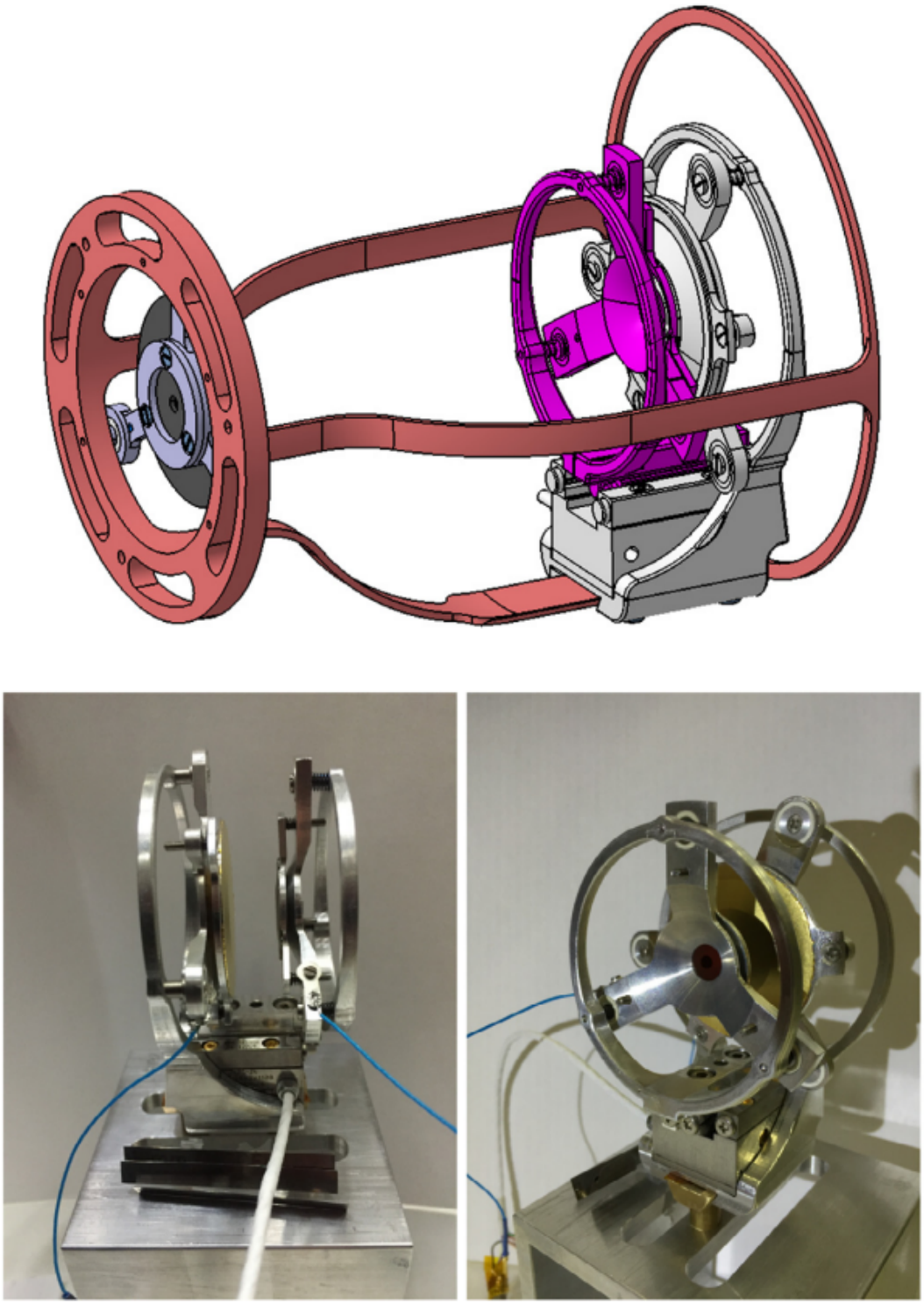

Figure 19: 3D visualization (top) and pictures (bottom) of the GALILEO Plunger device. The mechanical support fixed in the reaction chamber (not used in the present experiment, due to the requirements of the AGATA scattering chamber) is displayed in red, while the motor is drawn in gray. Stopper holder and stretcher are colored in gray, while target stretcher and holder in violet. Taken from [123].

distance (mm)	time
0.7	10h 10’
1	6h 5’
1.5	13h 1’
2	7h 51’
3	14h 41’
3.8	6h 39’
5	17h 10’
7	13h 8’
10	8h 8’

Table 6: Plunger distances and relative approximate measuring time. These times account for beam interruptions.

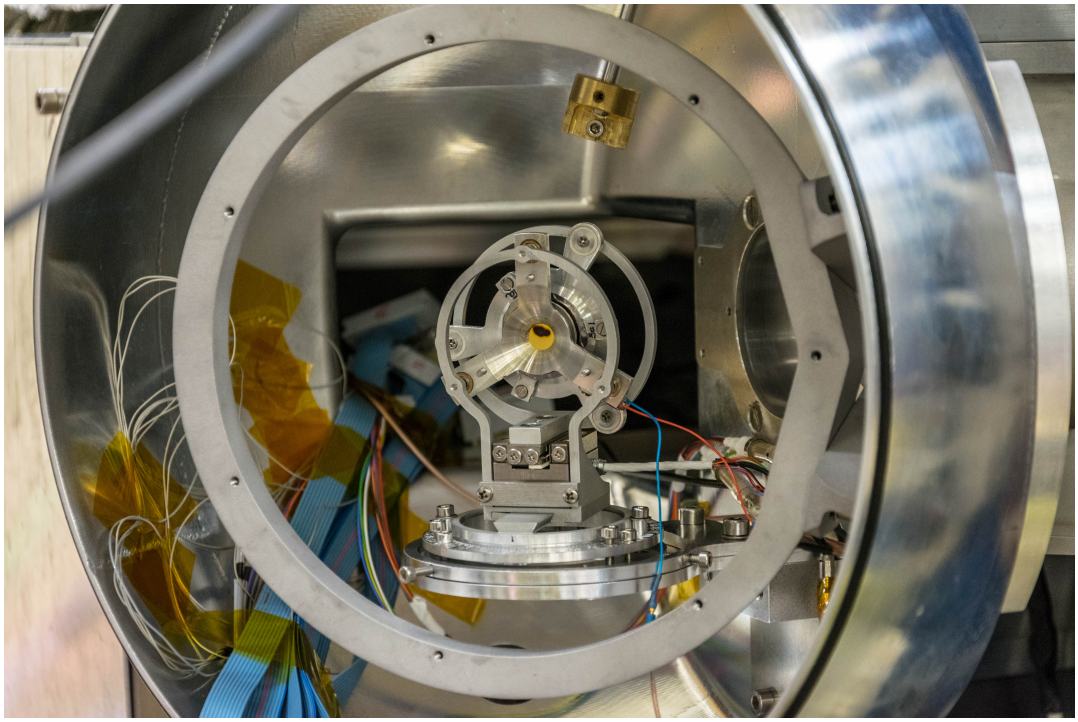

Figure 20: Photo of the Plunger device installed in the scattering chamber, as seen from the beamline. The picture was taken during the experiment, on 2 June 2022, as the beam spot is clearly visible on the target. Around the Plunger, the SPIDER aluminium chassis is visible. Courtesy of M. Balogh.

Support	CD_2 (mg/cm^2)	^{197}Au (mg/cm^2)	^{181}Ta (mg/cm^2)
Plunger	0.505	6.18	30
Plunger	0.497	4.08	30
Ladder	1.00	30.0	–
Ladder	0.337	–	–

Table 7: List of targets used during the experiment.

2.6 The targets

The targets used for the present experiment were produced by the target laboratory of LNL. Four different targets were used during the experiment, one being of self-supporting deuterated polyethylene (C_2D_4, denoted CD_2 in the following for simplicity), while the other three of CD_2 on ^{197}Au backing. In the self-supporting case, the target was produced from the CD_2 target via heating and pressing of the CD_2 powder. In the other cases, the ^{197}Au sheet was produced first via rolling and the CD_2 was then evaporated on it. A picture of these targets can be found in Figure 21. For the Plunger targets, the Au foil was produced first via rolling and then stretched on the target cone. The CD_2 polymer was then evaporated directly on the stretched foil. This ensured that the stretching process would not damage the polymer, or detach the evaporated material from the backing. The thicknesses of the targets [125] are listed in Table 7, along with the support structure (Plunger cone or target ladder).

For the Plunger, a stopper of 30 mg/cm^2 of ^{181}Ta was produced. This foil was stretched on the stopper holder of the Plunger.

All targets were produced with the objective of performing RDDS and DSAM measurements at the same time. As CD_2 targets are non-conductive, a metallic support is needed in order to create the potential difference used by the Plunger device to measure online the distance between the two foils. Gold was chosen therefore as material not only because of its durability, mechanical resistance and stretchability, but also because of its relatively high stopping power. Thus, ions produced in the CD_2 target travel first through the target, then in the gold backing, where they lose part of their energy. The energy loss process induces a lineshape in the γ-ray spectrum which the DSAM method employs to deduce the lifetime. The gold backing therefore acts as a velocity degrader for

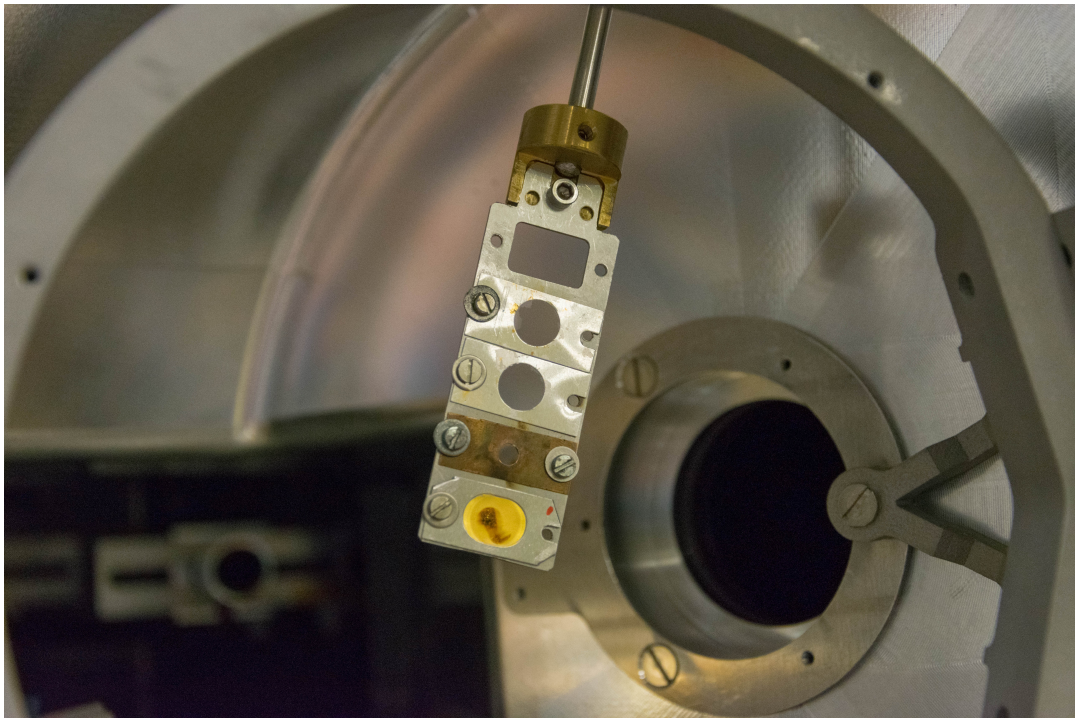

Figure 21: Photo of the target ladder after the end of the experiment. In order, from top to bottom, the collimating quartz, two 0.330 mg/cm^2 CD_2 self-supporting targets, the 1.5 mm beam collimator, and the CD_2 target with 30 mg/cm^2 ^{197}Au backing. In the background, the beam dump is also visible. In foreground, partially cut, is the SPIDER aluminium chassis. Taken on 4 June 2022. Picture courtesy of M. Balogh.

the produced ions. As the lineshape spread is maximum when the produced ion reaches null velocity in the degrader, for DSAM measurement usually the backing has sufficient thickness to completely stop the ions. However, in the present case, such spread cannot be achieved, as stopping the ions in the gold backing would prevent RDDS measurement. Therefore, the gold thickness was chosen as a balance between the opposing requirements of inducing a sufficient lineshape so that DSAM measurements could be performed effectively, and minimizing the velocity and angle spread at the exit of the gold foil, so that RDDS resolution would not be affected. Ions are then completely stopped in the Ta foil mounted on the second support of the Plunger in order to observe the "unshifted" component needed by the RDDS technique.

2.7 The experiment

The experiment aims at measuring lifetimes of excited states in ^{37}S. The isotope is populated via the direct one-neutron-adding (d,p) reaction in inverse kinematics. The reaction was chosen because it allowed clean selection of the excited states of interest through the use of a particle detector at very backwards angles. While the maximum of the cross section falls between 80 and 120 deg (in the laboratory frame) for the states of interest, angles between 60 and 120 deg are covered by the Plunger support structure. For the particle detector, SPIDER was therefore chosen since it provided the maximum solid angle coverage at backwards angles among all available detectors present at the time at LNL.

These reactions are usually performed at higher energies, but it was chosen to limit the beam energy to 168 MeV (8.8 MeV in the CM) in order not to be too much above the Coulomb barrier of the S-Au system (141 MeV, according to PACE4 [126], against a CM energy of 142 MeV). This was done in order to avoid protons and α particles coming from fusion-evaporation (FE) reactions on gold in addition to the ones coming from FE reaction on ^{12}C. Indeed, according to reaction kinematics and PACE4 calculations (performed with the software LISE++ [126]) that can be found in Figure 22 and 23 respectively, the recoiling protons coming from the direct reaction and the evaporated protons coming from the fusion with ^{12}C cover the same energy range. Contamination from ^{37}S γ-ray decay coming from FE on ^{12}C is not expected, as the probability to produce it is lower than 0.1% (see Table 8).

These conditions, as mentioned already in the previous Chapter, are not ideal to perform particle spectroscopy, as the resulting angular distributions of the emitted protons, on top of the kinematical compression, are quite flat and not too dependent on the transferred L at the very backward angles covered by SPIDER. The angular distributions of all states for which the spectroscopic factor is known in literature have been drawn in Figure 24. However, with the energy and position resolution available, it still possible to perform an angular distribution and spectroscopic factor measurement which can be compared with the previous results. All available spectroscopic information for states below 3.5 MeV, as reported in the Adopted Values [47], is listed in Table 10. Furthermore, the distinction between L=1 and L>1 angular distributions

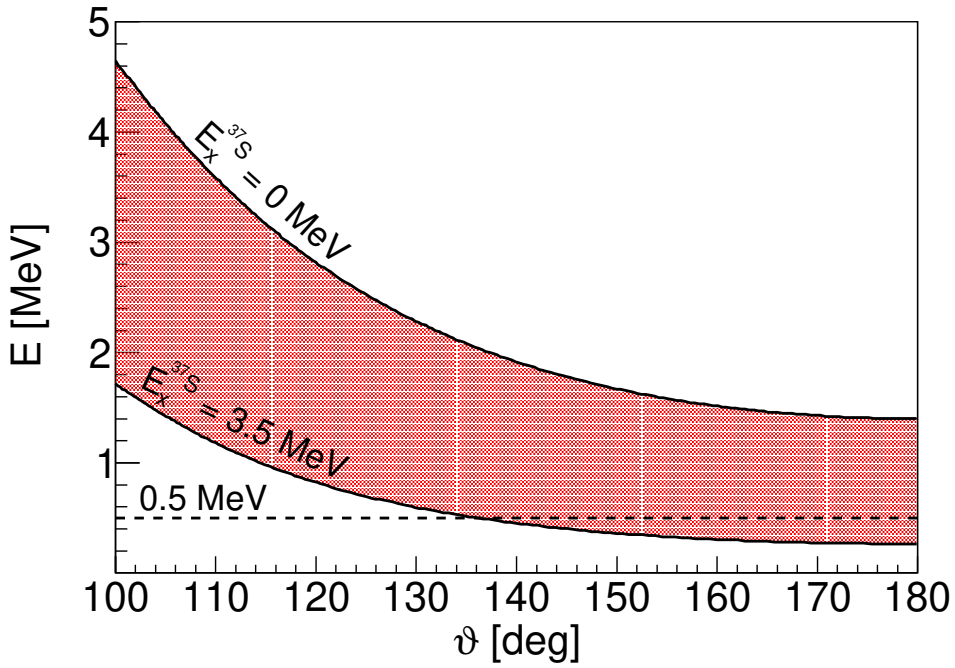

Figure 22: Kinetic energy of the recoiling protons as a function of the laboratory emission angle in the range of interest for SPIDER. Calculations take into account the loss of energy in the target. The shaded area represents the whole energy range covered by the recoiling protons as a function of the populated excited state in ^{37}S, from the ground state to 3.5 MeV. The 0.5 MeV line corresponds to the nominal threshold of SPIDER. The angular range covered with the detector spans from about 120 to 160 deg.

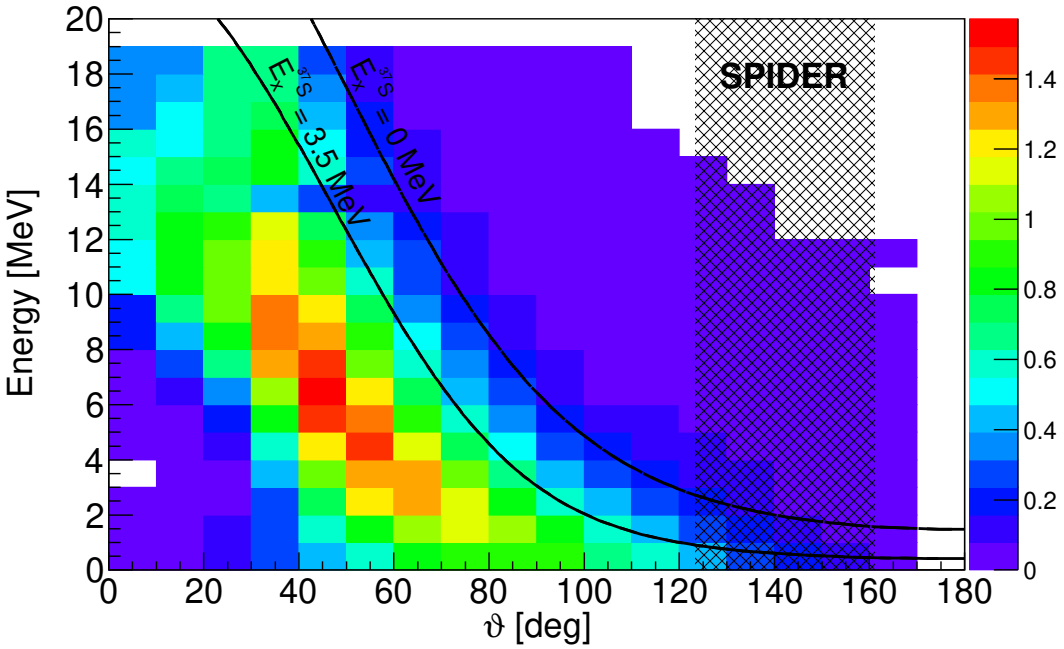

Figure 23: α and proton emission spectrum of the $^{36}S+^{12}C$ reaction calculated by PACE. The bin content is proportional to the emission probability (in %). On top of the matrix, the two kinematic lines corresponding to the population of the ground state and a state at 3.5 MeV in ^{37}S (as in Figure 22) are drawn in black lines. The angular coverage of SPIDER is also drawn as shaded band.

Z	N		σ %	Channel
21	24	^{45}Sc	28.8%	1p2n
20	22	^{42}Ca	15.1%	2p4n
22	23	^{45}Ti	13.6%	3n
21	23	^{44}Sc	8.1%	1p3n
18	21	^{39}Ar	7.12%	4p5n
19	23	^{42}K	6.92%	3p3n
20	25	^{45}Ca	4.16%	2p1n
20	23	^{43}Ca	4.16%	2p3n
20	21	^{41}Ca	3.93%	2p5n
19	22	^{41}K	2.02%	3p4n
20	24	^{44}Ca	1.59%	2p2n
22	24	^{46}Ti	1.09%	2n
19	24	^{43}K	0.757%	3p2n
21	25	^{46}Sc	0.749%	1p1n
18	22	^{40}Ar	0.595%	4p4n
16	20	^{36}S	0.342%	6p6n
22	22	^{44}Ti	0.341%	4n
18	20	^{38}Ar	0.2%	4p6n
17	22	^{39}Cl	0.113%	5p4n

Table 8: PACE4 calculation of the ^{36}S+^{12}C FE products. Only channels with probability greater than 0.1% are reported.

are clear in these conditions, fact that can be exploited to assign spins, in conjunction with the γ-ray decay pattern, to newly-observed states.

As spectroscopic factors are known, the population rates for the states of interest can be calculated with a relatively high confidence in their accuracy. These estimates are reported in Table 9, assuming 7 days of beam time and 0.1 pnA of beam current. Despite the low spectroscopic factors, the high inclusive cross section of the reaction guarantees the sufficient population of the states of interest so that their lifetime can be measured.

According to PACE4 calculations, the fusion cross-section for the ^{36}S+^{12}C system is 1.2 b, while for the ^{36}S+^{197}Au is 38 mb. Integrated on SPIDER angular range, the ^{36}S+^{12}C reaction has a cross-section of 48 mb, comparable with the 54 mb of the ^{36}S(d,p) reaction. This might make necessary the use of $\gamma-\gamma$ coincidences to clean the spectra from FE contamination, but the expected rates would allow to set such condition retaining sufficient statistics.

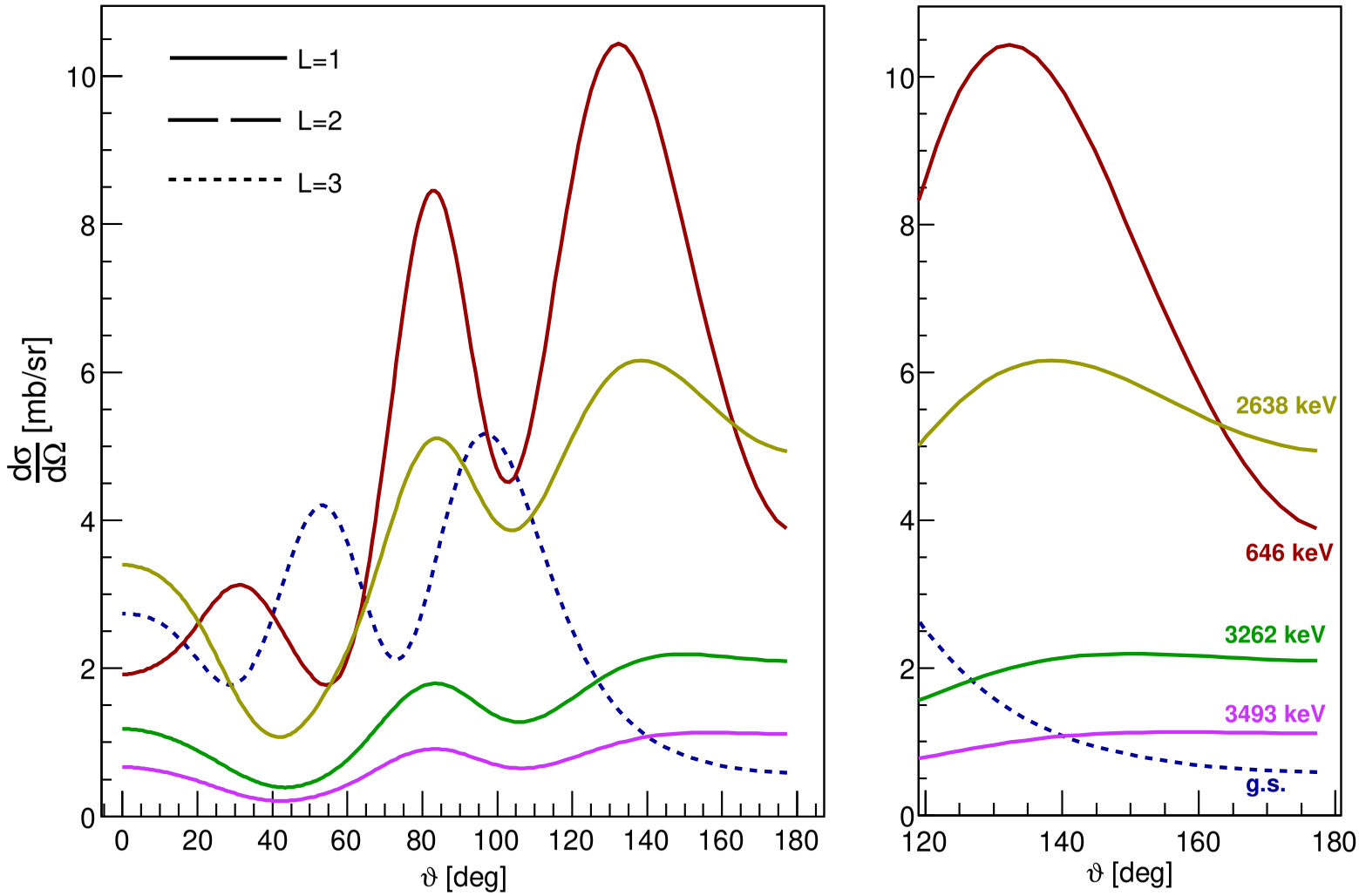

Figure 24: Angular distribution in the laboratory frame of the low-lying states in ^{37}S. L=1 transfers are in continuous line, L=2 in long dashed line and L=3 in short dashed line. On the left, the whole distribution, while on the right a zoom in the region covered by SPIDER.

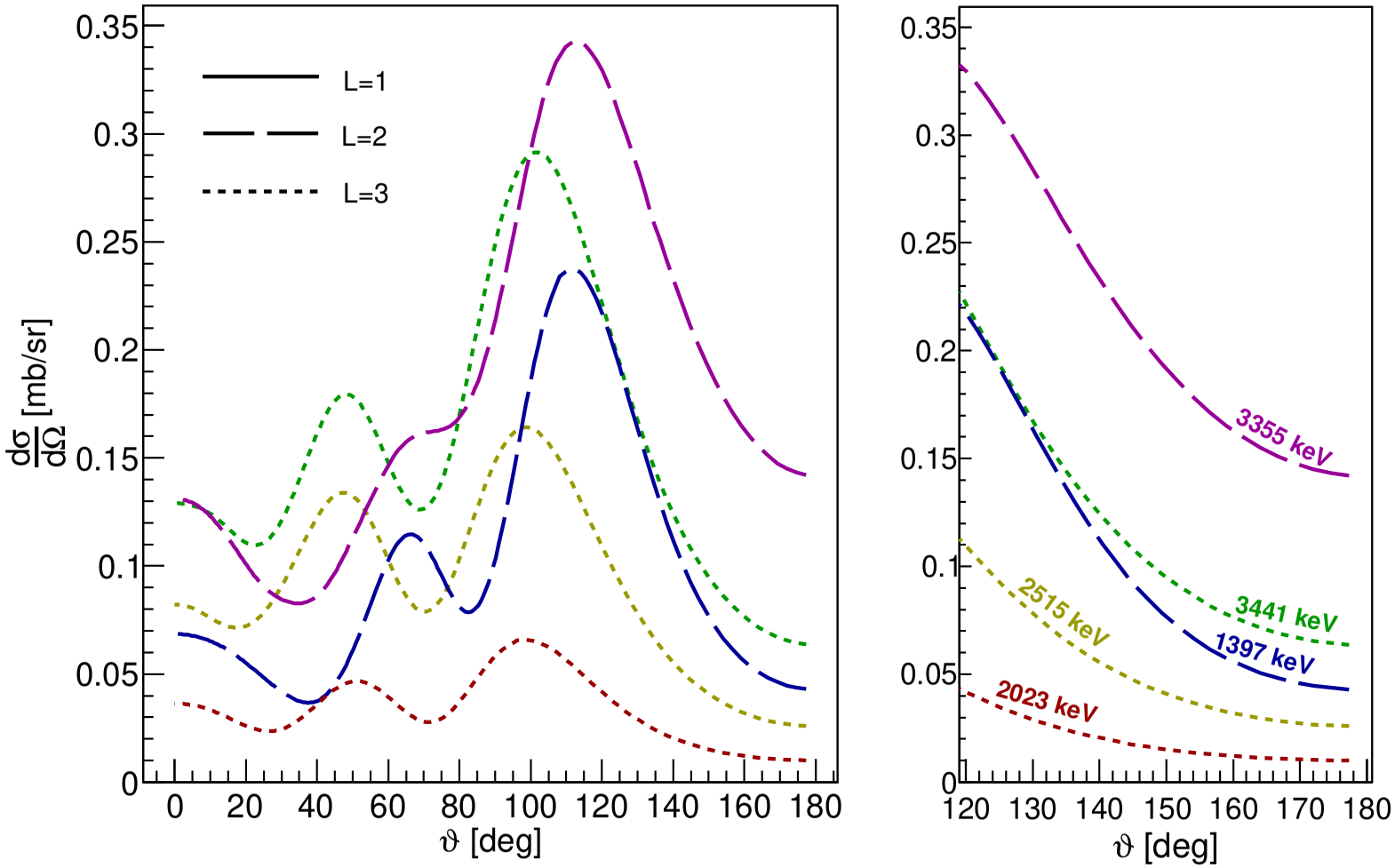

Figure 25: As in Figure 24, but for the intruder states of ^{37}S.

State	σ_{tot} [mb]	protons/s	E_γ [keV]	ϵ_γ [%]	γ/s	γ/7d
0	36.1	230	–	–	–	–
0.646	72	850	646	5.8	100	$6 \cdot 10^7$
1.397	1.5	23.5	751	5.5	1	$7 \cdot 10^5$
1.992	6.3	150	1346	4.3	6	$3.8 \cdot 10^6$
2.023	0.5	4	1377	4.25	0.18	$1 \cdot 10^5$
2.638	50	1100	1992	3.7	41	$2.5 \cdot 10^7$
3.262	17	385	2616	3.3	12	$7 \cdot 10^6$
3.493	8.8	195	1470	4.1	8	$4.8 \cdot 10^4$

Table 9: Rate estimates with 0.1 pnA of ^{36}S.

Regarding lifetime measurements, the choice of the backing thickness is of paramount importance, since it should provide sufficient slowing-down to maximise DSAM sensitivity but not so much that it impairs plunger measurements. The choice of the gold layer thickness was optimized on a range of lifetimes between 100 to 500 fs. The lifetimes of the goal $3/2^-_2$ and $7/2^-_1$ state were estimated by considering the reduced transition probabilities of the decays of the analogue states in ^{39}Ar as lower limits for the values of the corresponding decays in ^{37}S. The calculated lifetimes for these states lie in the mentioned range.

For the measurement of the lifetime of the $3/2^+$ state, a lifetime of about 100 ps was estimated under the same assumptions. At approximately 9% speed of light (average between the velocity of the produced ^{37}S ions after 4 and 6 mg/cm^2 of gold), the distances that correspond to a ratio of 10, 25, 50, 75, 90% between the shifted and unshifted components are 0.3, 0.75, 1.8, 3.5 and 6 mm.

E_i [keV]	J_i^π	E_γ [keV]	BR [%]	E_f	J_i^π
646	$3/2^-$	646	100	0	$7/2^-$
1397	$(3/2)^+$	751	100	646	$3/2^-$
1992	$(3/2)^-$	1346 1992	78(2) ≈22	646 0	$3/2^-$ $7/2^-$
2023	$(7/2)^-$	1377 2023	29(5) ≈71	646 0	$3/2^-$ $7/2^-$
2515	$(5/2)^-$	2515	100	0	$7/2^-$
2638	$1/2^-$	1992	100	646	$3/2^-$
2776	$(11/2^-)$	2776	100	0	$7/2^-$
2978	(1/2,3/2)	2332	100	646	$3/2^-$
3120	$(9/2)^+$	3120	100	0	$7/2^-$
3262	$3/2^-$	2616 1239	34(5) 66(5)	646 2023	$3/2^-$ $(5/2,7/2)^-$
3341	(7/2,9/2)	3341	100	0	$7/2^-$
3442	$(7/2)^-$	3442	100	0	$7/2^-$
3493	$3/2^-$	1470	100	2023	$(5/2, 7/2)^-$

Table 10: Known γ-ray lines of ^{37}S. Only levels below 3.5 MeV have been considered. Taken from Adopted Levels [47] and Chapman *et al.* [71].

3 Analysis, Optimizations and Simulations

In this Chapter, the preliminary data analysis procedure is described. In §3.1, the so-called *data sorting* procedure, which takes the raw data from the acquisition system, calibrates and selects them to give meaningful physical data that can be then subject to a more refined analysis is illustrated. The procedure is detailed in §3.1.1 and 3.1.2 for SPIDER and AGATA, respectively. In §3.2 it is described how positions relative of the detectors to the target and to each other is adjusted with respect to the nominal values to produce more accurate results. The performance of the detection apparatus is assessed in §3.3. Finally, in §3.4, some benchmark simulations are presented, validating the simulations used in the remainder of the analysis.

3.1 Data sorting

In general, data sorting (for both AGATA and SPIDER) consists of two different levels: a *local level*, where all data streams are treated separately, and a *global level*, where the streams of different processed data are time sorted and combined into events, array by array. The last step of sorting is the merging of data streams coming from different arrays into a single physical event that contains all available information.

In the *agapro* [127, 128] suite language, the sorting code distributed and maintained by the AGATA collaboration, this process is called *data replay*, and each class performing a set of predefined operations is called an *actor*. Actors can then be grouped into *Producers*, which take data from disks and sends into the data stream, *Filters* which apply a set of operations and forwards the data on, and *Consumers*, which take data from the data stream and write it to disk. Although SPIDER local level processing is not part of the *agapro* suite,

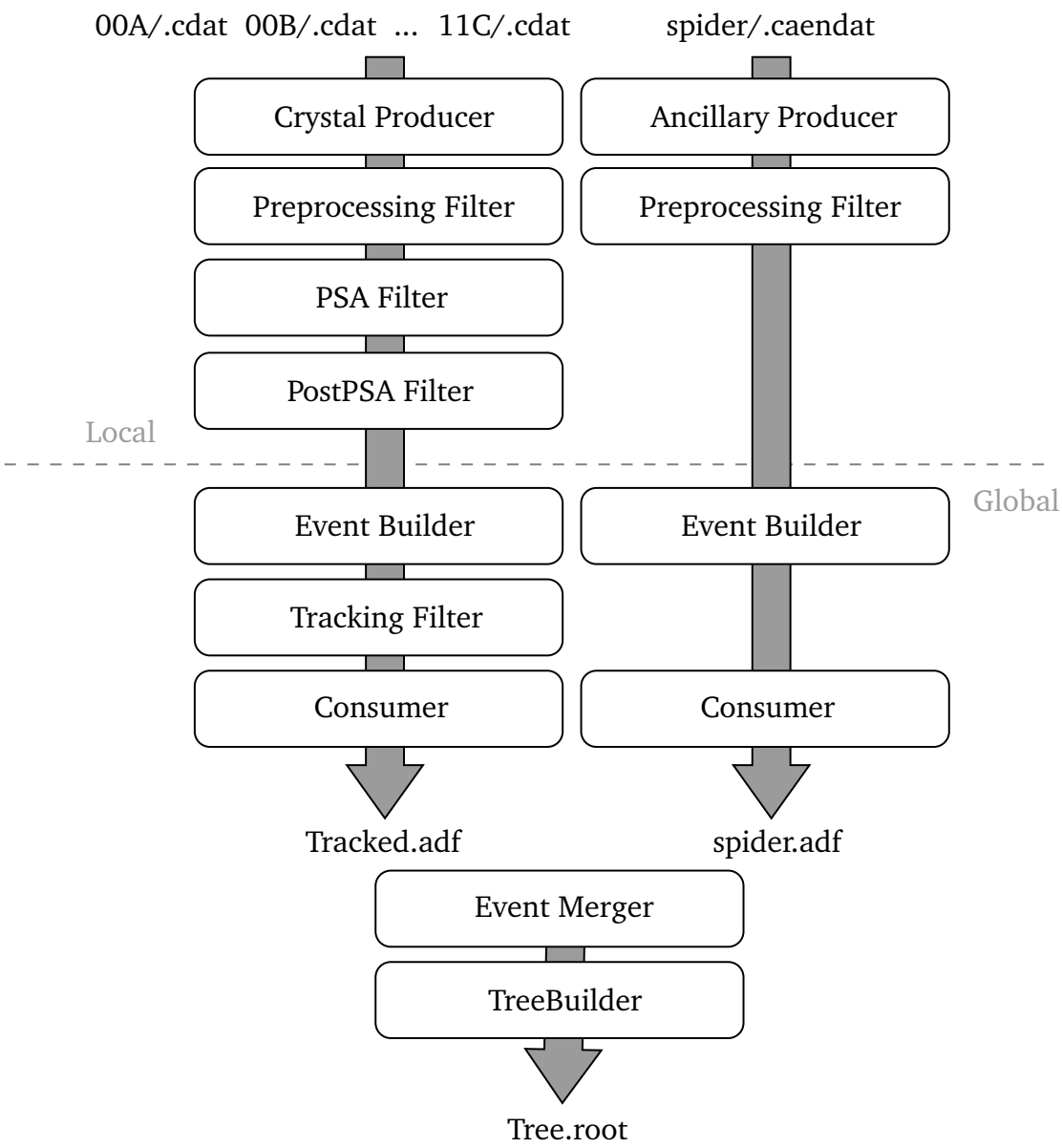

Figure 26: Data sorting flow chart.

the same language is adopted. In Figure 26, the whole sorting processes is represented in a flowchart.

At the end of the sorting process, ROOT [129] files are produced. These files contain all events acquired. These are then analyzed via the *agataselector* code [130] developed and maintained by the LNL team. This code performs the last steps of the analysis: reaction reconstruction, energy losses evaluation, and Doppler correction of the observed γ rays.

Nuclide	E [MeV]	Branching [%]
^{239}Pu	5.15659(14)	70.77(14)
	5.11443(8)	17.11(14)
	5.1055(8)	11.94(14)
^{241}Am	5.48556(12)	84.8(5)
	5.44280(13)	13.1(3)
	5.388(1)	1.66(20)
^{244}Cm	5.80477(5)	76.40(12)
	5.76264(3)	23.60(12)

Table 11: Partial α-decay spectrum of the Am-Cm-Pu 3α source. Taken from Adopted levels [47].

3.1.1 SPIDER data processing

SPIDER data frames are written in CAEN data format, as mentioned in Section 2.4 of the previous Chapter. Therefore, the SPIDER producer needs to read the CAEN format and translate them into the AGATA data format (ADF) [131]; the Preprocessing actor needs to apply a threshold and calibration; the Event Builder first sorts all data according to timestamp, then merges data that are deemed in coincidence into a single event. Finally, the consumer writes the final ADF frames to disk, so it can be later read and forwarded to the Merger Actor.

Calibration SPIDER segments calibration has been performed with a 3α source of Am-Cm-Pu, whose energies and branching ratio are reported in Table 11. The three most intense peaks were visible in all segments, but not all segments had the resolution to distinguish the less intense decays (also called "satellite peaks"), as it is visible in Figure 27. The presence of additional decay branches can only be inferred by a clear asymmetry between the two tails of the peak, but its centroid cannot be used for calibration. Therefore, a triple gaussian fit and a linear function was used to calibrate most of the segments, with the addition of another triple gaussian fit when resolution allowed. Figure 28 shows the result of the calibration procedure.

Threshold estimation The Preprocessing Filter is also in charge of rejecting an event due to not reaching the threshold. As the protons coming from the (d,p) reaction are on the edge of the sensitivity range, a threshold

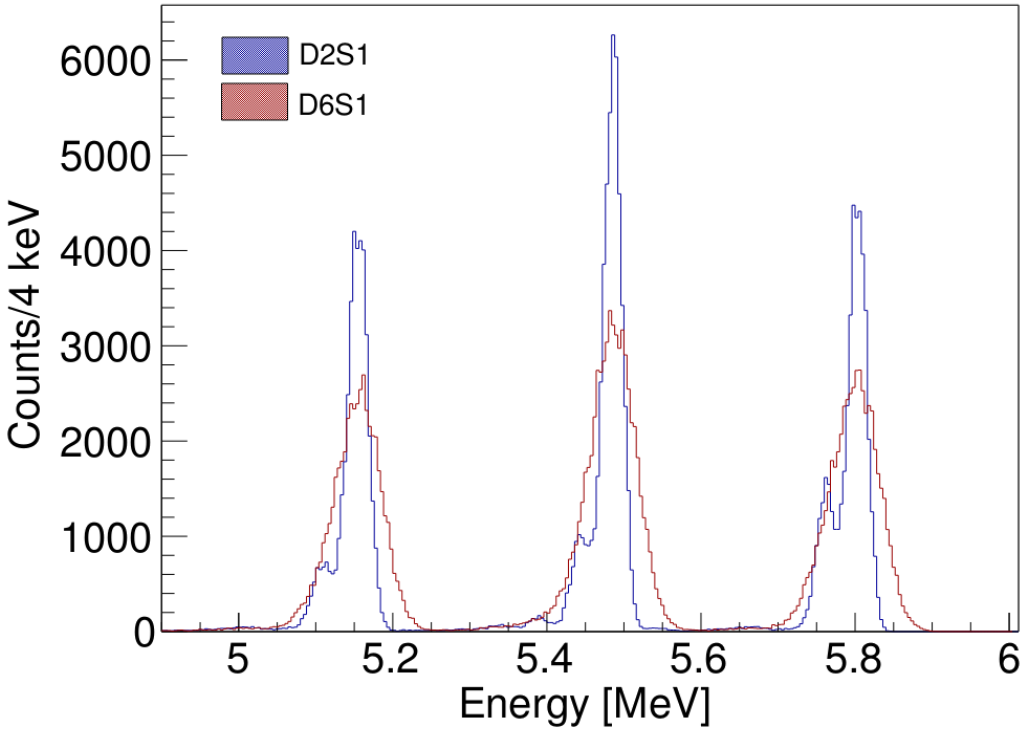

Figure 27: Am-Cm-Pu spectrum (calibrated) for two SPIDER channels: the better resolution in D2S1 (blue) allows to distinguish and fit the satellite peaks, while the worse resolution of D6S1 (red) only allows to see the three main peaks. Full discussion on the resolution of the individual channels is postponed to §3.3.

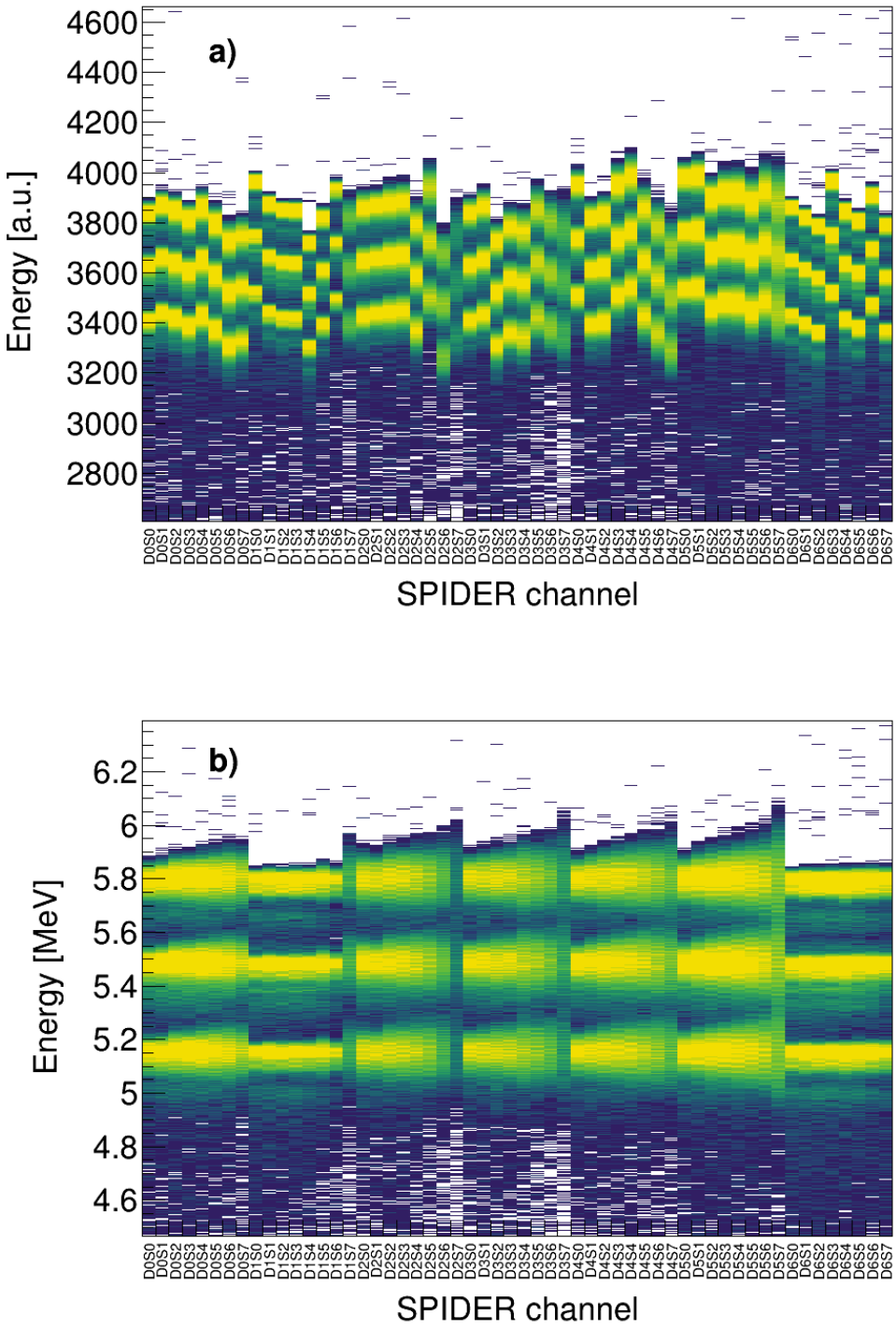

Figure 28: Comparison of the ^{241}Am-^{244}Cm-^{239}Pu spectrum for all SPIDER channels before (a), and after (b) the calibration procedure. Full discussion on the resolution of the individual channels is postponed to §3.3.

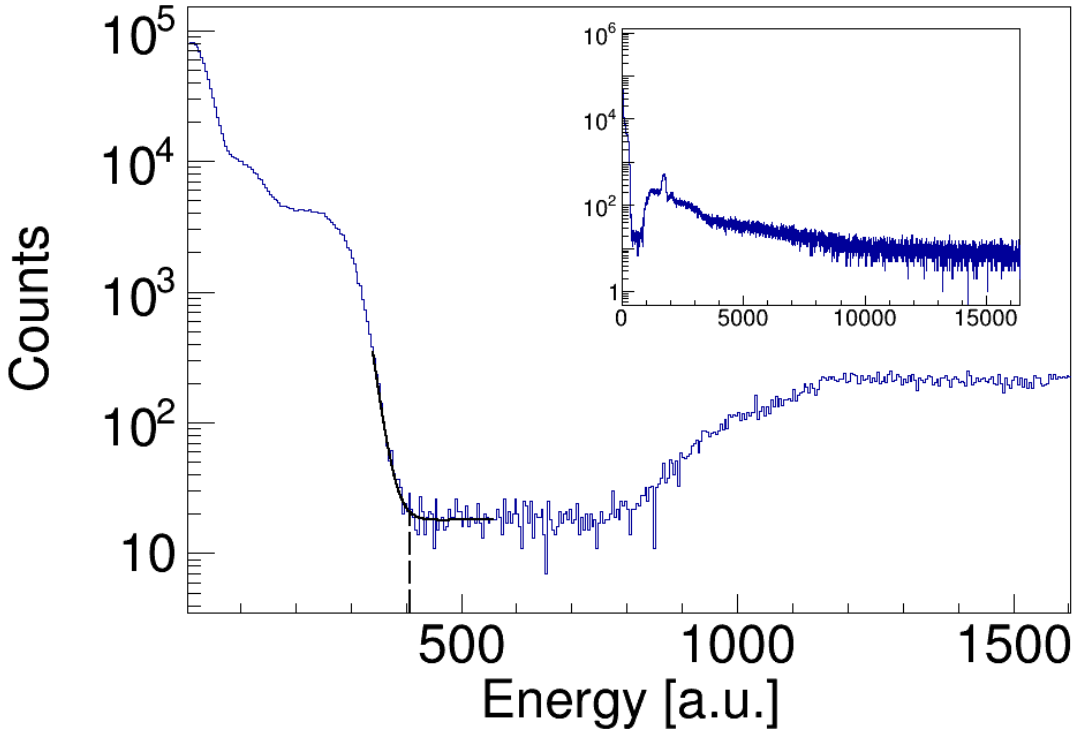

Figure 29: Lower threshold estimation for channel D2S0 of SPIDER. In the inset of the figure, the whole spectrum.

cannot be put on 3α data, but have to be extracted from the data. However, as it is clear from Figure 29, the high-statistics pedestal (visible in the Figure from about channel 0 to 400) makes it very hard to precisely assess the hardware threshold that was put during the experiment. In order to reduce the amount of fake coincidences between a γ-ray and a pedestal event, a software threshold was put on the energy spectrum for all channels of SPIDER. The software threshold was estimated by fitting with a parabola the region between the tail of the pedestal and the start of the FE proton spectrum, and taking the minimum of such function. The results of this procedure clearly either approximate or underestimate the hardware threshold. Since SPIDER is tasked to detect low-energy protons, the threshold value has an effect on the efficiency of the detector, which might be lower than the geometric one. This topic will be expanded upon in §3.4.

Time alignment While it is guaranteed that the timestamp of the CAEN digitizers increases synchronously with the GTS, it is instead not guaranteed that there is a common zero between all channels and the GTS. Time

shifts are actually expected due to the signal propagation in the CAEN digitizers chain. To check the time alignment between SPIDER and AGATA, events with coincidences in a window of 1 μs are built. Then, the time difference between the SPIDER and AGATA timestamp of data belonging to the same event is calculated and plotted as a function of the SPIDER channel, as in Figure 30(a). True coincidences should lie in a peak, which should be centered at zero for all channels. This procedure assumes that all AGATA crystals are already time-aligned. The procedure to do this will be explained in §3.1.2. All peaks in this matrix are fitted with a gaussian and stored. These value are then subtracted from the raw timestamp value at the Preprocessing Filter level of SPIDER, before sending the data forward to the Event Builder.

3.1.2 AGATA data processing

Similarly to SPIDER data, also AGATA raw data have to be processed before assuming physical meaning. During the present experiment, the DAQ dumped to disk all raw traces signals coming from the pre-processing electronics, allowing for full offline reprocessing.

The full AGATA processing consists in a series of operations applied to all written data that is organized in various stages, called *Preprocessing*, *Pulse-Shape Analysis* ((PSA), *Post-PSA* and *Event Builder* and *Tracking*. All stages are handled by a dedicated C++ actor in the femul chain of actors, ending finally with Consumer Actor which prints data in the final ADF format.

Preprocessing

The *Preprocessing Actor* (Prepro) is tasked to prepare the data for PSA. It handles the first calibration, time alignment and cross-talk corrections, along with the recovery of possible lost segments.

Calibration The first calibration is done with a ^{60}Co source so that all segments are calibrated within 2 keV for correct cross-talk correction. At this level, the offset is assumed to be constantly null for all segments, and only events with multiplicity 1 are taken into account, so to exclude

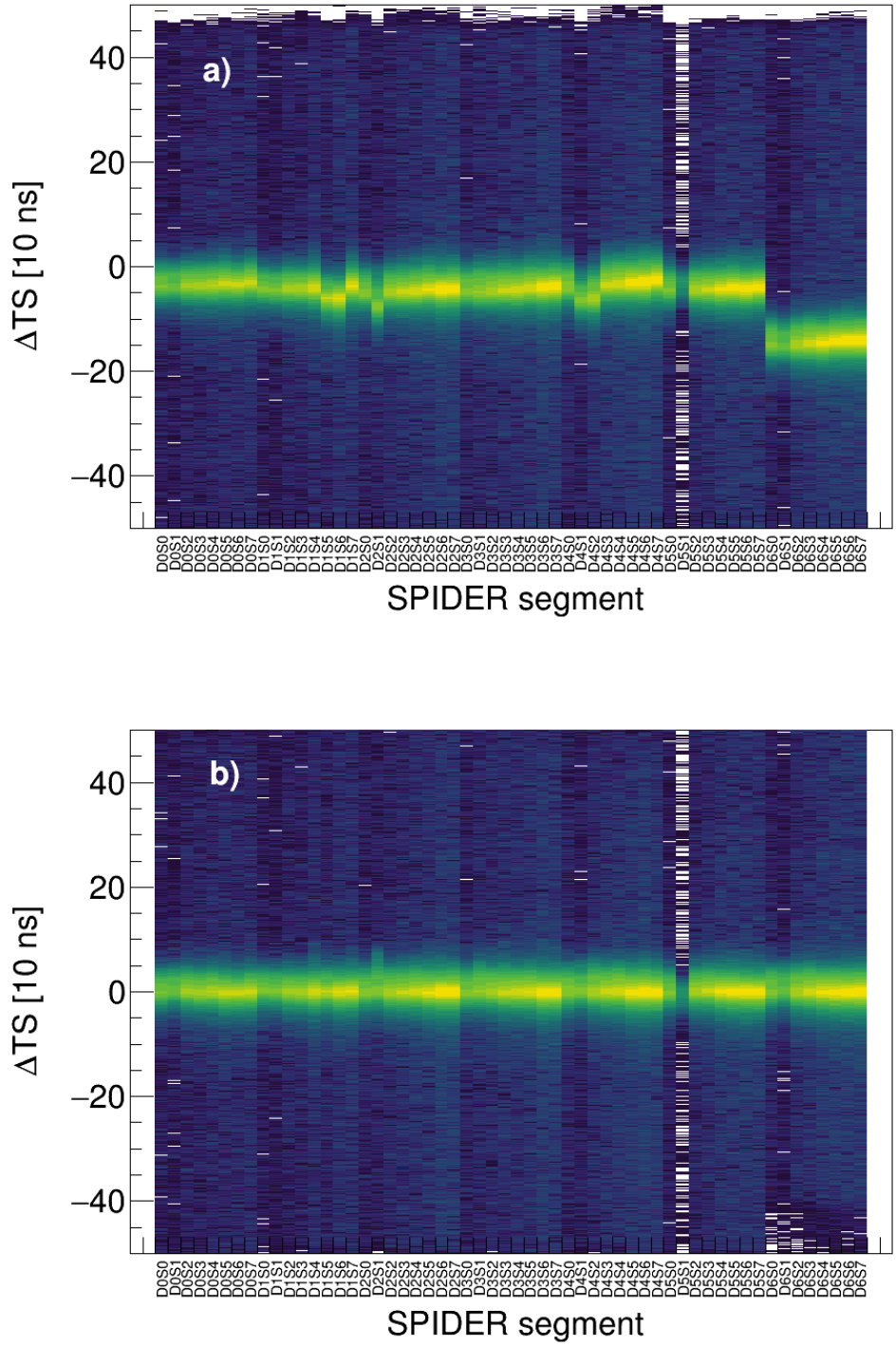

Figure 30: Difference in timestamp between AGATA and SPIDER, sorted by SPIDER channel. Spectrum obtained using experimental data before (a), and after (b) time alignment procedure. Before the alignment procedure, each channel has a non-zero average shift with respect to the timestamp of AGATA; this shift is removed in the alignment procedure so that the average shift with respect to the timestamp of AGATA is null.

any cross-talk contribution from the calibration. A comparison between the raw spectra and the first calibrated spectra can be found in Figure 31.

Cross-talk correction Cross-talk effects are observed in any electrically segmented detector, and need to be corrected in order to recover the exact energy deposition. In AGATA, two kinds of cross-talk effects are considered and corrected: proportional cross-talk and differential cross-talk. Proportional cross-talk depends on the capacitive coupling between all channels of the crystal (segments and core). The net effect is a dependence of the energy with the segment multiplicity and a degradation of the core resolution. The energy multiplicity dependence effect can be seen in Figure 32, where the centroid of the sum energy shifts as a function of the number of firing segments. Differential cross-talk depends instead on the resistance coupling between (mainly) segments and core. While there is not discernible net effect on the energy spectrum, differential cross-talk creates currents that mimic transient signals in the collected traces (see §3.1.2). Differential cross-talk therefore has a serious impact on the PSA quality.

Cross-talk correction is done via the theory of linear cross-talk of Bruyneel *et al.* [132], already implemented in the `agapro` package via the `xTalkSort` executable. Using a ^{60}Co source data, the program first sorts the events according to their multiplicity. Then, it sums the energy measured by each segment, and calculates the difference between this energy and the nominal energy of 1332.5 keV. From this set of differences, the cross-talk coefficient matrix is extracted. This procedure corrects the proportional cross-talk effects in the energy spectrum. Differential cross-talk cannot be corrected, as it is intrinsic with the crystal. Since differential cross-talk affects PSA performance, cross-talk effects are taken into account by the PSA actor. The same matrix calculated in the preprocessing stage is used later by the PSA actor to introduce in the ADL library the differential cross-talk effects. In this way, the χ^2 minimization procedure used to calculate the interaction position inside the crystal takes into account cross-talk effects.

Recovery of lost segments It might happen that not all 36 segments inside a crystal work properly. In case only one segment is not working, it can be recovered at this stage using the same linear cross-talk theory. A not

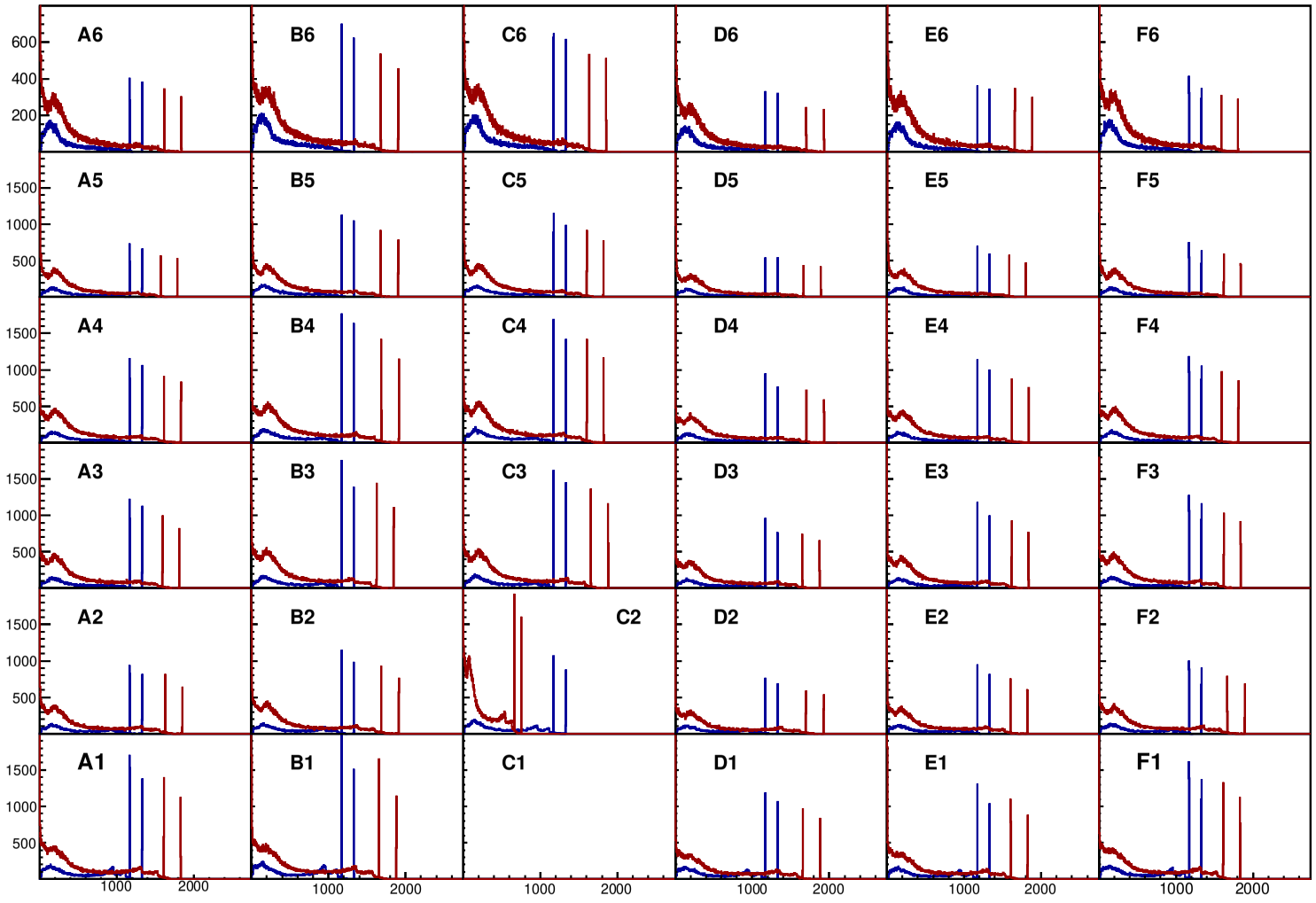

Figure 31: Preprocessing Actor spectrum: ^{60}Co spectrum before (red) and after (blue) calibration for crystal 00A. Segment C1 is clearly missing, while segment C2 has a lower gain with respect to all other segments. The first calibration takes care of the former, while the latter will be adjusted in the cross-talk correction phase.

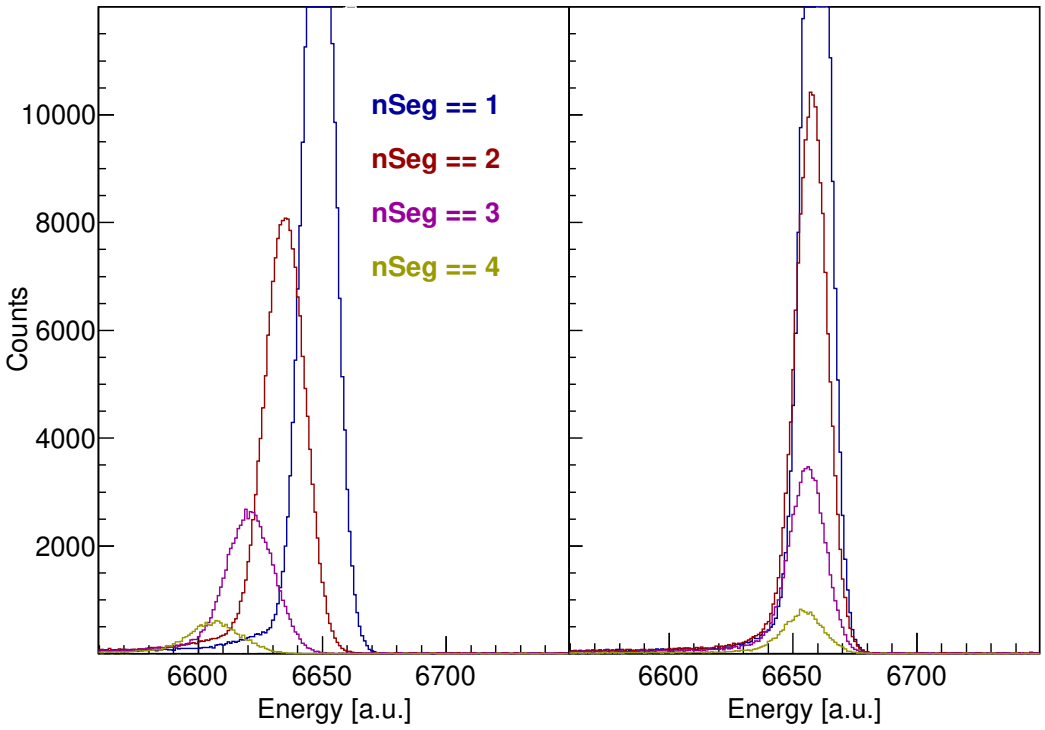

Figure 32: ^{60}Co spectrum: sum of the energy of the segments as function of the number of firing segments (indicated with nSeg) before (left) and after (right) cross-talk correction.

functioning segment can be either *unstable*, *broken* or *lost*. *Unstable* segments have a periodic gain jump that creates two sets of peak in the ^{60}Co spectrum. *Broken* segments are results of a problem at FET level, so that the charge of the segment is not collected but flows to the neighbouring channels. This produces a loss of gain in the affected segment and the appearance of low-energy “ghost peaks" in the neighbouring segments. *Lost* segments are produced when the detector works normally but the channels is not present in the data, due to, e.g., broken wire or faulty digitizer channels. In this case, the affected segment has no statistics and all other channels are unaffected. Such is the case, for example, of segment C1 in Figure 31.

Recovery of these cases is also done via the `xTalkSort` executable, which calculates the missing energy of the segment from the core energy. In case a crystal has more than one faulty channel, recovery is not possible.

Time alignment The PSA algorithm implicitly assumes that all traces start at the same moment in time. Therefore, if there is any big time mismatch

between the segments, this might produce some clusterization patterns in the output of the PSA. In order to account for this effect, the digital CFD zero-crossing of the segment is corrected by a time shift. This time shift is calculated minimizing the time difference of the CFD zero-crossing with the core trigger timestamp. Figure 33 shows the spectra of the difference between the the core timestamp and the segment timestamp obtained from the CFD algorithm. Data were taken with a ^{60}Co source, and are shown before (red) and after (blue) such correction.

Pulse-Shape Analysis (PSA)

The *Pulse-Shape Analysis* (PSA) actor is in charge of performing the pulse-shape analysis algorithm on the data. The PSA consists in comparing the shape of the measured signal traces (both charge and induced) with a reference library of traces associated with a specific interaction point.

When a γ ray interacts with the active material of the crystal, a signal is created in the hit segment, while an induced signal is also produced in the neighbouring segments. The direct signal is called the *net-charge* signal, while the others are called the *transient* signals. In the case of a perfect detector, the integrated current of the net-charge signal should be equal to the deposited energy, while the integrated charge of the transient signals should vanish. Applied voltage, detector geometry, impurity concentration and different mobilities of charge carriers introduce a spatial dependence in the induced signal shape that can be exploited to recover the interaction position.

By means of χ^2 minimization procedure, the PSA is able to determine, with a FWHM of 4 mm [133], the γ-ray interaction point inside the crystal. The standard library of traces used in AGATA is the AGATA Data Library (ADL), also called PSA basis [134]. This library, generated via Geant4 simulations, contains about 10^5 simulated pulses of every segment and core for every possible interaction point inside each AGATA crystal with a grid size of 2 mm.

Different PSA algorithms have been implemented, result of a compromise between resolution and computing time. The standard one that has been adopted by the collaboration, and in this work, is the *Adaptive Grid-Search* [135]. The

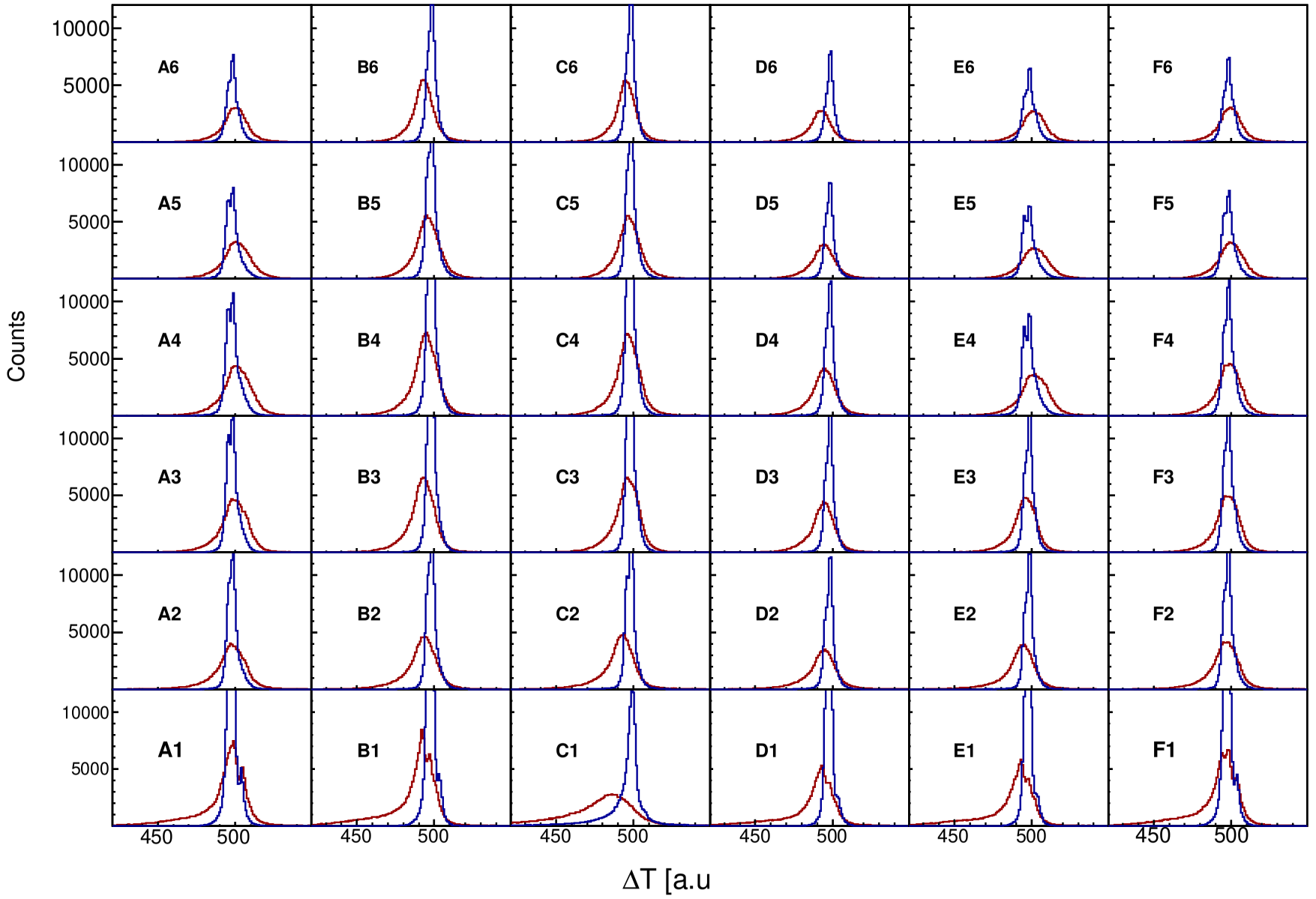

Figure 33: ^{60}Co spectrum: spectrum of the time difference between core timestamp and segments timestamp from CFD algorithm of crystal 00A before (red) and after (blue) time alignment. After time alignment procedure, all segment-segment time differences are distributed on a narrow peak centered at the middle of the spectrum (i.e. 500 a.u.).

Adaptive Grid-Search algorithm first does a scan on a coarse grid of 6 mm all around the crystal. Then, selects the region with the lowest χ^2 value and performs a second, finer, scan, with a grid length of 2 mm per point. Only the hit segment, its nearest neighbours and the core signal are considered in the evaluation.

Post-PSA

The *Post-PSA Actor* (Post-PSA) allows one to make the final operations on the local level of data. It handles the final neutron-damage correction, the final linear recalibration and the final global time alignment between all crystals to prepare them for tracking. At this level it is also possible to choose whether to use the core energy as energy reference or the sum of all segments as energy reference.

Neutron damage correction High flux of fast neutrons is known to damage the energy resolution of n-type HPGe detectors such as the AGATA crystals. Fast neutrons damage the crystal lattice of the detector, producing traps in which charge carriers (mainly holes) can be captured with very long ($\sim$ ms) release time. The net effect on the energy spectrum is the appearance of an exponential tail on the low energy side of the photopeak. However, in the case of AGATA, the high segmentation of the crystals and the possibility of PSA, allows to partially compensate the neutron damage effects. The standard approach adopted by the AGATA collaboration is the one of Bruyneel *et al.* [136]. Energies of the channel i (core or segment) are recalibrated according to

$$E* = \frac{E}{1 + s_e/\lambda_e + s_h/\lambda_h} \tag{19}$$

where $s_{e,h}$ are the electron/hole sensitivity (given by PSA) and $\lambda_{e,h}$ are experimental parameters to quantify the neutron damage of the detector. They are estimated using the 1332.5 keV ^{60}Co line and the agapro executable `SortPsaHits`. This program performs a grid search of the two parameters trying to maximise the integral of the peak and minimize FWHM. The combination of values that yield the best parameters is chosen, and kept constant throughout the experiment.

During the present experiment, being the first experiment of the campaign, neutron damage is found to be negligible for most of the crystals, with measurements performed both before and after the experiment. Only crystals 05B, 08A, 08B, 08C, 11A, 11B presented non-negligible neutron damage in some segments, which could be corrected. An example, crystal 11A, is shown in Figure 34.

Final calibration The final energy recalibration has been performed using a combination of ^{152}Eu, ^{226}Ra, ^{60}Co and experimental lines. Parasitic reactions and β decay lines have been used as cross-check and reference to recursively calibrate all segments and cores up to 4 MeV of energy. A full list of the experimental lines used, with their origin, can be found in Table 12. In case of low-statistics peaks, more experimental runs were joined together in the calibrations, using the higher statistics ones to ensure proper alignment. In this way, any change in experimental conditions that might have affected the calibration (change in shaping time, voltage, temperature) has also been compensated for. Figure 35 shows the residuals of all calibrated segments. As it can be seen, no residual falls more than 0.5 keV from 0, and the dispersion is roughly gaussian around 0. However, a clear energy dependence can be seen in the inset of Figure 35. However, this dependence is still inside experimental tolerance and is neglected. At this level a total of 20 AGATA segments have been eliminated to preserve maximum resolution of the apparatus - either because of calibration non linearity, gain jump or poor resolution at high energy. Other 3 crystals, namely 04C, 05C and 07C, were excluded from the analysis because of an intermittent gain jump in both cores and segment signals.

ForceSegmentsToCore After calibration, it is possible to choose whether the core signal is better than the signal of the sum of the segments. If the resolution of the core is better, then the core energy is assumed to be the total energy, and the single energies of the segments are renormalized to the core one. Figure 36 shows the evolution of the full-width half maximum for all crystals as a function of energy, both for cores and sum of the segments. It can be seen that in almost all cases the resolution of the sum of the segments is better or comparable to the core one. In these data, the option `ForceSegmentsToCore` was therefore not used for any crystal.

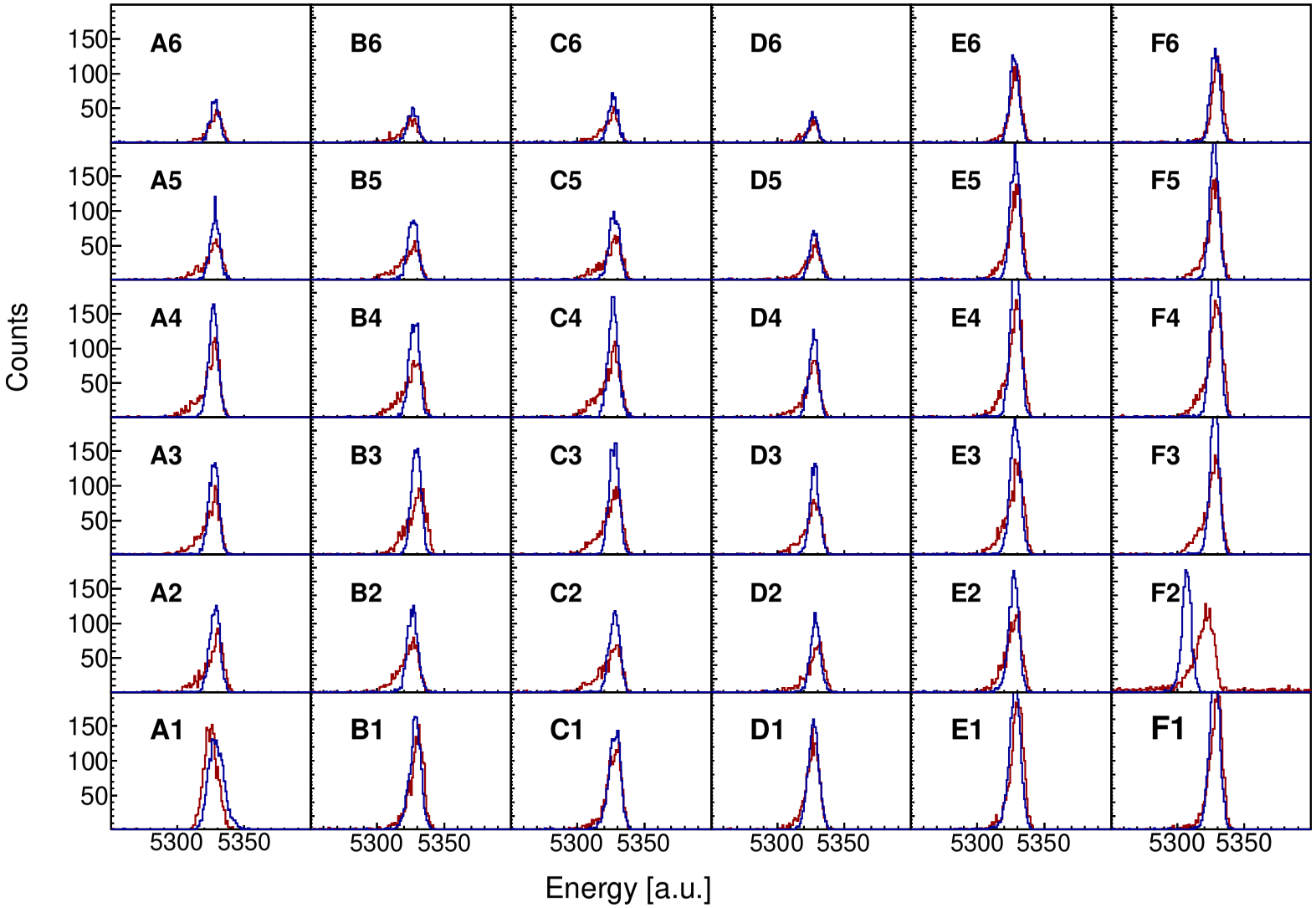

Figure 34: Neutron damage correction for crystal 11A: non corrected (red) and corrected (blue). The calibration of segment F2 has been changed sensibly by the neutron damage correction procedure; this effect is going to be adjusted in the final recalibration step.

Energy (keV)	Origin
136	^{181}Ta $9/2^+ \rightarrow 7/2^+_{gs}$; Coulex
165	^{181}Ta $11/2^+ \rightarrow 9/2^+$; Coulex
278	^{197}Au $5/2^+ \rightarrow 3/2^+_{gs}$; Coulex
301	^{181}Ta $11/2^+ \rightarrow 7/2^+_{gs}$; Coulex
359	^{181}Ta $13/2^+ \rightarrow 9/2^+$; Coulex
415	^{181}Ta $15/2^+ \rightarrow 13/2^+_{gs}$; Coulex
437	^{42}Ca $6^+ \rightarrow 4^+$; FE with ^{12}C
511	e^+e^- annihilation
547	^{197}Au $7/2^+ \rightarrow 3/2^+_{gs}$; Coulex
1015	^{27}Al $3/2^+ \rightarrow 3/2^+_{gs}$; Coulex
1228	^{42}Ca $4^+ \rightarrow 2^+$; FE with ^{12}C
1461	primordial ^{40}K β decay
1525	^{42}Ca $2^+ \rightarrow 0^+$; FE with ^{12}C
3103	^{37}Cl $7/2^- \rightarrow 3/2^+_{gs}$; β decay
4016	^{37}Cl $3/2^+ \rightarrow 3/2^+_{gs}$; β decay

Table 12: List of the γ-ray lines used for the final calibration, aside the ones from ^{152}Eu and ^{226}Ra. FE lines from ^{42}Ca are observed stopped mainly due to the population of the isomeric 6^+ states.

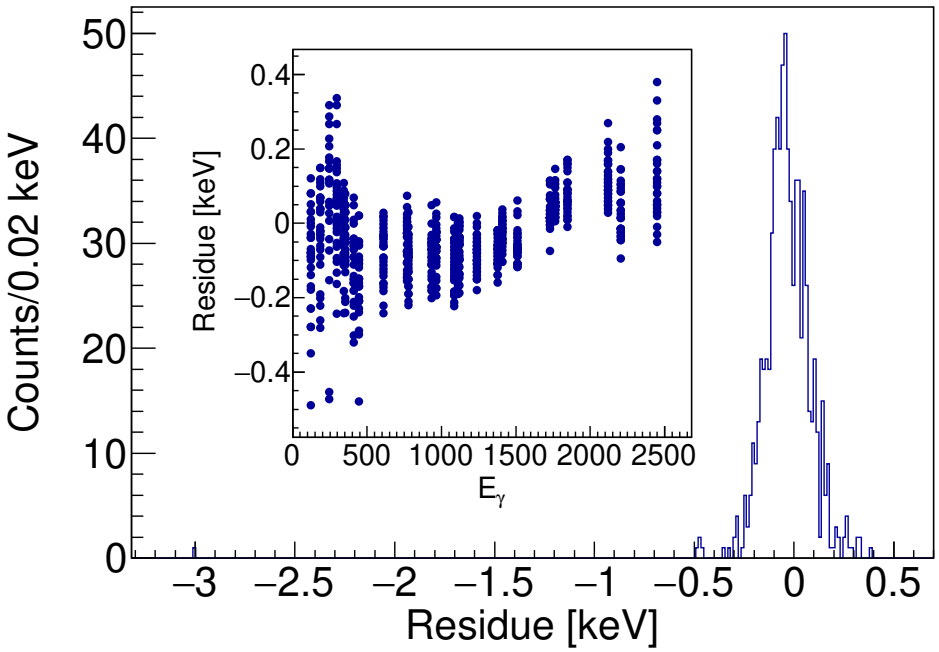

Figure 35: Residuals of the final calibration procedure. In the main picture, the residual distribution, which is approximately gaussian centered at -0.041(4) with FWHM of 0.211(7). In the inset, the dispersion of the residuals as a function of the γ-ray energy.

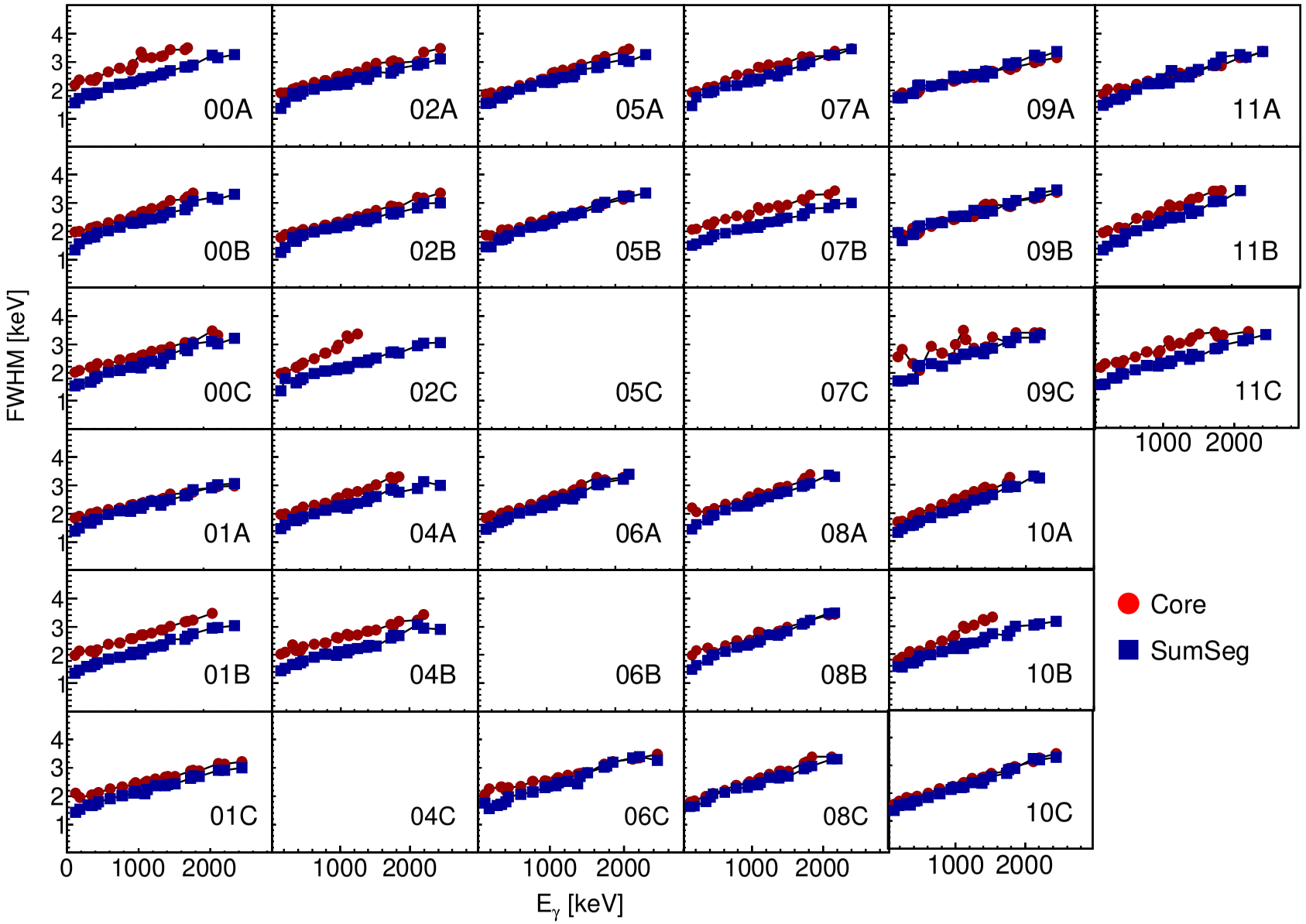

Figure 36: Evolution of the AGATA FWHM as a function of the γ-ray energy with data from ^{152}Eu and ^{226}Ra sources. Core resolution is displayed in red circles, while sum of segments resolution is displayed in blue squares. Crystals 04C, 05C and 07C had unstable core gain, thus were excluded from the analysis.

Global Time Alignment The last step needed to prepare data for tracking is the so called Global Time Alignment (GTA). Namely, the Event Builder actor assumes that γ rays detected simultaneously by different crystals have close (if not equal) timestamp. In reality, differences in the pre-processing chain, e.g. cable length, communication speed, event processing time might introduce artificial time shifts in the timestamps. These shifts need to be removed to obtain the true event timestamp. These are removed via the `solveTT.py` script, which calculates the centroid of all time differences between crystals and calculates the shifts that need to be applied in order to minimize the average difference. All these shifts are then applied to the data.

Tracking

The Tracking Actor is in charge of performing the trajectory reconstruction of the single γ rays from the multiple hits inside the active volume of the array (after PSA algorithm). Several methods have been developed over time for the tracking task, and can be mainly categorized in forward tracking, backward tracking, Bayes tracking and machine learning tracking methods [137]. Other kinds of tracking are also available and still under development. *Backward* and *forward tracking* have their root in the Klein-Nishina formula for Compton scattering, which is the main interaction of γ-rays in Ge in the energy range considered here. The main assumption is that, unless the energy of the incident γ-ray is very low, the scattering happens predominantly in the forward direction. Therefore, interactions created by Compton scattering should lie fairly close to each other in the (θ, ϕ) plane. Once a set of points is found, they are clustered, and the cluster is compared to the Compton scattering formula in order to find the interaction order. Forward tracking algorithms start from the identification of the first interaction point, via the minimization of some Figure-Of-Merit (FOM) based on the Compton scattering formula, while backward tracking assumes as last interaction point an interaction between 100 to 350 keV, and then tries to cluster close points recursively.

The algorithm used routinely in AGATA, and for this thesis, is the *Orsay Forward Tracking* (OFT) algorithm. This algorithm depends on three parameters [138]:

- σ_ϑ (angle uncertainty): quantifies the associated uncertainty in the determined ϑ angle of the interaction given by PSA. Large σ_ϑ relaxes how good a sequence of interactions must satisfy the Compton-scattering formula;

- $\mathrm{P_{sing}}$ (single interaction probability): quantifies the minimum probability for a γ-ray to interact via photo-electric effect;

- $\mathrm{P_{track}}$ (track probability): gives a threshold condition for the acceptance of having multiple-interaction points.

These parameters have to be case-by-case optimized to improve the performances of the tracking algorithm, as the optimum values are dependent also on the energy of the transition of interest. Actually, recent studies have proven that only two of these parameters are independent, namely σ_ϑ and $\mathrm{P_{track}}$, while the third can be fixed at 0.015.

Optimization of the tracking parameters The tracking parameters have been optimized via brute-force grid-search minimization. Since the ^{226}Ra source has γ-ray lines that are close in energy to the experimental ones, namely 609 and 2204-keV, the optimization was carried out on ^{226}Ra source data. The tracking algorithm was applied to the same dataset for every combination of parameters in the space $\sigma_\vartheta \in$[0.70 - 2.00] and $\mathrm{P_{track}} \in$ [0.00-1.00] in steps of 0.01. As Figure-of-Merit (FOM), a modification of the standard definition of the resolving power has been used. This was defined as

$$100 \cdot \frac{\mathrm{P/T}}{\mathrm{FWHM}} \frac{\mathrm{Area_{track}}}{\mathrm{Area_{sum-cores}}} \tag{20}$$

where $\mathrm{P/T}$ is the peak-to-total ratio, calculated on a range in the neighbourhood of the peak, FWHM the full-width-half-maximum of the peak and the ratio between the area between tracked spectrum and the sum of all cores spectra. The usual definition of resolving power has the mean separation energy between transitions instead of $\mathrm{Area_{track}/Area_{sum-cores}}$. As the FOM has to maximize the number of correctly tracked events, and not the separation between different close transitions, the definition was adjusted accordingly. All quantities were extracted from a gaussian fit

of the 609, 1378, 1847, 2119 and 2204-keV γ-ray lines of ^{226}Ra decay spectrum.

The spectra in Figure 37 convey the same message for all energies: for more "relaxed" tracking parameters ($\sigma_\vartheta \rightarrow 2$, $\mathrm{P_{track}} \rightarrow 1$) the peaks worsen, but efficiency is boosted, while stringent tracking acceptance criteria keep peaks well-shaped, but poorer in statistics. For fixed $\mathrm{P_{track}}$, the FOM value increases with increasing σ_ϑ, until it reaches a plateau. As the FWHM is slowly-varying, much of the change is due to the $\mathrm{Area_{track}}/\mathrm{Area_{sum-cores}}$. Large σ_ϑ decrease the physics information taken into account by the tracking algorithm, which then tends to sum all hits detected by neighbouring crystals (in a similar fashion to the addback procedure implemented in traditional Compton-suppressed clover detectors). For $\sigma_\vartheta \rightarrow \infty$, the tracking algorithm would sum all hits seen by the detector, which then would behave like a total absorption spectrometer. Too high values of σ_ϑ, on the other hand, are not desirable as both the probability to sum uncorrelated γ rays and the probability to mis-identify the first interaction point increase as well. Therefore, the σ_ϑ value just before the plateau was considered as the best compromise between maximizing efficiency and minimizing the probability of wrongly tracked events.

Since the peaks of main interest are near 2 MeV, the tracking parameters were fixed at $\sigma_\vartheta = 1.1$ and $\mathrm{P_{track}} = 0.05$. $\mathrm{P_{track}}$ was kept at the default value, as any further decrease of it produced the same effects of an increase in σ_ϑ. These values were then applied to all data.

3.2 Optimizations

Small differences between the real experimental conditions and the nominal parameters may lead to sub-optimal results. In particular, the relative positions of the detectors with respect to each other and the target introduces systematics on the angle determination, leading to a worse resolution in the Doppler-corrected experimental spectrum with respect to the ideal case.

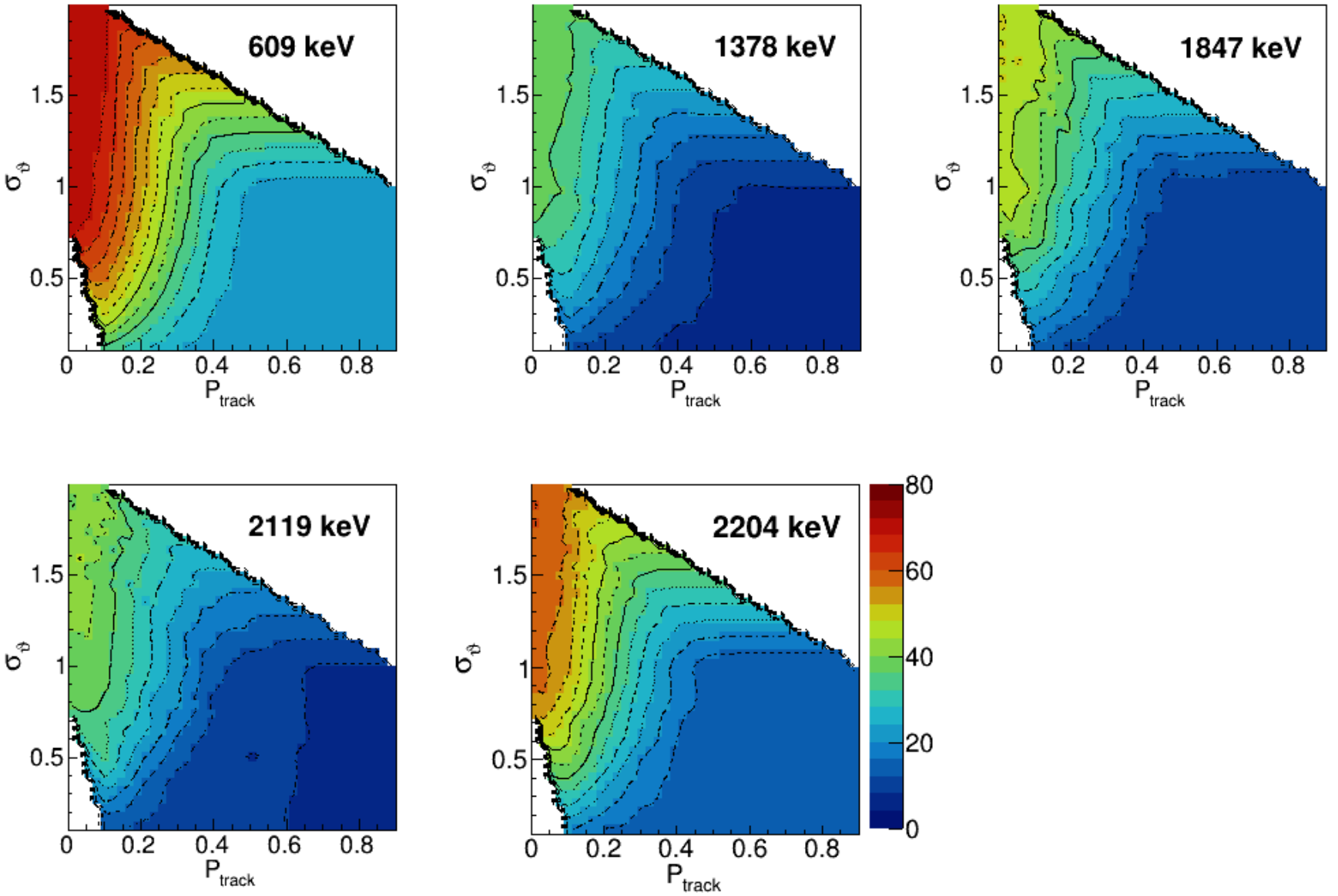

Figure 37: FOM as function of σ_ϑ and P_{track} and E_γ. Countour lines are drawn in black as guide to the eye.

Since the Doppler correction relies on the reaction reconstruction, the SPIDER detector position was optimized first, then the one of the AGATA detector. The method followed is the same: after choosing a reference figure-of-merit (FOM, presented below), a dataset is analyzed with a set of parameters; at the end of the analysis, the FOM is recalculated, and the set of parameters is slightly varied. The process is repeated as long as the absolute minimum is found. The MIGRAD algorithm of the Minuit2 library [139] was used to perform the minimization algorithm and find the minimum. These routines are implemented in the *agataselector* software.

Since there were 3 changes of the experimental conditions (one for the mounting of the first Plunger target, one for the second Plunger target, and the last for the DSAM and CD_2 only targets), the minimization procedure has been performed three separate times.

SPIDER and target optimization

In the analysis reference system, the beam spot is always located at $(0, 0, 0)$, while the beam axis is parallel to $\hat{z}$. In this reference system, SPIDER is considered as a rigid body, and its position can be expressed with the (x, y, z) coordinates of its center. SPIDER can also rotate along the y axis of an angle Θ, and around its symmetry axis (the beam axis, z) of an angle Φ. From the position of the center, the position of each segment is fixed thanks to the rigidity of the support. Nominally, SPIDER is centered on the beam axis, and translated in the z direction by -8.5 cm, with no additional rotation.

In the direct one-neutron-adding reaction, the recoiling proton is emitted with energy E_p that depends on the emission angle θ. Since the reaction is binary, the kinematics can be reconstructed to recover the trajectory and the excitation energy of the ejected ^{37}S (see §1.3). The excitation energy spectrum obtained with the thin CD_2 only target is shown in Figure 38.

Two peaks are clearly identifiable, which correspond to the 646 and 2638 keV states of ^{37}S, plus an additional smaller peak at 1992 keV (discussion on the physics results will be done in Chapter 4). The excitation energy, in the ideal case, should only depend on the structure of the ejected nucleus, and should not hold any residual dependence on the trajectory of the recoiling proton. As

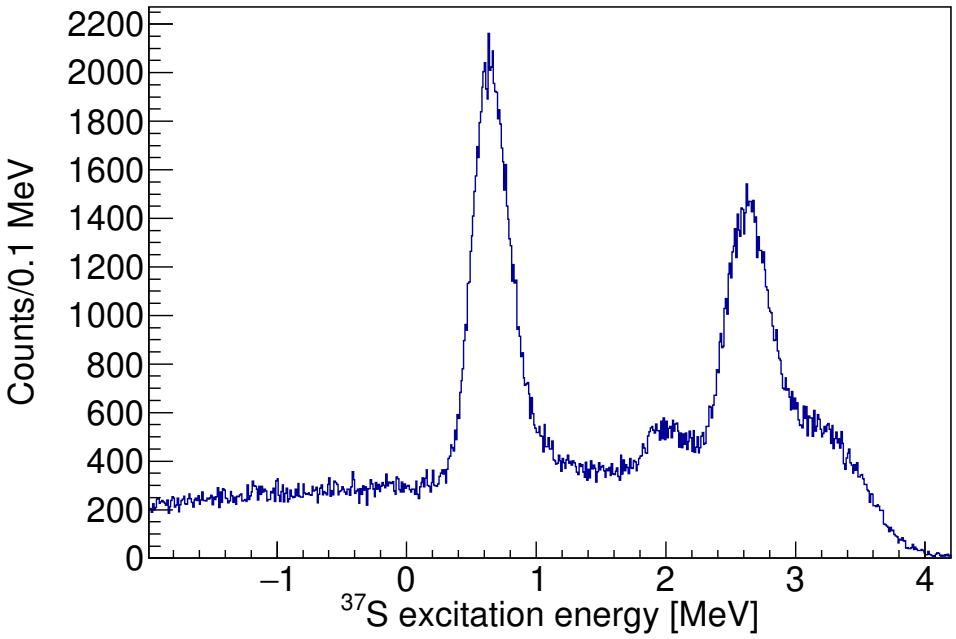

Figure 38: Experimental excitation energy (E_x) spectrum of the ^{37}S ions. Only events in coincidence with the observation of a γ ray are shown. FE reaction on ^{12}C produces the background events that reach negative excitation energy values.

it is clear from Figure 39(a), there is indeed a residual dependence that comes from a placement of the detector slightly different from the nominal one.

A 7-parameter optimization was carried out. The coordinates of the center (x, y, z) and the angles Θ and Φ were used as parameters, along with the target thickness d and its rotation θ with respect to the beam axis. The chosen FOM was

$$\mathrm{FOM} = \sum_{i}^{N} w_i[z_i(\mu_i^* - \mu_i)^2 + (1 - z_i)\sigma_i], \tag{21}$$

where the sum is carried on all reference peaks (in this case the 646- and 2638-keV peaks, therefore N=2), and w_i is a weight factor that scales the importance of the transition for the FOM calculations. The weight z_i instead determines whether to privilege a larger peak with correct centroid or a smaller peak at slightly wrong energy. In this case, equal weight were assumed for all transitions and parameters ($w_i = z_i = 1/N = 0.5$). The obtained optimal parameters can be found in Table 13.

Parameter	4 mg/cm^2 Au	6 mg/cm^2 Au	30 mg/cm^2 Au
x [mm]	1.8	0.	0.3
y [mm]	3.7	0.9	0.
z [cm]	-8.1	-7.6	-8.4
Θ [deg]	1.3	0.22	0.6
Φ [deg]	1.1	-0.16	0.0
d [mg/cm^2]	0.352	0.118	0.498
ϑ [deg]	0.7	-2.4	0.2

Table 13: SPIDER optimal parameters: the coordinates (x, y, z) of the center of SPIDER and its rotation around the y axis (Θ) and z axis (Φ) for each of the three datasets.

The effect that this procedure has on the experimental data is shown in Figure 39(b): the dependence is almost completely removed, and all centroids now lie withing 1σ from the average. The optimization procedure has to be repeated at every change of the target. In fact, in order to access the Plunger device or the target holder, SPIDER had to be completely unmounted from the reaction chamber. The optimal target thickness yielded by the optimizer, however, is a factor from two to five smaller than the nominal one. This fact, which hints to target damage due to irradiation, will be discussed in Section 3.4.

AGATA position optimization

For the AGATA γ-ray spectrometer, the reference system is the same of the one of SPIDER, with the same set of coordinates: AGATA is envisaged as a rigid body centered at coordinates (0, 0, 55 mm), with an additional rotation applied to these coordinates around the y axis (Θ angle) and the z axis (Φ angle). AGATA rotates solidarily with PRISMA, therefore in all cases $\Theta = \pi$ - Θ_{PRISMA}, where $\Theta_{\mathrm{PRISMA}} = 0$ if PRISMA is aligned with the beam line. In the case of the present experiment, PRISMA was rotated by 50 deg with respect to the beam line, therefore Θ is equal to 130°. No rotation is expected around the z axis. As FOM, the 646-, the 1992- and the 2616-keV peaks of ^{37}S in the Doppler-corrected spectra were chosen. Equal weigth was assigned again to all parameters and transitions ($w_i = z_i = 1/3$) The obtained parameter sets can be found in Table 14. As in the case of SPIDER, the optimization procedure had to be repeated at every target change. Indeed, in order to access the reaction chamber, the AGATA spectrometer had to be completely retracted from the

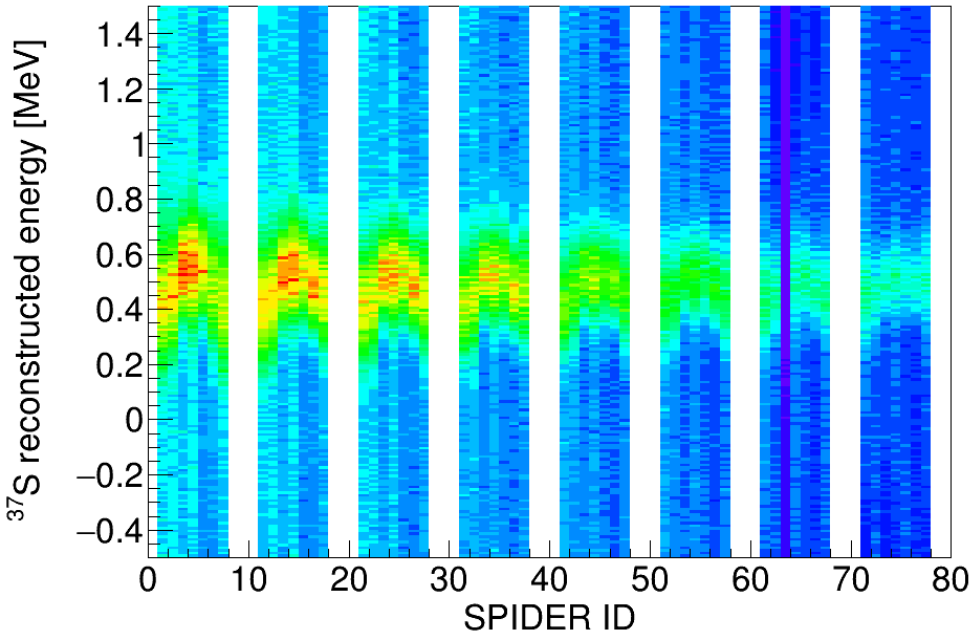

(a)

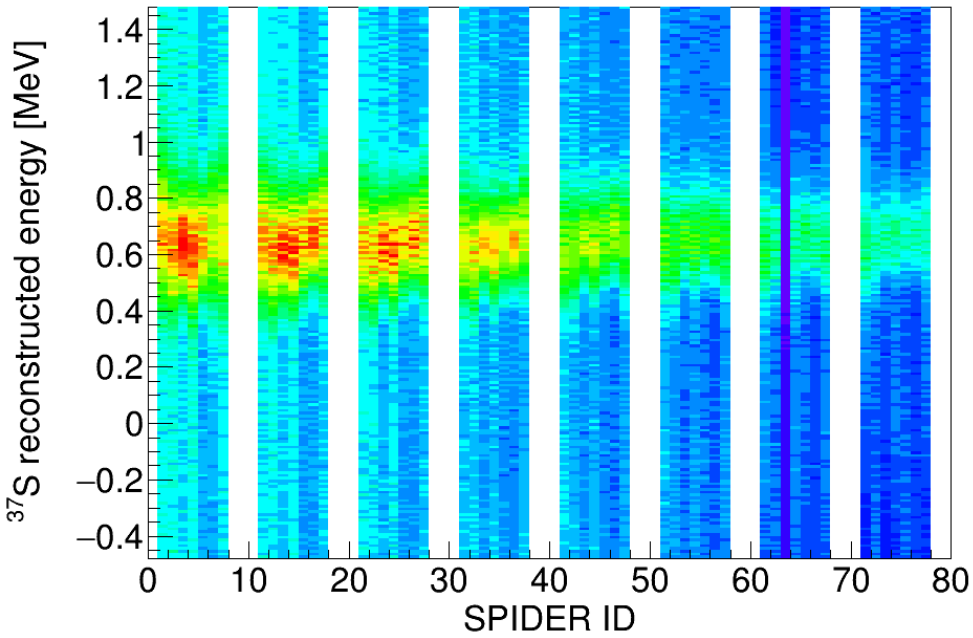

(b)

Figure 39: Experimental excitation energy (E_x) spectrum of the ^{37}S ions as a function of the SPIDER channel a) before and b) after optimization. Channels are ordered by increasing azimuthal and polar angles.

Parameter	4 mg/cm^2 Au	6 mg/cm^2 Au	30 mg/cm^2 Au
x [mm]	0.9	0.75	-2.1
y [mm]	1.0	1.0	-1.9
z [mm]	54.0	53.9	55.9
Θ [deg]	129.8	129.9	130.3
Φ [deg]	0.99	1.1	1.0

Table 14: AGATA optimal parameters: the coordinates (x, y, z) of the center of AGATA and its rotation around the y axis (Θ) and z axis (Φ) for each of the three datasets.

close-up position to a very backward one. Therefore, with every repositioning in the close-up position, slight changes in the z offset could be expected.

3.3 Performance

This Section assess the performance obtained after the Local Level Processing of the AGATA and SPIDER setup, in terms of efficiency and resolution. The values obtained in this Section represent the stepping stone for the benchmarking of the GEANT4 simulations that is illustrated in the next Section.

AGATA resolution

As it is shown in Figure 40, core resolution is well inside the specifications, while tracked resolution is worse, as expected, but still acceptable. At ^{60}Co, the FWHM is 2.43 and 2.54 keV for average cores, 2.7 and 2.8 keV for tracking. The FWHM energy dependence can be interpolated with the usual quadratic formula

$$\mathrm{FWHM} = \sqrt{A + BE_\gamma + CE_\gamma^2}, \tag{22}$$

yielding the parameters in Table 15. Data and interpolating functions for both cores and tracked spectra is displayed in Figure 40.

Type	A	B	C
Cores	2.11(6)	0.0033(1)	$5(5) \cdot 10^{-9}$
Tracked	1.4(4)	0.0050(4)	$0(5) \cdot 10^{-9}$

Table 15: AGATA resolution curves parameters, as defined in Equation 22.

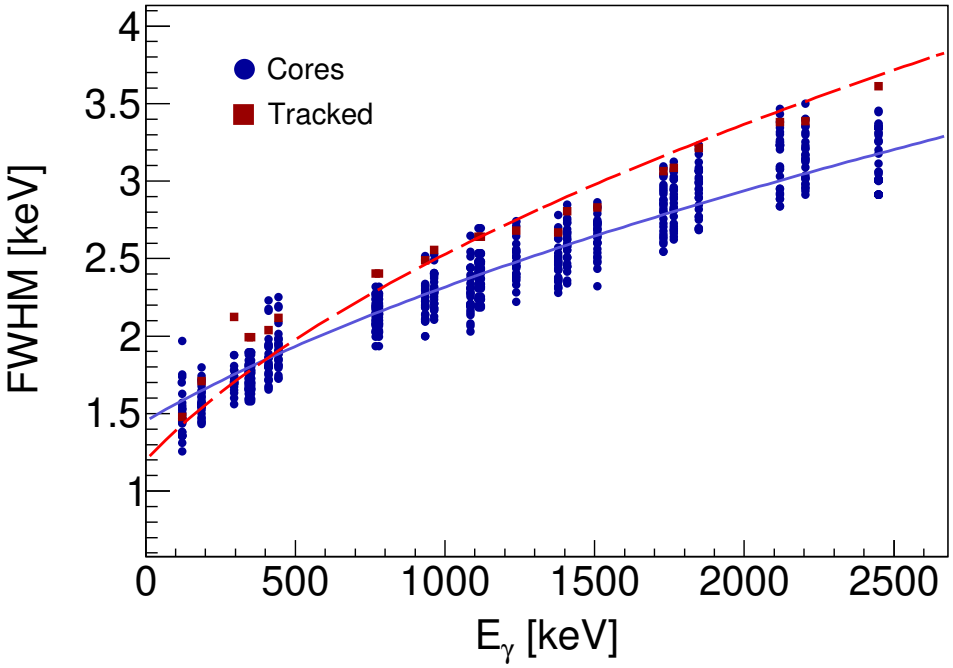

Figure 40: AGATA resolution curve. In blue circles, the resolution core by core at ^{152}Eu and ^{226}Ra lines, while red the total tracked resolution.

AGATA efficiency

The efficiency of AGATA has been measured several times with both source and in-beam data. In the LNL campaign, the reference measurement is the one of Pérez Vidal *et al.* [140]. This measurement however is not directly comparable with this experiment, as it was performed with 34 capsules, in nominal distance, and equipped with absorbers. Different tracking parameters also produce different efficiency values.

Efficiency runs were carried out with a combination of ^{152}Eu and ^{226}Ra source. The combination of the two sources, along with the close-up configuration, produced a high counting rate in the DAQ. The estimated dead-time was of about 33%. The experimental points obtained in singles are shown in Figure 41. However, differently than the previous publications, these points are not well represented by the common RadWare formula [141], namely

$$\begin{aligned} \log\epsilon(E_\gamma) &= \left[\left(A+Bx+Cx^2\right)^{-G}+\left(D+Ey+Fy^2\right)^{-G}\right]^{-1/G} \\ x &= \log\left(\frac{E_\gamma}{100\,\mathrm{keV}}\right) \quad y = \log\left(\frac{E_\gamma}{1000\,\mathrm{keV}}\right), \end{aligned} \tag{23}$$

as it poorly interpolates the high-energy region, as it is clear from the right inset of Figure 41. This problem was never mentioned in any previous publications, but appears clear in Figure 4 of Lalović *et al.*, where also high-energy points are poorly interpolated. Being an accurate definition of efficiency at high energy critical for the branching ratios in this nucleus, due to the presence of high-energy decays, the standard RadWare formula was modified to accomodate for two more parameters, namely

$$\begin{aligned} \log\epsilon &= \left[\left(A+Bx+Cx^2\right)^{-G}+\left(D+Ey+Fy^2\right)^{-G}\right]^{-1/G} \\ x &= \log\left(\frac{E_\gamma}{p1}\right) \quad y = \log\left(\frac{E_\gamma}{p2}\right), \end{aligned} \tag{24}$$

The choice of the fitting function is non-unique, as discussed by Kis *et al.* [142]. This choice allowed to keep the standard formula, for comparison, while improving the fit at high energy. The parameters obtained from the fitting pro-

Parameter	RadWare	modRadWare
A	1.9(7)	3.01(3)
B	3(4)	-0.86(1)
C	0.	0.
D	1.578(5)	1.55(1)
E	-0.413(7)	-0.72(4)
F	0.0153(8)	-0.14(1)
G	12.	12.
p1	100	80(10)
p2	1000	1272(20)

Table 16: AGATA efficiency fit parameters, for the RadWare and modified Radware formula. Parameters without errors were fixed during the fit.

cedure can be found in Table 16, along with the fitted Radware one. Errors on the final efficiency values were then extrapolated numerically using the covariance matrix provided by the ROOT fitter. The new function indeed improves the interpolation at high energy, but at the cost of a worse interpolation at low energy. Since however there are no peaks near or below 200 keV, the problem is not pursued further. The new function undershoots the RadWare one up to 1 MeV, where then it decays slower. While then the RadWare function above 2 MeV decays so slowly that is almost saturating, the modified RadWare falls more rapidly.

SPIDER resolution

The channel-by-channel resolution of SPIDER with the 3α source is shown in Figure 42. While the resolution is more or less constant among the 3α peaks, it is very sensitive to the damage of the detector. For new, high-quality detectors, such as D0 and D6, the FWHM is below 50 keV, while for more damaged segments like D4 and D5 it goes above 100 keV. This resolution is the source resolution of the detector; the experimental E_x resolution will be reported in the next Chapter, along with the results. The obtained energy resolution values presented here have been used as starting point for the simulations (as explained in the later Sections). As it is however clear from Figure 38, the E_x resolution of the detector, about 350 keV, is sufficient to clearly separate the two main single-particle fragments.

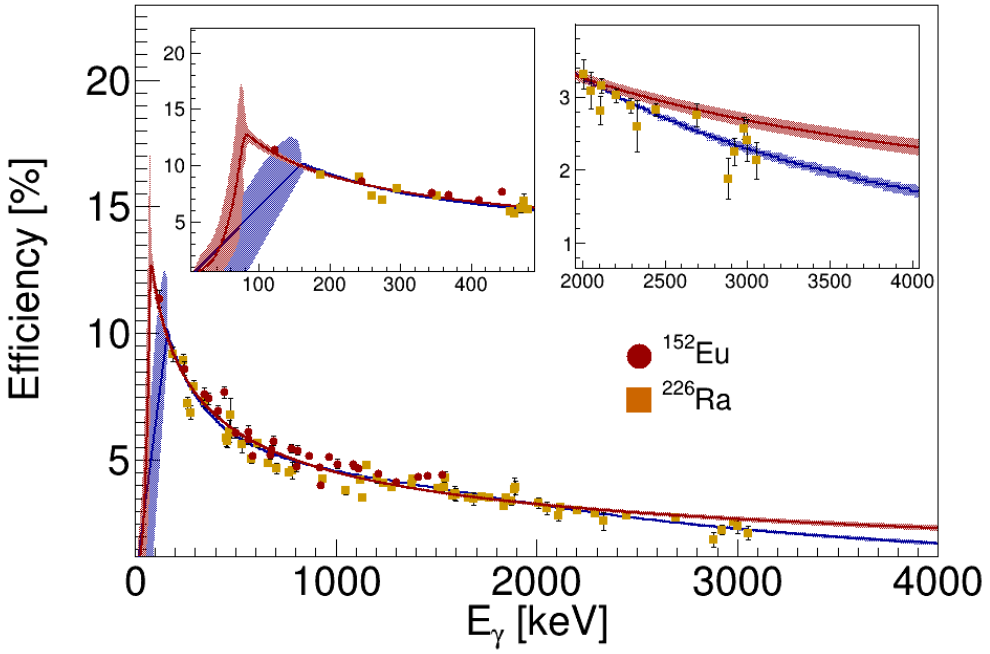

Figure 41: AGATA efficiency curve after tracking. The red one is calculated using the standard RadWare formula, while the blue one with the modified RadWare formula. In the two insets of the figure, a zoom in the low and high energy regions.

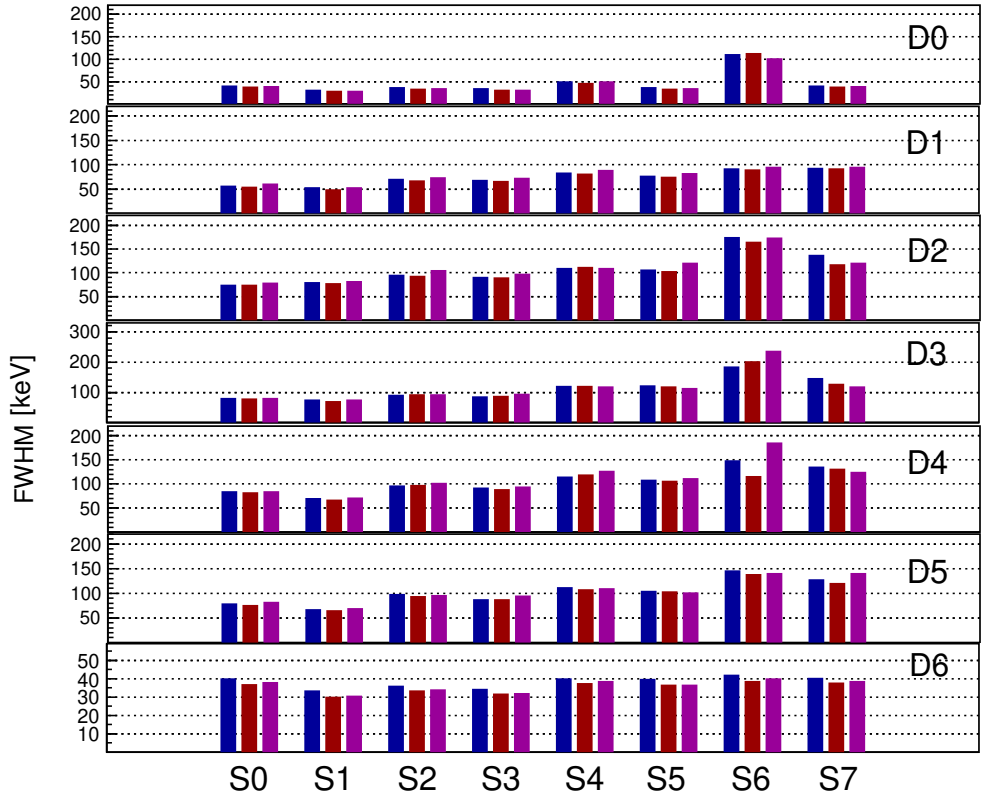

Figure 42: FWHM of each SPIDER detector for the three α peaks.

3.4 Simulations

Simulations were carried out using the standard Agata Simulation Code [143, 144], built on the Geant4 suite version 4.9.6 [145]. The code builds the detectors in 3D space using the Computer Assisted Drawings (CADs) of the single spectrometers (in this case, AGATA and SPIDER). All experimental runs were simulated then with the Agata Alternative Generator (AG), under some hypotheses:

- the only reaction happening is the (d, p) on the CD_2 target;
- the cross-section and angular distribution of the reaction is the one given by FRESCO (shown in Figure 24, this will be verified in the next Chapter);
- the slowing process is given by some known energy-loss tables (this assumption will be discussed in the next Section).

The output of the simulation consists of events that contain all ion information ($\vec{v}$, E), all γ-ray interactions produced, and protons detected by SPIDER. Background γ rays and peaks coming from parasitic reactions are added at simulation level when necessary. The background spectrum is generated sampling a probability distribution that falls exponentially with energy. The intensity and parameters of this distribution are recursively adjusted to reproduce the experimental background slope.

This file has to be processed by the OFT algorithm to reconstruct the original γ rays produced during the reaction by the simulation. The OFT algorithm applies smearing on energies and positions, and packs all interactions within a radius of 4 mm into a single event to reproduce the PSA spatial resolution, then performs tracking with the same parameters as the ones used on the experimental data. Finally, the output of the OFT algorithm is then fed to an executable (`readsimu`) that reconstructs the reaction, performs Doppler correction, applies additional appropriate smearing and converts data into a ROOT TTree.

Target thickness and energy loss

The DSAM technique relies critically on the knowledge of the stopping process of the ion inside the material [146]. Therefore, it is essential that the Geant4 energy loss tables (used in the simulation) reproduce the available experimental data on the stopping powers of ions inside materials. These data can be found in the evaluated database of IAEA [147]. Other sources of energy loss tables are SRIM [148] and the ICRU reports [149, 150]. Three stopping power tables have been used in the simulation: S in CD_2 (beam on target), S in Au (beam and ion in degrader), H in CD_2 (detected particle in target).

It is known that the nuclear component of the stopping power becomes relevant only for low energy ions. As ions were not completely stopped in the gold layer, but only slowed down, this component can be ignored with a good degree of approximation. This approximate stopping power is called "screened" in the following.

For sulphur on CD_2 virtually no data exists. The only available studies were made on polyethylene naphtalate or polypropylene, and not deuterated polyethylene, as in the present case, for Si and Cl ions. These data are shown in Figure 43(a). It can be seen while the ICRU report data lie between the Cl and Si experimental data, the SRIM energy loss table overestimates the energy loss of S in CD_2 by almost a factor of 1.5. The Geant4 tables instead reproduce the expected behaviour within the straggling for most of the energy range. The expected energy range covered by the simulations is between $\sim$120 and 168 MeV. In this region, despite being compatible within the straggling, the Geant4 energy loss seems to underestimate the expected stopping power. Indeed, the center of the shaded bands follows more closely the data of Si, rather than being centered between Si and Cl data. However, as data were taken with polyethylene naphtalate, some stopping power component is due to the O ions present in the compound, which implies that measured data should be somewhat larger than the Geant4 calculations. This considered, the agreement is considered acceptable.

Inversely, for sulphur on gold, various data sets exists, which are reproduced by all energy loss tables (see Figure 43(b)) with various degree of agreement. Geant4 simulations also reproduce the energy losses in the material within the straggling.

Finally, for protons in CD_2, the available datasets are shown in Figure 43(c). SRIM and ICRU data follow closely the available data. For protons below 1 MeV, Geant4 predicts a large energy straggling. This is not considered a serious issue. Indeed, the population of low-energy states in ^{37}S produces protons of energy between 5 and 1 MeV, therefore above the critical area. Lower-energy protons are around the threshold of detection, which means that if the calculated energy loss lies too much above the experimental curve, they are removed from the analysis. In this way, high energy loss values due to Geant4 values are cut, keeping the straggling contained and therefore the simulated resolution constant. Furthermore, this does not affect the generated lineshape directly, but only indirectly due to Doppler reconstruction. The high straggling is therefore somewhat compensated for by the choice of the smearing parameter in the energy resolution.

As stated in the Introduction, DSAM analysis relies on the knowledge of the stopping power of the produced ion inside the material. Poor knowledge of the energy loss process introduces systematics or systematic uncertainties in the DSAM measurement. The comparison between the different energy loss tables show that in all cases GEANT4 tables agree well with the measurements present in literature. On the other side, GEANT4 tables also estimates the energy straggling to be at least 15% of the energy loss value, larger than the error on the measurements. This implies that in the simulation process, the presence of a systematic uncertainty in the stopping power and associated straggling is integrated in the Monte-Carlo process without the need to consider it explicitly after the minimization. In other words, if the systematic uncertainty in the stopping power process is considered as nuisance parameter, the resulting likelihood is marginalized in the nuisance parameter.

Furthermore, beam impact on the target can degrade its thickness and/or chemical properties. Since CD_2 targets are organic targets, radiation can degrade the C-D and CD_2-CD_2 bonds at different rate. If the bonds between different CD_2 molecules are easily broken under irradiation, then uniform sputtering on the beam spot might be expected, which can be modeled as a non-constant target thickness for the duration of the experiment. If instead the bonds between C and D are more easily broken, C may stay inside the target, but deuteron might escape inside the scattering chamber. Conversely, carbon build-up on the beam spot due to or after irradiation might create additional atomic layers on or around the beam spot. Within the resolution of this setup,

this effect might be equaled to a constant target thickness but a non constant ^{37}S production rate during beamtime.

In order to estimate the target status during irradiation, three γ-ray lines were chosen: the 646-keV $3/2^-_1 \rightarrow 7/2^-_1$ decay of ^{37}S, the 1524-keV $2^+_1 \rightarrow 0^+_1$ transition of ^{42}Ca and the 548-keV $7/2^+_1 \rightarrow 3/2^+_1$ peak of ^{197}Au. These lines come exclusively from the (d,p) reaction on deuteron, fusion evaporation on carbon and Coulomb excitation of the gold degrader, respectively. The area of these peaks is proportional to the beam intensity, the measurement time, the reaction cross-section, the efficiency of the apparatus and the target/degrader thickness. Assuming that the gold thickness does not change during the beam time, the ratio between the area of the 646- or 1524-keV lines and the 548-keV peak is proportional to the target thickness and reaction cross section ratio. The evolution of the target composition can be estimated by evaluating

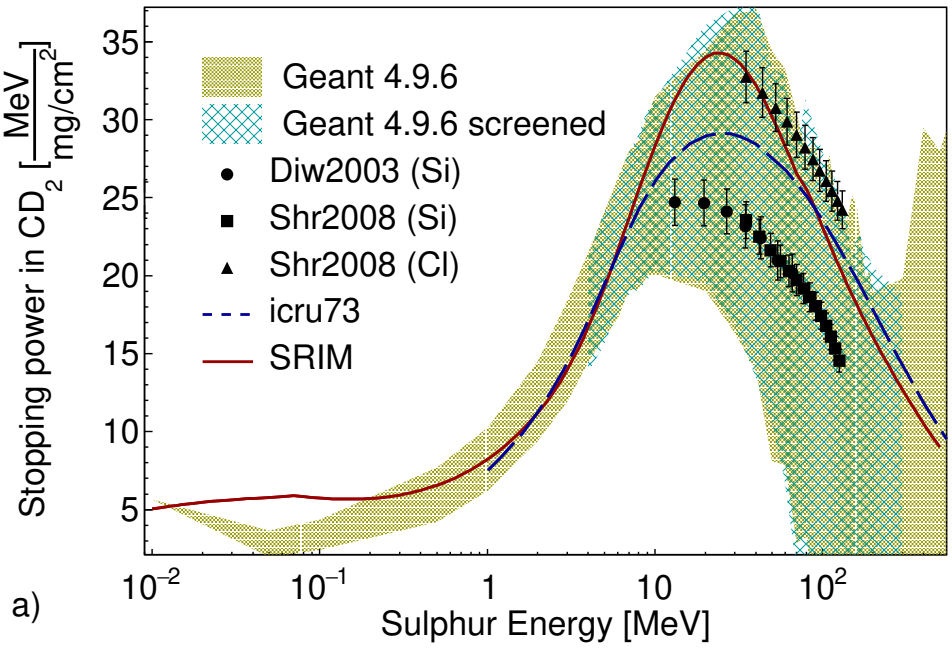

Figure 43: Comparison between different energy loss tables for a) S in CD_2, b) S in Au, c) p in CD_2. In shaded bands, the Geant4-9.6.4 [145] energy loss tables with and without nuclear screening and its predicted straggling. In dashed blue and continous red lines the results of ICRU reports [149, 150] and SRIM [148] computations, while in symbols the different measurements: for S in Au, Refs. [151–155]; for Si and Cl in polyethylene, Ref. [156, 157] (see text); for p in polyethylene, Refs. [158–160]. Measurement errors refer to the error on the measured stopping power, and not to straggling. Continues in the next page.

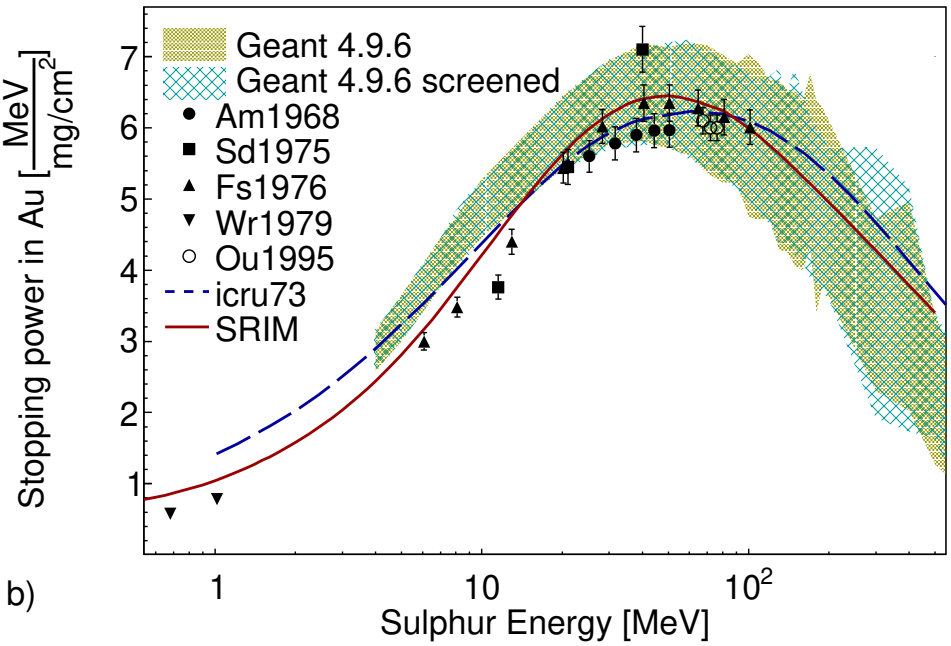

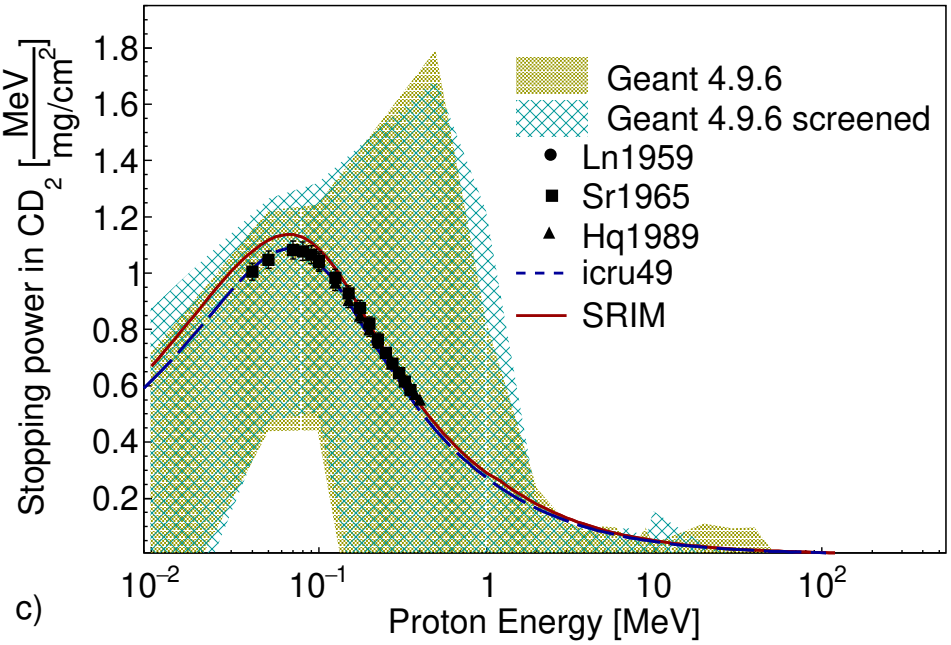

Figure 43: (cont.)

these quantities as a function of time. Since three targets with gold backing were used during the experiment (the two plunger targets and the standard target with 30 mg/cm^2 Au backing for DSAM), three of these graphs can be constructed. They are shown in Figure 44 for the plunger targets and in Figure 46(a) for the DSAM target.

It can be seen that both the deuteron and carbon content decrease with increasing irradiation. The different rates can be attributed to the carbon build-up effect and to the different probabilities of destroying a molecular bond with respect to an atomic one. In any case, since both C and ^{2}H quantities decrease with time, the whole target thickness decreases with time. The sudden jumps in the ratio value were due to the steering of the beam in non-irradiated areas of the same target. In order to estimate the effective target thickness, the 646-/548-keV ratio was fitted with an exponential function, and it was assumed that the value at time $t = 0$ of the interpolating function corresponds to the nominal target thickness declared by the manufacturer. The target thickness distribution can therefore be built, as in Figures 45 and 46(b). These histograms show for how much time the targets had a particular thickness.

These values are not in principle mg/cm^2, but arbitrary units proportional to it. As there is no way to determine the beam current delivered on target during the experiment, this procedure suffers from two strong assumptions: that the initial thickness is the one declared by the manufacturer and that there was no sudden decrease of the target thickness in the first instants of beam time. Typical confidence of the manufacturer on the thickness of evaporated targets is around 20% [125]. The second assumption is impossible to check with this dataset, as it would have happened even before data taking started. Despite these caveats, in the following these values have always been considered as in mg/cm^2, where most probably these are upper limits of the actual target thickness.

As it can be seen from the Figures, the average actual thickness of the targets are a factor from two to five lower than the nominal thickness declared by the manufacturer. This fact has a limited effect on the excitation energy resolutions, as the net energy loss of protons and sulphur in the CD_2 layer are quite limited. It has however paramount importance in the lifetime determination procedure, especially for fairly low lifetimes (< 100 fs) that are comparable with the travel time in CD_2. As the slow-down process starts earlier than expected,

γ-ray peaks start developing a lineshape earlier than simulated, which might lead to a systematical overestimation of the actual lifetime of the state. As side note, the values obtained in this way are similar to the ones obtained through the optimization of the SPIDER reaction reconstruction.

The time-dependent thickness is reproduced in the simulation in this way. The thickness distributions reported are histograms of N bins, in which the content n_i of each bin is proportional to the time the target had the thickness t_i. Therefore, a series of N simulations were performed, each with a target thickness t_i. The number of events in the simulation i was set proportional to the bin content n_i. The N simulations were then summed together.

SPIDER simulated data

For the SPIDER detector, a spatial smearing is applied: `readsimu` identifies the SPIDER channel that produced the hit, and assigns to the hit the position of the centroid of the detector instead of the simulated one. The segment centroids were calculated generating 10^6 isotropic 1 MeV protons. The assigned θ and ϕ of each segment is then the weighted average of the detected hits position. The detected energy is first smeared with a gaussian with the channel-by-channel resolution extracted from the 3α peak measurement shown in Figure 42, then with another gaussian of constant width to reproduce the experimental spectrum. The necessary width has been estimated recursively from comparison between the experimental and the simulated spectra. The final simulated excitation energy spectrum can be compared to the experimental one in Figure 47.

Furthermore, as it is shown in Figure 22, low-energy protons coming from the transfer to highly-excited states in ^{37}S fall below the detection threshold of SPIDER. In §3.1.1, the threshold estimation procedure has been illustrated, with the caveat that the software threshold does not correspond to the hardware threshold. Data falling below the hardware threshold were not written in the data stream, and are non-recoverable. The total effect is a net loss of data. In other words, the total efficiency of SPIDER can be decomposed in the product of three terms: geometrical, intrinsic and detection efficiency. The geometrical efficiency is given by the portion of solid angle covered by the detector, which is about 18%. The intrinsic efficiency is defined as the probability

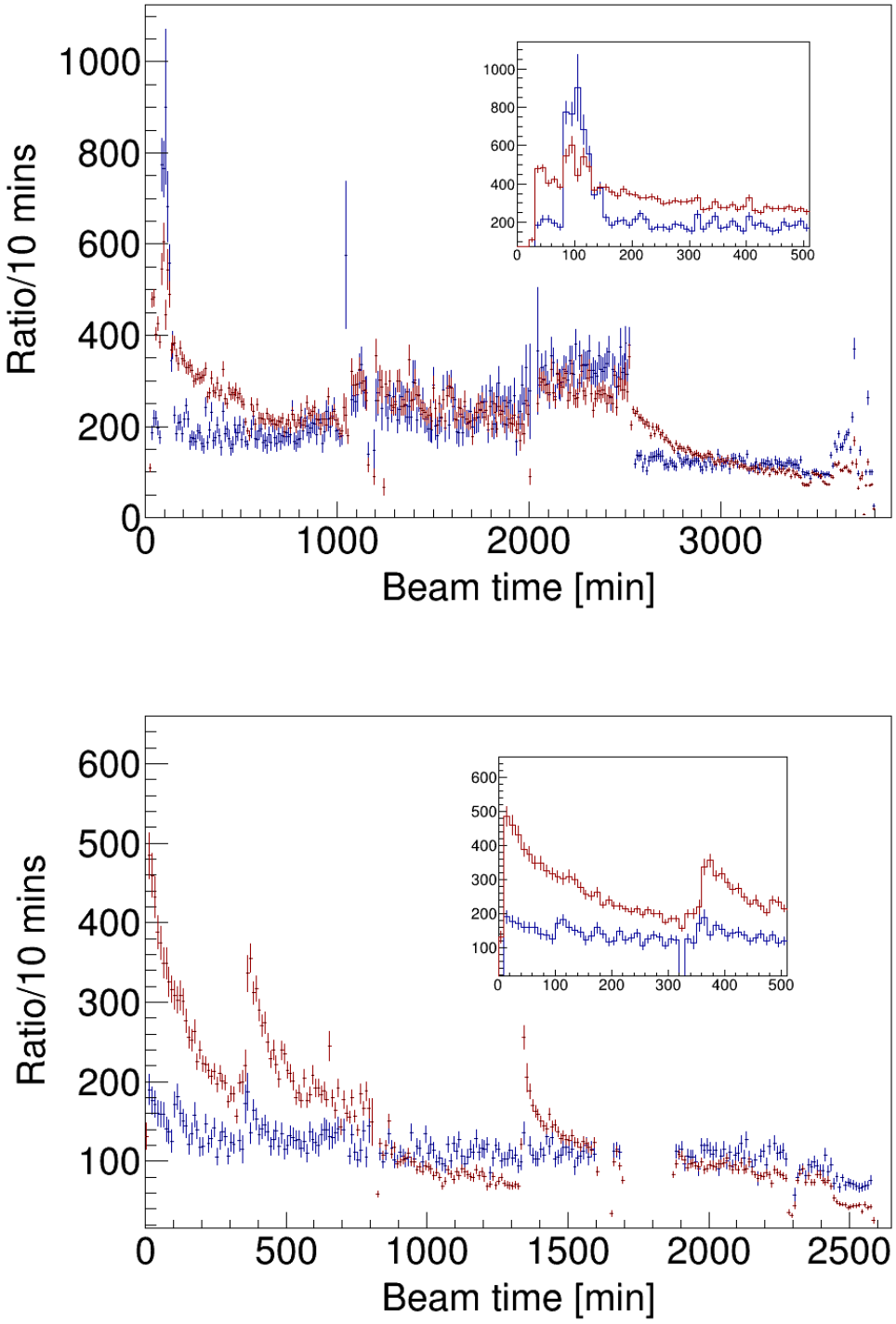

Figure 44: Intensity ratio between the decay of the first excited state of ^{37}S (red) and ^{42}Ca (blue) and the decay of the 548-keV $7/2^+$ state of ^{197}Au to the ground state for the plunger targets with 4 mg/cm^2 (top panel) and 6 mg/cm^2 (bottom panel) Au backing. Data are displayed as function of beam time. In the inset, a zoom on the first few hours region.

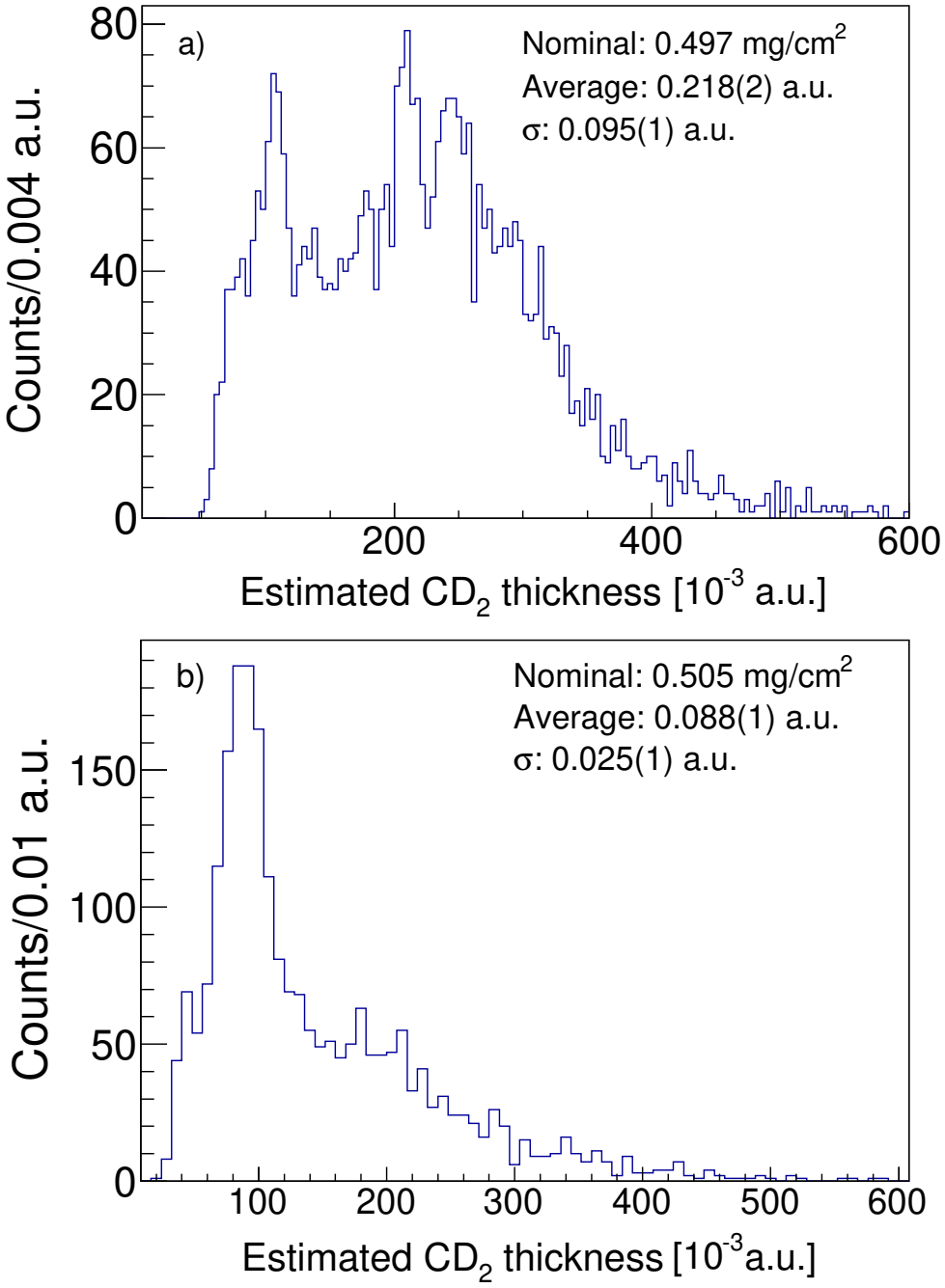

Figure 45: Thickness distribution during the experiment for the plunger target with 4 mg/cm^2 (top panel) and 6 mg/cm^2 (bottom panel) Au backing. 1 a.u. is equal to 1 mg/cm^2, but only on under strong assumptions, which are discussed in the text.

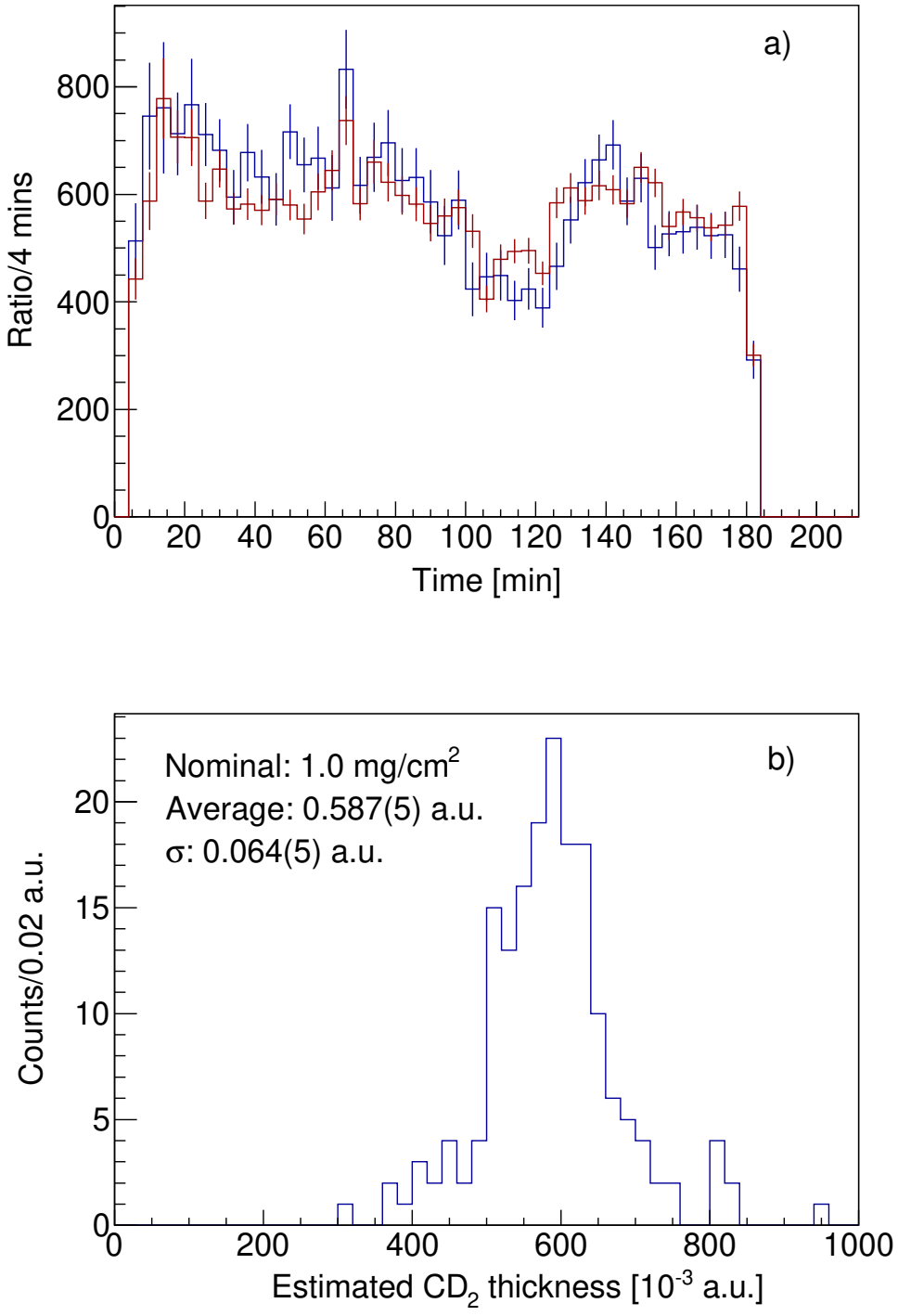

Figure 46: As a) Figure 44 and b) Figure 45, but for the standard target with 30 mg/cm^2 Au backing. In b) data are presented in a.u. as in Figure 45 for the same reasons.

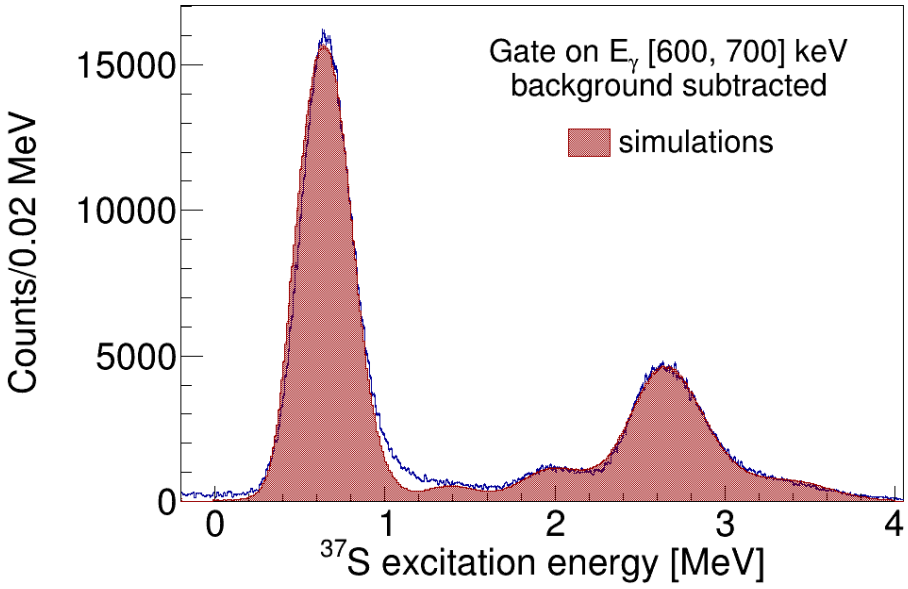

Figure 47: Comparison between the SPIDER experimental E_x spectrum (blue) and the simulated one (red). Experimental data come from the 4 mg/cm^2 ^{197}Au target run. The small left tail at 1 MeV is not reproduced correctly in the simulation, as it is due to non gaussian components of the peak shape. Since this was the only peak showing this tail (and not corresponding to a peak under analysis with the DSAM technique), the addition of non gaussian components in the smearing function was not deemed necessary.

that an incoming event produces a signal in the detector, i.e. are completely stopped in the active layer. LISE++ calculations show that protons from 1 to 5 MeV have a range in Si from 15 to 220 μm, losing about 2 keV in the 50 nm junction-side dead layer. Therefore, this value is approximately 100%. The detection efficiency is defined as the probability that the signal induced by a charged particle is detected and recorded in the data stream. The existence of said thresholds makes this term energy- and coordinate-dependent: this effect will be referred to as "threshold effect". This dependence can be assessed via simulation.

A known number (10^6) of isotropic protons were generated. The energy of the generated proton was assigned according to the kinematical line of the ^{37}S(d,p) reaction calculated by LISE++. Proton energy losses in the target were introduced with the SRIM energy loss table, assuming the reaction happened at the center of a 0.5 mg/cm^2 target. Straggling was reproduced by gaussian smearing of the calculated energy loss of the size of the Geant4 straggling shown in Figure 43. The same smearing parameters deduced in the previous paragraph were used to additionally smear the energy of the detected ion. This combination of subsequent smearings was enough to reproduce the experimental spectrum with a good degree of approximation.

Choosing the proton energy in this way, rather than scanning at regular intervals the energies from 0.5 to 5 MeV, is equivalent to numerically integrating the efficiency of the SPIDER array on the kinematic line of the reaction considering realistic energy losses. This integral allows a change in coordinates of the efficiency as a function of the detected proton energy to a function of the populated state in ^{37}S. Since protons are generated isotropically, there is no dependence on the transferred momentum l.

The number of detected protons over the total number of generated protons is thus the total efficiency, both for the whole array and channel-by-channel. The evolution of SPIDER detection efficiency (calculated as the total efficiency normalized by the geometrical one) as a function of the populated state in ^{37}S can be found in continuous blue line in Figure 48. It can be seen that SPIDER efficiency drops by almost a factor five between the population of the ground state of ^{37}S and the population of its 3493-keV level. If the threshold is underestimated, the efficiency drop is even larger. In order to assign a reasonable efficiency error, the calculation is repeated choosing a

different threshold value: with reference to Figure 29, the threshold chosen is where the FE spectrum increases with by a (rather arbitrary) factor e over the background. Taking the example Figure 29, this point would be approximately at 950 a.u., with respect to the 400 a.u. value obtained in §3.1.1. In energy, these points would correspond to approximately 1.3 and 0.55 MeV. The choice of threshold at 1.3 MeV would clearly suppress the population any state above 2 MeV excitation energy in ^{37}S, contrary to the experimental spectrum shown in Figure 38. This is one of the most extreme cases, as in general the two points were closer in energy. On the other hand, this criterion, which was not adopted in the analysis, definitely overestimates the hardware thresholds that were present during the experiment. These two choices of software thresholds represent therefore the two extremes of the distribution. An actual threshold estimate could be drawn from the ratio of the γ-ray decays seen with and without imposing the condition of observing a proton in coincidence. Unfortunately, without the kinematical reconstruction given by SPIDER, the Doppler-corrected spectrum does not have enough resolution to allow for a reliable extraction of the area of the peak. The comparison between the efficiency calculated with the two threshold values as a function of the populated state in ^{37}S is shown in Figure 48. The relative difference between the two curves stays below 2% up to 2 MeV, then increases from 2 to 20% between 2 and 3 MeV and from 20% to 40% between 3 and 3.5 MeV. Since the threshold position is unknown, the error on the efficiency has been fixed to be 2% up to 2 MeV, 20% from 2 to 3 MeV, and 40% from 3 to 3.5 MeV of excitation energy.

AGATA simulated data

Good control on the simulated peak shape is essential for the DSAM technique. Indeed, most of the lineshape is on the left side of the peak, which is also the one affected by net-charge loss effects (incomplete charge collection, neutron damage, missed charge due to thresholds). It is therefore fundamental to parametrize the detector response function in order not to introduce systematic effects in the lifetime measurement. As in the case of SPIDER, for the AGATA spectrometer events are generated, then smeared appropriately.

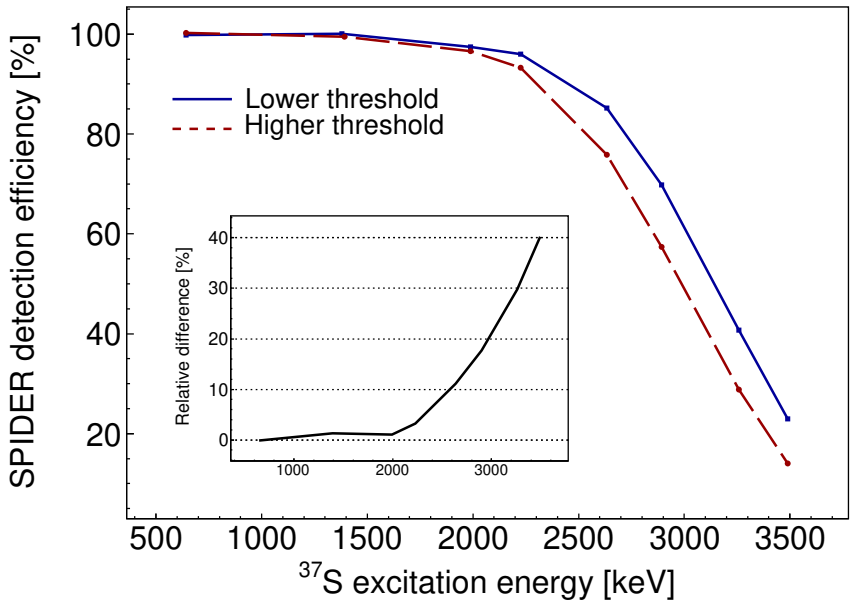

Figure 48: Simulated SPIDER detection efficiency as a function of the excitation energy of ^{37}S for a 0.5 mg/cm^2 CD_2 target. In continuous blue line the efficiency curve obtained with the thresholds estimated as in §3.1.1. In dashed red line the curve obtained imposing the thresholds with the $1/e$ criterion presented in this paragraph. In the inset, the relative difference between the two curves.

Since the spatial smearing is already applied at OFT level, only an energy smearing is applied. The smearing is applied sampling from a exponentially modified gaussian distribution as in Galinski *et al.* [161]:

$$\begin{aligned} G(x) &= \frac{1}{\sqrt{2\pi\sigma}} \exp\left(-\frac{(x-\mu)}{\sigma^2}\right) \\ L(x) &= \frac{1}{2\beta} \exp\left(\frac{\sigma^2}{2\beta^2} - \frac{(x-\mu)}{\beta}\right) \operatorname{erfc}\left[\frac{1}{\sqrt{2}}\left(\frac{(x-\mu)}{\sigma} + \frac{\sigma}{\beta}\right)\right] \\ R(x) &= \frac{1}{2}\operatorname{erfc}\left(\frac{(x-\mu)}{\sqrt{2}\sigma}\right) \end{aligned} \tag{25}$$

where $G(x)$ denotes the Normal distribution with mean μ and width σ, and $L(x)$ and $R(x)$ are the left and right tail, respectively. They are modeled one with an exponential distribution modulated by the cumulative error function, to reproduce the low-energy tail of the γ-ray peak plus the step-like Compton scattering background, the other with only a cumulative error function to reproduce the higher-energy background. This modelization introduces another parameter, the decay constant β, which should account for imperfections in the charge collection process, net-energy losses due to thresholds and wrong identification of the first interaction point by the tracking algorithm. The complete peak function, therefore, is assumed to be:

$$P(x) = [\, p \cdot G(x) + (1-p) \cdot L(x) + b \cdot R(x) \,] \tag{26}$$

where p the degree of normality and b the high-energy background component. In order to have proper normalization, $p + b = 1$, but this additional condition was relaxed to improve fit convergence. The values of σ, β, p and b may vary with the energy of the γ-ray. Their dependence was extracted from experimental data: the same peaks used for the final calibration (see Tab. 12) were fitted with this fit function to extract the energy dependence of the parameters. For p and b no dependence from the energy was found. Their values were then fixed to 0.6 and 0.0, respectively, based on the values that produced a simulated ^{152}Eu and ^{226}Ra spectrum close to the experimental one. For σ, the function in §3.3 was used. For β, the dependence in energy is extracted by first performing a fit of source data, then recursively applying different values of β to simulated spectra to find the one that produced a spectrum most similar to the experimental one. This evolution is then fitted with a quadratic, and applied to all subsequent simulations. The parameters for the quadratic interpolation of β can be found in Table 17.

Parameter	p0	p1 [keV^{-1}]	p2 [keV^{-2}]
Value	0.663	-1.254 $\cdot$ 10^{-4}	2.777 $\cdot$ 10^{-7}

Table 17: Parameters of the second order polynomial that interpolates the evolution of β with the γ-ray energy.

4 Spectroscopy

In this Chapter, the main spectroscopic results are illustrated. In the first Section, particle spectroscopy is examined with reliance only on SPIDER data, while in the second Section the full resolving power of the AGATA+SPIDER apparatus is employed, revisiting particle spectroscopy with conditions in γ-ray energy and performing γ-ray spectroscopy.

4.1 Particle spectroscopy

As anticipated in §2.7, the detection of the recoiling proton is enough to completely reconstruct the reaction. Since the energy depends on the emission angle, a kinematical line as a function of the polar angle of detection is expected, superimposed on an almost constant background of particles (protons and α particles) coming from the fusion-evaporation reaction of ^{36}S on ^{12}C.

Since there were 4 different targets used during the experiment, four different matrices can be produced. One of these, for the target with 6 mg/cm^2 ^{197}Au backing, is reported in Figure 49.

The four excitation energy spectra obtained with the different targets are shown in Figure 50. The two kinematic lines visible in Figure 49 correspond to the excited states at 0.646 and 2.638 MeV. Two other peaks can be observed in Figure 50, namely the population of the ground state and the population of the 1.992 MeV state. Finally, the multiplet at 3 MeV (3.262 and 3.493 MeV states, mainly) populates the "knee" at the high end of the excitation energy spectrum, but due to low spectroscopic factors and resolution the individual states cannot

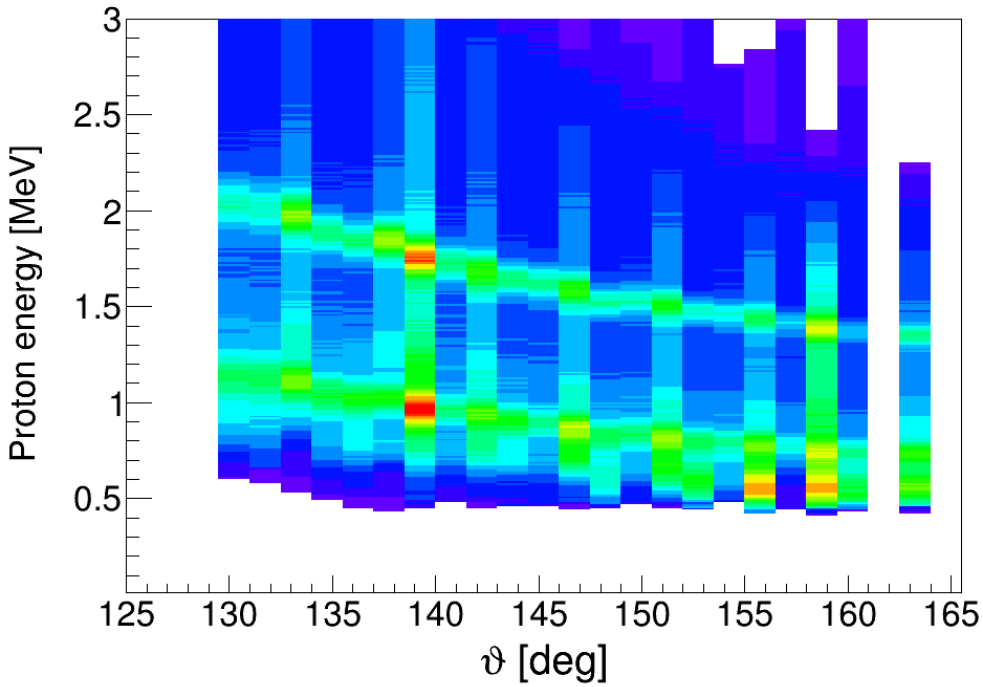

Figure 49: SPIDER energy spectrum as a function of emission angle. Two kinematical lines are clearly visible in the spectrum, and correspond to the population of the 646 and 2638-keV states. Dataset acquired with the 6 mg/cm^2 ^{197}Au backing.

be disentangled. This is clear from Figure 51, where the excitation energy spectrum is shown, compared to the states and spectroscopic factors reported in the Adopted Level Scheme [47]. The excitation energy resolution obtained during the experiment is reported in Table 18.

Since SPIDER is segmented in the polar angle in 8 strips, it would be possible to measure the angular distributions of the ejected protons and their (relative) spectroscopic factors. However, the spatial and energy resolution of SPIDER

Target [mg/cm^2]	FWHM^{gs}	FWHM^{646} [keV]	FWHM^{2638} [keV]
0.5 CD_2 + 4 Au	275.5(3)	326.3(3)	459(1)
0.5 CD_2 + 6 Au	292.0(4)	329.5(2)	419(1)
0.337 CD_2	244(2)	310(1)	371(3)
1.0 CD_2 + 30 Au	300	760	1020

Table 18: Peak FWHM as a function of energy and target thickness. In the DSAM (1 mg/cm^2 CD_2 + 30 mg/cm^2 ^{197}Au) target, the peak at 646 keV had a strong exponential tail, while the peak at 2638 keV is completely merged with the 3262 keV one.

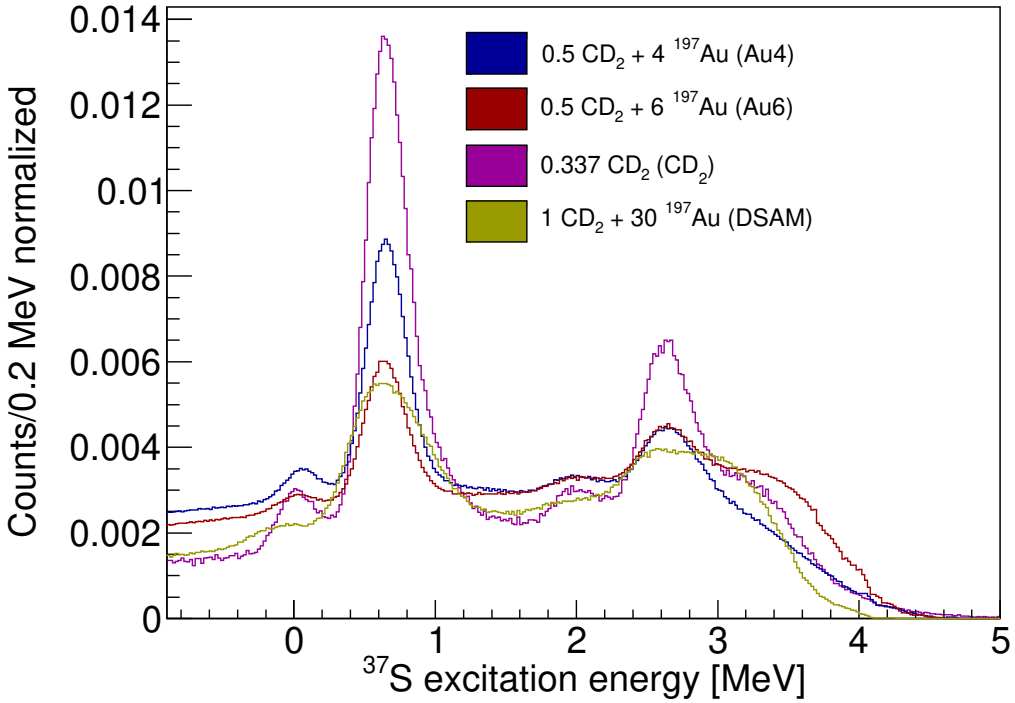

Figure 50: ^{37}S reconstructed energy spectrum. The plots have been normalized to their integral to obtain an improved graphical overlap.

does not allow for the full discrimination of neighbouring states, so it is preferable to carry out this analysis with a condition of the de-exciting γ-ray emitted in coincidence, as will be discussed in the next section. The only level that cannot be extracted by imposing a condition on a γ-ray transition is of course the ground state. In this case, only a condition on the excitation energy was put, and the results are displayed in Figure 63, where the expected L=3 transfer is reproduced.

4.2 Gamma-ray spectroscopy

Using the combined information between AGATA and SPIDER, the γ rays observed can be Doppler corrected using the reconstructed direction and velocity of the ejected ^{37}S nuclei. Data from both detectors were combined into the same event in a window of total width of 1 μs. Events that come from the (d,p) reaction should be strongly time-correlated with γ-rays (as well as events coming from FE reactions), while coincidences of prompt particle radiation with γ rays not produced in the reaction (β decay of the reaction

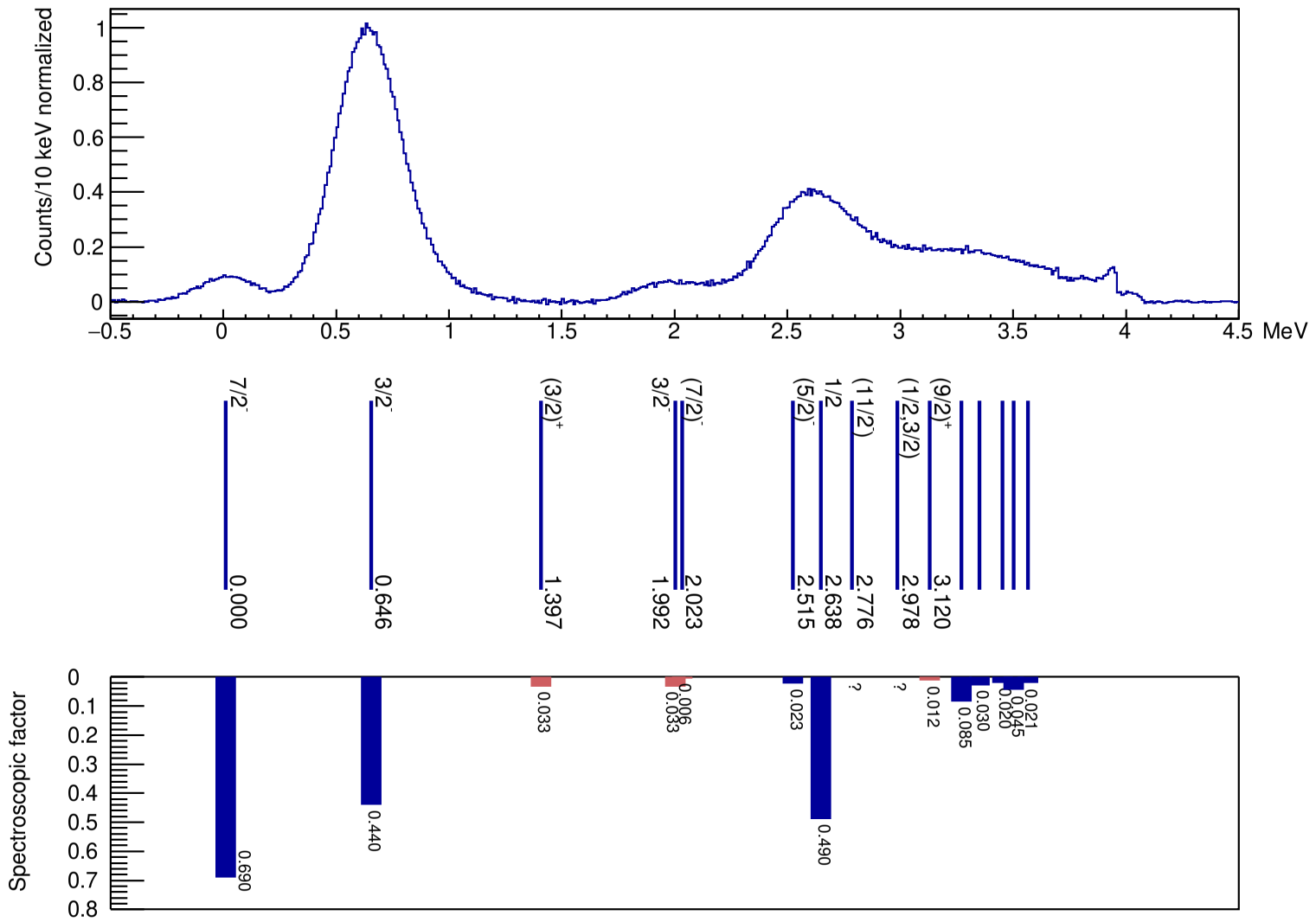

Figure 51: ^{37}S reconstructed energy spectrum compared to the Adopted Level Scheme [47]. Measured spectroscopic factors, energy and spin values are taken from the Adopted Values. Higher lying states are not labeled, but can be found in Table 10 at page 59. The structures around 4 MeV are due to electronic noise.

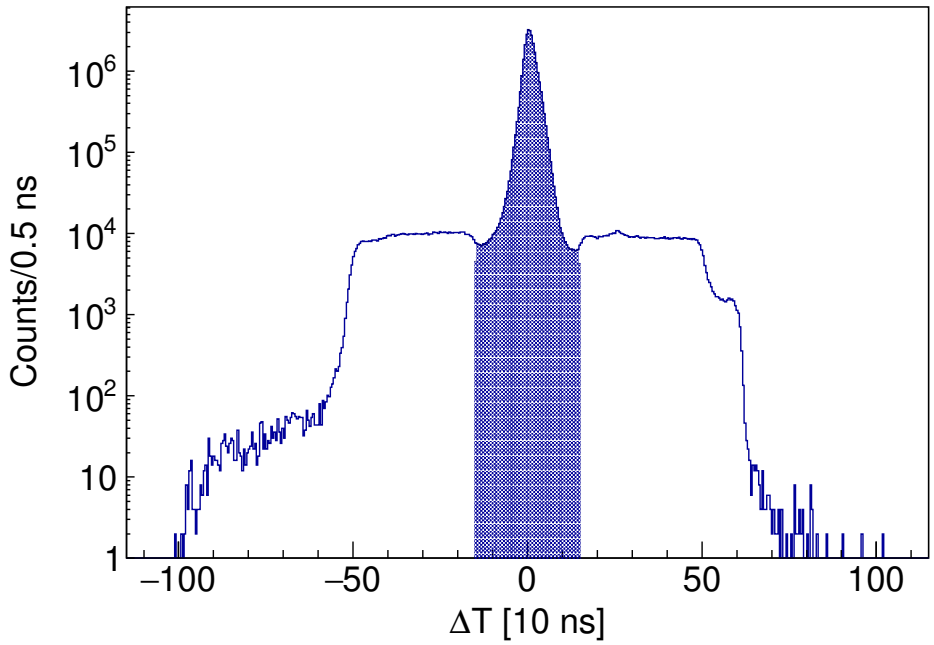

Figure 52: Time difference distribution between AGATA and SPIDER data belonging to the same event. The central structure, called coincidence peak, contains events from the (d,p) reaction. The constant background comes from particles detected in coincidence with uncorrelated γ rays coming from β decays and target activation, plus a small component from environmental radiation. Events considered in the analysis are only the ones belonging to the shaded area.

products or from beam dump activation) should be randomly correlated. The time difference distribution between events can be found in Figure 52. The structure around 0 shows that indeed there is a strong time correlation between AGATA and SPIDER data, the so-called coincidence peak, on top of a constant background. In order to further reduce the background component in the γ-ray spectrum, only events in a narrow window around the coincidence peak ($\pm$150 ns) were selected. This window is highlighted in Figure 52 as the blue shaded area.

A particle-γ matrix can therefore be built, with the reconstructed excitation energy in abscissa and the Doppler-corrected γ-ray energy on the ordinate axis. This matrix can be found in Figure 53. The same matrix, zoomed in different γ-ray energy regions, can be found in Figure 54. This matrix allows one to unambigously assign every γ ray to the decay of a particular excited state and to discriminate transitions decaying directly to the ground state (along the

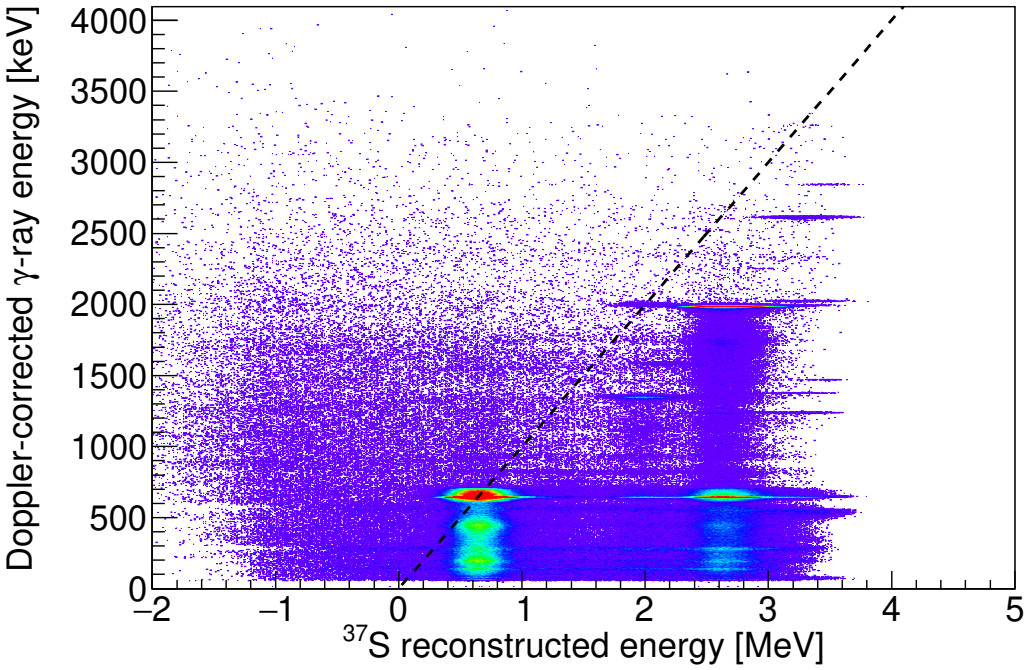

Figure 53: Proton-γ coincidence matrix. The black dashed line corresponds to the $E_x = E_\gamma$ locus. Background was subtracted by averaging the γ-ray spectrum in the excitation energy region between -1.0 and 0.0 MeV. A cut of at least 5 counts/bin was imposed to better highlight ^{37}S peaks.

diagonal $E_x = E_\gamma$) from transition feeding other excited states. To maximize statistics and observe even the lowest-populated channels, data coming from all plunger distances are summed together.

Since the ejected ^{37}S nuclei start decelerating as soon as they are produced, there are several choices for the Doppler correction. The first choice is to assume that the nucleus decays as soon as it is produced, i.e. at the middle of the target. Otherwise, for longer lifetimes, it can be assumed that the nucleus decays between the target and the stopper. Since this experiment combined both RDDS and DSA technique together, the gold backing was used as degrader foil to slow down the ions before stopping them in the stopper. Therefore, Doppler correction can also be performed with the velocity calculated at the end of the degrader foil. The former choice will induce a lineshape on the γ-ray peaks emitted by "long-living" ($\sim$1 ps) state, while the latter on those produced by the short-living ones ($\sim$10 fs). In Figure 53, the chosen Doppler correction is the one assuming mid-target decay.

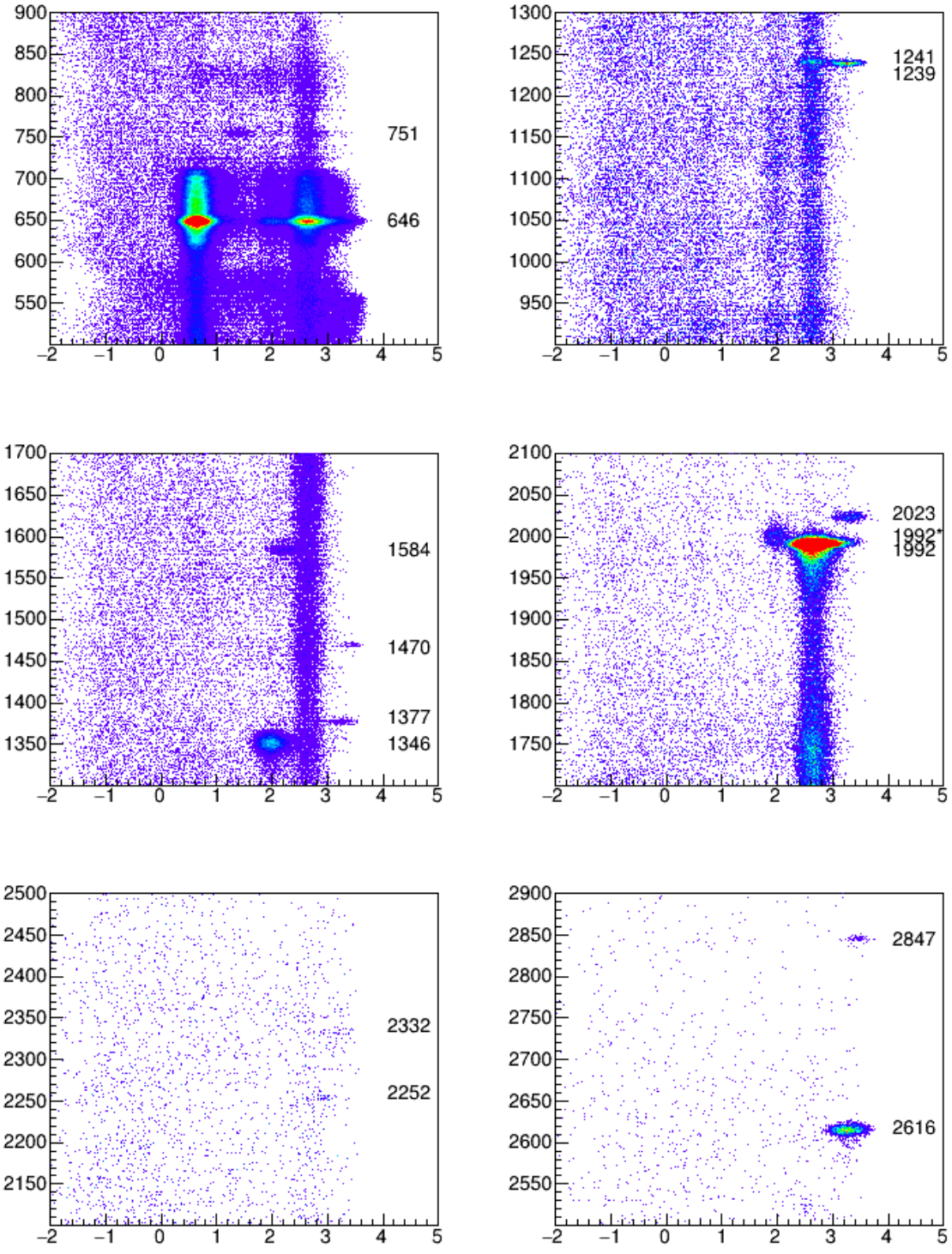

(a)

Figure 54: Proton-γ coincidence matrix. Zoom in different γ-ray energy regions of Figure 53. The most visible γ-ray lines are indicated to the nearest integer.

The observed and assigned γ-ray lines can be found in Table 19. The assignments, which are discussed on a level-by-level basis in the following, have been made according to previous literature results (mainly Refs. [66, 71]), particle-γ (Figures 53 and 54) and particle-γ-γ coincidences (Figures 60 and 61). The reconstructed level scheme can be found in Figure 65.

As anticipated in the previous Section, particle spectroscopy can be revisited with a condition on the de-exciting γ-ray. The existence of multiple states close in energy does not allow for a reliable extraction of angular distributions and relative spectroscopic factors with a condition on the excitation energy alone without a high risk of contamination from neighbouring states. Imposing a condition on the de-exciting transition allows one to put a selective constraint on the direct population of the chosen state, thus preventing contamination, at the cost of statistics. As already pointed out, the deduction of spectroscopic factors and angular distributions was not the primary goal of the experiment, and therefore the experimental conditions were not optimized for this objective. That is why the condition on the γ-ray emission is necessary. Since however the dataset allows for it, the deduction of spectroscopic factors from this dataset provides a direct comparison with the previous experimental work and a benchmark for the simulations (in particular, it verifies that indeed the emitted protons follow an angular distribution calculated in DWBA framework). The procedure followed to extract both quantities was this:

- the number of protons observed in each SPIDER strip in coincidence with a particular γ-ray transition is obtained; background subtraction was performed by gating on the same γ-ray energy but outside of the prompt coincidence peak, and by gating on a slightly higher and lower γ-ray on the prompt coincidence peak;

- each value was then corrected by the efficiency of each SPIDER strip obtained in §3.4, to account for the mentioned energy threshold effect;

- channels positioned at the same polar angle value were then summed, unless the number of protons observed was distant more than 3σ the average (this was the case, for example, of noisy or low-statistics strips), in which case they were just excluded and the efficiency was then corrected accordingly;

E_i (keV)	J^π	E_f (keV)	J^π	BR (%)	E_γ (keV)
646	$3/2^-$	0	$7/2^-$	100	646
1397	$(3/2^+)$	646	$3/2^-$	100	751
1992	$3/2^-$	646	$3/2^-$	73(1)	1346
		0	$7/2^-$	27(1)	1992
2023	$(7/2^-)$	646	$3/2^-$	33(2)	1377
		0	$7/2^-$	67(2)	2023
2230	$(1/2^+)$	646	$3/2^-$	100	1584
2515	$(5/2)^-$	0	$7/2^-$	100	2515
2638	$1/2^-$	1397	$(3/2^+)$	2.03(7)	1241
		646	$3/2^-$	98.0(9)	1992
2898	–	646	$3/2^-$	83(8)	2252
		0	$7/2^-$	17(8)	2898
2978	$(1/2, 3/2)^-$	646	$3/2^-$	100	2332
3120	$(9/2)^+$	0	$7/2^-$	100	3120
3262	$3/2^-$	2023	$(7/2^-)$	33.7(6)	1239
		1992	$3/2^-$	5.3(2)	1270
		1397	$(3/2)^+$	2.3(2)	1865
		646	$3/2^-$	55.9(8)	2616
		0	$7/2^-$	2.7(2)	3262
3355	$(3/2)^+$	1397	$(3/2)^+$	49(3)	1958
		646	$3/2^-$	51(3)	2709
3441	$(7/2)^-$	0	$7/2^-$	100	3441
3493	$3/2^-$	2023	$(7/2^-)$	57(1)	1470
		646	$3/2^-$	39(1)	2847
		0	$7/2^-$	4.0(5)	3493

Table 19: Observed ^{37}S γ-ray lines and their attribution. Spin assignments come mainly from the Adopted Values, the publication of Warburton and Becker [162], and the work of Chapman *et al.* [71].

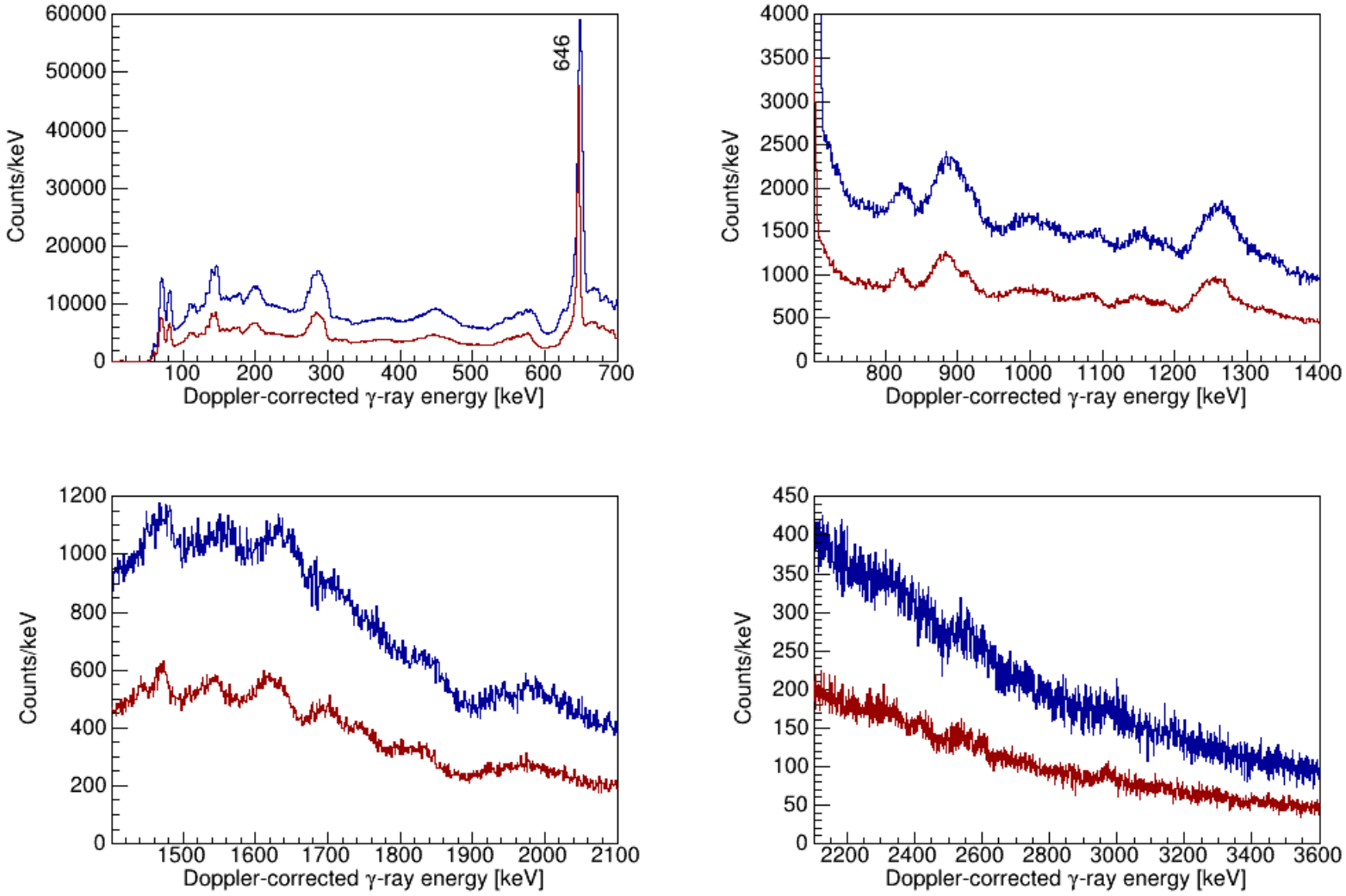

Figure 55: Doppler-corrected γ-ray spectrum in coincidence with SPIDER, assuming mid-target velocity (blue) or after degrader velocity (red). The red spectrum is scaled by a factor 0.5 for better graphical comparison. Gate in excitation energy between 0.2 and 1.0 MeV.

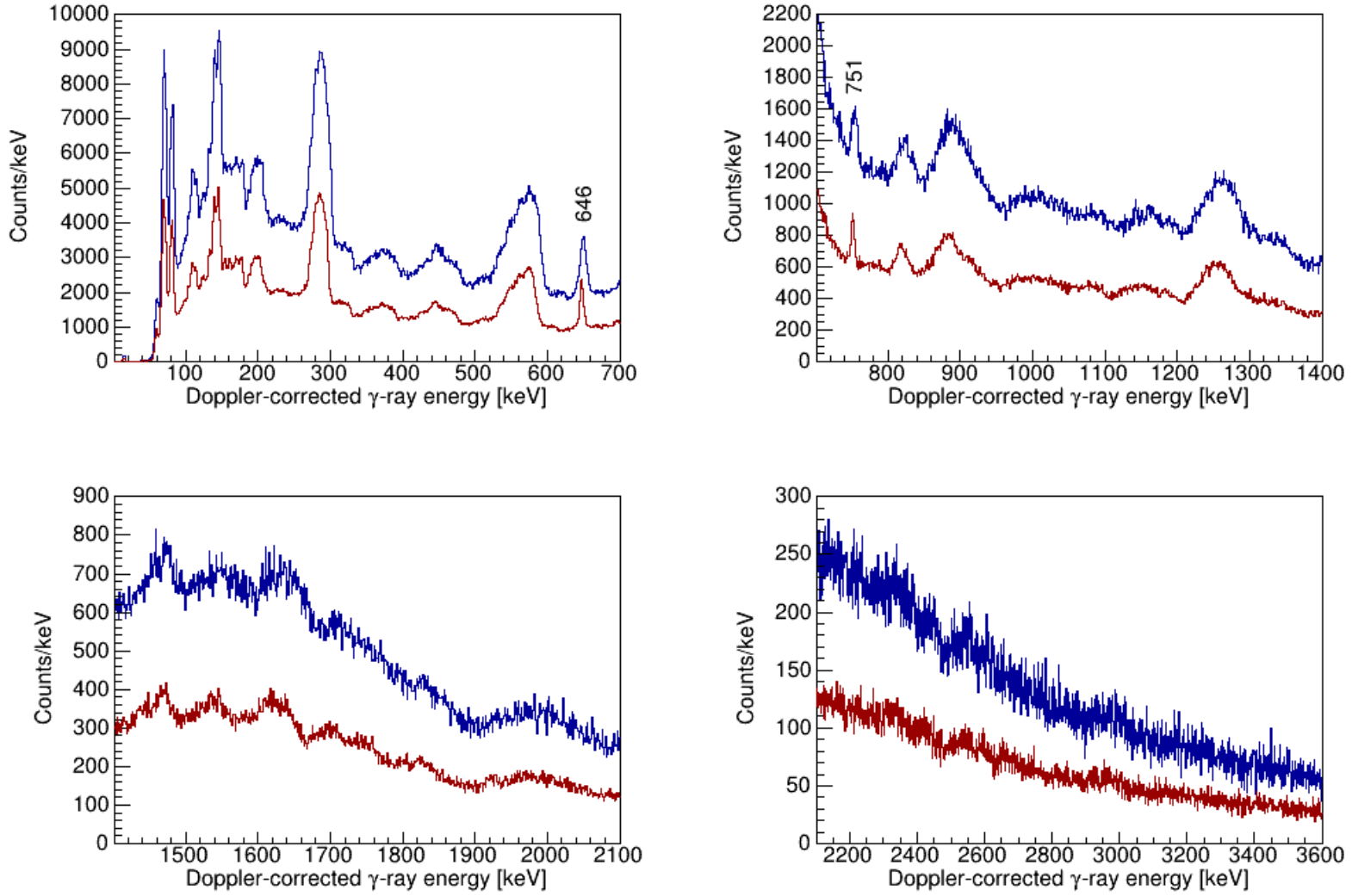

Figure 56: Doppler-corrected γ-ray spectrum in coincidence with SPIDER, assuming mid-target velocity (blue) or after degrader velocity (red). The red spectrum is scaled by a factor 0.5 for better graphical comparison. Gate in excitation energy between 1.0 and 1.6 MeV.

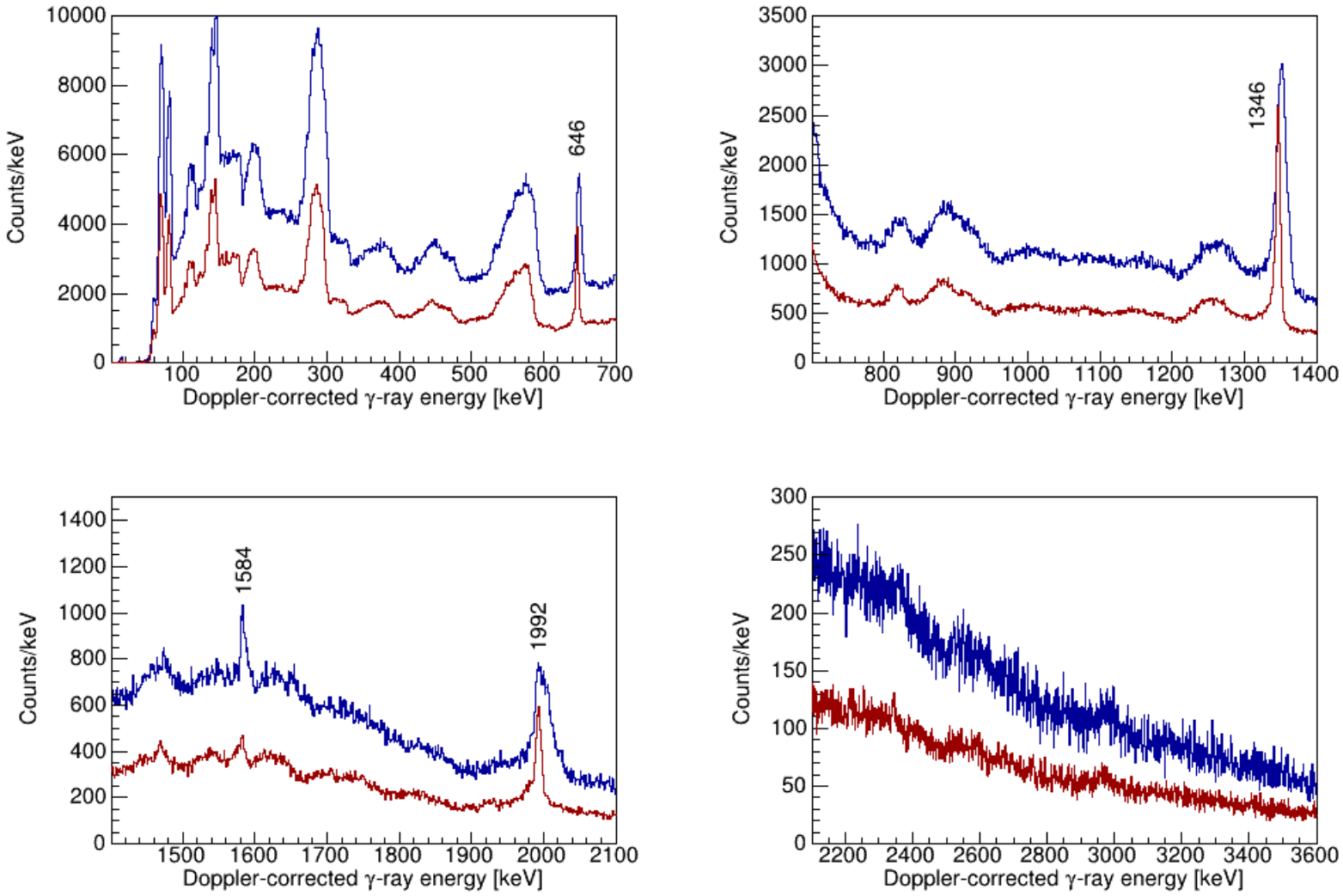

Figure 57: Doppler-corrected γ-ray spectrum in coincidence with SPIDER, assuming mid-target velocity (blue) or after degrader velocity (red). The red spectrum is scaled by a factor 0.5 for better graphical comparison. Gate in excitation energy between 1.6 and 2.2 MeV.

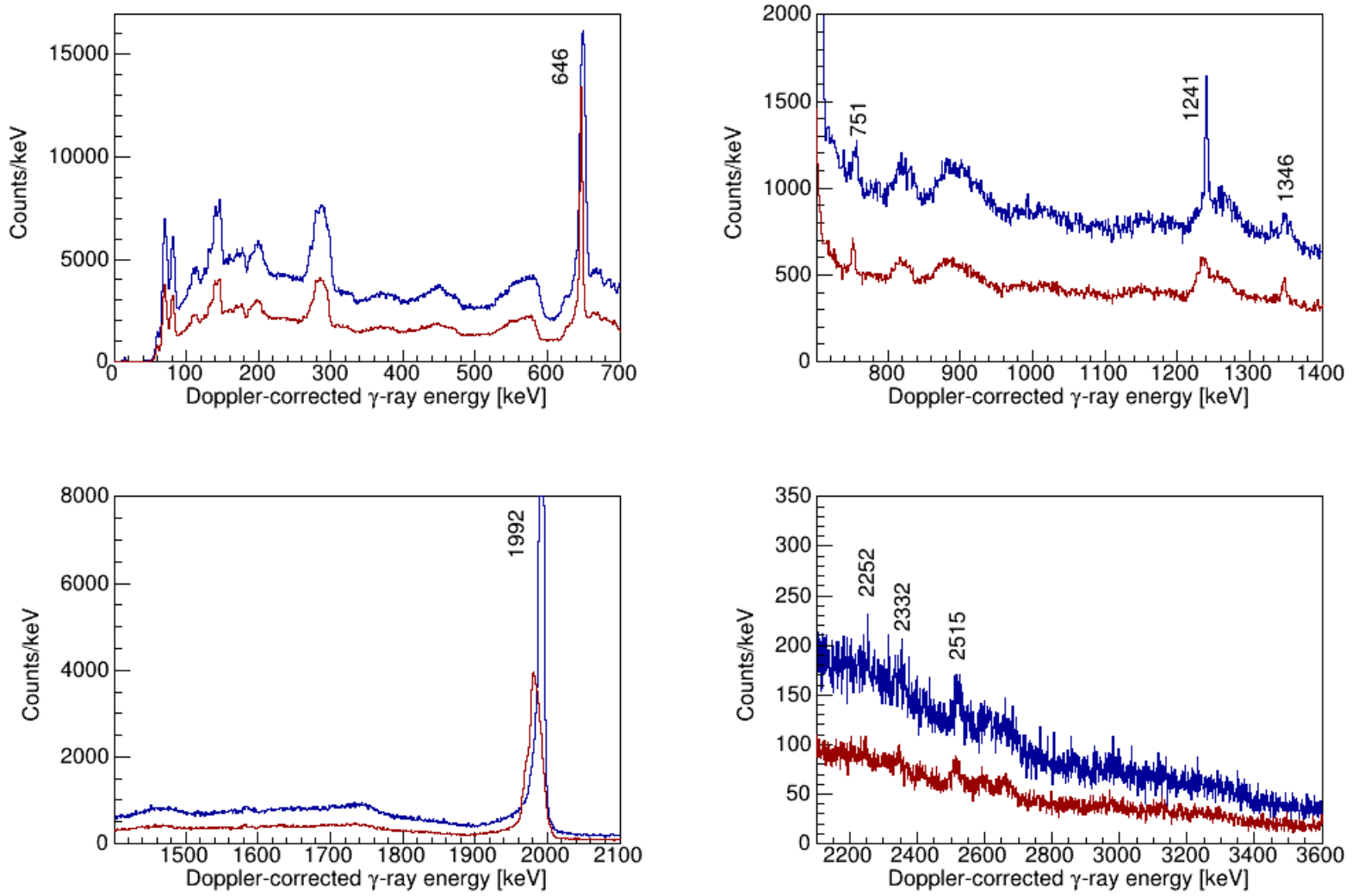

Figure 58: Doppler-corrected γ-ray spectrum in coincidence with SPIDER, assuming mid-target velocity (blue) or after degrader velocity (red). The red spectrum is scaled by a factor 0.5 for better graphical comparison. Gate in excitation energy between 2.2 and 2.8 MeV.

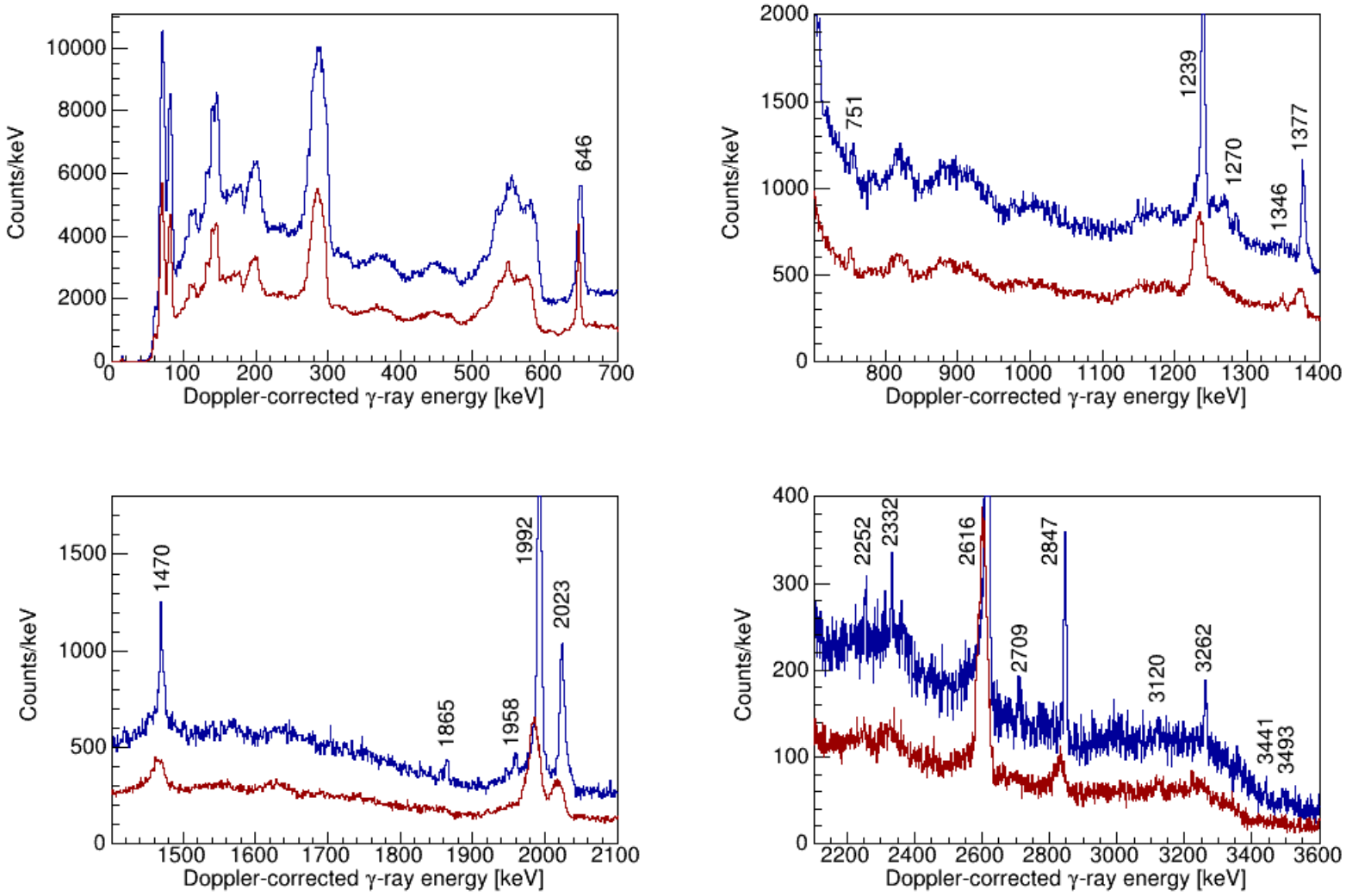

Figure 59: Doppler-corrected γ-ray spectrum in coincidence with SPIDER, assuming mid-target velocity (blue) or after degrader velocity (red). The red spectrum is scaled by a factor 0.5 for better graphical comparison. Gate in excitation energy between 2.8 and 3.5 MeV.

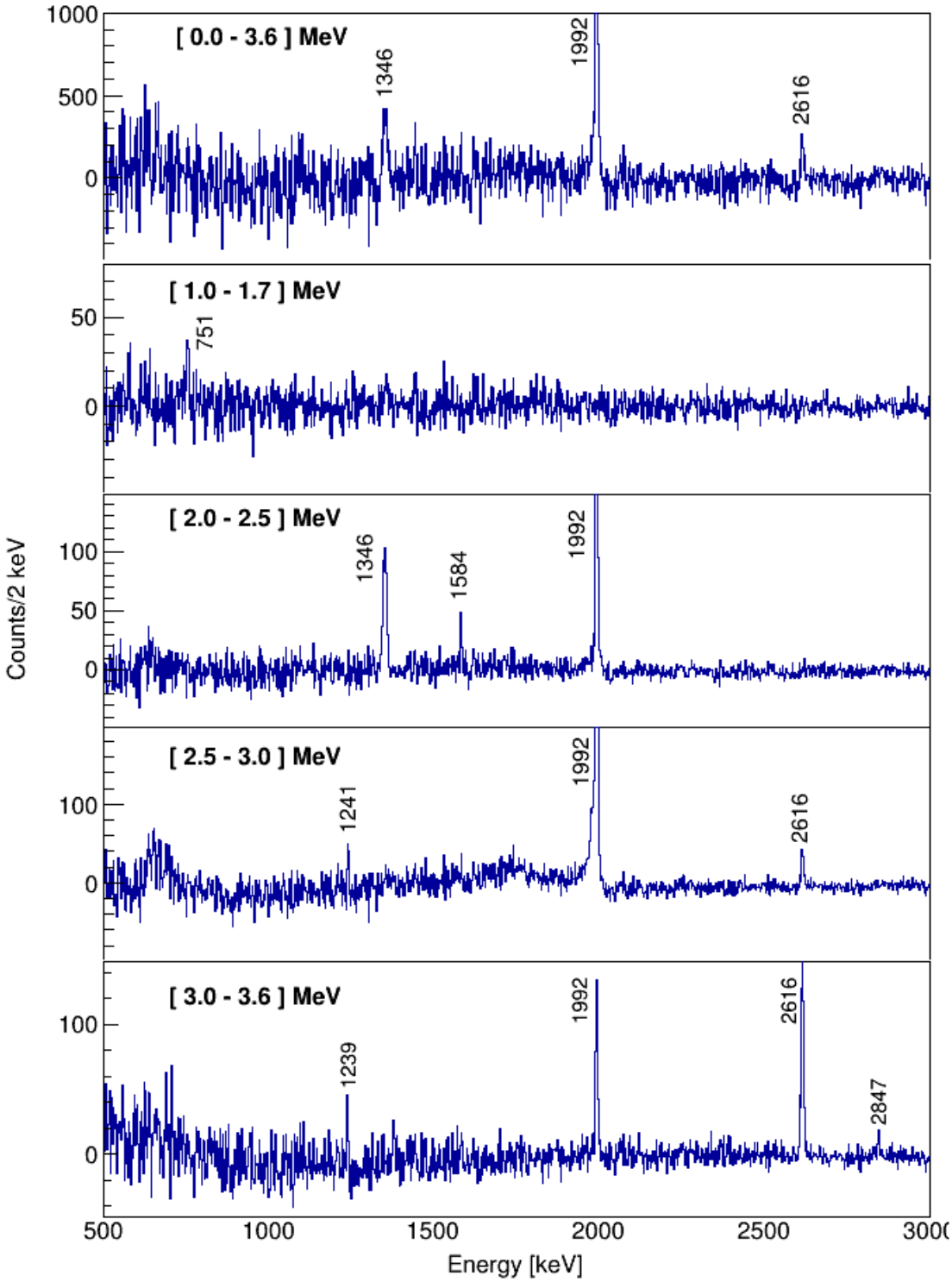

Figure 60: Proton-γ-γ coincidence matrix projections, built with the requirement to observe the 646-keV peak. Coincidence peaks are indicated to the nearest integer. The different projections correspond to different excitation energy ranges, reported in between square brackets in each panel.

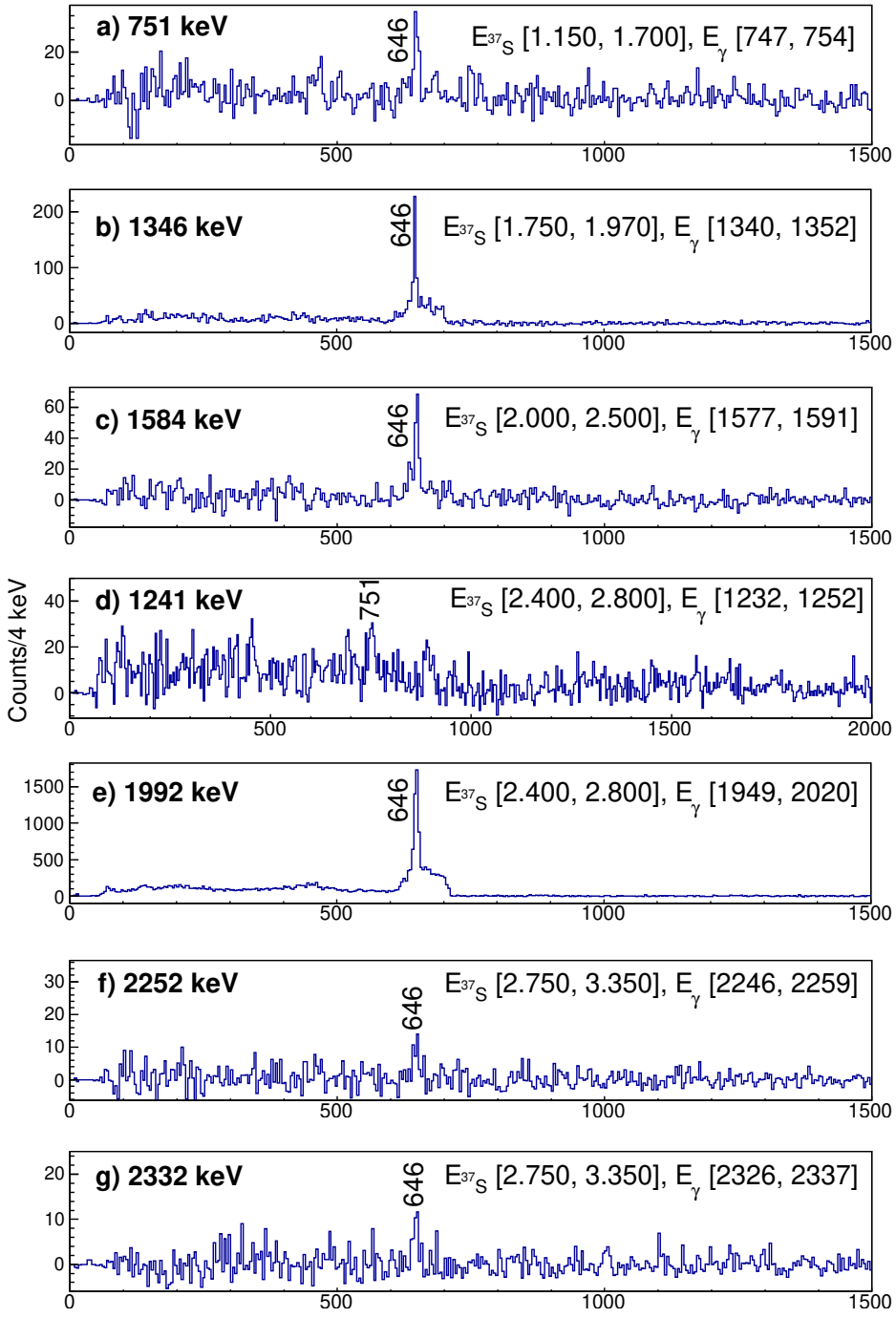

Figure 61: Proton-γ-γ coincidence matrix projections with different excitation energy and γ-ray energy conditions. Coincidence peaks are indicated to the nearest integer. The excitation energy (noted with E_{37S}) condition and γ-ray energy condition used to generate the spectrum are reported in each panel. Continues on the next page.

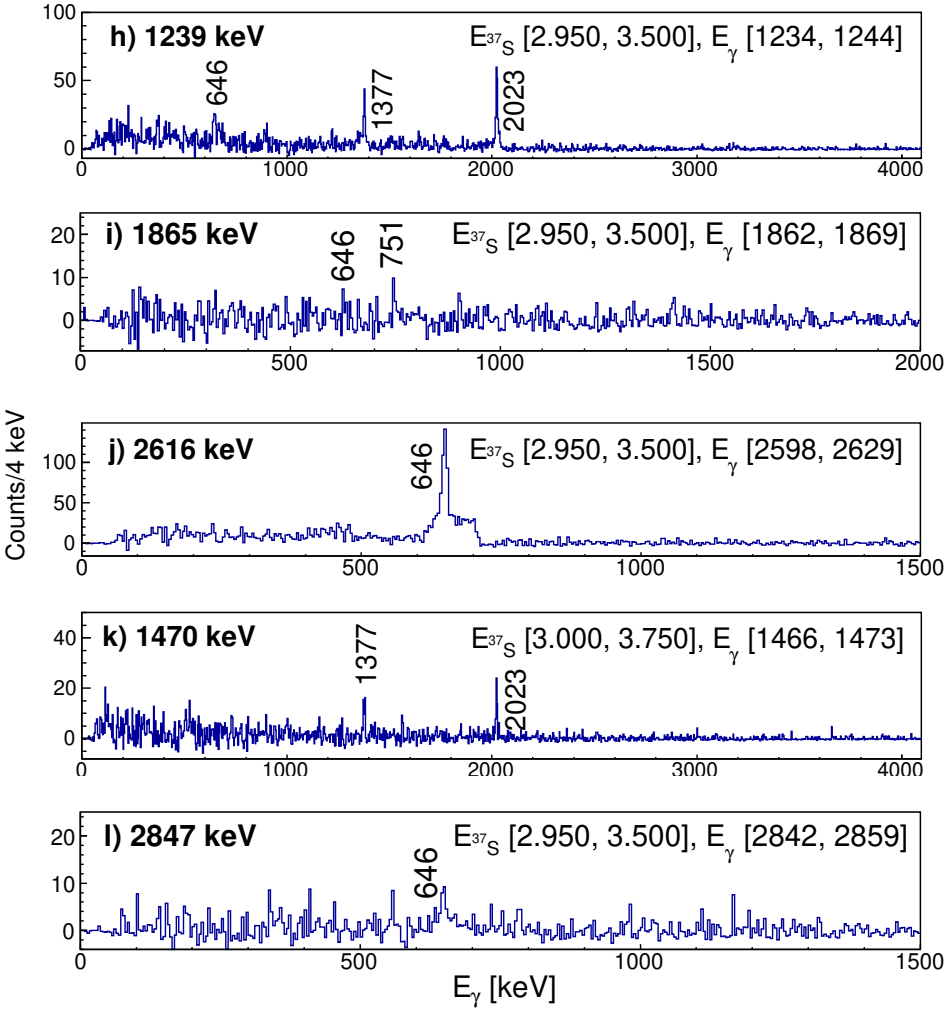

Figure 61: (cont.)

- the obtained values were then divided by the sine of the polar angle and scaled by the factor that minimized the χ^2 distribution with the FRESCO function, assuming only a multiplicative factor. Explicitly,

$$\begin{aligned} \chi^2 &= \sum_i \frac{(d\sigma/d\Omega(\theta_i) - \alpha N^{\mathrm{exp}}(\theta_i))^2}{\sigma^2_{\mathrm{exp},i}}, \\ \alpha &= \left[\sum_i d\sigma/d\Omega(\theta_i)\right] / \left[\sum_i N^{\mathrm{exp}}(\theta_i)\right], \end{aligned} \tag{27}$$

where α is the multiplicative factor to obtain, and $\sigma_{\mathrm{exp},i}$ is the error on the experimental angular distribution point, obtained by propagation assuming a Poisson distribution of the number of counts in each SPIDER strip.

On the other hand, due to the condition on the γ rays, the extracted angular distribution (and, subsequently, the spectroscopic factor) is not the true proton angular distribution, but a convolution between the proton and the proton-γ correlation distributions. Indeed, the implicit assumption in the procedure just described is that the efficiency of AGATA is uniform throughout the surface of the detector. However, it is known that γ rays emitted after a nuclear reaction are not emitted isotropically, but according to a distribution that can be in general written as:

$$W(\theta) \sim 1 + a_2 P_2(\cos\theta) + a_4 P_4(\cos\theta), \tag{28}$$

where $a_{2,4}$ are multiplicative factors that depend on the initial and final state, multipolarity and mixing ratio of the transition, $P_{2,4}$ are the Legendre polynomials of order 2 and 4, and θ is the relative angle between the particle momentum and the γ-ray emission direction [24]. This function is non-constant on the angular range covered by the AGATA+SPIDER setup. Since ^{37}S ions are emitted within a kinematical cone of 3 deg with respect to the beam direction, the θ angle in the previous equation can be approximated with the angle of detection of the γ ray. In other words, the existence of proton-γ correlations is equivalent to considering the efficiency of AGATA non constant, but θ-dependent. However, several factors reduce the severity of this effect:

- for E1 and M1/E2 transitions connecting states of half-integer spin, in general, the contribution $a_{2,4}$ are low in magnitude ($\leq$0.4). In particular, for E1 and M1 transitions, $a_4 = 0$ exactly. For mixed transitions, moreover, these factors are scaled by a factor $1/(1+\delta^2)$, where δ is the mixing ratio. As all contributions to $a_{2,4}$ are multiplicative, this reduces the total effect of the angular correlation;

- orientation is a statistical process with a certain probability. This factor (lower than 1) has been reabsorbed in the definition of $a_{2,4}$. Furthermore, alignment of the product nucleus increases with the transferred angular momentum L, which for most states is $1\hbar$;

- the response function and tracking algorithm of AGATA, coupled with the relatively big polar angle coverage of each channel of SPIDER, further contribute to smear out the features of angular correlations distribution. The effect of tracking was discussed for γ-γ correlations by Ljungvall *et al.* [85], and it can be assumed to be partially valid also in this context.

All these facts point towards a negligible contribution of the non-isotropic terms of the proton-γ angular correlation function. It has to be stressed that these conclusions are valid in the present experiment, as particle-γ angular correlation functions have been used successfully in other experiments with other setups, e.g. Ref. [163] for ^{39}Ar.

In order to check these assumptions, the proton angular distributions of the 646-keV state with and without condition on the presence of a γ-ray were compared, as well as the distributions of the 3262-keV state with a condition on the presence of only the 2616-keV γ ray and with the presence of the 1239- and 2616-keV γ transitions. In all cases, there is no qualitative difference between the obtained distributions, as shown inFigure 62.

Furthermore, the distribution in polar angle of the emitted γ-rays was examined. The chosen transitions were the pure-E2 646-keV $3/2^- \rightarrow 7/2^-_{\text{g.s.}}$, mixed M1/E2 1992-keV $1/2^- \rightarrow 3/2^-$ and the mixed M1/E2 2616-keV $3/2^- \rightarrow 3/2^-$. All distributions were produced requiring direct population of the state. Again, no statistical difference between the distributions was found further reassuring that proton-γ correlations effects are not observable at this analysis level.

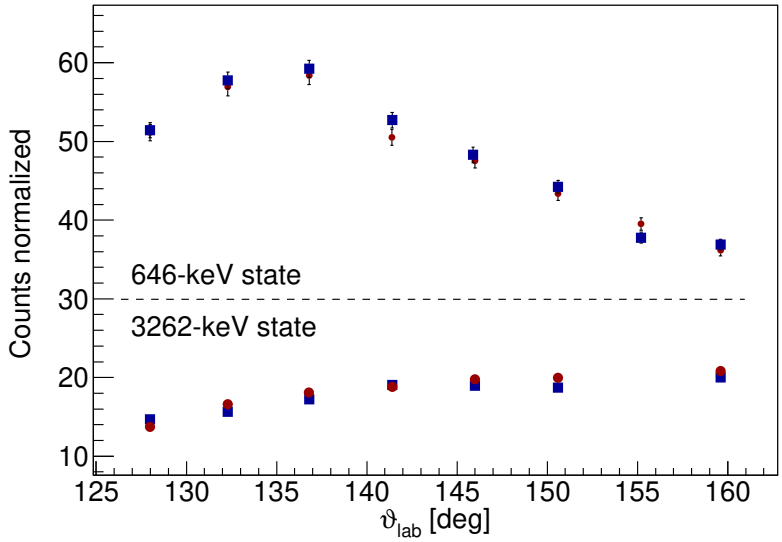

Figure 62: Comparison between proton angular distributions populating the 646- (top) and 3262-keV (bottom) level. In the case of the 646-keV level, the distribution in blue squares is obtained by imposing the condition to observe a proton in coincidence with a 646-keV γ ray, while the one in red circles with no condition. In the case of the 3262-keV level, the distribution in blue squares is obtained requiring the observation of a γ ray of 1239 or 2616 keV, while the one in red circles with the observation of a 2616-keV γ ray only. Errors on angles are omitted for easier comparison. Curves are normalized for better graphical comparison.

The angular distributions measured with this procedure can be found in Figures 63 and 64, compared to the DWBA calculated ones. In the calculations, it was assumed negligible the contribution from multi-step transfer reactions, which might be important for small-strenght states. A state-by-state discussion is postponed to the following section.

For the relative spectroscopic factors, the procedure followed is described in the following. The expected number of protons N_p populating a specific state i for each channel of SPIDER is

$$N_p = \int_{t_i}^{t_f} K(t) \int_{\phi_{\min}}^{\phi_{\max}} \int_{\vartheta_{\min}}^{\vartheta_{\max}} \int_{\mathrm{E}_{\min}}^{\mathrm{E}_{\max}} \epsilon(E) \frac{d\sigma}{d\Omega}(\theta) \sin\theta d\theta d\phi dt \tag{29}$$

where $\theta_{\min,\max}$ and $\phi_{\min,\max}$ indicate the angular extension of the SPIDER channel, ϵ its efficiency for detecting protons which impact with energies spanning from $\mathrm{E}_{\min}$ to $\mathrm{E}_{\max}$ (which are themselves a function of ϑ, as the integral runs over the kinematic line), and K is a multiplicative time-dependent factor taking into account target thickness and beam current. Defining the efficiency as in §3.4, the integral over the kinematic line of the efficiency can be substituted with the quantity $\varepsilon_{\mathrm{eff}}$:

$$N_p = K_{\mathrm{eff}} \varepsilon_{\mathrm{eff}} \Delta\phi_{\mathrm{eff}} S \int_{\theta_{\min}}^{\theta_{\max}} \frac{d\sigma^{\mathrm{DWBA}}}{d\Omega}(\theta) \sin\theta d\theta = K_{\mathrm{eff}} \varepsilon_{\mathrm{eff}} \Delta\phi_{\mathrm{eff}} S \sigma^{\mathrm{DWBA}}. \tag{30}$$

In the last equation, the physical cross-section $d\sigma/d\Omega$ has been substituted with the DWBA calculated cross-section scaled by the spectroscopic factor S. By imposing a condition on a de-exciting transition, this quantity is to be multiplied by the γ-ray efficiency ϵ_γ of AGATA at the energy of the transition and the branching ratio of the transition itself. Since K_{eff} cannot be measured precisely, only relative spectroscopic factors can be given. Namely, the relative spectroscopic factors are given by the ratio

$$\frac{N_{i|\gamma}}{N_{646|646}} = \frac{K\varepsilon_{\mathrm{i}}\Delta\phi_{\mathrm{i}}S_i\sigma_i^{\mathrm{DWBA}}\epsilon_\gamma \mathrm{BR}_{i|\gamma}}{K\varepsilon_{646}\Delta\phi_{646}S_{646}\sigma_{646}^{\mathrm{DWBA}}\epsilon_{646}\mathrm{BR}_{646|646}} = \\ = \frac{\varepsilon_i}{\varepsilon_{646}}\frac{S_i\sigma_i^{\mathrm{DWBA}}}{S_{646}\sigma_{646}^{\mathrm{DWBA}}}\frac{\epsilon_\gamma}{\epsilon_{646}}\mathrm{BR}_{i|\gamma}. \tag{31}$$

In the previous equation, $N_{i|\gamma}$ means the number of protons populating the state i that were observed to decay with a γ-ray of energy γ. In this way, the K dependence is removed, and the formula can be solved for S_i. All results, for easier comparison, are rescaled by a factor 0.438, the Adopted spectroscopic factor of the 646-keV level. The results of this procedure can be found in Table 20. The contribution due to fusion-evaporation reaction of ^{36}S+^{2}H is not accounted in this calculation. In general, it can be observed that the obtained spectroscopic factors are within 1σ from the Adopted ones. This is not true only for the 1397- and 3493-keV levels, where the agreement is within 2σ.

In the following paragraph, a detailed state-by-state discussion of the results can be found.

646-keV state

The first excited state found in the p-γ matrix in Figure 53 is the 646-keV $3/2^-_1$ state, which can only decay to the ground state. Its de-excitation γ ray shows two different components, one Doppler shifted and one instead not Doppler shifted, which is characteristic of a state lifetime in DCM range. From Figure 55, it is clear that the Doppler correction that produces the smaller FWHM is the one with the velocity calculated after the Au backing, further confirmation that all in-flight decays happen between the two plunger foils. No other γ-ray is visible in the spectrum. The proton angular distribution reproduces a L=1 transfer (see Figure 63), while the integral of this distribution has been used to normalize all other spectroscopic factors, therefore has been assigned the exact literature value.

E [keV]	J^{π}_{lit}	$S_{lit} \cdot 100$ [%]	L	J^{π}_{exp}	$S_{exp} \cdot 100$ [%]
0	$7/2^-$	69.3	3	$7/2^-$	65(4)
0.646	$3/2^-$	43.8	1	$3/2^-$	43.8
1.397	$(3/2)^+$	3.3	2	$3/2^+$	4(1)
1.992	$(3/2)^-$	3.3	1	$3/2^-$	2.9(6)
2.023	$(7/2)^-$	0.63	3	$5/2^-$	<0.7
2.230	$(1/2^+)$	–	0	$1/2^+$	1.2(3)
2.638	$1/2^-$	48.5	1	$1/2^-$	46(9)
2.898	–	–	(2,3)	$5/2^+$, $5/2^-$, $7/2^-$	0.3(1), 1.4(6), 0.8(4)
2.978	(1/2, 3/2)	–	(1)	$1/2^-$,$3/2^-$	0.2(1), 0.12(5)
3.262	$3/2^-$	8.5	1	$3/2^-$	5(2)
3.355	$(3/2)^+$	3.0	2	$3/2^+$	2(2)
3.493	$3/2^-$	4.5	1	$3/2^-$	3(1)

Table 20: Measured relative spectroscopic factors and adopted spectroscopic factors from literature [47]. All measured spectroscopic factors are normalized to the one of the 646-keV state, which has been assigned exactly the literature value for easier comparison. States for which S could not be calculated are omitted from this table. J^{π}_{exp} indicates the spin assumed to calculate the measured relative spectroscopic factors. Where multiple spin assignments are possible, they are listed in the same order of the spins.

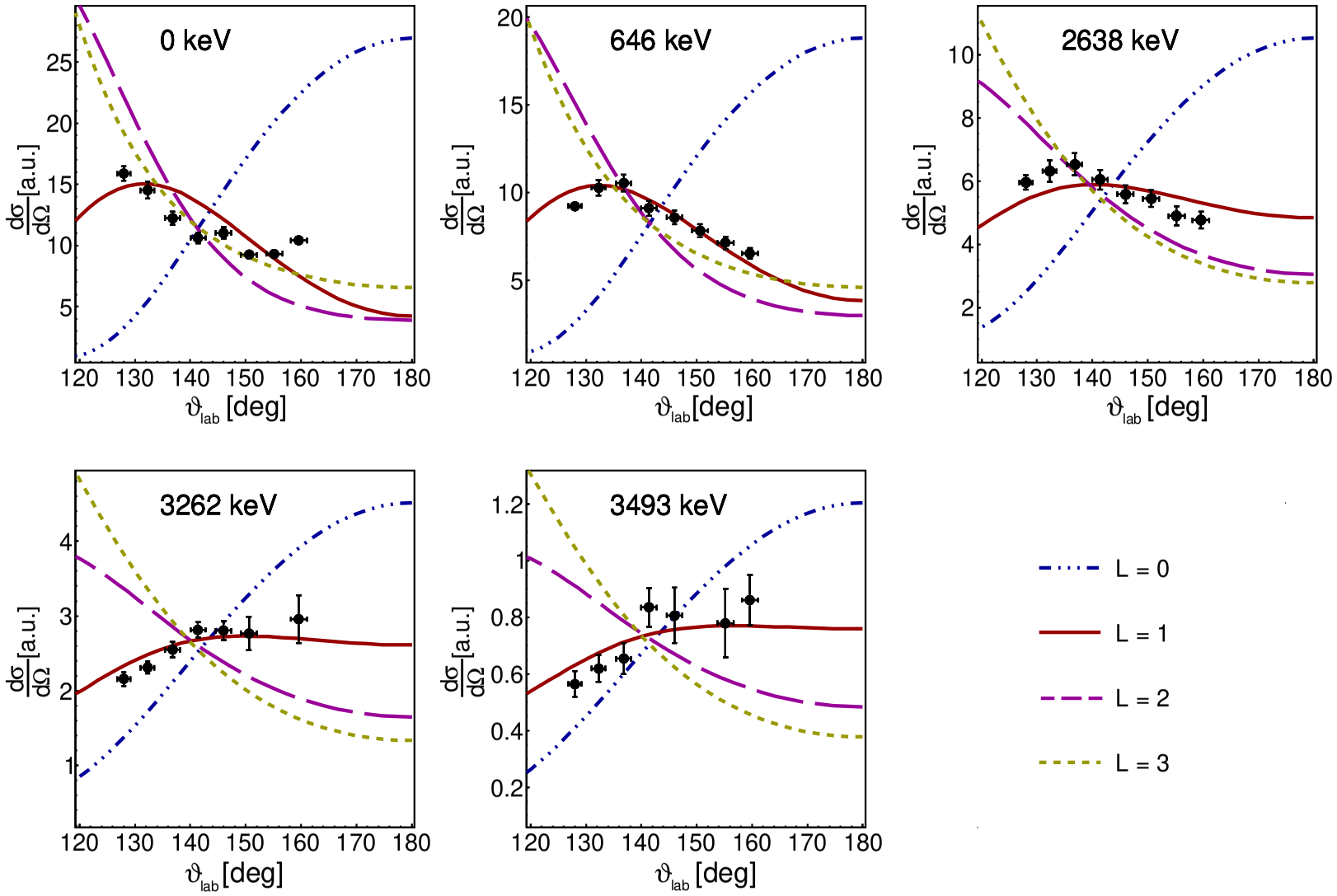

Figure 63: Angular distributions for the low-lying single particle states of ^{37}S in the laboratory frame. Since no absolute normalization can be derived from this dataset, experimental data were rescaled with a factor that minimized the χ^2 value with the DWBA-calculated angular distribution multiplied by the relative spectroscopic factor measured.

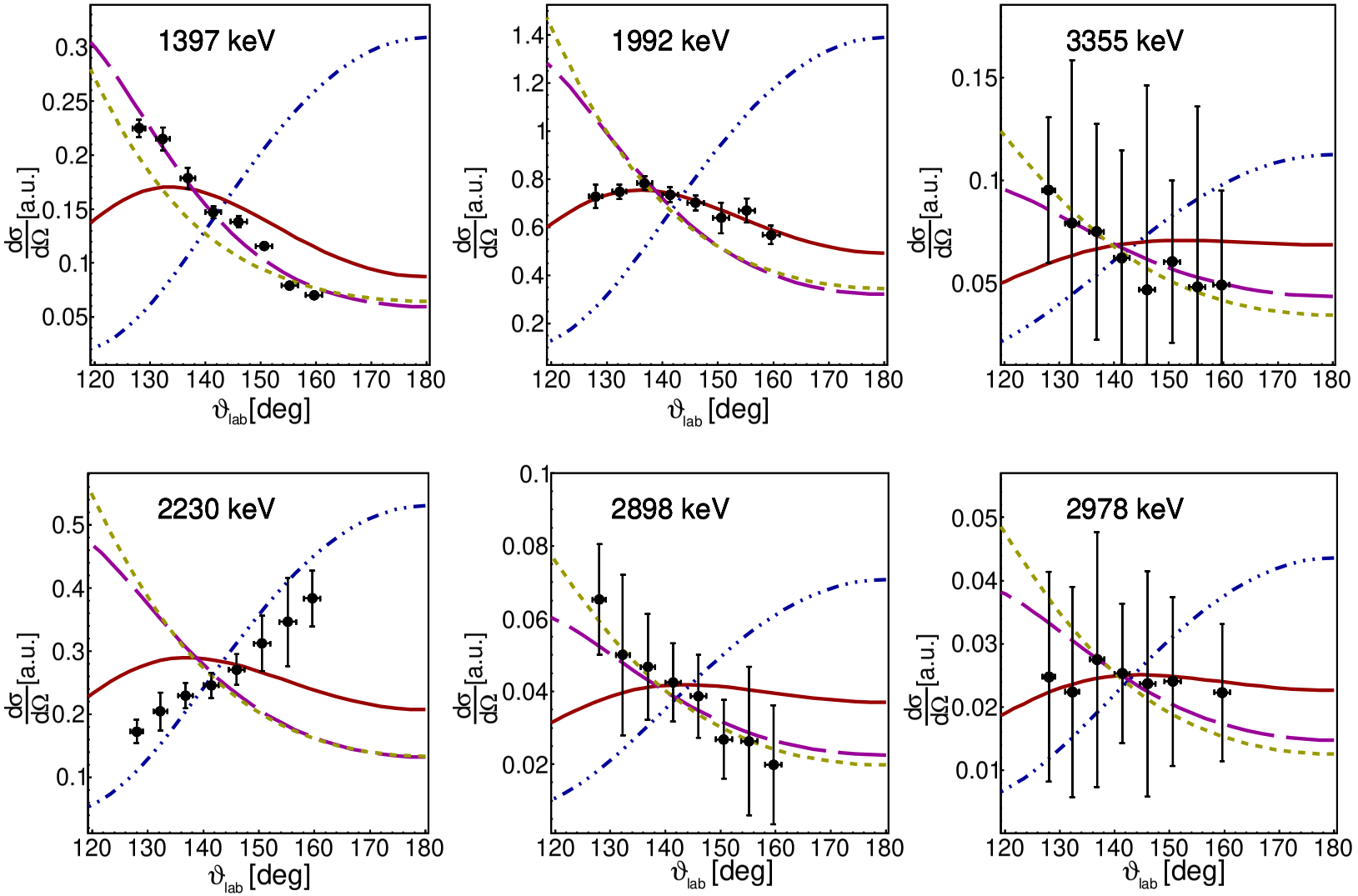

Figure 64: Angular distributions for the low-lying intruder (top row) or unknown (bottom row) states of ^{37}S in the laboratory frame. Scaling factors are as in Figure 63.

1397-keV state

Above the 646-keV state, a 751-keV γ ray can be observed coming from a state at about 1.4 MeV of excitation energy. This would correspond to the intruder 1397-keV $3/2_1^+$ state. As for the 646-keV photon, this γ ray shows two components, signaling that this state has a long lifetime in DCM range. Coincidences can also be observed by gating both on the 751-keV (Figure 61(a)) and the 646-keV (Figure 60(b)) γ ray, confirming the 751-646 cascade. No other γ ray is visible in Figure 56.

1992-keV state

A 1992-keV γ ray coming from a 1992-keV state is clearly visible in Figure 53. Indeed, the 1992-keV γ-ray doublet coming from the decay of the 1992 and 2638-keV states is known in literature, e.g. see Chapman *et al.* [71]. The existence of the doublet is clear in Figure 54, where it can also be noticed that the 1992-keV transition feeding the ground state is visibly larger than the one feeding the 646-keV state. The difference is even clearer in Figure 57, where the after target backing correction has no lineshape, while the mid-target correction has a clear lineshape. However, since no double component is present, this would suggest that this state has a lifetime between several hundreds of fs up to tens of ps. The second branch of this state, the 1346-keV γ-ray feeding the 646-keV state, can be seen in Figure 57 as well, and in γ-γ coincidences both from below (see Figure 60(a) and (c)) and from above (see Figure 61(b)). Branching ratios are also compatible with the ones reported in literature (and Table 10).

2023-keV state

The existence of this state is known from literature, however no γ-ray decay coming from the direct population of this state is visible in Figure 57. The 2023- and 1377-keV γ-ray decays are only visible in Figure 53 coming after the population of a state above 3 MeV, which is either the 3262 or the 3493-keV state, or both. Decay coming from these levels to the 2023-keV state are indeed known. The branching ratio is compatible with the one provided in literature, but in Table 19 it is given with improved precision. An upper limit on the spectroscopic factor (which has been measured from previous (d,p)

experiments to be 0.6%) can be given by considering the state populated with the lowest cross section. The cross section has been estimated as the integral of the DWBA angular distribution on the SPIDER angular coverage multiplied by the spectroscopic factor. This state is the 2978-keV, with a cross section around 0.02 and 0.04 mb, depending on the J assignment. Taking the highest between the two, dividing this value by the cross section of the 2023-keV state (calculated in DWBA), and correcting by the different efficiencies one obtains 0.7% minimum spectroscopic factor. Therefore, states with L=3 transfer with spectroscopic factor lower than 0.007 would have not been observed in the present experiment in direct population. As this is the case of the 2023-keV level, the only value that can be drawn from this data is this upper limit.

2230-keV state

This level has never been observed in any (d,p) experiment. However, Dufour *et al.* [70] had observed in 1986 a 1583-keV γ-ray coming from ^{37}P β decay. More recently, Wang *et al.* [74] state that in order to measure the lifetime of the 646-keV state, they required a coincidence between a 1584-keV transition and the 646-keV γ ray. The authors of both publications however did not assign this decay to any state. The first assignment to a 2230-keV state was done by Warburton and Becker [162]. Given the high β-decay branching ratio (which they state they deduced from data of Dufour *et al.*), they assign spin $(1/2)^+$ to this state. Furthermore, Kardonsky *et al.* [63] observe an α group which they assign to the population of a 2.20(5) MeV state. Then, in their Table II, they match this state to the 2.02(2) observed by Ajzenberg-Selove *et al.* [164], i.e. the 2023-keV intruder state. A 1584-keV transition coming from a 2.2 MeV state is clearly visible in Figure 54 and 57. Particle-γ-γ coincidences both on the 646-keV (Figure 60(c)) and the 1584-keV (Figure 61(c)) γ rays clearly place the 1584-keV γ ray as a decay branch of the 2230-keV state. No 2230-keV γ ray is observed, suggesting that the 1584-keV is the only decay branch of this level. The proton angular distribution in Figure 64 is compatible with a L=0 assignment. This would mark the first observation of a L=0 state in this nucleus, with 0.012(3) spectroscopic factor. However, this begs the question of why this state was not observed by either Piskoř *et al.* [64], Thorn *et al.* [65] or Eckle *et al.* [66], which had greater resolution in particle detection than this setup. In the case of Piskoř *et al.* and Eckle *et al.*, this energy region is heavily contaminated by ^{35}S or Cl peaks, which were present as contaminants

in the target. In the case of Thorn *et al.*, two clear peaks can be observed in their energy spectrum between 2 and 2.5 MeV. Whether they were considered contaminant peaks, or ^{35}S peaks, it is unknown, since the authors did not comment on it.

2515-keV state

This state is very weakly populated in this experiment, consistently with the measured spectroscopic factor reported in Table 3. The 2515-keV γ-ray peak in Figure 58 is also fairly broad, suggesting that this level has a lifetime in the hundreds of fs range. Due to the very low population of this state, no reliable spectroscopic factor or angular distribution can be extracted. Only the decay to the ground state is observed, consistently with Chapman *et al.* [71].

2638-keV state

The 1992-keV γ-ray decay from this state has already been discussed with the decay of the 1992-keV level. However, a second 1241-keV γ-ray branch feeding the 1397-keV state is also observed (see γ-γ coincidence matrix projection in Figure 61(d)), which was not reported by Chapman *et al.* [71]. In this case, this γ ray was probably not observed as it formes a doublet with the much stronger 1239-keV decay from the 3262-keV state. The resolution in Q-value available with PRISMA, along with the very low branching ratio, was probably not sufficient to distinguish the two lines. The proton angular distribution reproduces a L=1 transfer (see Figure 63), and its relative spectroscopic factor is compatible with the literature value.

2776-keV state

Coherently with the results of Piskoř *et al.* [64] and Thorn *et al.* [65], this state is not present in our data. Indeed, this state has been assigned by Chapman *et al.* [71] a $(11/2)^-$ spin. The authors suggest that this state belongs to the $(2_1^+)_{^{36}\mathrm{S}} \otimes \nu f_{7/2}$ multiplet. Being the $h_{11/2}$ strength centroid far in energy, this state is hardly populated by (d,p) in this nucleus.

2898-keV state

As for the 2230-keV state, this work marks the first observation of this state in (d,p), thanks to its 2252-keV γ-ray decay to the 646-keV level (see Figure 61(f)) and the 2898-keV decay to the ground state. A 2254-keV decay to the first excited state was already observed by Dufour *et al.* [70]. Warburton and Becker [162] assigned spin $3/2^+$ to this state, based again on the β-decay branching ratio, which seems consistent with $\Delta J = 1$. The proton angular distribution in Figure 64 indeed favours L>1 assignment. However, the decay to the ground state rules out the $3/2^+$ possibility, as an M2 to the $7/2^-$ ground state would not be competitive with a E1 to the $3/2^-$ (as in the case of the 1397-keV state). The possible spin assignments are therefore $5/2^+$, $5/2^-$ and $7/2^-$.

2978-keV state

This state was not observed in (d,p), but reported by Chapman *et al.* [71] and Ajzenberg-Selove *et al.* [164]. The proton angular distribution favours L=1 assignment, consistent with the (1/2, 3/2) spin assignment of Chapman *et al.*, albeit statistical errors make this transfer compatible with a transfer of any L. Only the decay to the first excited state is observed.

3120-keV state

This state is populated with very low cross section. Only the direct decay to the ground state is observed, in accordance with Chapman *et al.* [71] and Eckle *et al.* [66]. No angular distribution or spectroscopic factor could be calculated. This state was tentatively assigned $(9/2)^+$ spin by Eckle *et al.*, based on the angular distribution features.

3262-keV state

This state is fairly strongly populated. With a measured spectroscopic factor of 8.5%, this state was identified as a $p_{3/2}$ fragment by Eckle *et al.* [66]. A part from its previously-known 2616 and 1239-keV γ-ray decays to the 646 (see Figure 61(j)) and 2023-keV levels (Figure 61(h)), observed also by Chapman

et al. [71], three other decays have been observed, namely to the 1992-keV, 1397-keV (Figure 61(i)) and ground state levels. No coincidence was found for the 1270-1992 or 1270-1346 keV γ-ray chains, but this is compatible with the low population of the 1270-keV line. The proton angular distribution reproduces the expected L=1 transfer (see Figure 63). Neglecting the new branches observed, the branching ratios calculated are consistent with ones in the literature.

3341-keV state

This state is not observed in our data, in agreement with the other (d,p) studies on this isotope. Chapman *et al.* [71] assigned it (7/2, 9/2) spin mainly via comparison with SM calculations with the SDPF-U interaction. The authors argue that this state, along with the 2776-keV ($11/2^-$), is a member of the $(2_1^+)_{^{36}\mathrm{S}} \otimes \nu f_{7/2}$ multiplet.

3355-keV state

This intruder state has been assigned $(3/2)^+$ spin by Thorn *et al.* [65] and Piskoř *et al.* [64]. The proton angular distribution favours L=2 assignment, despite the large errors. This result is compatible with the results in literature. Despite the low population, two clear γ-rays can be observed, at 2709 and 1958 keV, in coincidence with the 646 and 751-keV transitions. This confirms the observation of this state and the placement of the two lines.

3441-keV state

This state was observed by Piskoř *et al.* [64] and Chapman *et al.* [71], and is also present in this dataset. The very low population does not allow for a reliable extraction of the relative spectroscopic factor or angular distribution. Only the decay to the ground state can be observed, in accordance with Chapman *et al.*, who also do not observe any other decays. Piskoř *et al.* and Eckle *et al.* [66] agree on the L=3 character to the transfer, based on the angular distribution features, tentatively assigning $(7/2)^-$ spin.

3493-keV state

The results of Chapman *et al.* [71] are consistent with the results from this data, but two additional γ-ray branches have been observed for this level, one populating the 646-keV state, and one the ground state. Coincidence matrix projections are shown in Figure 61(k) and (l). The angular distribution shows the L=1 transfer expected (see Figure 63) in the population of this $3/2^-$ state. Neglecting the new transitions, the branching ratios are consistent with the Adopted Values [47].

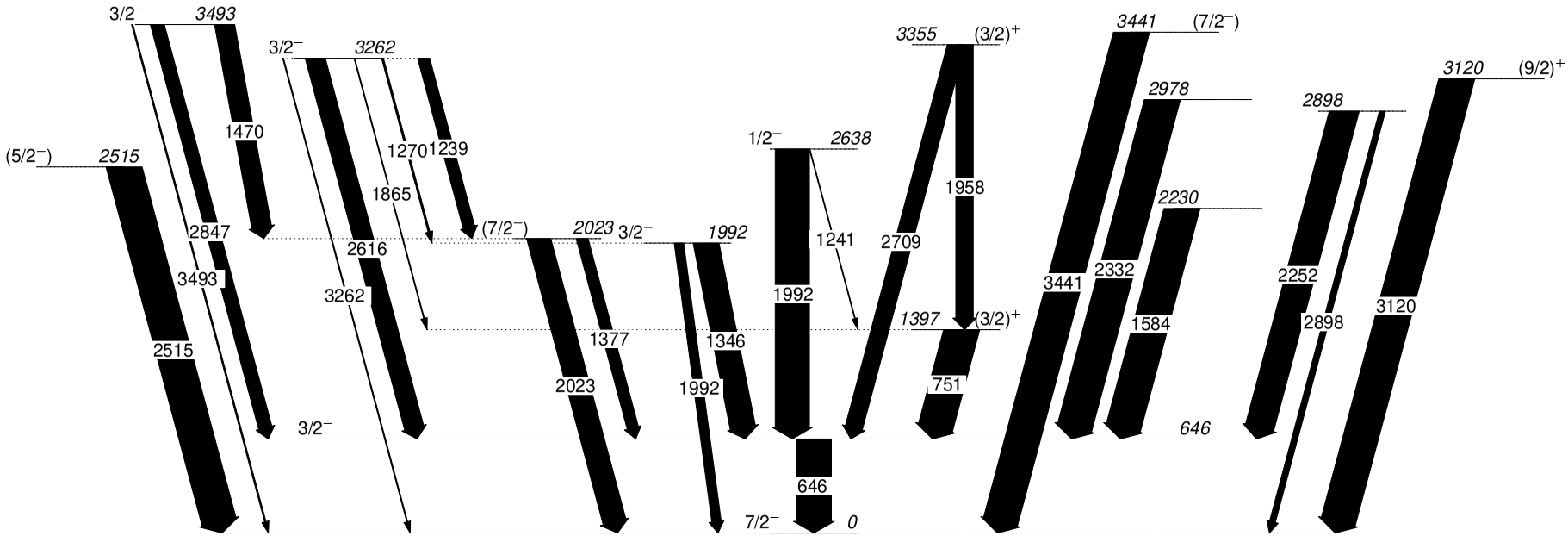

Figure 65: ^{37}S level scheme, as observed in this experiment. Spin assignments are the Adopted ones [47], where present. Arrow width is proportional to the branching ratio of the decay.

5 Lifetimes

This Chapter will present the results of the lifetime measurements performed on the dataset of this thesis. Section 5.1, will describe the results of the lifetime measurement of the 646 and 1397-keV states, obtained through Decay Curve Method (DCM) and Differential Decay Curve Method (DDCM), two variants of the RDDS analysis. Section 5.2 instead will focus on the lifetime measurement of the other excited states with the DSAM technique. Based on the lifetimes obtained, the reduced transition probabilities are deduced.

As mixing ratios in ^{37}S were never measured, reduced transition probabilities of mixed character will be given in the two limits of pure multipolarity. In other words, in the case of mixed M1/E2 transitions, reduced transition probabilities are reported first considering pure M1 character ($\delta^2 = 0$), then pure E2 ($\delta^2 \to \infty$). The reduced transition probabilities calculated in this work are therefore upper limits of their corresponding true values.

5.1 RDDS measurements

This Section presents the lifetime measurements performed for the 646 and 1397-keV states. Since the statistics for the direct population is very different, not all methods that have been employed for the 646-keV level can be applied to the 1397-keV one. However, the fundamental analysis is common. The area of the photopeak of the de-exciting transition is estimated through a gaussian fit, first in the non-Doppler-corrected spectrum, then in the Doppler-corrected one. This allows to obtain the unshifted (U) and shifted (S, according to the notation used in §1.2.1) components, and their ratio R. These spectrum have

been obtained by requiring a proton in prompt coincidence that corresponded to a ^{37}S ion produced in the excited state of interest (however, since the lifetimes of these states are three orders of magnitude larger than all other ones, and the direct population of the 1397-keV state estimated less than 1% the population of the 646-keV level, this requirement can be dropped without the need to explicitly consider higher-lying feeders). Background was subtracted using the off-coincidence spectrum and the spectrum produced by gating on fusion evaporation reactions only, i.e. negative excitation energy.

For DCM, the ratio R can be expressed as a function of the (known) distance x between the foils of the Plunger. The unknown parameter τ can then be extracted as fit parameter of the obtained data points with an exponential function. However, as two targets with two different backing thicknesses (4 and 6 mg/cm^2) were used, the value of R depends also on the velocity β of the emitting ion between the foils of the Plunger. This dependence can be removed by a change of coordinates from $R = R(x)$ to $R = R(t)$, where

$$R(t) = e^{-t/\tau} = e^{-\frac{x}{\beta\gamma c\tau}} = R(x). \tag{32}$$

In this way, the explicit dependence of R from β is removed and both datasets can be fitted with one function, doubling the available statistics. The velocity β of the emitting ion can be estimated either from the kinematical reconstruction given by SPIDER, or from the fit of the γ-ray energy distribution with the Doppler effect formula. The error on the velocity value propagates then in the fit as error on the proper time coordinate.

In DDCM, instead, the lifetime can directly be estimated from each distance, without a global fit. Differentiating the previous equation:

$$\frac{d}{dx}R(x) = -\frac{1}{\beta\gamma c\tau}e^{-\frac{x}{\beta\gamma c\tau}} \tag{33}$$

and therefore

$$\frac{R(x)}{-\frac{d}{dx}R(x)} = \beta\gamma c\tau. \tag{34}$$

The same formula, with minor differences, can be obtained for $R(t)$. In this way, all lifetime estimates coming from each distance can be averaged to

produce the final estimate. Since however there is a limited number of points in each curve, the derivative has to be calculated by numerical differentiation. Three derivatives can be considered: the forward derivative, the backward derivative, and the central derivative. Explicitly,

$$\begin{aligned}\frac{d^{\mathrm{f}}}{dx}R(x_i) &= \frac{R(x_{i+1}) - R(x_i)}{(x_{i+1} - x_i)} \\ \frac{d^{\mathrm{b}}}{dx}R(x_i) &= \frac{R(x_{i-1}) - R(x_i)}{(x_i - x_{i-1})} \\ \frac{d^{\mathrm{c}}}{dx}R(x_i) &= \frac{R(x_{i-1}) - R(x_{i+1})}{(x_{i+1} - x_{i-1})}\end{aligned} \tag{35}$$

If h is the separation between contiguous points, the error of these approximations is $\mathcal{O}(h)$ for the forward and backward derivative, while $\mathcal{O}(h^2)$ for the central one, at the cost however of one more experimental point. Since during the experiment a total of 9 distances were taken, this one is preferred.

646-keV state

As mentioned in the previous Chapter, this line shows both shifted and unshifted components. Their relative population, as a function of the plunger distance, is shown in the series of matrices of Figure 66. The spectra have been produced requiring direct population of the state. Due to the very large statistics, of the order of 10^4 events, the 2D matrices can be binned along the angular range. For sufficiently small bins, the distribution resembles two gaussians that can be fitted with very low background. The mean of the distributions will yield the velocity of the ion, while the amplitudes the ratio $R(x)$. In both cases, the most likely value can be obtained via fit of the Doppler formula, in the case of the velocity, and by simple average, in the case of the ratio R. As the shifted and unshifted components overlap for angles close to 90 deg, the angular range between 80 and 110 deg has been excluded from the analysis to avoid double counting. By fitting the exponential distribution and calculating the central derivative, the half-life estimates of 117.2(5) and 120(2) ps can be extracted, as shown in Figure 67. Deviations from the exponential trend, which are not accounted for by statistical errors alone, can be clearly noticed in the graph. These have been suggested to arise from deorientation effects by Fransen *et al.* [165] and Radeck *et al.* [166]. Indeed, the CHARGE [126] code predicts that the most likely electronic configuration after

the gold backing is the lithium-like, which is the second strongest configuration (after the hydrogen-like) in which deorientation effects can be observed.

The presence of possible systematic effects may be highlighted by the correlation between the DDCM-extracted values, which seem to show an upward trend. These values are not statistically independent, due to the fact that two different DDCM points share a common DCM point. The correlation between the calculated points produces a larger lifetime value with higher error bar. However, it also seems that the DDCM values follow the same oscillatory pattern as their DCM counterparts, suggesting a link with the discussed deorientation effects. The advantage of the DCM approach, over the DDCM, is that the oscillatory effects are averaged out, instead of being propagated on the error bar due to the mentioned correlations. The DCM value is therefore preferred.

These estimates can be compared to the 134(3) ps estimate of Wang *et al.* [74], which is 10-15% larger than the value extracted from this dataset. The incompatibility may stem from systematics not accounted for in one of the two measurements.

The final value of half-life yields a B(E2) value of 42.9(2) e^2fm^4, or 5.90(3) W.u..

1397-keV state

As it is clear from Figure 68, the data collected, of the order of 10^2 events per distance, does not allow for the extraction of this lifetimes as the previous one. In this case, the area was calculated by projecting the whole matrix on the energy axis, excluding the range between 80 and 110 degrees, where the two components overlap. Background is removed by subtracting the off-coincidence and FE evaporation spectrum as in the case of the 646-keV state. The results of this procedure can be found in Figure 69. As for the previous state, oscillations are visible in the calculated data points. The values extracted, 76.6(8) and 77(5) ps, match within errors. On the other hand, it can be noticed that the fit function interpolates better points at low time values due to their lower error bar, which probably determines most of the curvature of the χ^2 minimization surface mapped by the fitting algorithm. Therefore, differently than in the previous case, deorientation effects would not be averaged out, but

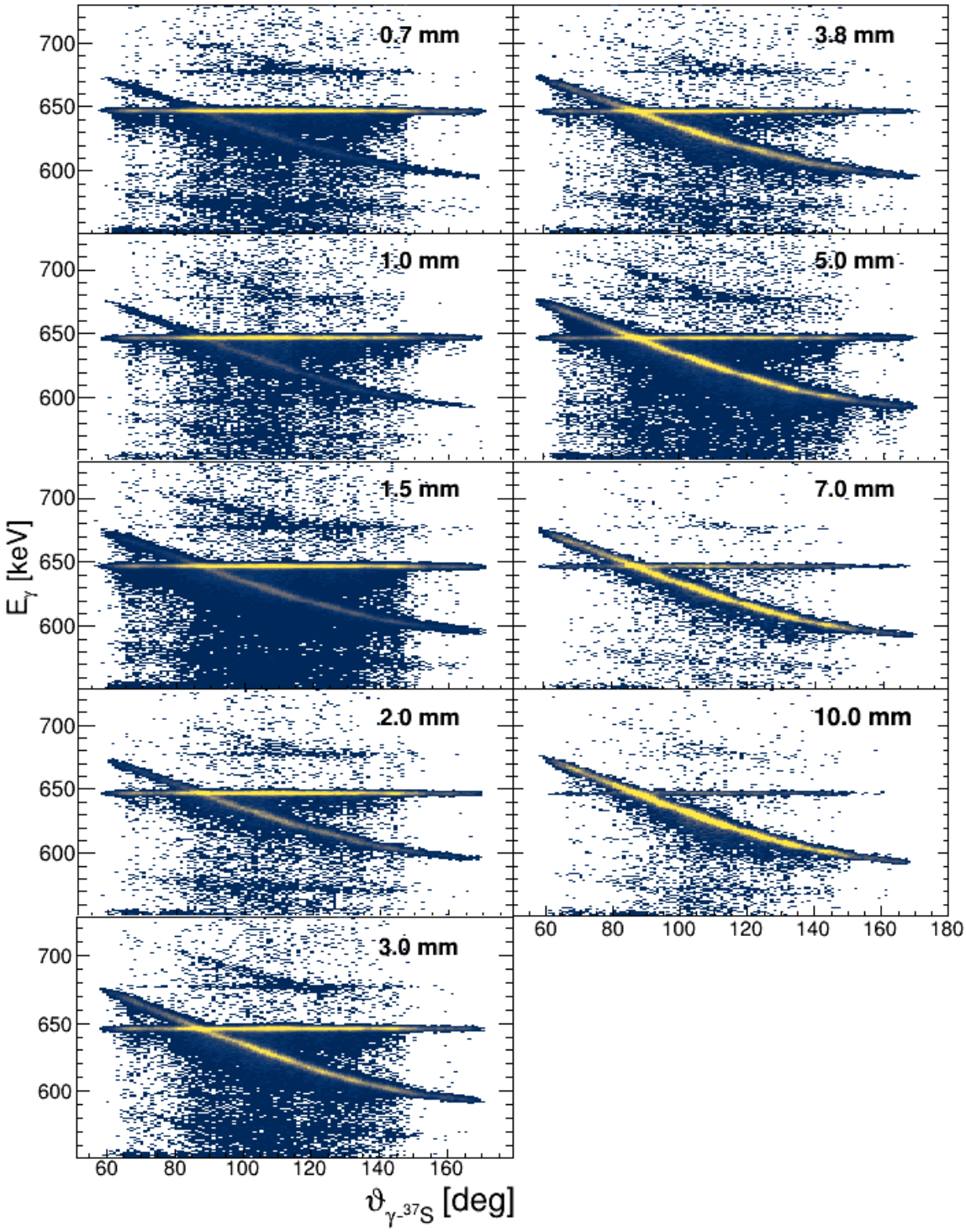

Figure 66: 2D γ-θ matrix of the 646-keV line, showing the different population of the shifted and unshifted component as a function of the plunger distance. The spectra have been produced requiring a proton in the kinematical line populating an excitation energy region between 0.2 and 0.85 MeV.

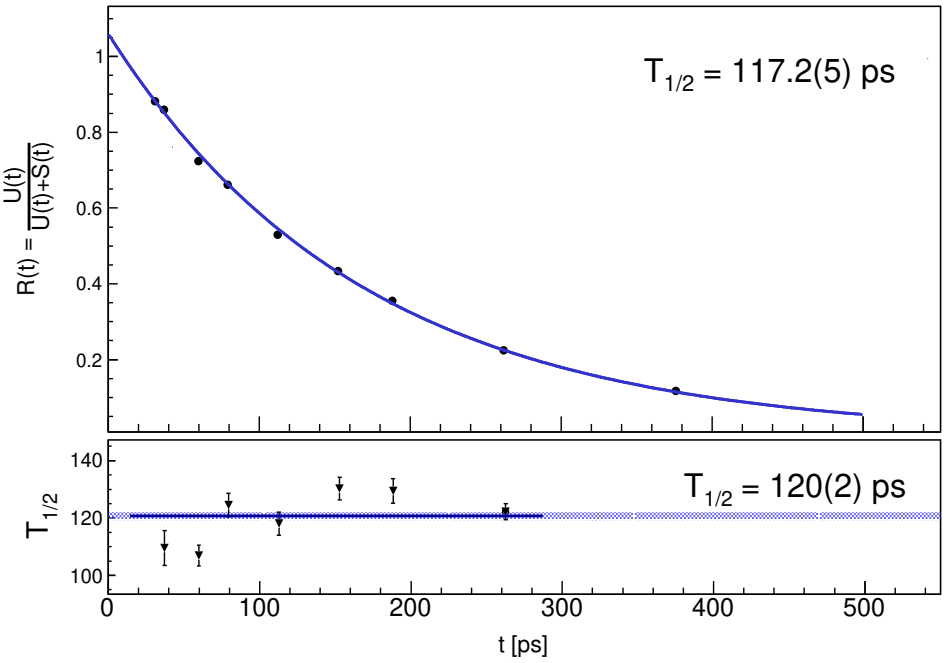

Figure 67: DCM and DDCM fits for the 646-keV level, decaying through the 646-keV γ ray. Errors on DCM values are too small to be seen.

enhanced. In any case, the compatibility between the two values suggests that however the results from both methods are consistent, but the error bar of the DCM method would be mainly determined by only half of the data points, and not by the whole distribution. The DDCM values therefore is considered as a better estimate of the error bar of the measurement. The deduced B(E1) value is $1.34(9) \cdot 10^{-5}$ e^2fm^2, or $1.9(1) \cdot 10^{-5}$ W.u..

5.2 DSAM measurements

This section will focus on levels with shorter lifetimes that can be measured with the DSAM technique. As mentioned in §1.2.1, DSAM consists in comparing the experimental spectrum with a series of realistic MC simulations that only depend on the lifetime of the state of interest. In the present case, imposing an excitation energy condition allows one to select only the direct population of the state, removing the influence of any feeding transitions. Only in the case of the 2023-keV level, the presence of a higher-lying feeder is considered in the simulations, as its decays are not observed after direct

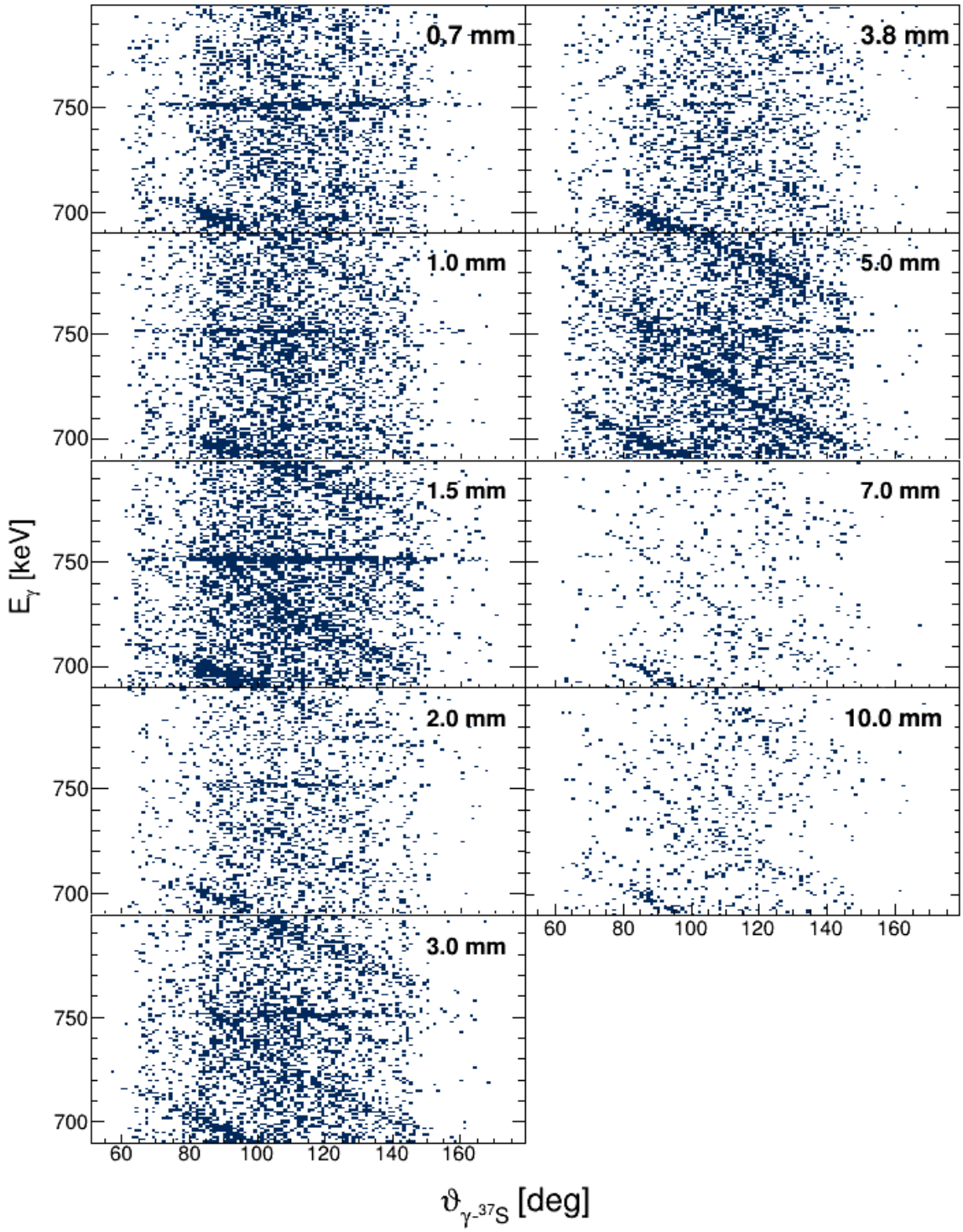

Figure 68: 2D γ-ray energy-θ matrix of the 751-keV line, showing the different population of the shifted and unshifted component as a function of the plunger distance. The spectra have been produced requiring a proton in the kinematical line populating an excitation energy region between 1.1 and 1.75 MeV.

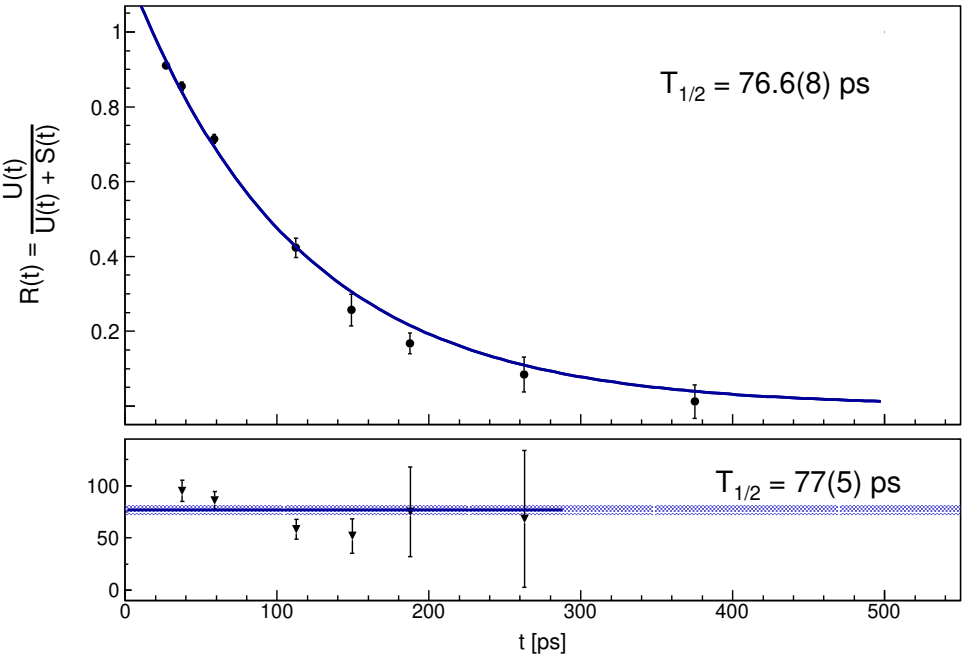

Figure 69: DCM and DDCM fits for the 1397-keV level, decaying through the 751-keV γ ray.

population of this state. For this reason, the discussion of this state will be treated last, while all others are discussed in order of energy.

For all states considered, the analysis procedure is as follows: generating the events, smearing the data to replicate the experimental resolution, applying Doppler correction and calculating the χ^2 value of the simulation with respect to the experimental spectrum in an appropriate energy range. Events generation and smearing have been discussed in §3.4. The χ^2 definition used is the one of Neyman, using the error of the experimental data only. The energy range for the χ^2 calculation has been chosen as a compromise between different necessities. Indeed, the greater statistical difference among simulations of different lifetimes are at the tails of the γ-ray peaks. Therefore, using the full Doppler range ensures that the full probability distribution is considered. On the other hand, random fluctuation of the background might generate statistical differences which increase the χ^2 value even though there should not be. Furthermore, other transitions might be lying near or even in the region of interest. This adds degrees of freedom to the simulation (population of the transition, energy, emission velocity, lifetime) that might decrease the

definition of the minimum of the χ^2 curves. In these cases, it was preferred to restrict the χ^2 calculation in a cleaner range.

The χ^2 minimization procedure can be performed for each target (4, 6 and 30 mg/cm^2 Au backing) and γ ray for which there is enough statistics, providing a set of independent measurements that should be consistent with each other. The curve with minimum χ^2 value has been taken as the most likely value of the measured lifetime. For the confidence interval, the $\min(\chi^2) + 1$ rule has been followed.

Very short lifetimes may fall below the DSAM sensitivity region. Indeed, if the nucleus decay in a very short time with respect to the slow-down process, the difference in lineshape may be too little to be statistically significant, even at the asymptotic limit. This effect is even more severe for limited statistics. This sensitivity region depends in general on the energy of the examined transition, the initial production velocity of the decaying nucleus, the resolution and angular coverage of the detection apparatus, and the target and backing properties. In this work, experimental conditions were optimize to measure lifetimes in the range between 100 and 500 fs, based on the reduced transitions probabilities derived from ^{39}Ar, with γ-ray transitions of energy between 1 and 2 MeV. For lifetimes below or around this limit, no precise lifetime estimate can be given, as the χ^2 curve flatten to a constant value and show a minimum for $\tau \leq$0 fs, which is not physical. In this case, only an upper limit can be given. However, since the χ^2 minimum lies at the boundaries of the allowed region, the likelihood ratio theory's $\min(\chi^2)+1$ rule for the confidence intervals cannot be applied, as half of the interval would fall in the unphysical region. This problem would be circumvented with a Bayesian approach. This is currently still being explored in the context of DSAM measurements [167]. Keeping the frequentist approach, the confidence interval in the instances where the minimum falls at the boundary should be constructed on a case-by-case basis to ensure proper coverage. This is computationally unfeasable. On the other hand, the χ^2 test shows that longer lifetimes, in the range of sensitivity, do not reproduce the experimental spectrum. Therefore, for lack of better alternative, the upper limit for the lifetime of these states is chosen as the one corresponding to $\min(\chi^2) + 2$: this rule does not ensure coverage, but allows to give reasonable (although somewhat arbitrary) limits on the basis of the χ^2.

For the 3441-, 3355-, 3120-, 2978- and 2515-keV states, the statistics collected was not enough to yield meaningful results. No χ^2 trend was observed, and therefore it is impossible with this data to provide an estimate on their lifetime. The same applies to almost the entire dataset collected with the CD_2 target with 30 mg/cm^2 Au backing. Due to the small statistics collected with this target, the population of the levels of interest was not strong, and the χ^2 curves do not show any curvature of statistical significance, i.e. they never surpass the $\min(\chi^2)+1$ level. Only for the 1992-keV state this dataset has been used.

For the 646- and 751-keV levels, the approximate stopping time in 30 mg/cm^2 of gold, at the production velocity (9.84% of c), is 1 ps. Given the half-lives measured in the previous Section, these states fall outside of the sensitivity range of DSAM. Regarding the other states, all results can be found from Figure 70 to Figure 73. They are illustrated on a level-by-level basis in the following. The full list of deduced reduced transition probabilities can be found in Table 21.

1992-keV state

For the 1992-keV state, the χ^2 curve for the two plunger targets, shown in Figure 70 shows only a broad minimum for $\tau > 400$ fs. For lower lifetimes, the χ^2 increase rapidly. This signals that the lifetime of this state is long enough to completely traverse the target and the backing, but not to reach in excited state the ^{181}Ta stopper mounted on the plunger device. Recalling the thickness distribution in Figure 46, the travel time in the 1 mg/cm^2 CD_2 target with 30 mg/cm^2 is about 1 ps. This is consistent with the χ^2 minimization results. Taking the $\min(\chi^2)+2$ rule explained in the beginning of the Section, with the $\min(\chi^2)$ value calculated as the average of all points after the flattening of the curve, this yields a lower bound of $\tau > 0.4$ ps. Assuming, on the other hand, that in order to observe both the shifted and the unshifted components, at least 10% of nuclei should arrive at the stopper in this excited state, the upper bound for this lifetime is 10 ps. This value has been calculated solving Equation 8 (page 13) for τ and evaluating it at the lowest plunger distance acquired, namely 0.7 mm. Combining the two ranges, the final lifetime estimate for this state is 0.4 ps $< \tau <$ 10 ps, or equivalently, 0.3 ps $< T_{1/2} <$ 7 ps.

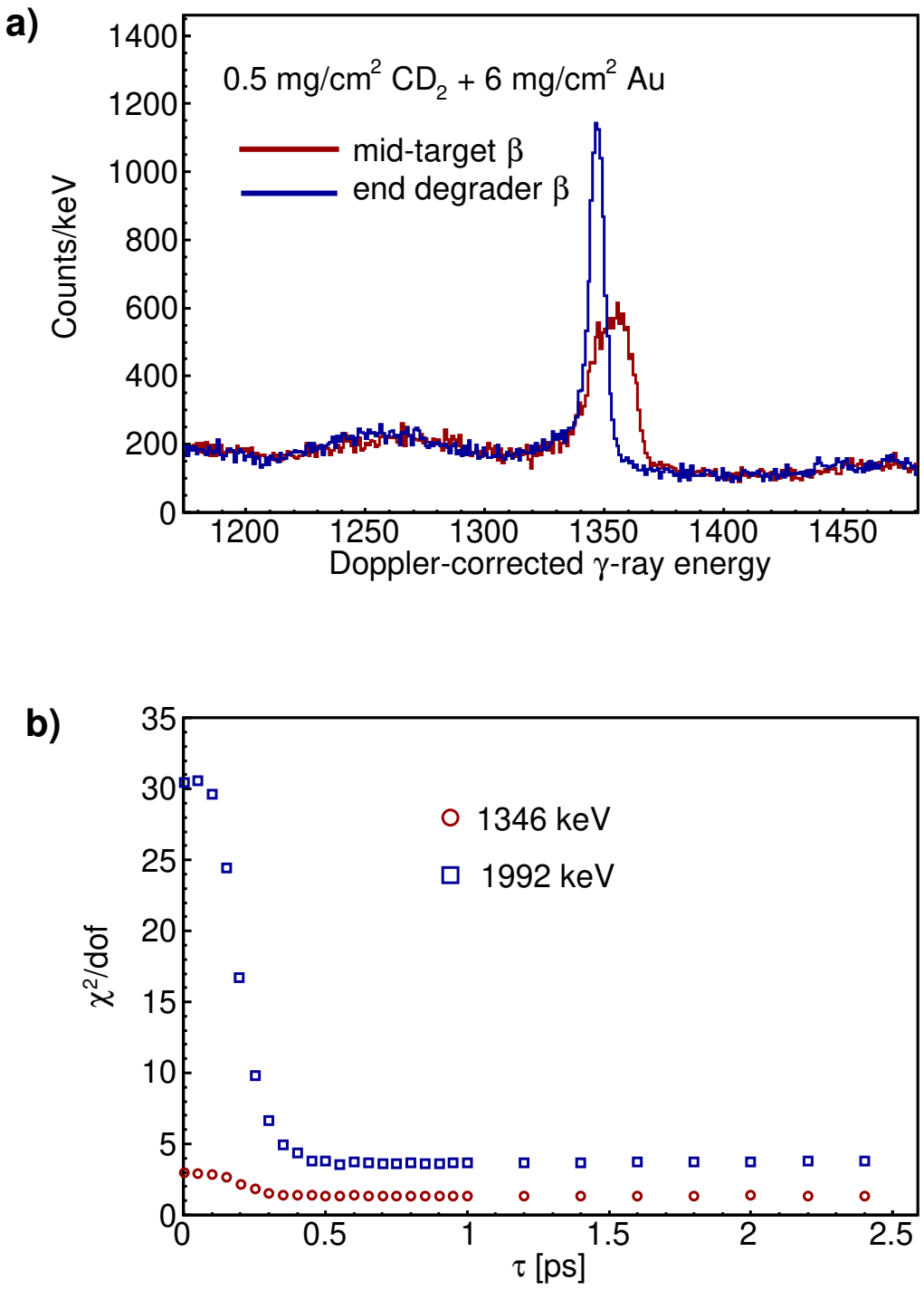

Figure 70: Lifetime measurement of the 1992-keV state. In panel a) the comparison between the Doppler-corrected spectra assuming velocity at mid-target (red) and after the degrader (blue). Since the peak corrected assuming the velocity after the degrader does not show a lineshape, the lifetime of this state is longer than the time ^{37}S ions take to traverse the target and the degrader. In panel b) the χ^2 value as function of the lifetime for the 1346-keV line (red circles) and the 1992-keV line (blue squares).

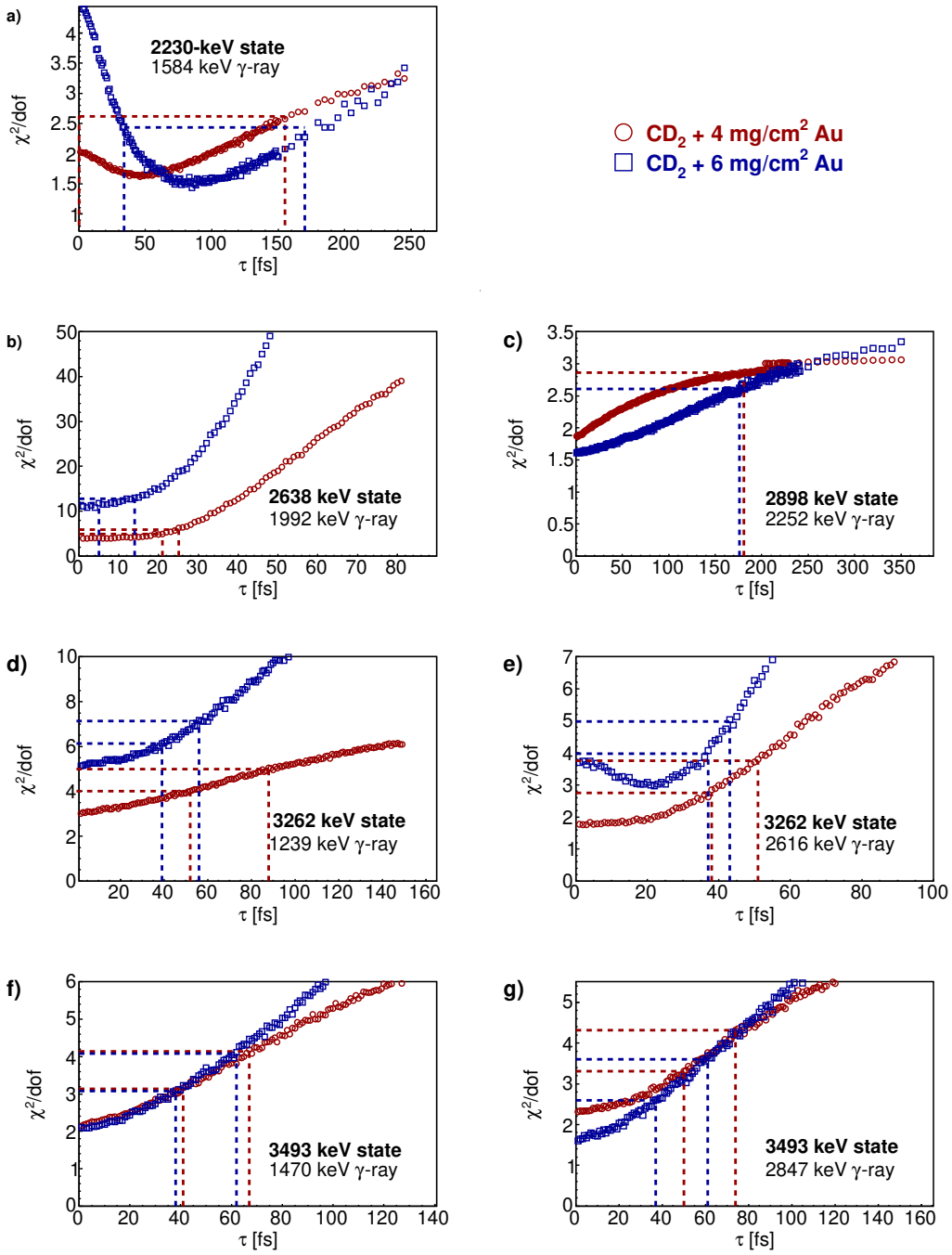

Figure 71: Lifetime measurements with DSAM technique. The normalized χ^2 curves as a function of the lifetime are shown for the a) 2230-, b) 2638-, c) 2898-, d) and e) 3262-, f) and g) 3493-keV state. Data from the target with 4 mg/cm^2 Au backing are indicated with red circles, while from the one with 6 mg/cm^2 gold backing in blue squares. The γ-ray line used in the analysis is indicated in the picture. In the case of the 2230-keV state, the $\min(\chi^2)+1$ level is drawn with dashed lines. In all other cases, dashed lines are drawn for both the $\min(\chi^2)+1$ and $\min(\chi^2)+2$ levels.

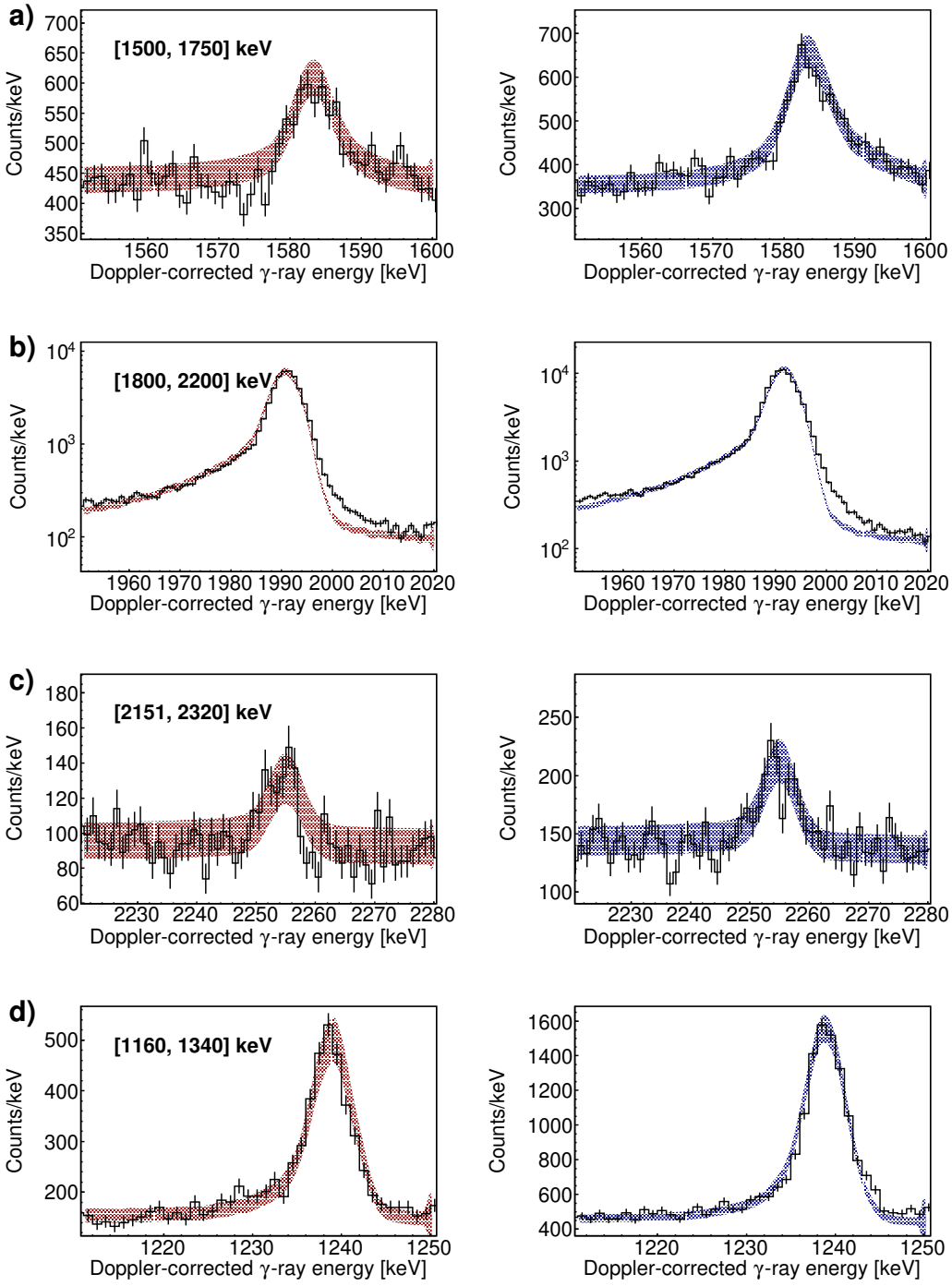

Figure 72: Lifetime measurements with DSAM technique. Comparison between the simulated (shaded areas) and experimental spectrum (black solid line) for the target with 4 mg/cm^2 Au backing (left) and 6 mg/cm^2 Au backing (right). The color code of the simulated spectra (red for the 4 mg/cm^2 Au backing and blue for the 6 mg/cm^2 one) is the same as in Figure 71. States are labeled as in Figure 71. The range for χ^2 calculation (equal for both targets) is reported in parentheses. Continues on the next page.

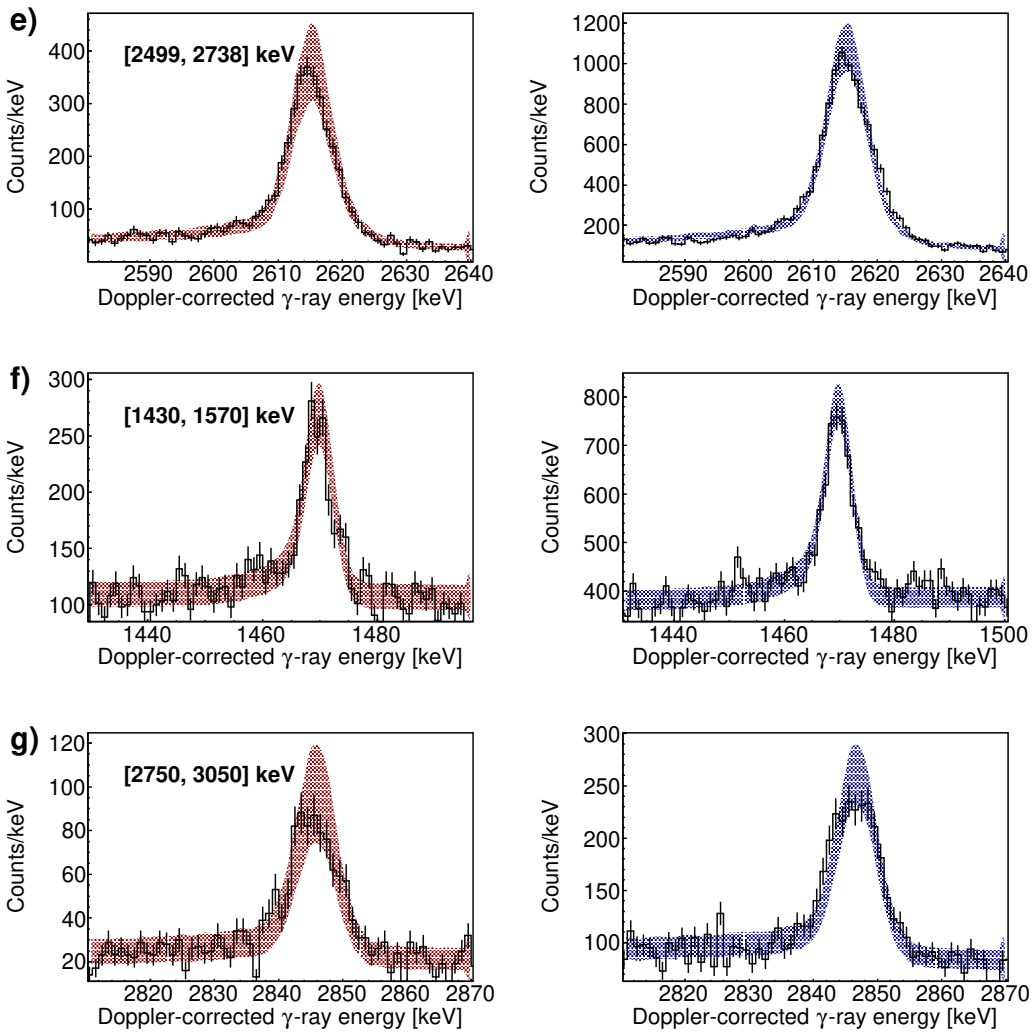

Figure 72: (cont.)

2230-keV state

The χ^2 curve for this state is shown in Figure 71a). This is the only lifetime with minimum not at the boundaries. The 4 and 6 mg/cm^2 Au backings yield lifetimes of 46^{+109}_{-45} and 85^{+85}_{-51} fs, respectively. Equivalently, the half-life estimates are 32^{+75}_{-31} and 59^{+59}_{-35} fs. The two estimates are compatible within errors. The value extracted from the 6 mg/cm^2 Au dataset has the lowest χ^2 value, and therefore is taken as final estimate. The comparison between the simulations at these values and the experimental spectrum can be found in Figure 72a). This state was assigned $1/2^+$ spin in the previous Chapter, thus making the 1584-keV transition to the first-excited $3/2^-$ state purely of E1 character. A B(E1) $= 2(1)\cdot10^{-3}$ W.u. value would then be deduced. Taking the most probable value obtained, this would correspond to a fairly enhanced E1 transition.

2638-keV state

This level, as mentioned in the previous Chapter, is one of the most populated, as it is the main fragment of the $p_{1/2}$ shell. Its decay to the $p_{3/2}$ fragment would then be a spin-flip M1 transition. Indeed, the lifetime obtained for this state is below the experimental sensitivity (see Figure 71b)). The high values of χ^2 obtained mostly come from contributions on the right wing, as it can be seen from Figure 72b). The excess of counts at ∼2010 keV, observed in both targets, cannot be reproduced by a longer lifetime, and is suspected to be of tracking origin, most probably because of the mis-identification of the first interaction point. Since this is the most populated line emitted by a state with lifetime in DSAM range, the high-energy tail component might not have been modeled correctly for lack of experimental points to have a meaningful physical trend. If this was the case, the given estimate, $\tau < 13$ fs, or equivalently $T_{1/2} < 9$ fs, would be overestimated with respect to the actual one. Since it is however below the experimental sensitivity, the problem has not been pursued further. Worth of notice is the 1241-keV decay to the 1397-keV state, which would have a transition probability of B(E1) $> 5 \cdot 10^{-4}$. This lower limit is about one order of magnitude larger than the value obtained for the 751-keV $3/2^+_1 \rightarrow 3/2^-_1$ transition, and about the same order of the $1/2^+ \rightarrow 3/2^-$, suggesting a similar enhancement.

2898-keV state

The χ^2 curve for the lifetime of this state can be found in Figure 71c). For both targets, the minimum of the χ^2 seems to lie at null lifetime, indicating no sensitivity, but due to the small statistics of the peak results are not conclusive. The simulations at 1 fs are compared to the experimental spectrum in Figure 72c). A noticeable double-peak structure can be noticed in the dataset for both targets. Due to the low statistics, it cannot be ruled out that this structure is purely due to statistical fluctuation. The $\min(\chi^2)+1$ and $\min(\chi^2)+2$ limits are 95 and 120 fs for the 6 mg/cm^2 Au backing target, while for the 4 mg/cm^2 Au target the $\min(\chi^2)+1$ limit lies at 138 fs, while the $\min(\chi^2)+2$ limit lies outside of the simulated range. Assuming that the linear trend of the curve continues at higher lifetimes, this limit should lie at 360 fs, which is given as upper limit. The corresponding half-life limit is therefore $T_{1/2} < 250$ fs.

3262-keV $3/2_2$ state

Out of the many decay branches of this state, only two are viable to measure the lifetime of this state, namely the 1239- and 2616-keV transitions. From the χ^2 curves in Figure 71d) and e), it can be observed that all targets and transitions show a minimum for null lifetime, meaning that the lifetime is too short to be measured with this technique, except for the curve based on the 2616-keV transition and the 6 mg/cm^2 Au backing target, which shows minimum at about 30 fs barely below statistical significance. As no other curve shows a minimum for such lifetime, it cannot be ruled out that it is purely due to statistical fluctuations. The comparison between simulations at 1 fs and the experimental spectrum can be found in Figure 72d) and e). The $\min(\chi^2)+2$ levels are 75 and 59 fs for the 1239-keV transitions and the 4 and 6 mg/cm^2 Au backing respectively. For the 2616-keV peak, the $\min(\chi^2)+2$ levels are instead 46 and 51 fs. Since the lowest χ^2 value is obtained for the 2616-keV and the 4 mg/cm^2 combination, this value is taken as the most representative. The upper limit that is drawn from these data is therefore $\tau <$51 fs, or, equivalently, $T_{1/2} <$35 fs. The deduced matrix elements for this state can be found in Table 21. The strongest decay of this state is the 2616-keV γ-ray transition to the first excited 646-keV state. The lower limit for the B(E2) suggests a fairly collective transition. The second strongest branch is instead to the intruder 2023-keV state. However, if we assume that this state has $7/2^-$ spin, then the

E2 transition probability would most likely exceed 400 W.u., which is a value well above any other transition in this region. This fact casts some doubts on the correctness of the spin assignment of the 2023-keV state. If the spin assignment for this state was switched to $5/2^-$, then the M1 character would also be possible, and actually dominate the decay with a value of 0.2 W.u., in fair agreement with other M1 decays in the region.

Spin assignments come from the ^{36}S(pol d, p) experiment of Eckle *et al.* [66]. Attribution of L and J values has been made based on proton angular and asymmetry distributions. In particular, the 646-, 1992-, 1397-, 2638-, 3262-, and 3493-keV states have definite spin assignment due to the clarity of the experimental distributions. On the other hand, Eckle *et al.* recognize that, due to the experimental conditions, the asymmetry distributions for states with L>1 are quite "structureless". A symptomatic case of this is the wrong reproduction of the asymmetry distribution of the ground state, which suggests $5/2^-$ spin attribution, in contrast with the measured spectroscopic factor. Spin assignments for the L=3 levels have been given therefore, according to the authors, based on the degree of similarity they recognized with the asymmetry distribution of the ground state. These are in particular the case of the 2023-, 2515- and 3441-keV states. Since no firm experimental evidence has been established for the J, both spin orbit partners, i.e. $(5/2, 7/2)^-$ are possible.

The measured lifetime for the 3262-keV state (and later, of the 3493-keV state) clearly rules out the possibility of a $7/2^-$ spin attribution for the 2023-keV state.

3493-keV state

To measure the lifetime of this state, the two strongest branches, at 1470 and 2847 keV, were used. The χ^2 curves are shown in Figure 71f) and g). All results converge to a lifetime below sensitivity. The comparison between the simulated transition assuming 1 fs lifetime and the experimental spectrum can be found in Figure 72f) and g). The $\min(\chi^2)+1$ and $\min(\chi^2)+2$ levels for the 4 mg/cm^2 Au backing are at 146 and 260 fs, and 43 and 64 fs for the 1470-keV line, with the 4 and 6 mg/cm^2 Au backing respectively, and 64 and 107 fs, and 43 and 64 for the 2847-keV transition. The 2847-keV and 4 mg/cm^2 has the

lowest χ^2 value among the considered ones, therefore the upper value given to this state is τ <107 fs, or equivalently $T_{1/2} < 74$ fs.

Assuming spin $7/2^-$ for the 2023-keV state, the pure E2 1470-keV decay branch of this level would have a transition probability greater than 90 W.u.. Even though not exceptional as the 1239-keV decay from the 3262-keV level, this would make this transition one of strongest of the sd shell. If instead the spin of the 2023-keV state was $5/2^-$, also the M1 character would be allowed, and the respective transition probability (assuming pure character) would be greater than 0.05 W.u, in line with other M1 transitions in this nucleus. This fact is further reassurance of the hypothesis of an incorrect spin assignment.

2023-keV state

This level is not observed in direct population. Its only observation is from the decay of the 3262- and 3493-keV levels through the 1239- and 1470-keV γ rays. Due to the difference in spectroscopic factors and the rapidly dropping SPIDER efficiency, most of the population of the 2023-keV state comes from the decay of the 3262-keV level, rather than the 3493-keV one. Suppressing one of the two branches is fundamental in order to constrain the degrees of freedom of the simulation and improve χ^2 convergence, as only an upper limit can be given for the lifetime of these two states. This suppression has to be performed with more restrictive conditions on excitation energy, as the use of a γ-γ matrices reduces the available statistics to a few tens of counts. The 2616- and 1239-keV lines of the 3262-keV state are not visible above 3.65 MeV of excitation energy. On the other hand, the 1470- and 2847-keV lines of the 3493-keV state are not visible below 3.3 MeV of excitation energy. It is reasonable then to assume that the components of the 2023- and 1377-keV lines that lie below 3.25 MeV and above 3.7 MeV of excitation energy come from the sole decay of the 3262- and 3493-keV levels, respectively, while the decay coming from the other state is negligible. This cut comes at high cost of statistics, but otherwise the lifetime of this state would be dependent on the unknown SPIDER efficiency at high excitation energy. This cut cannot be performed in the dataset using the 30 mg/cm^2 Au backing, as this line is too weakly populated. This dataset therefore is excluded from the analysis. From the previous paragraphs, the half-lives of the 3262- and 3493-keV states have been bound by the upper limits of 23 and 70 fs. Two series of simulations have

been performed: one assuming the upper limit for the lifetime of the feeding state, one assuming instead a lifetime of 1 fs. The lifetime of the 2023-keV state then was varied from a range of 1 fs to 300 fs. For the 3493-keV state, the statistics obtained (less than 100 counts) after the cut was too low to produce meaningful χ^2 results. The χ^2 curve calculated had the same features of the one assuming feeding from the 3262-keV state, but the curvature was not steep enough to surpass the required $\min(\chi^2)+1$ or $\min(\chi^2)+2$ levels. The results of the analysis for the 3262-keV feeder can be found in Figure 73.

As expected, the lifetime measured assuming 1 fs lifetime for the 3262-keV state is longer than the one assuming its maximum value. In fact, while assuming 1 fs feeder lifetime the χ^2 curve shows a minimum around 55 fs for both targets, assuming the maximum value of the feeder lifetime the χ^2 curve does not show a minimum in the boundaries of the parameter for both targets, suggesting again that the lifetime of this state is below the experimental sensitivity. The $\min(\chi^2)+2$ levels lie both at approximately the lifetime of the feeder state, further reassurance of the correctness of the estimation. The curve with minimum χ^2 value, namely the 6 mg/cm^2 Au backing target with 51 fs feeder lifetime, yields the upper limit $\tau < 67$ fs, or equivalently $T_{1/2} < 47$ fs. As the value obtained is fairly close to the upper value for the lifetime of the 3262-keV state, it seems that the lifetime of the 2023-keV state is lower or at most comparable to the lifetime of the feeder state.

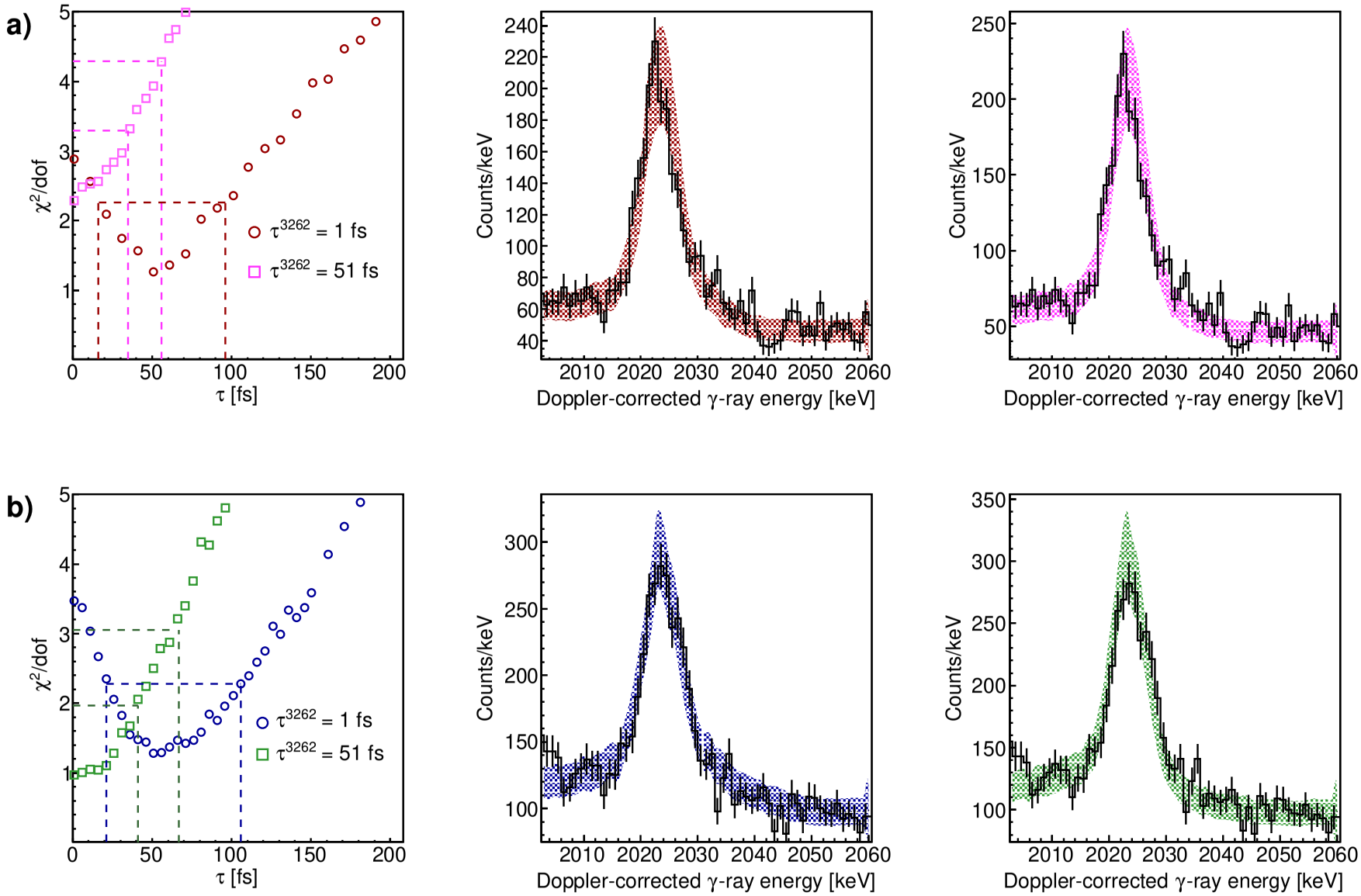

Figure 73: Lifetime measurement of the 2023-keV state. In panel a) the dataset with the 4 mg/cm^2, in b) with the 6 mg/cm^2 Au backing target. In the left panels, the χ^2 curves assuming different lifetimes for the feeder 3262-keV state. In a) results assuming 1 fs feeder lifetime are in red circles, 51 fs in magenta squares, in b) blue circles and green squares. Dotted lines in matching color show the $\min(\chi^2)+1$ and $\min(\chi^2)+2$ levels. In the central panels, the comparison between experimental spectrum and lifetime at minimum χ^2 assuming no feeder lifetime. In the right panels, the same in the middle panels but assuming feeder lifetime of 51 fs. Color code in both reflects the one of the left panels.

E_i	J^π	$T_{1/2}$	E_f	J^π	E_γ [keV]	B(E1) 10^{-4} e^2fm^2	B(E1) 10^{-4} W.u.	B(E2) e^2fm^4	B(E2) W.u.	B(M1) 10^{-2} μ_N^2	B(M1) 10^{-2} W.u.
646	$3/2^-$	117.2(5) ps	0	$7/2^-$	646	–	–	42.9(2)	5.90(3)	–	–
1397	$(3/2)^+$	77(5) ps	646	$3/2^-$	751	0.134(9)	0.19(1)	–	–	–	–
1992	$3/2^-$	0.3 ÷ 7 ps	646	$3/2^-$	1346	–	–	13 ÷ 135	1.8 ÷ 43	0.17 ÷ 4	0.1 ÷ 2
			0	$7/2^-$	1992	–	–	0.7 ÷ 17	0.1 ÷ 2	–	–
2023 †	$5/2^-$	<47	646	$3/2^-$	1377	–	–	>750	>100	>10	>6
			0	$7/2^-$	2023	–	–	>230	>31	>7	>3.5
2230	$1/2^+$	59^{+43}_{-35}	646	$3/2^-$	1584	20^{+10}_{-20}	30^{+20}_{-30}	–	–	–	–
2638	$1/2^-$	<9	646	$3/2^-$	1992	–	–	>1940	>270	>50	>30
			1397	$(3/2)^+$	1241	>5	>7	–	–	–	–
2898	$(5/2^-)$	<250	646	$3/2^-$	2252	–	–	>29	>4	>1	>0.6
			0	$7/2^-$	2898	–	–	>1	>0.1	>0.06	>0.06
3262	$3/2^-$	<35	646	$3/2^-$	2616	–	–	>70	>10	>3	>2
			2023	$(5/2)^-$	1239	–	–	>1800	>250	>20	>10
			1992	$(3/2)^-$	1270	–	–	>250	>35	>3	>1.5
			1397	$(3/2)^+$	1865	>0.4	>0.5	–	–	–	–
			0	$7/2^-$	3262	–	–	>1.1	>0.15	–	–
3493	$3/2^-$	<74	2023	$(5/2)^-$	1470	–	–	>620	>85	>9	>5
			646	$3/2^-$	2847	–	–	>15	>2	>0.9	>0.5
			0	$7/2^-$	3493	–	–	>0.5	>0.07	–	–

† original spin assignment of Eckle *et al.* is $7/2^-$, proposed here is $5/2^-$

Table 21: Deduced reduced transition probabilities. Energies are in keV, half-lives measured in this work in fs (except when noted). For comparison, 1 W.u. in ^{37}S equals 0.712 e^2fm^2, 7.3 e^2fm^4 and 1.77 μ_N^2. Where mixed M1/E2 transitions are present, the reduced transition probabilities are deduced in the two limits of pure M1 and pure E2 transition.

6 Comparison with Shell Model and discussion

In the previous Chapters, several states of ^{37}S have been discussed and spin assignments, based on their decay pattern and spectroscopic factor, have been proposed. In this Chapter, these results are compared to the predictions of shell-model calculations and the excitation spectrum of the isotone ^{39}Ar.

In the latter case, namely the ^{39}Ar excitation spectrum, all results are taken from the Evaluated database [47]. In the former, shell-model calculations with the *sdpf-u-mix* interaction were performed by Prof. A. Poves (UAM) [48], and with the *sdpf-u* interaction by A. Gottardo (INFN-LNL). These calculations were performed with the *m*-scheme code ANTOINE and the coupled-scheme code NATHAN, respectively. Excited states energies and reduced transition probabilities were obtained with both interactions. Spectroscopic factors were only calculated with the *sdpf-u* interaction and the Lanczos strength function method.

As mentioned in the introduction, the *sdpf-u* interaction was not tuned to reproduce intruder levels near the N=20 IoI. This shortcoming is instead addressed by the *sdpf-u-mix* interaction, which provides excellent prediction capabilities not only in the N=20 region, but also its mirror at Z=20 (see Valiente Dobón *et al.* [168] and Lalanne *et al.* [169]). Therefore, it can be expected that the transitions connecting single-particle and intruder states in ^{37}S are reproduced with the *sdpf-u-mix*, but not with the *sdpf-u*. On the other hand, if the low-energy spectrum is dominated by the single-particle structure, one might expect that excitation energies and reduced transition probabilities are approximately reproduced already by the *sdpf-u* interaction. The comparison between the two interactions might therefore give additional insight on the role played by the proximity of the IoI in building the low-energy spectrum of this nucleus. The full set of reduced transition probabilities and occupation numbers using the *sdpf-u-mix* interaction can be found in A2, while the spectrum can be found in Figure 74.

The Chapter is organized as follows: in Section 6.1, states with high experimental spectroscopic factor (>0.05) are discussed. As much of the single-particle strength of the *f* and *p* shells, above N=20, should be contained in these states, they should be correctly reproduced by both interactions and their assignment should be unambiguous.

In the following Section 6.2, states with small measured spectroscopic factor are discussed. *A priori*, it is difficult from the low magnitude of the spectroscopic factor alone to discriminate between "normal" and intruder states, as it indicates a small overlap between the observed state and a $^{36}S(0_1^+) \otimes \nu$ configuration. On the other hand, reduced transition probabilities are sensitive to variations in the wavefunction components, even small. Hence, the combined measurement of transition probabilities and spectroscopic factor can achieve a better understanding of the microscopic nature of these states. In particular, the assignment of the spin $3/2^-$, $5/2^-$ and $7/2^-$ states is illustrated, as the measurement of the lifetimes of the negative parity intruders at 1992 and 2023 keV was the main goal of the experiment.

In light of the proposed assignments, Section 6.2.3 will re-examine the question posed in Chapter 1, on whether there is or not an increase in mixing in the low-lying intruder states of ^{37}S with respect to ^{39}Ar. This Section contains the main physics contribution of this work.

In the last Section, the remaining observed states, for which almost only branching ratios were measured, will be discussed.

Synoptic tables will report all values compared in the text. However, in order to fairly compare calculated values and experimental results, some elaborations were applied to the bare predicted values. Calculated spectroscopic factors were quenched by a factor 0.7 [31, 170]. Half-lives were calculated assuming for all decays the transition elements calculated by the interaction, but using the experimentally observed energies. Since no mixing ratio is measured in ^{37}S, in case of mixed M1/E2 transitions there is no way to obtain the true reduced probability values. On the other hand, shell-model calculations give reduced transition probabilities, and the mixing ratio can be deduced from them via the same equation. The calculated mixing ratio $|\delta|$ is indicated in the tables as well. Throughout the text, when comparing reduced transition probabilities, the experimental values are scaled by the shell-model calculated

mixing ratio. Therefore, the values in the Tables in this Chapter are different from the ones presented in Table 21, which were derived in the two limits of pure character. While there is no guarantee that this value is correct, it is the best approximation currently available. When the mixing ratio in ^{39}Ar has not been measured, they will be multiplied by the mixing ratio calculated for analogue transition in ^{37}S. All reduced transition probabilities are given in Weisskopf units.

Particularly different values, which are commented in the text, are highlighted in bold characters in the Tables.

The assignment for these states is discussed in the text. A table containing the major wavefunction component can be found at the end of the Chapter, in Table 27. Next to the component, the associated probability calculated by the interaction is reported, i.e. if the state wavefunction $|\Psi\rangle$ can be decomposed in a weighted sum of $|\psi_i\rangle$ configurations, $|\Psi\rangle = \sum_i \alpha_i |\psi_i\rangle$, with $\sum_i |\alpha_i|^2$=1, then the associated probability of the configuration i is given by $|\alpha_i|^2$.

6.1 High spectroscopic factor states

Four states with high spectroscopic factor (>0.05) are observed below 3.5 MeV: these are the ground, 646-, 2638-, and 3262-keV states. Analogously, both interactions also predict four 1p0h states with high spectroscopic factor, with $7/2^-$, $3/2^-$, $1/2^-$ and $3/2^-$ spin, respectively. Given the measured angular distribution and spectroscopic factors, the assignment as fragments of the $f_{7/2}$, $p_{3/2}$ and $p_{1/2}$ strength is unambiguous.

The comparison between the properties of each state can be found in Table 22. As it can be seen, the agreement between the calculations (with both *sdpf-u* and *sdpf-u-mix*) and the experimental evidence, and between the excitation spectrum of ^{39}Ar and ^{37}S is fair across all states. Indeed, as it was already noticed by Grocutt *et al.* [72], the *sdpf-u* interaction is already able to reproduce correctly the decay properties of these states, as their bulk properties are determined by the large single-particle component. Therefore, the removal of two protons does not drastically change the strength distribution or the mixing of these states, and this fact is reflected in the predictions of the *sdpf-*

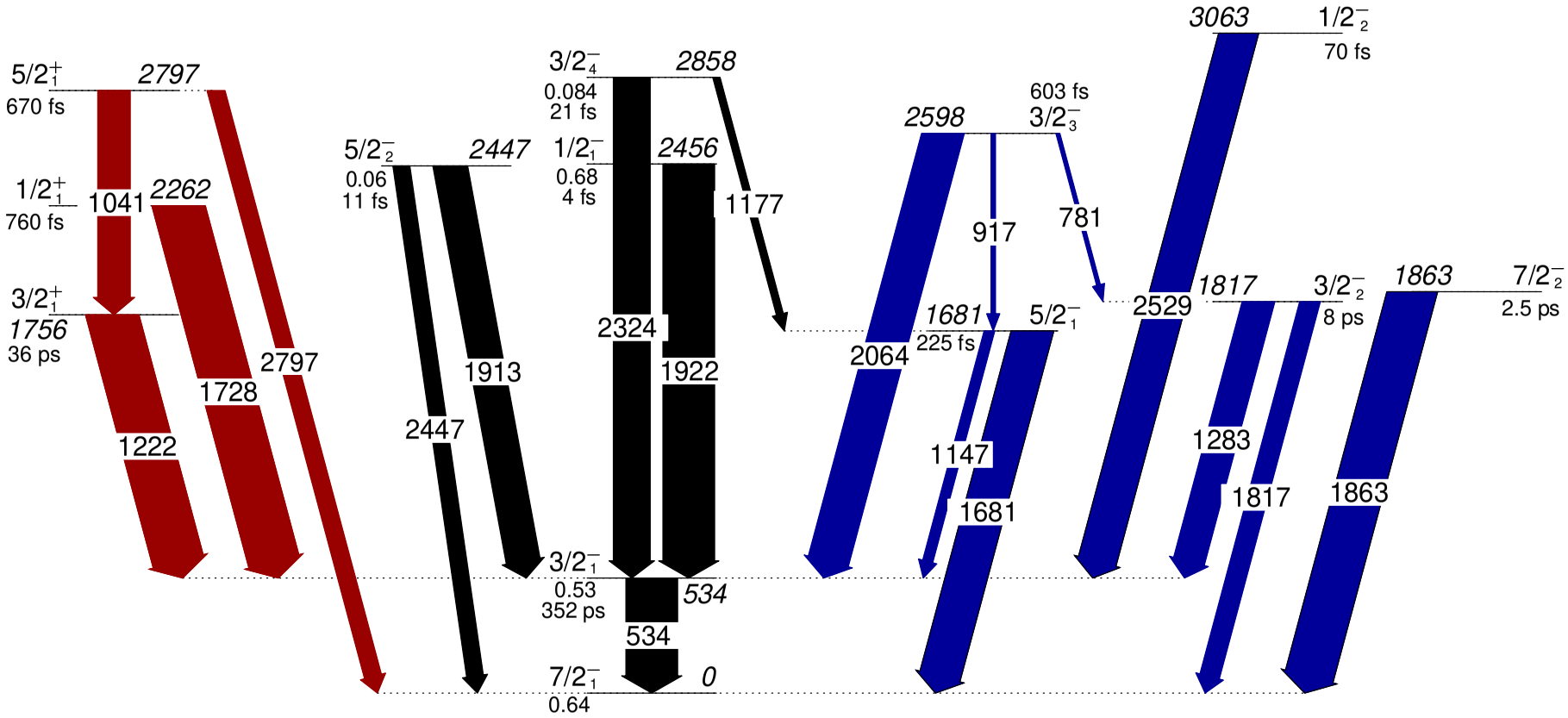

Figure 74: Shell-model calculations for the low energy spectrum of ^{37}S. with the *spdf-u-mix* interaction. Arrow width is proportional to the branching ratio. Only decays with BR $> 5\%$ are represented. Color code and band organization is: left band, in red color, positive parity intruder states; central band and black color, single-particle states; right band and blue color, odd parity intruder states. Spectroscopic factors of the single-particle states calculated with the *sdpf-u* interaction. Near the level, the half life predicted by the *sdpf-u-mix* interaction is also written.

u-mix interaction. On the other hand, as highlighted already by Chapman *et al.* [71] and Wang *et al.* [74], configurations different than single-particle one are already present in the ground state. Indeed, no wavefunction calculated by the *sdpf-u-mix* interaction is pure with more than 70% probability (see Table 27). Most of the residual wavefunction comes from the mixing with the 3291-keV 2^+ state of ^{36}S already at low energy. The contribution of intruder 3p2h configurations is predicted to be around 10% for each state.

Regarding the $1/2^-_1$ state, the main $p_{1/2}$ fragment, while the main decay is predicted to be to the first excited $3/2^-$ state, the mixing ratio predicted by the interaction points towards an almost pure M1 transition, while in ^{39}Ar the transition has a strong E2 component. The 1241-keV $1/2^- \rightarrow 3/2^+$ E1 decay, observed for the first time in this experiment, has a rather large strength, two orders of magnitude larger than the one of the $3/2^+ \rightarrow 3/2^-$ decay (which will be reported in the next Section). The transition is two-body, thus forbidden at first order for a one-body operator, but could be enhanced by the $\Delta L = \Delta J = 1$ $p_{3/2} \rightarrow d_{5/2}$ component, or possibly by the presence of configurations coupled to the 1^+ state of ^{36}S, located at 4526 keV. A 6% probability of the $1^+ \otimes p_{3/2}$ is predicted by the *sdpf-u* calculations in the wavefunction of the $1/2^-$ state. This transition was not observed in ^{39}Ar.

The spectroscopic factor of the second $p_{3/2}$ fragment, at 3262 keV, is well reproduced, although slightly overestimated, by the *sdpf-u* interaction. Furthermore, there is difference of about a factor two with respect to the analogue state ^{39}Ar, hinting that some of the $p_{3/2}$ strength might have been transferred to other states. The main decay branch predicted by the *sdpf-u* and the *sdpf-u-mix* is the one to the first $p_{3/2}$ fragment, the 646-keV state, consistently with experimental evidence. Despite the large errors in the lifetime estimate of the ^{39}Ar state, the decay to the first excited state is about one to two orders of magnitude weaker than the corresponding decay in ^{37}S.

Furthermore, in ^{37}S this state has strong decay branches to the intruder states, which occupy a sizeable portion of the branching ratio. This is reflected in the shell-model calculations, which also predict decays with sizeable branches to a $5/2^-$ and $3/2^-$ intruder states. The *sdpf-u* interaction is not able to reproduce these branches. The observed transitions to the 1992- and 2023-keV states determines their assignment. Their nature is discussed further in the next sections.

Overall, from the comparison between the results of the two interactions and the experimental results of this work, it can be observed that in order to get accurate reproduction of the high spectroscopic factor states the inclusion of the IoI is not necessary, as the predictions obtained through the *sdpf-u* interaction are equal to the ones of the *sdpf-u-mix*. The low-energy sigle-particle states of ^{37}S are therefore dominated by the single-particle component, with little to no mixing with intruder configurations. The only exception is the 3262-keV state, which exhibits strong decays to intruder configurations which are not reproduced by the *sdpf-u* interaction. On the other hand, the *sdpf-u-mix* interaction predicts that about 10% of the ground-state wavefunction is of intruder origin already at Z=16.

6.2 Small spectroscopic factor states

In total, the *sdpf-u-mix* interaction predicts the existence of five positive parity and five negative parity intruder states. This Section discusses the assignment of these states. The assignment of the positive parity states is discussed first, as these have distinctive decay patterns that allows a rather unambiguous identification. The assignment of negative parity states will then be discussed, first examining the $3/2^-_2$ intruder state at 1992-keV, then the 2023- and 2898-keV, which were suggested to have $5/2^-$ spin in the previous Chapter. The assignment of the $5/2^-$ states in this nucleus shows that these states have such similar properties that the experimental fingerprints used to discriminate single-particle from intruder configurations are not reliable.

As mentioned in the beginning of the Chapter, Section 6.2.3 builds on the discussion of the negative parity states assessing whether or not, based on the data collected, there is an increase in mixing in the low-energy excitation spectrum of ^{37}S with respect to ^{39}Ar.

The following Section discusses the assignment of the 3493-keV state, which was shown to be a state with fairly high spectroscopic factor that, on the other hand, decays preferentially to intruder configurations. The last Section discusses other tentative assignments of states for which the lifetime has not been measured, but could be identified thanks to their branching ratio.

$7/2^-_1$ ground state				
	^{37}S exp	*sdpf-u-mix*	*sdpf-u*	^{39}Ar
S [%]	65(4)	–	59	62.5

646-keV $3/2^-_1$ state					
		^{37}S exp	*sdpf-u-mix*	*sdpf-u*	^{39}Ar
	E [keV]	646	534	516	1267
	$T_{1/2}$	117.2(5) ps	136 ps	140 ps	<0.5 ns
	S [%]	43.8$^{\#}$	–	53	52.5
	E [keV]	646	534	516	1267
$\rightarrow 7/2^-_1$	BR [%]	100	100	100	100
	B(E2) [W.u.]	5.90(3)	5.0	4.9	>0.04

2638-keV $1/2^-_1$ state					
		^{37}S exp	*sdpf-u-mix*	*sdpf-u*	^{39}Ar
	E [keV]	2638	2456	2352	3266
	$T_{1/2}$ [fs]	<9	4	4	<48
	S [%]	43.8	–	53	52.5
	E_γ [keV]	1992	1922	1836	1998
	BR [%]	98.0(9)	99.7	99.6	97.9(3)
$\rightarrow 3/2^-_1$	B(M1) [W.u.]	>0.3	0.74	0.8	$>1.2 \cdot 10^{-4}$
	B(E2) [W.u.]	>0.9	2.18	1.9	>45
	$\lvert\delta\rvert$	–	**0.06**	**0.05**	**16(6)**
	E_γ [keV]	1241	700	-44†	–
$\rightarrow 3/2^+_1$	BR [%]	2.03(7)	0.3	0.4	–
	B(E1) [W.u.]	$>7 \cdot 10^{-4}$	$2.3 \cdot 10^{-4}$	$3.7 \cdot 10^{-4}$	–

$^{\#}$ Value fixed in the present experiment as normalization for all others. Taken from Eckle *et al.* [66], who quote 15% error due to uncertainties in the global potentials.

† E_γ <0 means the final state is predicted higher in energy, B(σL) given are however B(σL$\downarrow$).

Table 22: Comparison between the obtained data, interaction predictions and decay properties of ^{39}Ar: single particle states with high spectroscopic factor. Dashes throughout the last column are put if the analogous transition is unobserved in ^{39}Ar. Reduced transition probabilities of ^{37}S M1/E2 transitions are deduced from the lifetime assuming mixing ratio predicted by the *sdpf-u-mix* interaction. Continues in the next page.

3262-keV $3/2^-_3$ state

		^{37}S exp	*sdpf-u-mix*	*sdpf-u*	^{39}Ar
	E [keV]	3262	2858	2844	2632
	$T_{1/2}$	<35 fs	15 fs	14 fs	$0.7^{+1.0}_{-0.4}$ ps
	S [%]	**5(2)**	–	**13**	**18**
$\rightarrow 7/2^-_1$	E [keV]	3262	2858	2844	–
	BR [%]	2.7(2)	5	9	–
	B(E2) [W.u.]	>0.15	0.95	1.24	–
$\rightarrow 5/2^-_1$	E_γ [keV]	1239	1177	-794†	539
	BR [%]	33.7(6)	15	4	81(2)
	B(M1) [W.u.]	>0.1	0.095	0.03	0.16^{+10}_{-16}
	B(E2) [W.u.]	**>0.3**	**0.26**	**1.4**	
	$\lvert\delta\rvert$	–	0.03	0.14	0.07(14)
$\rightarrow 3/2^+_1$	E_γ [keV]	1865	1102	448	1114
	BR [%]	2.3(2)	0.1	0.8	13(1)
	B(E1) [W.u.]	$>5\cdot10^{-5}$	$2.4\cdot10^{-5}$	$5\cdot10^{-5}$	$8^{+5}_{-8}\cdot10^{-5}$
$\rightarrow 3/2^-_2$	E_γ [keV]	1270	1041	-1217†	–
	BR [%]	5.3(2)	2	13	–
	B(M1) [W.u.]	**>0.015**	**0.02**	**0.1**	–
	B(E2) [W.u.]	**>0.6**	**0.69**	**0.06**	–
	$\lvert\delta\rvert$	–	0.13	0.02	–
$\rightarrow 3/2^-_1$	E_γ [keV]	2616	2324	2328	1365
	BR [%]	55.9(8)	72	68	5.7(8)
	B(M1) [W.u.]	**>0.02**	**0.06**	**0.06**	$\mathbf{7^{+4}_{-7}\cdot10^{-3}}$
	B(E2) [W.u.]	**>0.14**	**0.43**	**0.23**	$\mathbf{0.02^{+0.01}_{-0.02}}$
	$\lvert\delta\rvert$	–	0.12	0.09	–

† E_γ <0 means the final state is predicted higher in energy, B(σL) given are however B(σL$\downarrow$).

Table 22: (cont.)

6.2.1 The positive-parity intruder states

Below 3.5 MeV, the *sdpf-u-mix* interaction predicts that positive parity states are composed mainly of 2p1h configurations, with small admixtures of 4p3h excitations. The assignment of the 1397- and 2230-keV states to their counterpart in ^{39}Ar and the *sdpf-u-mix* predictions was based on the fact that they are the lowest states of positive parity and the same spin. The comparison can be found in Table 23.

Regarding the $3/2^+_1$ state, the strength of the decay to the first-excited $3/2^-$ level is reproduced by the interaction, and is found almost identical to the one of the analogue decay in ^{39}Ar. However, in the latter, the $3/2^+$ state shows an M2/E3 decay to the ground state that is not observed in ^{37}S. Assuming the strength of this transition in ^{37}S is the same of the analogue in ^{39}Ar, this 1397-keV decay would have approximately 2% branching ratio and would not have been observed in this dataset. The wavefunction of this state, as reported in Table 27, is fairly fragmented, with the dominant component with only 30% probability. This component shows a neutron promoted from the $d_{3/2}$ shell to the $f_{7/2}$ orbital. The transition to the first excited state can only proceed via the lowering of two neutrons from the $f_{7/2}$ shell to the $p_{3/2}$ and $d_{3/2}$ orbitals, thus justifying the high suppression of this decay.

The large error band on the lifetime of the 2230-keV $1/2^+$ state do not allow to quantify how well it is reproduced by the interaction, or the resemblance with its ^{39}Ar counterpart. It has to be noticed, however, how the $1/2^+ \rightarrow 3/2^-$ transition might be enhanced by one order of magnitude with respect to the $3/2^+ \rightarrow 3/2^-$ decay, probably due to the presence of a $\Delta L{=}\Delta J{=}1$ $s_{1/2} \rightarrow p_{3/2}$ component. The wavefunction of this state is fairly fragmented, with the dominant component (reported in Table 27) contributing only by 15%. The same enhancement seems to be present in the 1241-keV $1/2^- \rightarrow 3/2^+$ decay. This component would be absent in the $3/2^+ \rightarrow 3/2^-$ transition, thus showing a suppressed strength.

For the 3355-keV level, lacking reduced transition probabilities, only decay branches can be compared. Assigning this state to the $3/2^+_2$ state does not reproduce the equally-split branching ratio observed experimentally. Agreement can only be recovered by artificially increasing the E1 matrix element

by one order of magnitude. Since the calculated probability is of the order of 10^{-6}, a disagreement by one order of magnitude is not unlikely. With this change, the predicted lifetime for this state decreases from 500 to 300 fs. It is unclear the location of the corresponding state in ^{39}Ar, for the lack of γ-ray decay information and uncertain spin assignments.

6.2.2 The low-lying $3/2^-$ intruder state

The 1992-keV state has been identified as intruder as early as in 1988, with the calculations of Warburton and Becker [162].

The counterpart of this state in ^{39}Ar is the 2433-keV state, as it is the lowest $3/2^-$ state of low spectroscopic factor. With the given limits, ^{37}S agrees with both ^{39}Ar and *sdpf-u-mix* values. On the other hand, the results of the *sdpf-u-mix* do not agree with the measured transition probabilities in ^{39}Ar. For the branch to the ground state, both *sdpf-u-mix* and ^{39}Ar show similar strength values, indicating a smooth strength evolution with the removal of two protons. Inversely, the predicted properties for the M1/E2 strength are more than an order of magnitude different. This large difference implies that the interaction is predicting a large change in composition of the $3/2^-_2$ states when moving from ^{39}Ar to ^{37}S. Since this difference is attributed to mixing, as the difference in the composition of the $5/2^-$ states that is discussed in the next Section, the full discussion on this subject is delayed to Section 6.2.3.

6.2.3 The $5/2^-$ states

In Section 5.2, it was suggested that the spin of the 2023-keV state was incorrectly assigned $7/2^-$ based on the reduced transition probabilities deduced for the decays from the higher-lying $3/2^-$ states. Analogously, based on the measured angular distribution (presented in §4.2), a tentative $(5/2, 7/2^-)$ spin value was assigned to the 2898-keV state.

Regarding the assignment of the 2023-keV state, the *sdpf-u-mix* interaction predicts intruder $5/2^-$ and $7/2^-$ states lying close in energy. Both in principle can decay to the ground state via M1/E2. However, while the $5/2^-$ state can also decay to the first excited state via a mixed transition, only the much slower

1397-keV $3/2^+_1$ state				
		^{37}S exp	*sdpf-u-mix*	^{39}Ar
	E [keV]	1397	1756	1517
	$T_{1/2}$	77(5) ps	155 ps	0.95(5) ns
	S [%]	4(1)	–	7
$\to 3/2^-_1$	E [keV]	751	1222	250
	BR [%]	**100**	**100**	**54.1(8)**
	B(E1) [W.u.]	$1.9(1) \cdot 10^{-5}$	$0.9 \cdot 10^{-5}$	$2.13^{+0.17}_{-0.15} \cdot 10^{-5}$

2230-keV $1/2^+_1$ state				
		^{37}S exp	*sdpf-u-mix*	^{39}Ar
	E [keV]	2230	2256	2358
	$T_{1/2}$	59^{+43}_{-35} fs	850	>0.42 ps
	S [%]	1.2(3)	–	3
$\to 3/2^-_1$	E [keV]	1584	1728	1091
	BR [%]	100	86	94.8(1)
	B(E1) [W.u.]	$3^{+2}_{-3} \cdot 10^{-3}$	$2 \cdot 10^{-4}$	$< 1 \cdot 10^{-3}$

3355-keV $3/2^+_2$ state			
		^{37}S exp	*sdpf-u-mix*
	E [keV]	3355	2963
	$T_{1/2}$	–	470 fs
	S [%]	2(2)	–
$\to 3/2^-_1$	E [keV]	2709	1222
	BR [%]	51(3)	5
	B(E1) [W.u.]	–	$3.2 \cdot 10^{-6}$
$\to 3/2^+_1$	Eγ [keV]	1958	2429
	BR [%]	49(3)	70
	B(M1) [W.u.]	–	0.001
	B(E2) [W.u.]	–	2.7
	$\lvert\delta\rvert$	–	1.47

Table 23: Comparison between the obtained data, interaction predictions and decay properties of ^{39}Ar: the positive parity states. Notation as in Table 22.

1992-keV $3/2^-_1$ state				
		^{37}S exp	*sdpf-u-mix*	^{39}Ar
E [keV]		1992	1817	2433
$T_{1/2}$		0.3 ÷ 7 ps	6 ps	0.69(28) ps
S [%]		2.9(6)	–	2
$\rightarrow 7/2^-_1$	E [keV]	1992	1817	2433
	BR [%]	27(1)	43	24.1(8)
	B(E2) [W.u.]	0.1 ÷ 2	0.18	$0.30^{+0.25}_{-0.10}$
$\rightarrow 3/2^-_1$	E [keV]	1346	1283	1166
	BR [%]	73(1)	50	70(1)
	B(M1) [W.u.]	$(0.08 \div 2) \cdot 10^{-2}$	$0.07 \cdot 10^{-2}$	$1.2^{+1.1}_{-0.5} \cdot 10^{-2}$
	B(E2) [W.u.]	0.3 ÷ 8	0.3	5^{+8}_{-3}
	$\lvert\delta\rvert$	–	0.47	0.41(11)

Table 24: Comparison between the obtained data, interaction predictions and decay properties of ^{39}Ar: the first $3/2^-$ intruder. Notation as in Table 22.

E2 multipolarity is allowed for the $7/2^- \rightarrow 3/2^-$ decay. This is reflected in the calculations with predictions on the lifetime of these two states that differ by more than three orders of magnitude, with a much longer lifetime calculated for the $7/2^-$ intruder.

Another hint on the assignment comes from the branching ratio of the 3262-keV state, the second $p_{3/2}$ fragment. This state decays mainly to the first excited state, the other $p_{3/2}$ fragment, but the decays to the 2023- and to the 1992-keV states take a sizeable portion of the branching ratio. The 1992-keV state was identified as the $3/2^-_2$ intruder state. The 2023-keV level, instead, has been proposed to be a $5/2^-$ state due to its very short lifetime.

Consistently, the interaction predicts that the second $p_{3/2}$ fragment decays mostly to the first $p_{3/2}$ fragment, but also decays to an intruder $5/2^-$ state and the already mentioned $3/2^-_2$ have non-negligible branching ratio. Therefore, to reproduce the observed experimental branching ratio of the 3262-keV state, the 2023-keV state has to be assigned to the $5/2^-$ intruder state predicted by the shell-model calculations.

Regarding the 2898-keV state, angular distributions were compatible with both L=2 and L=3 transfers. A $5/2^+$ spin assignment can be ruled out on the basis that all calculated $5/2^+$ states, as mentioned, decay preferentially to the $3/2^+_1$ state. As this decay is not experimentally observed, this assignment

is considered unlikely. The $7/2^-$ spin assignment can also be ruled out on the basis that the calculated $7/2^-_2$ state decays almost exclusively to the ground state via M1/E2 transition, while the decay to the first excited state is negligible. As this last transition is the preferential decay of the 2898-keV state, this assignment is also unlikely.

On the other hand, a second $5/2^-$ state is predicted by the *sdpf-u-mix* interaction at 2447 keV. The nature of this state would be 1p, with very small spectroscopic factor (less than 2%, according to the *sdpf-u* interaction) due to the distance from the centroid of the $f_{5/2}$ strength, located above 5 MeV. The 2898-keV is therefore tentatively assigned to this state.

From Table 25, where the excitation spectrum of ^{37}S, as derived from this dataset, is compared to the ^{39}Ar spectrum and the predictions of the *sdpf-u-mix* interaction, the agreement seems limited. In particular, the spectroscopic factors of the two states in ^{39}Ar seem to be the opposite of the ones measured in ^{37}S, with the $5/2^-_1$ state of ^{37}S sharing similar S with the $5/2^-_2$ of ^{39}Ar, and vice versa. However, the reduced transition probabilities obtained seem to agree more with the proposed assignment. In particular, the B(E2) and B(M1) values between the decays of the $5/2^-_1$ state of ^{37}S differ with the ones of the $5/2^-_2$ of ^{39}Ar by almost an order of magnitude. While therefore reduced transition probabilities seem to suggest the comparison proposed is correct, spectroscopic factor seem to imply that the 2023-keV state is the analogue of the 2756-keV state in ^{39}Ar.

Switching the assignment of the 2023- and 2898-keV levels does not change much the agreement between the predictions of the *sdpf-u-mix* interaction with the deduced strengths of these states, but worsens the agreement between the single-particle $3/2^-$ level and the 3262-keV state. Indeed, the interaction would predict that the dominant decay of this state is the 1239-keV branch to the 2023-keV state, at odd with the experimental evidence.

The question on the correct comparison between these two states in Ar and S can be rephrased in terms of their nature. As mentioned in the previous Section, in order to reproduce the experimental branching ratio of the 3262-keV state, the $5/2^-$ intruder state had to be assigned to the 2023-keV state. Therefore, the 2898-keV had to be assigned to the 1p $5/2^-$ state. Conversely, Warburton showed that the *sdpf* interaction can achieve good reproduction

of the decay properties of the 2093-keV state. The 2756-keV state is not discussed in the paper, but no clear assignment to any state predicted by the *sdpf* interaction is made. From this fact, one would infer the 1p nature of the lowest 2093-keV and the intruder one of the 2756-keV, at odd with the results of the *sdpf-u-mix* interaction that predict the intruder $5/2^-$ lower in excitation energy than the single-particle one.

While it is impossible with the available information to lay claims with sufficient confidence about the nature of any of these two states, it appears that $5/2^-$ states in both ^{39}Ar and ^{37}S share common properties: low spectroscopic factors, a ratio of one order of magnitude between the strength of the two decay branches, short lifetimes. The distance from the centroid of the $f_{5/2}$ strength and the important mixing between these two configurations blur the experimental fingerprints used in this work to identify 1p from intruder configurations. This similarity between the 2023- and 2898-keV states of ^{37}S thus reinforces the $5/2^-$ spin assignment for both of them, but prevents from making a definite identification of their nature.

Increased mixing in ^{37}S

In Chapter 1, it was mentioned that it seemed that, compared to ^{39}Ar, mixing between single-particle and intruder configurations might be enhanced in ^{37}S. In particular, it was noticed that $7/2^-$ intruder states seemed to have very different γ-ray decay paths towards the single-particle configurations: in ^{39}Ar the branch is dominated by the M1/E2 decay to the ground state, while in ^{37}S an additional pure E2 decay to the first excited state was competitive. A partial level scheme, supporting this comparison, was portrayed in Figure 5 at page 23. As decays from npnh to 1p configurations are suppressed, an E2 decay could not compete with a mixed M1/E2 transition unless its strength was sufficiently enhanced. This enhancement was hinted to derive from a stronger mixing between the two $7/2^-$ states. The main goal of the experiment was therefore to perform a lifetime measurement of the low-lying $3/2^-$ and $7/2^-$ intruder states to quantify the increase in mixing with comparison with shell-model calculations.

From the analysis performed, it is clear that the discrepancy between the low-energy spectrum of ^{39}Ar and ^{37}S, drawn in Figure 5, was due a misleading

2023-keV $5/2^-_1$ state

		^{37}S exp	*sdpf-u-mix*	^{39}Ar
	E [keV]	2023	1681	2093
	$T_{1/2}$	<47 fs	125 fs	<35 fs
	S [%]	<0.7%	–	2
	E [keV]	1377	1147	826
	BR [%]	33(2)	20	4.2(7)
$\to 3/2^-_1$	B(M1) [W.u.]	>0.05	0.013	>0.04
	B(E2) [W.u.]	>1	0.26	>2
	$\lvert\delta\rvert$	–	0.10	–
	Eγ [keV]	2023	1681	2093
	BR [%]	67(2)	80	
$\to 7/2^-_1$	**B(M1) [W.u.]**	**>0.03**	**0.015**	**>0.061**
	B(E2) [W.u.]	**>3**	**1.4**	**>1.1**
	$\lvert\delta\rvert$	–	0.33	0.21(6)

2898-keV $5/2^-_2$ state

		^{37}S exp	*sdpf-u-mix*	^{39}Ar
	E [keV]	2898	2447	2756
	$T_{1/2}$	<250 fs	7 fs	0.12(5) ps
	S [%]	2(2)	–	–
	E [keV]	2252	1913	1488
	BR [%]	83(8)	65	44(1)
$\to 3/2^-_1$	B(M1) [W.u.]	**>0.006**	**0.19**	$\mathbf{0.024^{+0.20}_{-0.08}}$
	B(E2) [W.u.]	**>0.04**	**1.3**	**<0.04**
	$\lvert\delta\rvert$	–	0.1	0.01(5)
	Eγ [keV]	2898	2447	2755
	BR [%]	17(8)	35	56(1)
$\to 7/2^-_1$	B(M1) [W.u.]	$>5 \cdot 10^{-4}$	0.04	$4.3^{+3.9}_{-1.6} \cdot 10^{-3}$
	B(E2) [W.u.]	>0.02	1.8	$0.26^{+0.44}_{-0.16}$
	$\lvert\delta\rvert$	–	0.32	0.37(10)

Table 25: Comparison between the obtained data, interaction predictions and decay properties of ^{39}Ar: the $5/2^-$ states. Notation as in Table 22.

spin assignment of the 2023-keV state. As the spin of this state has been assigned $5/2^-$, both the decay branches of the 2023-keV state are mixed M1/E2 transitions, therefore being competitive with each other without requiring any increase in mixing with respect to ^{39}Ar. A more accurate comparison between the two spectra is portrayed in Figure 75. In this Figure, the low-lying $3/2^-$ and $7/2^-$ states are portrayed, along with the first excited $p_{3/2}$ fragment. Lifetimes, spectroscopic factors, γ-ray energies and transition probabilities are reported. Compared to Figure 5, in this Figure the 2023-keV state has been substituted with the 2515-keV state, assigned $7/2^-$ spin (the full discussion on the spin assignment will be illustrated in §6.2.5), with the caveat that the apparent discrepancy between the reduced transition probabilities between the $7/2^-$ states of ^{37}S and ^{39}Ar is due to the mixing ratio, which is predicted by the *sdpf-u-mix* interaction one order of magnitude smaller than the measured one in ^{39}Ar. This might be due to an overestimation of the M1 strength by one order of magnitude, which is not unlikely as the transition probability is of the order of 10^{-3}. A general agreement between the strength values is obtained between the decays of the $3/2^+$ and $7/2^-$ intruder states, proving that no drastic change in mixing is detected in these states.

Conversely, it was also hinted in the previous Section that increased mixing needs to be invoked to explain the difference in reduced transition probabilities between the $3/2^-_2$ intruder states of ^{39}Ar and ^{37}S.

It was already mentioned that the *sdpf-u-mix* predictions for ^{37}S and the reduced transition probabilities deduced for ^{39}Ar agree well for the decay to the ground state, but disagree by an order of magnitude in the decay to the first-excited state. With such large error bars in the lifetime of the 1992-keV state, it is impossible to say whether the $3/2^-_2$ state is similar to its analogue in ^{39}Ar or the predictions of the *sdpf-u-mix*.

However, let us consider the two extreme cases, i.e. that the lifetime of the $3/2^-_2$ state of ^{37}S is 0.3 ps and 7 ps.

If the lifetime was 0.3 ps, all reduced transition probabilities are equal to their upper limit. That would imply that the decay to the first excited $3/2^-_1$ state does not change between ^{37}S and ^{39}Ar. On the other hand, the decay to the $7/2^-_1$ ground state would be enhanced by an order of magnitude with respect

to the analogous decay of ^{39}Ar. In this limit, the *sdpf-u-mix* interaction would not reproduce any of the decays of this state.

Conversely, if the lifetime of this state was 7 ps, the agreement between predictions of the *sdpf-u-mix* interaction and the reduced transition probabilities of ^{37}S would all agree within a factor two. However, when comparing to ^{39}Ar, the strength of the decay to the $3/2^-_1$ state would be suppressed by an order of magnitude.

Without a more precise lifetime value, it is not possible to quantify the resemblance. In both cases, however, the predictions of the *sdpf-u-mix* interaction would be one order of magnitude different than the experimental values, indicating either an abrupt change with respect to ^{39}Ar, or that this state is not correctly reproduced.

This fact suggests that in the wavefunction there are single-particle components that the interaction is seemingly not able to reproduce. The 1p0h component in the wavefunction of the $3/2^-_2$ is calculated to be 4%. In particular, the mixing with the 0^+ and 2^+ state of ^{36}S, i.e. the presence of 0^+, $2^+ \otimes f_{7/2}$ or 0^+, $2^+ \otimes p_{3/2}$ configurations, would increase the transition probability of the decay to the $7/2^-_1$ and $3/2^-_1$, respectively. For example, from NATHAN calculations the wavefunction of first-excited $3/2^-$ state is composed by the $0^+ \otimes p_{3/2}$ configuration with 80% probability, and by the $2^+ \otimes f_{7/2}$ with 20% probability. If a small component of $0^+ \otimes p_{3/2}$ configuration is also present in the wavefunction of the intruder $3/2^-_2$ state, the $3/2^-_2 \rightarrow 3/2^-_1$ decay would have strength contributions both via the $2^+ \rightarrow 0^+$ and the $p_{3/2} \rightarrow f_{7/2}$ transitions. The $3/2^-_2 \rightarrow 7/2^-_1$ decay, on the other hand, would have negligible contributions to its strength, as the only one-body transition allowed would be the $p_{3/2} \rightarrow f_{7/2}$ transition with the ^{36}S core in the excited 2^+ state. This component, in the ground state of ^{37}S, amounts to 6%.

This comparison shows how two apparently very similar states, in terms of spectroscopic factor and branching ratio, might have slightly different wavefunction content.

This finding underlines the sensitivity that reduced transition probabilities have in detecting even small changes in composition of the nuclear wave-

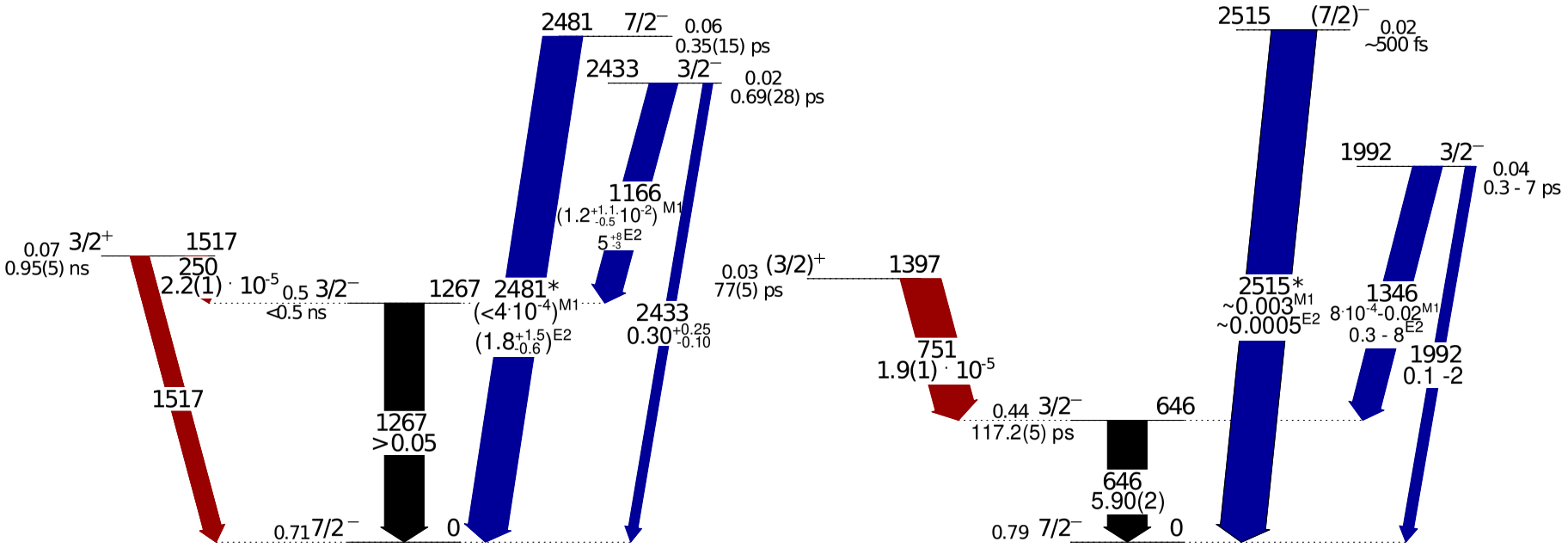

Figure 75: Comparison between the ^{39}Ar and ^{37}S low-energy partial level schemes and EM decay. Color code and band organization is as Figure 5 at page 23, with even intruder states on the left, in red color, single-particle levels in the middle and in black color, and odd intruders on the right, in blue color. With respect to the previous Figure, now the proposed $7/2^-$ state at 2515-keV is drawn, instead of the 2023-keV level. For this state, a half-life of about 500 fs was assumed, as in the text. In all other cases, the lifetimes measured in this work are reported. Reduced transition probabilities are indicated below the γ-ray energy, in W.u.. Where multiple characters are allowed, the reduced transition probabilities were calculated assuming the *sdpf-u-mix* predicted mixing ratio. In these cases, the corresponding character is indicated next to the value. Energy axis is not in scale.
*The *sdpf-u-mix* mixing ratio is one order of magnitude lower than the measured value for the 2481-keV transition, which therefore lead to very different values of reduced transition probabilities. Assuming the ^{39}Ar mixing ratio, the reduced transition probability values become compatible.

function, and the necessity to perform both lifetime and spectroscopic factor measurements in order to completely characterize nuclear excited states.

6.2.4 The 3493-keV state

This state was assigned $3/2^-$ spin in different (d,p) experiments based on the L=3 character of the proton angular distribution and fairly large spectroscopic factor, indicative of a $p_{3/2}$ fragment nature. Its γ-ray decays are fairly comparable with the ones of the 3262-keV $3/2^-$ state: namely the three strongest decays (in case of the 3493-keV state, the only ones observed) are to the ground, 646- and 2023-keV states.

However, while the 2616-keV decay dominates the branching ratio of the 3262-keV state, in the 3493-keV state the dominant branch is the one to the 2023-keV state. Whether this state is a $f_{5/2}$ fragment or a strongly mixed intruder, the wavefunction of this state is fairly fragmented, which would imply a suppression of the decays coming from 1p0h states, which would then preferentially decay to the 646-keV state. Such is the case, for example, of the 3262-keV state. On the other hand, an intruder configuration would decay preferentially to the 2023-keV state. The large number of possible configurations that compose the wavefunction could interfere constructively producing a strong transition that would determine the decay of the state.

Such seems to be the case of the 3493-keV state. Its 1470-keV γ-ray decay occupies almost 60% of the branching ratio, suggestive of an intruder nature. Indeed, the *sdpf-u-mix* interaction does not predict single-particle $p_{3/2}$ configurations below 3.5 MeV other than the ones assigned 646- and 3262-keV state. A $3/2^-$ intruder configuration is instead predicted at 2598 keV (thus lower in energy than the last $p_{3/2}$ fragment). The predictions of the *sdpf-u-mix* interaction in case the 3493-keV level was assigned to this configurations are reported in Table 26. In this case, no comparison with ^{39}Ar is possible, as the available spectroscopic information becomes scarce, and no similar state could be found among the observed ones.

The agreement between the *sdpf-u-mix* predictions and the deduced strengths is rather poor. Only the decays to the first-excited state are reproduced, while the other strengths are underestimated by an order of magnitude. This suggests

that the assignment proposed is wrong, and that therefore the 3493-keV is indeed a $p_{3/2}$ fragment.

On the other hand, no other single-particle fragment is predicted by the interaction below 3.5 MeV. It is possible that such a state is predicted higher in energy, and therefore it was not included in the calculations. Indeed, the *sdpf-u* interaction predicts two other $p_{3/2}$ fragments, one at about 4 MeV of excitation energy and the other at almost 5 MeV. The 3493-keV might be therefore assigned to one of these states. However, the branching ratio seems to indicate that intruder components, even if non-dominant, give important contributions to the strength of the decay to the $5/2^-$ state. Being the *sdpf-u* interaction not tailored to reproduce intruder excitations, the wavefunction of this state might not be accurately reproduced by the interaction, and therefore any comparison between the 3493-keV level and these two additional $3/2^-$ states would be misleading.

With the available information, it is not possible to state whether this state is a single-particle state with important intruder component, or an intruder configuration. This state has therefore been reported as "counterpart uncertain" in Table 27.

6.2.5 Other small-strength states

Three other states were observed in this work with little statistics, namely the 2515-, 3120- and 3441 keV levels. For these states, proton angular distributions, spectroscopic factors and lifetimes could not be measured. However, their characteristic decay pattern, with only one dominant transition to the ground state, could be used as fingerprint for their identification. One additional state, the 2978-keV level, was populated enough so that proton angular distributions and spectroscopic factor could be measured, albeit with large error bars. This level too shares the common feature of a single dominant decay branch, although to the first excited rather than the ground state.

Therefore, the assignment of these levels is based mostly on the observed branching ratio, as it is the only other spectroscopic information available other than previously measured spectroscopic factors (which have not been computed with the *sdpf-u-mix* interaction). As discussed in §6.2.3, however,

3493-keV $3/2^-_1$ state			
		^{37}S exp	*sdpf-u-mix*
	E [keV]	3493	2598
	$T_{1/2}$	<74 fs	135 fs
	S [%]	3(1)	–
$\rightarrow 7/2^-_1$	E [keV]	3493	2598
	BR [%]	4.0(5)	0.3
	B(E2) [W.u.]	>0.07	0.003
$\rightarrow 3/2^-_1$	E [keV]	2847	2064
	BR [%]	39(1)	48
	B(M1) [W.u.]	>0.005	0.003
	B(E2) [W.u.]	>0.1	0.8
	$\lvert\delta\rvert$	–	0.24
$\rightarrow 5/2^-_1$	E [keV]	1470	917
	BR [%]	57(1)	13
	B(M1) [W.u.]	>0.02	0.003
	B(E2) [W.u.]	>50	6.5
	$\lvert\delta\rvert$	–	1.19

Table 26: Comparison between the obtained data, interaction predictions and decay properties of ^{39}Ar: the 3493-keV state as $3/2^-$ intruder level. Notation as in Table 22.

branching ratios are not as indicative as reduced transition probabilities of the character of excited states. Moreover, while the observation of one decay branch for these states is consistent with the results of Chapman *et al.* [71], other decays might have not been observed either because they lie close to other decays of more populated excited states of ^{37}S, or because they were covered by decays from parasitic and background reactions. Indeed, most of these transitions are high-energy (above 2 MeV), where the spectrum is less contaminated. However, most of these transitions have been observed with statistics in the order of tens of counts. Recalling the measured efficiency of the AGATA spectrometer (shown in Figure 40 at page 88), it can be estimated that a γ-ray peak of energy between 500 and 1500 keV and of about 200-300 counts would already halve the branching ratio. One of such transitions would have been most likely observed in the spectra of Figure 59 at page 122. It seems therefore likely to conclude that the dominant branch of these states has been observed.

Regarding the 2515-keV level, this state has been suggested to be the counterpart $7/2^-_2$ state based on observed width of the peak, which suggests a lifetime

of the order of hundreds of fs. In §6.2.3, a tentative lifetime of 500 fs has been used as reference value for the estimation of the possible reduced transition probabilities. The *sdpf-u-mix* interaction predicts a $7/2^-$ intruder excitation at 1863 keV of excitation energy, almost degenerate with the intruder $3/2^-_2$, with dominant decay (85% branching ratio) to the ground state. The predicted lifetime for this state is of about 900 fs. Compared with ^{39}Ar, the agreement is seems very limited. The predicted mixing ratio of the M1/E2 transition to the ground state is one order of magnitude different than the measured one for the 2481-keV $7/2^-_2 \rightarrow 7/2^-_1$ transition in ^{39}Ar. With the ^{39}Ar mixing ratio, the agreement with the predicted value is recovered.

Regarding the 2978-keV level, this was assigned spin (1/2, 3/2) by Chapman *et al.*. The proton angular distribution measured in this work suggest the same assignment, with negative parity. Two intruder states are predicted compatible with the observed properties: the 2598-keV $3/2^-$ intruder state (tentatively assigned to the 3493-keV state, with poor reproduction), and the 3063-keV $1/2^-$. Only a lifetime measurement might define the spin assignment of these state, as the predicted lifetimes with the two assignments are 400 and 100 fs, i.e. sufficiently different to suggest a less tentative assignment than the present one.

The $(9/2)^+$ state at 3120-keV is a suggested $g_{9/2}$ fragment. Such high spins were not included in the calculations, and therefore nothing can be further inferred about this state.

Lastly, the 3441-keV state has been assigned $7/2^-$ spin value by Eckle *et al.* [66]. No other $7/2^-$ states are predicted below 3.5 MeV by the *sdpf-u-mix* interaction. Its observation in (t, ^{3}He) suggests a possible intruder nature.

E^{exp}	J^{π}	E^{u-mix}	E^{u}	$npnh$	Configuration	Amplitude	
0	$7/2^-$	0	0	1p0h	$\pi(\,d^6_{5/2}\,s^2_{1/2})\;\nu\;(d^6_{5/2}\,s^2_{1/2}\,d^4_{3/2}\,f^1_{7/2})$	68%	$f_{7/2}$ fragment
646	$3/2^-$	534	516	1p0h	$\pi(\,d^6_{5/2}\,s^2_{1/2})\;\nu\;(d^6_{5/2}\,s^2_{1/2}\,d^4_{3/2}\,p^1_{3/2})$	61%	$p_{3/2}$ fragment
1397	$3/2^+$	1756	2396	2p1h	$\pi(\,d^6_{5/2}\,s^2_{1/2}\,)\;\nu\;(d^6_{5/2}\,s^2_{1/2}\,d^3_{3/2}\,f^2_{7/2})$	30%	
1992	$3/2^-$	1817	–	3p2h	fragmented		
2023	$5/2^-$	1681	–	3p2h	$\pi(\,d^6_{5/2}\,s^1_{1/2}\,d^1_{3/2})\;\nu\;(d^6_{5/2}\,s^2_{1/2}\,d^3_{3/2}\,p^2_{1/2})$	12%	possibly the $5/2^-$ 1p0h state
2230	$1/2^+$	2262	–	2p1h	$\pi(\,d^6_{5/2}\,s^2_{1/2})\;\nu\;(d^6_{5/2}\,s^1_{1/2}\,d^4_{3/2}\,p^2_{1/2})$	15%	
2515	$7/2^-$	1863	–	3p2h	$\pi(\,d^6_{5/2}\,s^2_{1/2}\,)\;\nu\;(d^6_{5/2}\,s^2_{1/2}\,d^4_{3/2}\,p^1_{3/2})$	61%	$f_{7/2}$ fragment
2638	$1/2^-$	2456	2352	1p0h	$\pi(\,d^6_{5/2}\,s^2_{1/2})\;\nu\;(d^6_{5/2}\,s^2_{1/2}\,d^4_{3/2}\,p^1_{1/2})$	69%	$p_{1/2}$ fragment
2898	$5/2^-$	2447	–	1p0h	$\pi(\,d^6_{5/2}\,s^1_{1/2}\,d^1_{3/2})\;\nu\;(d^6_{5/2}\,s^2_{1/2}\,d^3_{3/2}\,f^2_{7/2})$	18%	possibly the $5/2^-$ 3p2h state
2978	$3/2^-$				counterpart uncertain, likely intruder		
3262	$3/2^-$	2858	2843	1p0h	$\pi(\,d^6_{5/2}\,s^1_{1/2}\,d^1_{3/2}\,)\;\nu\;(d^6_{5/2}\,s^2_{1/2}\,d^4_{3/2}\,f^1_{7/2})$	40%	$p_{3/2}$ fragment
3355	$3/2^+$				counterpart uncertain		
3441	$7/2^-$				counterpart uncertain, likely intruder		
3493	$3/2^-$				counterpart uncertain		

Table 27: Tentative assignment of the observed ^{37}S levels. The reported spin assignments are the ones proposed in the Chapter or based on the data of Eckle *et al.* [66].

7 Conclusions and future perspectives

This work is based on the analysis on an experiment held in Legnaro National Laboratories in Legnaro (PD), Italy, between May and June 2022. The experiment aimed at measuring lifetimes in excited states in ^{37}S to assess whether the mixing between single-particle and intruder configurations increases already at Z=16, above the north edge of the Island of Inversion.

The experiment was motivated by the appearance of a pure E2 γ-ray transition between the $(7/2)^-$ intruder state and the first excited $p_{3/2}$ fragment $3/2^-$ state. This transition competes with a mixed M1/E2 transition to the ground-state, taking a sizeable percentage of the branching. In ^{39}Ar, two protons above, the $7/2^-$ intruder state does not show this branching to the first excited single-particle $3/2^-$. This difference hints to a possible increase in mixing between the single-particle and intruder configurations in ^{37}S with respect to ^{39}Ar, so that the pure E2 transition, in principle much slower than a mixed M1/E2, becomes competitive thanks to the increased collectivity.

The main goal of the experiment was then to quantify this apparent increase in mixing by measuring the lifetimes of excited intruder states in ^{37}S. In particular, given the lifetime and the branching ratio, the reduced transition probability of the γ-ray decay can be deduced, which is related with the wavefunction overlap of the initial and final state. Through comparison with state-of-the-art shell-model calculations and the available spectroscopic information in ^{39}Ar, the evolution of mixing towards the N=20 Island of Inversion can be assessed.

^{37}S ions were produced through a direct (d,p) reaction in inverse kinematics. The reaction was chosen due to its selectivity in the population of excited states. As lifetime measurements are systematically biased in the presence of higher-lying states that decay to the measured state, high control on the

feeding is necessary. This reaction allows to quantify with good accuracy the exclusive cross sections to the excited states populated during the reaction.

Recoiling protons were detected via the charged-particle silicon array SPIDER. The detection of the light partner allowed for the kinematical reconstruction of the reaction. The obtained resolution was sufficient to discriminate the major single-particle fragments populated during the reaction.

Thanks to the segmentation of SPIDER, also angular distribution and spectroscopic factors were re-measured, albeit only as relative quantities. Although this was not the primary goal of the experiment, results compare well with the previous (d,p) measurements published in literature.

Photons were detected with the γ-ray tracking array AGATA, the European state-of-the-art tracking array. The high efficiency and granularity of the detector, thanks to its high electrical segmentation, the PSA algorithm and tracking capabilities, provide unprecedented resolving power and resolution in the Doppler-corrected spectrum.

Excited states with cross section as low as $\sim$20 μb were observed and identified thanks to their γ-ray decay. The level scheme built with this dataset is compatible with the ones already published. Three states, at 2230-, 2898- and 2978-keV were also observed for the first time in a (d,p) reaction, and their relative spectroscopic factor and angular distribution measured. In particular, the observation of the 2230-keV excited state marks the first identification of a L=0 transfer in a (d,p) reaction in ^{37}S. New γ-ray branches were also observed for the first time thanks to the powerful combination of the AGATA γ-ray spectrometer and the SPIDER array, expanding the known level scheme.

Nuclear lifetimes lying in different very ranges were measured with a combination of Recoil Distance Doppler Shift and Doppler Shift Attenuation methods. The RDDS technique was implemented with the use of the Plunger device, installed in the scattering chamber. Holding the production target and a stopper foil at a known distance, lifetimes of the order of hundreds of ps can be estimated by the ratio (at known distance) between the number of γ-rays emitted between the two foils (hence affected by Doppler effect) and the ones emitted after the ion has completely stopped in the stopper. This technique was used to measure the lifetime of the first excited single-particle $3/2^-_1$ and first

positive parity intruder $3/2^+_1$ states, finding a value of 117.2(5) and 77(5) ps, respectively.

The DSAM technique was instead devised to measure lifetimes of few hundreds fs. This method was implemented by evaporating the plastic polymer CD_2 on a gold backing, so that ^{37}S ions, populated in an excited state, were slowed down by the gold layer around 100 fs after production. If the slowing-down process is comparable with the lifetime of the state of interest, the γ-ray peak observed in the Doppler corrected spectrum shows a shape that is dependent on the slowing-down process and the lifetime of the decaying state. The experimental spectrum can then be compared with a set of realistic GEANT4 simulations that reproduce the experimental conditions and the slowing down process, given the lifetime of the excited state. The half-life of the excited state can then be measured by means of χ^2 minimization. With this method, lifetimes or upper limits could be measured for five states in ^{37}S, of which four for the first time.

Results obtained were compared with the experimental spectrum of ^{39}Ar and shell model calculations employing the *sdpf-u* and *sdpf-u-mix* interactions. General agreement was found between the experimental spectra of ^{39}Ar and ^{37}S, and between the predictions of shell-model calculations and the experimental evidence. The discrepancy between the different decay modes of the first intruder $7/2^-$ state has been explained by proving, thanks to the lifetime estimate provided, that an incorrect spin assignment led to a misleading comparison.

However, fingerprints of increased mixing in ^{37}S were indeed found. In particular, the first $3/2^-$ intruder state at 1.992 MeV is predicted to have decay properties fairly different from its analogous in the isotone ^{39}Ar, hinting to an increased mixing in this state with the removal of two protons that changes the reduced transition probabilities of this decay by about one order of magnitude. The *sdpf-u-mix* interaction seems not able to reproduce this effect.

A second $5/2^-$ state was also proposed as the 2898-keV state. Lying very far from the centroid of $f_{5/2}$ strength, the two $5/2^-$ predicted below 3.5 MeV by the *sdpf-u-mix* interaction present a challenge for the experimental identification of "intruder" and 1p0h states. Indeed, their large mixing and low spectroscopic strength lead to very similar decay properties between the predicted intruder

and the single-particle states. Therefore, at the level of resolution of this experiment, the identification has to rely purely on the predictions.

Two $3/2^-$ states above 3 MeV, the 3262- and 3493-keV levels, instead, show large mixing with intruder configurations. Experimentally, the decay to the intruder $5/2^-_1$ state at 2023 keV has been measured to take in both cases a sizeable share of the branching ratio. This feature is not reproduced by the interaction. The lowest of the pair, the 3262-keV $3/2^-_3$ state, has been assigned single-particle nature, but with higher intruder component than the one predicted by the interaction. Regarding the upper one, the 3493-keV $3/2^-_4$ level, on the other hand, there is no conclusive evidence on its nature. Indeed, no other single-particle state is predicted below 3.5 MeV by the interaction, but only an intruder one. It is therefore possible that either the 3493-keV level is a $3/2^-$ intruder state, but with higher single-particle component than the one predicted by the interaction, or that a higher-lying single-particle state is lowered in excitation energy by mixing.

Accurate comparison between the shell-model predictions, the spectrum of ^{39}Ar and the deduced transition probabilities of ^{37}S is limited by the fact that no mixing ratios of any mixed M1/E2 transition was measured in this nucleus. A γ-γ angular correlations measurement in ^{37}S, populated by a neutron capture reaction on the stable ^{36}S, would directly address this unknown and provide complementary information to the one of this thesis. Such experiment could be performed, for example, at the Laue Langevin Institute (ILL) in Grenoble, thanks to the availability of high-flux neutron beams coupled with the γ-ray spectrometer FIPPS. Assuming the spectrometer has a 6% efficiency at 0.6 MeV, a target of 100 μg of pure ^{36}S, and the γ-ray yields reported by Raman *et al.* [67], the obtained rates would be approximately one order of magnitude larger than the ones reported inTable 9. Furthermore, the $1/2^+$ state was observed for the first time in a (d,p) reaction. A high-statistics measurement of the β-decay spectrum of ^{37}P would therefore complement and expand the knowledge about positive parity intruder states in this nucleus. The LISE spectrometer at GANIL can produce this ion via fragmentation of a primary ^{40}Ar beam. The EXOGAM γ-ray array at the focal plane of LISE would then detect emitted γ rays after β decay of ^{37}P.

While the comparison between ^{37}S and ^{39}Ar holds well for most states, hinting at a smooth evolution of the nuclear structure between Z=18 to Z=16,

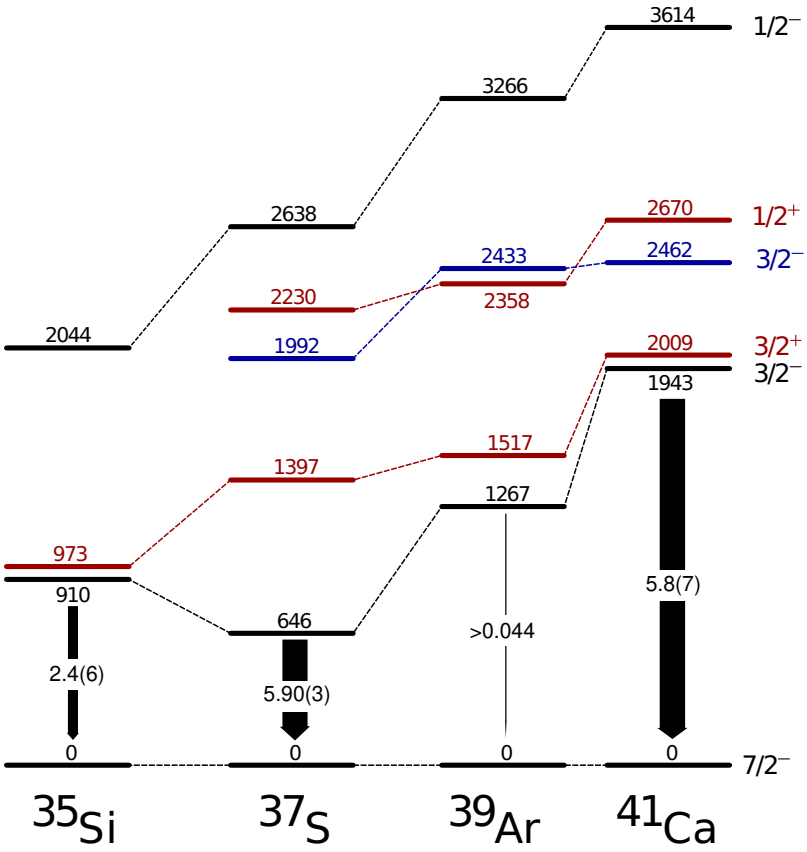

Figure 76: Evolution of a selection of excited states in the N=21 isotonic chain, from Ca to Si. In black, high-strength single-particle fragments, in blue negative parity intruder configurations, in red positive parity intruder states. The arrow width connecting the first excited $3/2^-$ state and the ground state is proportional to the B(E2) value, reported in W.u..

between Z=16 and Z=14 an abrupt change in the *p* spin gap has been observed [50]. A compilation of the evolution of selected states along the N=21 chain is reported in Figure 76. The origin of this reduction has been connected to the depletion of the $s_{1/2}$ shell, and the existence of a bubble structure in ^{34}Si [56, 61]. The findings of this work are in overall agreement with the shell-model calculations performed with the *sdpf-u-mix* interaction, highlighting some possible discrepancies at higher excitation energy that may hint to a larger role played by correlations in this energy region of ^{37}S than the one predicted by the interaction - such possible discrepancies require further investigation. Lifetime studies in ^{35}Si could also be then beneficial in the understanding of the contributions of nuclear correlations in the closure of the spin gap. In particular, the observation of the intruder $3/2^-_2$ state of ^{35}Si might play an important role. Unfortunately, the observation of states with less than 0.1 spectroscopic factor seems to be at the moment out of experimental reach.

With the continuous technological development, there is hope that ^{34}Si beams will be available with sufficient intensity to perform detailed spectroscopic studies in the near future, both on and beyond the strongest single-particle fragments. As this work has shown, complementary measurements of different observables is needed to understand the fragmentation of the single-particle strength.

On the particle spectroscopy side, GRIT [99] is envisioned to be the next-generation charged-particle silicon detector for radioactive ion beams. Upon its completion, it will combine an almost 4π solid angle coverage with particle identification capabilities based on both ΔE-E and pulse-shape analysis methods, making it one of the most versatile detectors for charged-particle spectroscopy. On the γ-ray spectroscopy side, the AGATA spectrometer has already been proven to provide superior efficiency and Doppler-correction capabilities. The current collaboration objective is to reach 3π solid angle coverage by 2030. In this configuration, the efficiency of the spectrometer would increase by more than a factor three with respect to the one of this experiment, allowing the detection of more exotic channels.

Only the combination of state-of-the-art detectors with high intensity beams of powerful facilities can tackle the challenges that the exploration of the most exotic regions of the nuclear chart poses. In this context, AGATA and GRIT will take a lead role in the future of the European experimental nuclear physics.

Appendix

A1 Fresco input

```
36S(d,p)37S @ 5.0 MeV/u - DWBA - An e Cai (d) - Koning-Delaroche (p);
NAMELIST
&FRESCO hcm=0.1 rmatch=40 rintp=0.1 hnl=0.1 rnl=5 centre=1.00
        jtmin=0.0 jtmax=30. absend=0.001
        thmin=0.0 thmax=180.0 thinc=1.0
        iter=1 iblock=0
        chans=1 smats=2 xstabl=1
        elab=8.6083 /

&PARTITION namep="d" massp=2.0141 zp=1 namet="36S" masst=35.967081 zt=16 qval=0.0 nex=1 /
&STATES jp=1 bandp=1  ep=0.0000 cpot=1 jt=0.0 bandt=1 et=0.0000 / #gs

&PARTITION namep="p" massp=1.0078 zp=1 namet="37S" masst=36.971126 zt=16 qval=2.079 nex=10 /
&STATES jp=0.5 bandp=1 ep=0.000 cpot=2 jt=3.5 bandt=-1 et=0.000 / #(7/2-) f7/2
&STATES copyp=1                cpot=2 jt=1.5 bandt=-1 et=0.646 / #(3/2-) p3/2
&STATES copyp=1                cpot=2 jt=1.5 bandt=+1 et=1.398 / #(3/2+) intruder
&STATES copyp=1                cpot=2 jt=1.5 bandt=-1 et=1.991 / #(3/2-) intruder
&STATES copyp=1                cpot=2 jt=3.5 bandt=-1 et=2.023 / #(7/2-) intruder
&STATES copyp=1                cpot=2 jt=0.5 bandt=-1 et=2.638 / #(1/2-)
&STATES copyp=1                cpot=2 jt=1.5 bandt=-1 et=3.262 / #(3/2-)
&STATES copyp=1                cpot=2 jt=1.5 bandt=+1 et=3.355 / #(3/2+)
&STATES copyp=1                cpot=2 jt=3.5 bandt=-1 et=3.441 / #(7/2-)
&STATES copyp=1                cpot=2 jt=1.5 bandt=-1 et=3.492 / #(3/2-)
&partition /

#d-36S (incoming scattering)
&POT kp=1 ap=0.0 at=36.0 rc=1.303 /
&POT kp=1 type=1 shape=0 p1=92.483 p2=1.150 p3=0.761 p4=1.726 p5=1.335 p6=0.525  /
&POT kp=1 type=2 shape=0                             p4=15.577 p5=1.328 p6=0.643 /
&POT kp=1 type=3 shape=0 p1=3.557  p2=0.972 p3=1.011                                /

#p-37S (outgoing scattering)
&POT kp=2 ap=0.0 at=37.0 rc=1.292 /
&POT kp=2 type=1 shape=0 p1=59.466 p2=1.182 p3=0.672 p4=0.273  p5=1.182 p6=0.672 /
&POT kp=2 type=2 shape=0                             p4=6.512  p5=1.290 p6=0.538 /
&POT kp=2 type=3 shape=0 p1=5.787 p2=0.991 p3=0.590  p4=-0.013 p5=0.991 p6=0.590 /

#p-36S (core-core)
```

```
&POT kp=3 ap=0.0 at=36.0 rc=1.295 /
&POT kp=3 type=1 shape=0 p1=59.014 p2=1.181 p3=0.672 p4=0.274 p5=1.181 p6=0.672 /
&POT kp=3 type=2 shape=0                            p4=6.382 p5=1.290 p6=0.537 /
&POT kp=3 type=3 shape=0 p1=5.784  p2=0.989 p3=0.590 p4=-0.013 p5=0.989 p6=0.590 /

#36S-n (binding and prior interaction)
&POT kp=4 ap=0.0 at=36.0 rc=1.25 /
&POT kp=4 type=1 shape=0 p1=50.0  p2=1.25  p3=0.65 /
&POT kp=4 type=3 shape=0 p1=6.0   p2=1.25  p3=0.65 /

#p-n (binding and post-interaction)
&POT kp=5 ap=1. at=0.0 rc=1.3 /
&POT kp=5 type=1 shape=0 p1=50.0 p2=1.25 p3=0.65 /
&POT kp=5 type=3 shape=0 p1=6.00 p2=1.25 p3=0.65 /
&pot /

&OVERLAP kn1=1 ic1=1 ic2=2 in=1 kind=0 nn=1 l=0 sn=0.5 j=0.5
               kbpot=5 be=2.2246 isc=1 ipc=1 / # <d|p> - gs
&OVERLAP kn1=2 ic1=1 ic2=2 in=2 kind=0 nn=1 l=3 sn=0.5 j=3.5
               kbpot=4 be=4.3036 isc=1 ipc=1 / # <36S|37S> - (7/2-) f7/2 gs
&OVERLAP kn1=3 ic1=1 ic2=2 in=2 kind=0 nn=2 l=1 sn=0.5 j=1.5
               kbpot=4 be=3.6574 isc=1 ipc=1 / # <36S|37S> - (3/2-) p3/2 646
&OVERLAP kn1=4 ic1=1 ic2=2 in=2 kind=0 nn=1 l=2 sn=0.5 j=1.5
               kbpot=4 be=2.9061 isc=1 ipc=1 / # <36S|37S> - (3/2+) intruder 1397
&OVERLAP kn1=5 ic1=1 ic2=2 in=2 kind=0 nn=2 l=1 sn=0.5 j=1.5
               kbpot=4 be=2.3126 isc=1 ipc=1 / # <36S|37S> - (3/2-) intruder 1992
&OVERLAP kn1=6 ic1=1 ic2=2 in=2 kind=0 nn=1 l=3 sn=0.5 j=3.5
               kbpot=4 be=2.2806 isc=1 ipc=1 / # <36S|37S> - (7/2-) intruder 2023
&OVERLAP kn1=7 ic1=1 ic2=2 in=2 kind=0 nn=2 l=1 sn=0.5 j=0.5
               kbpot=4 be=1.6656 isc=1 ipc=1 / # <36S|37S> - (1/2-) 2638
&OVERLAP kn1=8 ic1=1 ic2=2 in=2 kind=0 nn=2 l=1 sn=0.5 j=1.5
               kbpot=4 be=1.0416 isc=1 ipc=1 / # <36S|37S> - (3/2-) 3262
&OVERLAP kn1=9 ic1=1 ic2=2 in=2 kind=0 nn=1 l=2 sn=0.5 j=1.5
               kbpot=4 be=0.9486 isc=1 ipc=1 / # <36S|37S> - (3/2-) 3355
&OVERLAP kn1=10 ic1=1 ic2=2 in=2 kind=0 nn=1 l=3 sn=0.5 j=3.5
               kbpot=4 be=0.8626 isc=1 ipc=1 / # <36S|37S> - (3/2-) 3441
&OVERLAP kn1=11 ic1=1 ic2=2 in=2 kind=0 nn=2 l=1 sn=0.5 j=1.5
               kbpot=4 be=0.8116 isc=1 ipc=1 / # <36S|37S> - (3/2-) 3492
&overlap /

&COUPLING icto=-2 icfrom=1 kind=7 ip1=0 ip2=-1 ip3=3  / # finite range transfer (DWBA) - post interaction
&CFP in=1 ib=1 ia=1 kn=1 a=1.000 / # <p+n|d> - gs
&CFP in=2 ib=1 ia=1 kn=2 a=0.832 / # <36S|37S> - (7/2-) f7/2 gs
&CFP in=2 ib=2 ia=1 kn=3 a=0.662 / # <36S|37S> - (3/2-) p3/2 646
&CFP in=2 ib=3 ia=1 kn=4 a=0.167 / # <36S|37S> - (3/2+) intruder 1397
&CFP in=2 ib=4 ia=1 kn=5 a=0.182 / # <36S|37S> - (3/2-) intruder 1992
&CFP in=2 ib=5 ia=1 kn=6 a=0.077 / # <36S|37S> - (7/2-) intruder 2023
&CFP in=2 ib=6 ia=1 kn=7 a=0.696 / # <36S|37S> - (1/2-) 2638
&CFP in=2 ib=7 ia=1 kn=8 a=0.292 / # <36S|37S> - (3/2-) 3262
&CFP in=2 ib=8 ia=1 kn=9 a=0.173 / # <36S|37S> - (3/2-) 3355
&CFP in=2 ib=9 ia=1 kn=10 a=0.141 / # <36S|37S> - (3/2-) 3441
&CFP in=2 ib=10 ia=1 kn=11 a=0.212 / # <36S|37S> - (3/2-) 3493
&cfp /
&coupling /
```

J_i^π	J_f^π	B(E1) [W.u.]
$3/2_1^+$	$3/2_1^-$	$9.3 \cdot 10^{-6}$
	$5/2_1^-$	$6.1 \cdot 10^{-5}$
$3/2_2^-$	$3/2_1^+$	$3.4 \cdot 10^{-5}$
$1/2_1^+$	$3/2_1^-$	$1.5 \cdot 10^{-4}$
	$3/2_2^-$	$8.0 \cdot 10^{-6}$
$5/2_2^-$	$3/2_1^+$	$5.6 \cdot 10^{-8}$
$1/2_1^-$	$1/2_1^+$	$1.1 \cdot 10^{-4}$
	$3/2_1^+$	$2.3 \cdot 10^{-4}$
$3/2_3^-$	$3/2_1^+$	$4.9 \cdot 10^{-6}$
	$1/2_1^+$	$2.2 \cdot 10^{-4}$
$5/2_1^+$	$7/2_1^-$	$1.4 \cdot 10^{-5}$
	$3/2_1^-$	$1.4 \cdot 10^{-6}$
	$7/2_2^-$	$2.4 \cdot 10^{-5}$
	$5/2_1^-$	$5.9 \cdot 10^{-7}$
	$3/2_2^-$	$1.9 \cdot 10^{-6}$
	$5/2_2^-$	$5.3 \cdot 10^{-7}$
	$3/2_3^-$	$6.5 \cdot 10^{-6}$
$3/2_3^-$	$3/2_1^+$	$2.4 \cdot 10^{-5}$
	$5/2_1^-$	$9.9 \cdot 10^{-6}$

Table A.1: B(E1) reduced transition probabilities predicted by the *spdf-u-mix* interaction.

E	J^π	ν occupation							π occupation		
[keV]		$0d_{5/2}$	$1s_{1/2}$	$0d_{3/2}$	$0f_{7/2}$	$1p_{3/2}$	$0f_{5/2}$	$1p_{1/2}$	$0d_{5/2}$	$1s_{1/2}$	$0d_{3/2}$
0	$7/2^-_1$	5.967	1.963	3.874	1.099	0.065	0.027	0.005	5.804	1.745	0.451
534	$3/2^-_1$	5.965	1.964	3.842	0.405	0.790	0.008	0.025	5.965	1.964	0.511
1681	$5/2^-_1$	5.777	1.478	2.724	2.561	0.336	0.0991	0.0257	5.239	1.115	1.646
1756	$3/2^+_1$	5.921	1.882	3.030	1.777	0.263	0.102	0.025	5.588	1.391	1.021
1817	$3/2^-_2$	5.786	1.502	2.689	2.327	0.877	0.077	0.042	5.309	1.089	1.602
1863	$7/2^-_2$	5.772	1.448	2.726	2.617	0.306	0.111	0.021	5.236	1.134	1.630
2262	$1/2^+_1$	5.860	1.388	3.311	2.076	0.243	0.102	0.022	5.516	1.183	1.301
2447	$5/2^-_2$	5.967	1.963	3.874	1.099	0.065	0.027	0.005	5.804	1.745	0.451
2456	$1/2^-_1$	5.960	1.957	3.815	0.239	0.136	0.034	0.860	5.801	1.796	0.403
2599	$3/2^-_3$	5.764	1.517	2.664	2.224	0.700	0.085	0.046	5.093	1.209	1.697
2797	$5/2^+_1$	5.913	1.879	3.004	1.668	0.429	0.0745	0.034	5.636	1.219	1.145
2858	$3/2^-_4$	5.957	1.932	3.802	0.959	0.318	0.031	0.011	5.746	1.137	1.117
2963	$3/2^+_2$	5.795	1.533	2.697	2.377	0.443	0.123	0.033	5.412	1.056	1.532
3062	$1/2^-_2$	5.766	1.464	2.752	2.404	0.453	0.082	0.079	5.165	1.141	1.694
3329	$1/2^+_2$	5.706	1.391	2.421	2.888	0.399	0.161	0.034	5.176	1.115	1.709
3439	$5/2^+_2$	5.770	1.352	2.973	2.403	0.357	0.114	0.031	5.371	1.092	1.537

Table A.2: Shell-model occupation numbers for the states of ^{37}S below 3.5 MeV.

J^π		$7/2^-$		$5/2^-$		$3/2^-$				$1/2^-$	
	n	1	2	1	2	1	2	3	4	1	2
$7/2^-$	1	–	0.001 2.5(-4)	0.015 1.4	0.04 1.8	5.04	0.18	0.003	0.95		
	2		–	0.017 14.9	0.003 1.44	0.23	6.7	6.4	0.075		
$5/2^-$	1			–	2.6(-4) 0.62	0.013 0.26	8.4(-4) 12	0.003 6.6	0.095 0.26	0.09	1.24
	2				–	0.19 1.3	0.006 0.31	0.085 0.03	0.93 2.1	0.26	0.57
$3/2^-$	1					–	6.6(-4) 0.28	0.003 0.08	0.06 0.43	0.74 2.2	0.014 0.43
	2						–	0.006 7.80(-4)	0.02 0.69	0.014 0.13	0.03 13.8
	3							–	0.02 0.06	0.008 0.26	0.02 6.93
	4								–	0.067 0.14	0.05 0.04
$1/2^-$	1									–	4.0(-4)
	2										–

Table A.3: Shell-model mixed reduced transition probabilities for the negative parity states of ^{37}S below 3.5 MeV, listed by spin value and index number (J^π_n). Values are in W.u., and always calculated from the higher-lying state to the lower one. When both M1 and E2 characters are allowed, B(M1) is reported first, followed by B(E2). Numbers in parentheses are powers of 10.

Ringraziamenti

Ringrazio i miei genitori, Rosella e Gianfranco, e mia sorella Daniela. Grazie alla mia famiglia, zii e zie, cugine e cugini. Grazie alle nonne.

Grazie a Olga. Sopportarci e supportarci da sedici anni è un piacere e un privilegio. Grazie a Sara, Martina, Qi, Roberto, Edoardo, Giuseppe e Oscar - molti distanti, ma sempre vicini.

Grazie ai miei relatori, Javier, Andrea e Franco - per il sostegno, le indicazioni, la pazienza, la disponibilità, soprattutto nel *rush* finale degli ultimi giorni.

Grazie ad Alain, per così troppe cose che sarebbe difficile elencare. Per avermi insegnato molto di più della fisica, un insulto alla volta.

Grazie a Sara e Matuš, compagni di scrivania e di vita in questi tre anni passati assieme.

Grazie a tutti gli amici e colleghi di LNL, passati e presenti, con cui ho condisivo tutti o parte di questi tre anni. Rosa, Aysegul, Daniele, Irene, Julgen, Benito, Filippo, Elia, Raquel, Damiano, Giuseppe, Matus, Pablo, Marta. I caffè, i pranzi della mensa, i turni di notte e gli shift dell'azoto son stati più leggeri grazie a voi. Ogni giorno è un privilegio. Grazie anche agli amici di Padova, Milano e Firenze.

Grazie a Loris.

Bibliography

[1] A. Ekström, C. Forssén, G. Hagen *et al.*, "What is ab initio in nuclear theory?", Front. Phys. **11**, 10.3389/fphy.2023.1129094 (2023).

[2] E. Caurier, "Shell model and nuclear structure", Prog. Part. Nucl. Phys. **59**, International Workshop on Nuclear Physics 28th Course, 226–242 (2007).

[3] M. Bender, P.-H. Heenen and P.-G. Reinhard, "Self-consistent mean-field models for nuclear structure", Rev. Mod. Phys. **75**, 121–180 (2003).

[4] Bally, B. and Sánchez-Fernández, A. and Rodríguez, T. R., "Symmetry-projected variational calculations with the numerical suite taurus", Eur. Phys. J. A **57**, 69 (2021).

[5] Stroberg, S. Ragnar and Hergert, Heiko and Bogner, Scott K. and Holt, Jason D., "Nonempirical Interactions for the Nuclear Shell Model: An Update", Annu. Rev. Nucl. Part. Sci. **69**, 307–362 (2019).

[6] R. Casten, *Nuclear Structure from a Simple Perspective*, Oxford science publications (Oxford University Press, 2000).

[7] K. Krane, *Introductory Nuclear Physics* (John Wiley & Sons, 1991).

[8] H. Grawe, "Shell Model from a Practitioner's Point of View", in The Euroschool Lectures on Physics with Exotic Beams, Vol. I, edited by J. Al-Khalili and E. Roeckl (2004), pp. 33–75.

[9] K. Heyde, *Basic Ideas and Concepts in Nuclear Physics: An Introductory Approach, Third Edition*, Fundamental and applied nuclear physics series (CRC Press, 2020).

[10] M. Dufour and A. P. Zuker, "Realistic collective nuclear Hamiltonian", Phys. Rev. C **54**, 1641–1660 (1996).

[11]E. Caurier, G. Martínez-Pinedo, F. Nowacki *et al.*, "The shell model as a unified view of nuclear structure", Rev. Mod. Phys. **77**, 427–488 (2005).

[12]T. Otsuka, A. Gade, O. Sorlin, T. Suzuki and Y. Utsuno, "Evolution of shell structure in exotic nuclei", Rev. Mod. Phys. **92**, 015002 (2020).

[13]A. Poves and F. Nowacki, "The nuclear shell model", in An advanced course in modern nuclear physics, edited by J. Arias and M. Lozano, Lecture Notes in Physics Vol. 581 (2001), pp. 70–101.

[14]T. T. S. Kuo and G. E. Brown, "Reaction matrix elements for the 0f-1p shell nuclei", Nucl. Phys. A **114**, 241–279 (1968).

[15]B. Alex Brown and W. A. Richter, "A new interaction for the sd shell?", J. Phys.: Conf. Ser. **20**, 145 (2005).

[16]M. Honma, T. Otsuka, B. A. Brown and T. Mizusaki, "Effective interaction for pf-shell nuclei", Phys. Rev. C **65**, 061301 (2002).

[17]M. Honma, T. Otsuka, T. Mizusaki and M. Hjorth-Jensen, "New effective interaction for f_5pg_9-shell nuclei", Phys. Rev. C **80**, 064323 (2009).

[18]E. Caurier, F. Nowacki and A. Poves, "Merging of the islands of inversion at $N = 20$ and $N = 28$", Phys. Rev. C **90**, 014302 (2014).

[19]B. A. Brown, A. Etchedgoyen, W. D. M. Rae *et al.*, "The computer code OXBASH", MSU-NSCL Report **524** (1984).

[20]B. Brown and W. D. M. Rae, "The Shell-Model Code NuShellX@MSU", Nucl. Data Sheets **120**, 115–118 (2014).

[21]N. Shimizu, T. Mizusaki, Y. Utsuno and Y. Tsunoda, "Thick-restart block Lanczos method for large-scale shell-model calculations", Comp. Phys. Comm. **244**, 372–384 (2019).

[22]E. Caurier and F. Nowacki, "Present Status of Shell Model Techniques", Act. Phys. Pol. B **30**, 705 (1999).

[23]https://commons.wikimedia.org/wiki/File:Table_isotopes_en.svg, (accessed: 06.02.2024).

[24]H. Morinaga and T. Yamazaki, *In-beam Gamma-ray Spectroscopy* (North-Holland Publishing Company, 1976).

[25]V. F. Weisskopf, "Radiative Transition Probabilities in Nuclei", Phys. Rev. **83**, 1073–1073 (1951).

[26]G. Knoll, *Radiation Detection and Measurement* (Wiley, 2000).

[27]P. J. Nolan and J. F. Sharpey-Schafer, "The measurement of the lifetimes of excited nuclear states", Rep. Prog. Phys. **42**, 1 (1979).

[28]A. Dewald, O. Möller and P. Petkov, "Developing the Recoil Distance Doppler-Shift technique towards a versatile tool for lifetime measurements of excited nuclear states", Prog. Part. Nucl. Phys. **67**, 786–839 (2012).

[29]Pérez-Vidal, R. M., Galtarossa, F., Mijatović, T. *et al.*, "Nuclear structure advancements with multi-nucleon transfer reactions", Eur. Phys. J. A **59**, 114 (2023).

[30]J. Spencer and H. Enge, "Split-pole magnetic spectrograph for precision nuclear spectroscopy", Nucl. Instr. Meth. **49**, 181–193 (1967).

[31]K. Wimmer, "Nucleon transfer reactions with radioactive beams", J. Phys. G **45**, 033002 (2018).

[32]D. Mengoni, D. Beaumel, W. N. Catford *et al.*, "Advances in nuclear structure via charged particle reactions with AGATA.", Eur. Phys. J. A **59**, 117 (2023).

[33]W. N. Catford, "What Can We Learn from Transfer, and How Is Best to Do It?", in The Euroschool on Exotic Beams, Vol. IV, edited by C. Scheidenberger and M. Pfützner, Lecture Notes in Physics (2014), pp. 67–122.

[34]H. Bateman, "The solution of a system of differential equations occurring in the theory of radioactive transformations", in Proc. cambridge philos. soc. Vol. 15 (1910), pp. 423–427.

[35]I. Thompson and F. Nunes, *Nuclear Reactions for Astrophysics: Principles, Calculation and Applications of Low-Energy Reactions* (Cambridge University Press, 2009).

[36]A. M. Moro, "*Calculations for nuclear reactions*" *course for Padova University Master course in Physics*, https://github.com/ammoro, (accessed: 05/03/2024).

[37]S. Bottoni, "Cluster-transfer reactions with radioactive beams: a spectroscopic tool for neutron-rich nuclei", PhD thesis (Università Statale degli Studi di Milano, KU Leuven, 2015).

[38]P. D. Kunz and E. Rost, "The Distorted-Wave Born Approximation", in *Computational Nuclear Physics 2: Nuclear Reactions*, edited by K. Langanke, J. A. Maruhn and S. E. Koonin (Springer New York, 1993), pp. 88–107.

[39]M. H. MACFARLANE and S. C. PIEPER, "PTOLEMY: a program for heavy-ion direct-reaction calculations", ANL–76-11 (1978).

[40]TOSTEVIN, J. A., *Surrey version of the TWOFNR code (of M. Toyama, M. Igarashi and N. Kishida)*, 1972.

[41]http://www.fresco.org.uk/, (last accessed: 06.03.2024).

[42]H. AN and C. CAI, "Global deuteron optical model potential for the energy range up to 183 MeV", Phys. Rev. C **73**, 054605 (2006).

[43]A. KONING and J. DELAROCHE, "Local and global nucleon optical models from 1 keV to 200 MeV", Nucl. Phys. A **713**, 231–310 (2003).

[44]O. SORLIN and M.-G. PORQUET, "Nuclear magic numbers: New features far from stability", Prog. Part. Nucl. Phys. **61**, 602–673 (2008).

[45]B. V. PRITYCHENKO, T. GLASMACHER, P. D. COTTLE *et al.*, "Role of intruder configurations in ^{26,28}Ne and ^{30,32}Mg", Phys. Lett. B **461**, 322–328 (1999).

[46]K. WIMMER, T. KRÖLL, R. KRÜCKEN *et al.*, "Discovery of the Shape Coexisting 0^+ State in ^{32}Mg by a Two Neutron Transfer Reaction", Phys. Rev. Lett. **105**, 252501 (2010).

[47]*National Nuclear Data Center*, https://www.nndc.bnl.gov/, information extracted from the NuDat 3.0 database.

[48]A. POVES, private communication.

[49]M. GOEPPERT MAYER, *The Shell Model* (Elsevier, 1972).

[50]G. BURGUNDER, O. SORLIN, F. NOWACKI *et al.*, "Experimental Study of the Two-Body Spin-Orbit Force in Nuclei", Phys. Rev. Lett. **112**, 042502 (2014).

[51]N. IMAI, Y. HIRAYAMA, Y. X. WATANABE *et al.*, "Isobaric analog resonances of the $N = 21$ nucleus ^{35}Si", Phys. Rev. C **85**, 034313 (2012).

[52]S. R. STROBERG, A. GADE, J. A. TOSTEVIN *et al.*, "Single-particle structure of silicon isotopes approaching ^{42}Si", Phys. Rev. C **90**, 034301 (2014).

[53]B. V. PRITYCHENKO, T. GLASMACHER, P. D. COTTLE *et al.*, "Structure of the "island of inversion" nucleus ^{33}Mg", Phys. Rev. C **65**, 061304 (2002).

[54]M. BARANGER, "A definition of the single-nucleon potential", Nucl. Phys. A **149**, 225–240 (1970).

[55]B. P. KAY, C. R. HOFFMAN and A. O. MACCHIAVELLI, "Effect of Weak Binding on the Apparent Spin-Orbit Splitting in Nuclei", Phys. Rev. Lett. **119**, 182502 (2017).

[56]O. Sorlin, F. de Oliveira Santos and J. P. Ebran, "Reduced spin-orbit splitting in ^{35}Si: Weak binding or density-depletion effect?", Phys. Lett. B **809**, 135740 (2020).

[57]T. Duguet and G. Hagen, "Ab initio approach to effective single-particle energies in doubly closed shell nuclei", Phys. Rev. C **85**, 034330 (2012).

[58]V. Somà and T. Duguet, "On the calculation and use of effective single-particle energies: the example of the neutron $1d_{3/2}$-$1d_{5/2}$ splitting along N=20 isotones", Philos. Trans. R. Soc. A **382**, 10.1098/rsta.2023.0117 (2024).

[59]T. Duguet, V. Somà, S. Lecluse *et al.*, "Ab initio calculation of the potential bubble nucleus ^{34}Si", Phys. Rev. C **95**, 034319 (2017).

[60]M. Grasso, L. Gaudefroy, E. Khan *et al.*, "Nuclear "bubble" structure in ^{34}Si", Phys. Rev. C **79**, 034318 (2009).

[61]A. Mutschler, L. A., O. Sorlin *et al.*, "A proton density bubble in the doubly magic ^{34}Si nucleus", Nat. Phys. **13**, 152–156 (2017).

[62]E. Davis, T. Bonner, D. Worley and R. Bass, "The disintegration of Ar36 and Ar40 by neutrons", Nucl. Phys. **55**, 643–656 (1964).

[63]S. Kardonsky, H. L. Finston and E. T. Williams, "$^{40}\mathrm{Ar}(n,\alpha)^{37}\mathrm{S}$ Reaction at 14.4 MeV", Phys. Rev. C **4**, 840–846 (1971).

[64]Š. Piskoř, P. Franc, J. Křemének and W. Schäferlingová, "Spectroscopic information on ^{35}S and ^{37}S from the (d, p) reaction", Nucl. Phys. A **414**, 219–239 (1984).

[65]C. E. Thorn, J. W. Olness, E. K. Warburton and S. Raman, "^{36}S(d,p)^{37}S and ^{34,36}S(d,^{3}He)^{33,35}P reactions", Phys. Rev. C **30**, 1442–1453 (1984).

[66]G. Eckle, H. Kader, H. Clement *et al.*, "A ^{36}S(d,p) study with high energy resolution", Nucl. Phys. A **491**, 205–226 (1989).

[67]S. Raman, W. Ratynski, E. T. Jurney *et al.*, "$^{36}\mathrm{S}(n,\gamma)^{37}\mathrm{S}$ reaction with thermal neutrons and decay of ^{37}S to levels in ^{37}Cl", Phys. Rev. C **30**, 26–30 (1984).

[68]S. Raman, R. F. Carlton, J. C. Wells *et al.*, "Thermal neutron capture gamma rays from sulfur isotopes: Experiment and theory", Phys. Rev. C **32**, 18–69 (1985).

[69]H. Beer, C. Coceva, R. Hofinger *et al.*, "Measurement of direct neutron capture by neutron-rich sulfur isotopes", Nucl. Phys. A **621**, 235–238 (1997).

[70]DUFOUR, J.P., DEL MORAL, R., FLEURY, A. AND OTHERS, "Beta decay of ^{17}C, ^{19}N, ^{22}O, ^{24}F, ^{26}Ne, ^{32}Al, ^{34}Al, $^{35-36}$Si, $^{36-37-38P,40}$S.", Z. Physik A, 487–488 (1986).

[71]R. CHAPMAN, Z. M. WANG, M. BOUHELAL *et al.*, "Particle-core coupling in ^{37}S", Phys. Rev. C **93**, 044318 (2016).

[72]L. GROCUTT, R. CHAPMAN, M. BOUHELAL *et al.*, "Lifetime measurements of states of ^{35}S, ^{36}S, ^{37}S, and ^{38}S using the AGATA γ-ray tracking spectrometer", Phys. Rev. C **106**, 024314 (2022).

[73]R. NICOLÁS DEL ÁLAMO, to be submitted, PhD thesis (University of Padova, 2026).

[74]K. L. WANG, J. G. WANG, X. H. ZHOU *et al.*, "Lifetime measurement of the first excited state in ^{37}S", Phys. Rev. C **94**, 044316 (2016).

[75]*Infn-lnl official website*, https://www.lnl.infn.it/en/tandem-2/, (accessed: 17/06/2024).

[76]S. AKKOYUN, A. ALGORA, B. ALIKHANI *et al.*, "AGATA - Advanced GAmma Tracking Array", Nucl. Instr. Meth. Phys. Res. A **668**, 26–58 (2012).

[77]PASCHALIS, S. AND LEE, I.Y. AND MACCHIAVELLI, A.O. AND OTHERS, "The performance of the Gamma-Ray Energy Tracking In-beam Nuclear Array GRETINA", Nucl. Instr. Meth. Phys. Res. A **709**, 44–55 (2013).

[78]I. LEE, "Gamma-ray tracking detectors", Nucl. Instr. Meth. Phys. Res. A **422**, 195–200 (1999).

[79]E. CLÉMENT, A. BRACCO, A. GADEA *et al.*, "Organisation of the AGATA collaboration and physics campaigns", Eur. Phys. J. A **59**, 10.1140/epja/s10050-023-01057-w (2023).

[80]A. GADEA, E. FARNEA, J. J. VALIENTE-DOBÓN *et al.*, "Conceptual design and infrastructure for the installation of the first AGATA sub-array at LNL", Nucl. Instr. Meth. Phys. Res. A **654**, 88–96 (2011).

[81]E. FARNEA, F. RECCHIA, D. BAZZACCO *et al.*, "Conceptual design and Monte Carlo simulations of the AGATA array", Nucl. Instr. Meth. Phys. Res. A **621**, 331–343 (2010).

[82]C. DOMINGO-PARDO, D. BAZZACCO, P. DOORNENBAL *et al.*, "Conceptual design and performance study for the first implementation of AGATA at the in-flight RIB facility of GSI", Nucl. Instr. Meth. Phys. Res. A **694**, 297–312 (2012).

[83]N. Lalović, C. Louchart, C. Michelagnoli *et al.*, "Performance of the AGATA γ-ray spectrometer in the PreSPEC set-up at GSI", Nucl. Instr. Meth. Phys. Res. A **806**, 258–266 (2016).

[84]E. Clément, C. Michelagnoli, G. de France *et al.*, "Conceptual design of the AGATA 1π array at GANIL", Nucl. Instr. Meth. Phys. Res. A **855**, 1–12 (2017).

[85]J. Ljungvall, R. M. Pérez-Vidal, A. Lopez-Martens *et al.*, "Performance of the Advanced GAmma Tracking Array at GANIL", Nucl. Instr. Meth. Phys. Res. A **955**, 163297 (2020).

[86]J. J. Valiente-Dobón, R. Menegazzo, A. Goasduff *et al.*, "Conceptual design of the AGATA 2π array at LNL", Nucl. Instr. Meth. Phys. Res. A **1049**, 168040 (2023).

[87]M. Ballan, S. Bottoni, M. Caamaño *et al.*, "Nuclear physics midterm plan at Legnaro National Laboratories (LNL).", Eur. Phys. J. Plus **138**, 709 (2023).

[88]A. M. Stefanini, L. Corradi, G. Maron *et al.*, "The heavy-ion magnetic spectrometer PRISMA", Nucl. Phys. A **701**, 217–221 (2002).

[89]M. Rocchini, K. Hadyńska-Klęk, A. Nannini *et al.*, "SPIDER: A Silicon PIe DEtectoR for low-energy Coulomb-excitation measurements", Nucl. Instr. Meth. Phys. Res. A **971**, 164030 (2020).

[90]D. Testov, D. Mengoni, A. Goasduff *et al.*, "The 4π highly-efficient light-charged-particle detector EUCLIDES, installed at the GALILEO array for in-beam -ray spectroscopy", Eur. Phys. J. A **55**, 47 (2019).

[91]J. J. Valiente-Dobón, A. Gadea, L. Corradi *et al.*, "Studies of the neutron-rich nuclei with the CLARA-PRISMA setup and description of the heavy-ion detector DANTE", Act. Phys. Pol. B **37**, 225–229 (2006).

[92]A. Gottardo and J. J. Valiente-Dobon, "Performance of the DANTE detector", Nucl. Phys. A **805**, 606 (2008).

[93]D. Mengoni, J. A. Dueñas, M. Assié *et al.*, "Digital pulse-shape analysis with a TRACE early silicon prototype", Nucl. Instr. Meth. Phys. Res. A **764**, 241–246 (2014).

[94]S. Capra, D. Mengoni, J. A. Dueñas *et al.*, "Performance of the new integrated front-end electronics of the TRACE array commissioned with an early silicon detector prototype", Nucl. Instr. Meth. Phys. Res. A **935**, 178–184 (2019).

[95]D. Dell'Aquila, I. Lombardo, G. Verde *et al.*, "OSCAR: A new modular device for the identification and correlation of low energy particles", Nucl. Instr. Meth. Phys. Res. A **877**, 227–237 (2018).

[96]J. J. Valiente-Dobón, G. Jaworski, A. Goasduff *et al.*, "NEDA — NEutron Detector Array", Nucl. Instr. Meth. Phys. Res. A **927**, 81–86 (2019).

[97]A. Maj, F. Azaiez, D. Jenkins *et al.*, "The PARIS project", Act. Phys. Pol. B **40**, 565 (2009).

[98]R. J. Aliaga, V. Herrero-Bosch, S. Capra *et al.*, "Conceptual design of the TRACE detector readout using a compact, dead time-less analog memory ASIC", Nucl. Instr. Meth. Phys. Res. A **800**, 34–39 (2015).

[99]*GRIT webpage*, `https://grit.in2p3.fr/`, (accessed: 17/06/2024).

[100]M. Sedlák, A. Gottardo, R. Pengo *et al.*, "The Cryogenic TArget for DIrect Reactions (CTADIR) project", Nuov. Cim. C **5**, 108 (2022).

[101]A. Gillibert, A. Corsi, F. Flavigny *et al.*, "Windowless thin solid-hydrogen target: CHyMENE", Eur. Phys. J. A **49**, 155 (2002).

[102]F. Favela, L. Acosta, E. Andrade *et al.*, "New supersonic gas jet target for low energy nuclear reaction studies", Phys. Rev. Accel. Beams **18**, 123502 (2015).

[103]N. Bez, M. Rampazzo, L. Ramina *et al.*, "Mechanical infrastructure for AGATA at LNL", LNL Ann. Rep., 197–198 (2020).

[104]Smith, R., Menegazzo, R., Aufranc, C., Bez, N. *et al.*, "Agata: mechanics and infrastructures", Eur. Phys. J. A **59**, 166 (2023).

[105]W. Raniero, H. Hess, D. R. Napoli *et al.*, "AGATA triple cluster detector installation at LNL-INFN", LNL Ann. Rep., 25–26 (2021).

[106]D. Scarpa, N. Bez, F. Veronese *et al.*, "AGATA installation and alignment at LNL", LNL Ann. Rep., 185–186 (2021).

[107]A. Wiens, H. Hess, B. Birkenbach *et al.*, "The AGATA triple cluster detector", Nucl. Instr. Meth. Phys. Res. A **618**, 223–233 (2010).

[108]A. Pullia, G. Pascovici, B. Cahan *et al.*, "The AGATA charge-sensitive preamplifiers with built-in active-reset device and pulser", in IEEE Symposium Conference Record Nuclear Science 2004. Vol. 3 (2004), pp. 1411–1414.

[109]V. T. Jordanov, G. F. Knoll, A. C. Huber and J. A. Pantazis, "Digital techniques for real-time pulse shaping in radiation measurements", Nucl. Instr. Meth. Phys. Res. A **353**, 261–264 (1994).

[110]V. T. JORDANOV and G. F. KNOLL, "Digital synthesis of pulse shapes in real time for high resolution radiation spectroscopy", Nucl. Instr. Meth. Phys. Res. A **345**, 337–345 (1994).

[111]A. GEORGIEV and W. GAST, "Digital pulse processing in high resolution, high throughput, gamma-ray spectroscopy", IEEE Trans. Nucl. Sci. **40**, 770–779 (1993).

[112]G. BENZONI, S. COELLI, A. CAPSONI *et al.*, "Scattering chamber for AGATA installation at LNL", LNL Ann. Rep., 37–38 (2020).

[113]G. BENZONI, R. M. PÉREZ-VIDAL, R. ESCUDEIRO *et al.*, "Installation of the Scattering Chamber for the AGATA-PRISMA Campaign", LNL Ann. Rep., 41–42 (2021).

[114]A. GOASDUFF, D. MENGONI, F. RECCHIA *et al.*, "The GALILEO γ-ray array at the Legnaro National Laboratories", Nucl. Instr. Meth. Phys. Res. A **1015**, 165753 (2021).

[115]J. PELLUMAJ, "Study of the collectivity of intruder states in ^{83}Se and development of a new technique to measure lifetimes in the N=126 region", PhD thesis (Università degli Studi di Ferrara, 2022).

[116]M. BALOGH, M. ROCCHINI, M. SEDLÁK *et al.*, "Coupling of the SPIDER charged-particle detector to AGATA", LNL Ann. Rep., 16–17 (2021).

[117]D. BARRIENTOS, V. GONZÁLEZ, M. BELLATO *et al.*, "Development of the control card for the digitizers of the second generation electronics of AGATA", in 2012 18th IEEE-NPSS Real Time Conference (2012), pp. 1–3.

[118]J. GUTLEBER, S. MURRAY and L. ORSINI, "Towards a homogeneous architecture for high-energy physics data acquisition systems", Comp. Phys. Comm. **153**, 155–163 (2003).

[119]S. BRAMBILLA, A. GOASDUFF, N. TONIOLO and J. SKOWRONSKI, "Coupling the CAEN digitizers to the GTS system and XDAQ Data Acquisition system", LNL Ann. Rep., 121–122 (2020).

[120]*DPP-PHA Registers Manual* (CAEN S.p.A., 2021).

[121]M. BELLATO, D. BORTOLATO, J. CHAVAS *et al.*, "Sub-nanosecond clock synchronization and trigger management in the nuclear physics experiment AGATA", J. Instr. **8**, P07003 (2013).

[122]A. GOASDUFF, C. FRANSEN, A. DEWALD *et al.*, "A new dedicated plunger device for the GALILEO γ-ray array", LNL Ann. Rep., 91–92 (2015).

[123]C. Müller-Gatermann, F. von Spee, A. Goasduff *et al.*, "A new dedicated plunger device for the GALILEO γ-ray detector array", Nucl. Instr. Meth. Phys. Res. A **920**, 95–99 (2019).

[124]I. Zanon, A. Goasduff and N. Bez, "The AGATA Plunger", LNL Ann. Rep., 29 (2021).

[125]M. Loriggiola and L. Loriggiola, private communication.

[126]O. B. Tarasov and D. Bazin, "LISE++: Radioactive beam production with in-flight separators", Nucl. Instr. Meth. Phys. Res. B **266**, 4657–4664 (2008), http://lise.nscl.msu.edu.

[127]*agapro repository*, `https://gitlab.in2p3.fr/ip2igamma/agapro`, (accessed: 17/06/2024).

[128]Stézowski, O., Dudouet, J., Goasduff, A. *et al.*, "Advancements in software developments", Eur. Phys. J. A **59**, 119 (2023).

[129]R. Brun and F. Rademakers, "ROOT — An object oriented data analysis framework", Nucl. Instr. Meth. Phys. Res. A **389**, New Computing Techniques in Physics Research V, 81–86 (1997).

[130]D. Brugnara, M. Sedlák, E. Pilotto *et al.*, *Agataselector*, version 0.3.0, Sept. 2023.

[131]*adf repository*, `https://gitlab.in2p3.fr/ip2igamma/adf`, (accessed: xx.yy.zzzz).

[132]B. Bruyneel, B. Birkenbach and P. Reiter, "Pulse shape analysis and position determination in segmented HPGe detectors: The AGATA detector library", Eur. Phys. J. A **52**, `10.1140/epja/i2016-16070-9` (2016).

[133]P.-A. Söderström, F. Recchia, J. Nyberg *et al.*, "Interaction position resolution simulations and in-beam measurements of the AGATA HPGe detectors", Nucl. Instr. Meth. Phys. Res. A **638**, 96–109 (2011).

[134]A. J. Boston, F. C. L. Crespi, G. Duchêne *et al.*, "Agata characterisation and pulse shape analysis.", Eur. Phys. J. A **59**, 213 (2023).

[135]R. Venturelli and D. Bazzacco, "Adaptive Grid Search as Pulse Shape Analysis Algorithm for γ-Tracking and Results", LNL Ann. Rep., 220–221 (2004).

[136]B. Bruyneel, B. Birkenbach, J. Eberth *et al.*, "Correction for hole trapping in AGATA detectors using pulse shape analysis", Eur. Phys. J. A **49**, 61 (2013).

[137]A. Korichi and T. Lauritsen, "Tracking γ rays in highly segmented HPGe detectors: A review of AGATA and GRETINA", Eur. Phys. J. A **55**, 121 (2019).

[138]F. C. L. Crespi, J. Ljungvall, A. Lopez-Martens *et al.*, "AGATA: performance of γ-ray tracking and associated algorithms.", Eur. Phys. J. A **59**, 111 (2023).

[139]F. James and M. Roos, "Minuit: A System for Function Minimization and Analysis of the Parameter Errors and Correlations", Comput. Phys. Commun. **10**, 343–367 (1975).

[140]R. M. Pérez-Vidal, F. Angelini, A. Ertoprak *et al.*, "AGATA Performance II: Efficiency and P/T", LNL Ann. Rep., 56–57 (2022).

[141]D. Radford, "ESCL8R and LEVIT8R: Software for interactive graphical analysis of HPGe coincidence data sets", Nucl. Instr. Meth. Phys. Res. A **361**, 297–305 (1995).

[142]Z. Kis, B. Fazekas, J. Östör *et al.*, "Comparison of efficiency functions for Ge gamma-ray detectors in a wide energy range", Nucl. Instr. Meth. Phys. Res. A **418**, 374–386 (1998).

[143]M. Labiche, J. Ljungvall, F. C. L. Crespi *et al.*, "Simulation of the AGATA spectrometer and coupling with ancillary detectors", Eur. Phys. J. A **59**, 10.1140/epja/s10050-023-01036-1 (2023).

[144]*Agata Simulation Code repository*, https://gitlab.com/malabi-agata/agata, (accessed: 07/06/2024).

[145]S. Agostinelli, J. Allison, K. Amako *et al.*, "Geant4 — a simulation toolkit", Nucl. Instr. Meth. Phys. Res. A **506**, 250–303 (2003).

[146]P. Petkov and C. Müller-Gatermann, "On the imprecisions that may be induced when applying the Blaugrund approximation for the analysis of Doppler-shift attenuation lifetime measurements", Nucl. Instr. Meth. Phys. Res. A **915**, 40–46 (2019).

[147]*IAEA Stopping Power Database, version 2024-03*, https://nds.iaea.org/stopping, (accessed: 15/03/2024).

[148]J. F. Ziegler, M. Ziegler and J. Biersack, "SRIM – The stopping and range of ions in matter (2010)", Nucl. Instr. Meth. Phys. Res. B **268**, 19th International Conference on Ion Beam Analysis, 1818–1823 (2010).

[149]M. J. Berger, M. Inokuti, H. H. Andersen *et al.*, "Stopping Powers and Ranges for Protons and Alpha Particles", J. ICRU **os-25**, 107–181 (1993).

[150]R. Bimbot, H. Geissel, H. Paul *et al.*, "Stopping of Ions Heavier than Helium", J. ICRU **5**, i–253 (2005).

[151]B. Armitage and B. Hooton, "Energy loss of oxygen and sulphur ions in matter", Nucl. Instr. Meth. **58**, 29–38 (1968).

[152]H. Schmidt-Böcking, G. Rühle and K. Bethge, "A New Method to Determine the Energy Loss of Heavy Ions in Solids", in *Atomic Collisions in Solids: Volume 1*, edited by Datz, S. and Appleton, B. R. and Moak, C. D. (Springer US, Boston, MA, 1975), pp. 77–83.

[153]J. S. Forster, D. Ward, H. R. Andrews *et al.*, "Stopping power measurement for ^{19}F, ^{24}Mg, ^{27}Al, ^{32}S and ^{35}Cl at energies ∼0.2 to ∼3.5 MeV/nucleon in Ti, Fe, Ni, Cu, Ag and Au", Nucl. Instr. Meth. **136**, 349–359 (1976).

[154]D. Ward, H. R. Andrews, I. V. Mitchell *et al.*, "Systematics for the Z_1-oscillation in stopping powers of various solid materials", Can. J. Phys. **57**, 79–92 (1979).

[155]S. Ouichaoui, L. Rosier, E. Hourany *et al.*, "Stopping powers of Al, Cu, Ag and Au media for 1.47 MeV/u ^{127}I, 2 MeV/u ^{32}S and ^{79}Br ions", Nucl. Instr. Meth. Phys. Res. B **95**, 463–469 (1995).

[156]P. K. Diwan, S. Kumar, V. Sharma *et al.*, "Slowing down of MeV heavy ions with Z=6–29 in PEN (C7H5O2)", Nucl. Instr. Meth. Phys. Res. B **201**, 389–395 (2003).

[157]V. Sharma, P. Diwan, Pratibha *et al.*, "Stopping power of polymeric foils for swift heavy ions", Nucl. Instr. Meth. Phys. Res. B **266**, 3988–3992 (2008).

[158]D. C. Lorents and E. J. Zimmerman, "Stopping of Low-Energy H^+ and He^+ Ions in Plastics", Phys. Rev. **113**, 1199–1203 (1959).

[159]C. A. Sautter and E. J. Zimmerman, "Stopping Cross Sections of Carbon and Hydrocarbon Solids for Low-Energy Protons and Helium Ions", Phys. Rev. **140**, A490–A498 (1965).

[160]A. K. M. M. Haque, A. Mohammadi and H. Nikjoo, "Stopping power for low-energy protons", J. Phys. D **22**, 1196 (1989).

[161]N. Galinski, S. K. L. Sjue, G. C. Ball *et al.*, "Lifetime measurements of states in ^{15}O", Phys. Rev. C **90**, 035803 (2014).

[162]E. K. Warburton and J. A. Becker, "Shell-model description of the β^- decay of the N=21 and 22 isotones ^{34}Al,^{36}Si, and ^{37}P", Phys. Rev. C **37**, 754–765 (1988).

[163]W. A. Sterrenburg, G. van Middelkoop, J. A. G. de Raedt *et al.*, "Spectroscopy of ^{39}Ar with the (α, nγ) and (d, pγ) reactions", Nucl. Phys. A **306**, 157–172 (1978).

[164]F. Ajzenberg-Selove and G. Igo, "A study of triton induced reactions in ^{37}Cl and ^{44}Ca", Nucl. Phys. A **142**, 641–648 (1970).

[165]C. Fransen, A. Dewald, T. Baumann *et al.*, "New developments on the recoil distance doppler-shift method", J. Phys.: Conf. Ser. **205**, 012043 (2010).

[166]D. Radeck, V. Werner, G. Ilie *et al.*, "Simultaneous deorientation and lifetime measurement in ^{98}Ru using the recoil distance Doppler shift method in inverse Coulomb excitation", Phys. Rev. C **85**, 014301 (2012).

[167]L. J. Sun, C. Fry, B. Davids *et al.*, "First application of Markov chain Monte Carlo-based Bayesian data analysis to the Doppler-shift attenuation method", Phys. Lett. B **839**, 137801 (2023).

[168]J. J. Valiente-Dobón, A. Poves, A. Gadea and B. Fernández-Domínguez, "Broken mirror symmetry in ^{36}S and ^{36}Ca", Phys. Rev. C **98**, 011302 (2018).

[169]L. Lalanne, O. Sorlin, A. Poves *et al.*, "Structure of ^{36}Ca under the coulomb magnifying glass", Phys. Rev. Lett. **129**, 122501 (2022).

[170]J. Lee, J. A. Tostevin, B. A. Brown and others., "Reduced neutron spectroscopic factors when using potential geometries constrained by Hartree-Fock calculations", Phys. Rev. C **73**, 044608 (2006).